UNIVERSITAT DE BARCELONA
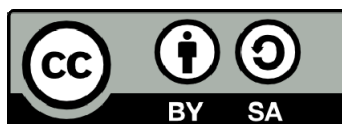
Star formation in cluster environments at Mm and Submm wavelenghts

Aina Palau Puigvert

UNIVERSITAT DE BARCELONA

DEPARTAMENT D'ASTRONOMIA I METEOROLOGIA

Star Formation in Cluster Environments at Mm and Submm Wavelengths

Memòria presentada per
Aina Palau Puigvert
per optar al grau de
Doctora en Ciències Físiques
Barcelona, gener de 2006

PROGRAMA DE DOCTORAT D'ASTRONOMIA I METEOROLOGIA

BIENNI 2000–2002

Memòria presentada per **Aina Palau Puigvert** per optar al grau de
Doctora en Ciències Físiques

DIRECTORS DE LA TESI

Dr. Robert Estalella   Dr. Paul T. P. Ho

Agraïments

Si hi ha moltes coses a la vida que un no pot fer sol, l'elaboració d'una tesi doctoral és un exemple molt clar. Per això, almenys en aquesta tesi, els agraïments són un 'capítol' molt important, sense el qual el lector podria fer-se una idea molt equivocada del que ha suposat realment aquest treball.

En primer lloc vull agrair molt sincerament tota l'ajuda, el recolzament i l'orientació rebuda per part dels directors, Robert Estalella i Paul Ho. Si bé m'han deixat prendre moltes iniciatives per la meva part, el seu suport científic i la seva disponibilitat per a guiar-me en cada una d'elles han estat constants i infal·libles, fins i tot en petits detalls. Moltes gràcies per exigir de mi tenacitat, rigurositat, i un esperit molt crític i molt lluitador. Sobretot, gràcies per exigir-me, ni més ni menys que el millor de mi: *just do your best!*

En el Departament d'Astronomia i Meteorologia, he rebut molt per part de molta gent. En particular, agraeixo amb profunditat l'ajuda del Dr. Josep Miquel Girart en molts aspectes científics del contingut d'aquest treball, així com les discussions científiques i l'ajuda informàtica del Dr. Òscar Morata, i també de la Dra. Rosario López i la Dra. Maite Beltrán. No ha estat menys valuosa l'atenció i la paciència d'en José Ramon Rodríguez, pel que refereix a tota la part burocràtica de la tesi. Per descomptat, el suport i l'ajuda també han vingut dels altres estudiants del Robert, el Josep Maria i la Gemma, amb qui he pogut discutir molts dels temes que apareixen en aquest treball. I tampoc hi poden faltar en aquesta llista els companys de despatx que he anat tenint: la Neus, la Inma i el Francesc.

Durant els viatges al Center for Astrophysics (CfA), hi ha molta gent a qui he d'agrair la seva actitud, especialment als Dr. Qizhou Zhang i Charlie Qi, que no han dubtat en cap moment a respondre amb tota la dedicació necessària qualsevol dubte, sobretot referent a les dades obtingudes amb el Submillimeter Array. D'una forma

i

molt particular, agraeixo al Dr. Todd Hunter l'estona de conversa durant la qual va sortir l'objectiu que ha definit aquesta tesi. Agraeixo moltíssim la col·laboració del Dr. Henrik Beuther, sempre disponible a contrastar els resultats, així com a proveir les dades necessàries per a procedir amb l'anàlisis i la interpretació de les dades. En aquest sentit, també agraeixo molt la col·laboració per part de la Dra. Serena Viti, del Dr. M. S. Nanda Kumar i de la Dra. Jennifer Hatchell.

Del CfA, el meu agraïment també és molt gran als estudiants del Paul, que van saber fer, des del primer dia, que em trobés gairebé 'com a casa'. Em refereixo a la Jenny, el Peter, la Robin, i la Maria. També des del primer dia l'Aurora i la Dra. Núria Calvet van oferir-me la seva ajuda. Del CfA no puc deixar de citar el personal administratiu, en particular la Margaret Simonini i la Muriel Hodges, que han demostrat tenir una gran paciència. En aquests viatges a l'estranger s'agraeix sempre d'una forma molt sincera aquelles persones que no han dubtat d'oferir la seva casa o el seu temps. Penso especialment en la Tracy i la Rima Rocha.

I ara ve un grup de persones a qui l'agraïment és especialment intens i sincer. El suport dels pares durant tota aquesta etapa, tant 'material' com sobretot 'moral' ha contribuït en gran part a que tot tirés endavant. M'atreveixo a dir que han estat també 'co-directors'! I dins d'aquest grup de persones hi ha totes les amigues 'del pis'. També a elles els hi dec molt de suport moral, ajuda pràctica i orientació.

Finalment, moltes gràcies també a tanta gent que ha col·laborat, de manera potser 'invisible' als ulls humans, pero de forma molt eficaç i molt real.

Moltíssimes gràcies a tots!

a la meva família

i a tots aquells que es deixen sorprendre per les meravelles del cel... i de la terra.

Contents

Resum de la tesi: Formació Estel·lar en Cúmuls a Longituds d'Ona Mm i Submm

Introducció

En contemplar un cel de nit ple d'estrelles moltes preguntes, algunes molt profundes, passen pel nostre cap, i quan veiem la Via Làctea creuant el cel, amb tantíssimes estrelles tan a prop les unes de les altres quedem sorpresos i meravellats. Fins i tot observant amb un telescopi petit es pot observar molts grups o cúmuls d'estrelles, cadascun amb estrelles molt a prop les unes de les altres i que semblen tenir un mateix origen. Es podria pensar que la majoria de les estrelles es formen en grup. Però, per què les estrelles haurien de 'preferir' formar-se en grup més que de forma aïllada? Aquest treball intenta respondre aquesta pregunta o, com a mínim, trobar algunes pistes que ens puguin indicar on està la resposta.

A la Via Làctea les estrelles es formen principalment als braços espirals i a prop del centre galàctic. En particular, les estrelles neixen en condensacions de gas on l'hidrogen es troba en forma molecular, els anomenats 'núvols moleculars'. Els núvols moleculars són les parts més denses i fredes del medi interestel·lar, envoltats per gas menys dens en forma atòmica. L'estudi del contingut estel·lar en núvols moleculars ha fet sorgir la idea que la formació estel·lar és un procés bimodal, és a dir, en algunes regions la formació estel·lar té lloc de forma més o menys dispersa en el núvol, formant-se típicament una estrella per cada nucli dens del núvol molecular (Lada et al. 1993b; Nikolić 2004). Aquest és el mode de formació estel·lar aïllat. En altres casos, en canvi, les estrelles es formen en mode de cúmul, és a dir, una

sola condensació de gas conté diferents nuclis densos i acabarà formant un grup d'estrelles, amb la distància entre elles molt més petita que pel cas de formació estel·lar aïllada. Els processos físics que regeixen la formació estel·lar en un mode in en un altre poden ser diferents i, mentre que existeix una teoria generalment acceptada de formació estel·lar aïllada (per ex., Shu et al. 1987), aquest no és el cas per la formació estel·lar en cúmul, tot i que s'han començat a fer algunes teories (Mac Low & Klessen 2004).

La majoria d'estrelles a la Galàxia es formen en mode de cúmul (Lada et al. 1991; Lada et al. 1993a; Zinnecker et al. 1993; Carpenter et al. 1995; Phelps & Lada 1997; Lada & Lada 2003; Hatchell et al. 2005). A més, a partir d'estudis fets al voltant d'estrelles de massa intermitja/alta s'ha trobat que aquestes tenen al seu voltant un nombre d'estrelles de baixa massa formant un cúmul i que com més massa té l'estrella central, més ric és el cúmul que té associat (Hillenbrand 1995; Testi et al. 1997, 1998, 1999; Massi et al. 2000; 2003). Això fa pensar que les estrelles massives es formen només en cúmuls i que estan relacionades amb el medi que les envolta.

En el mode de formació estel·lar en cúmul la interacció d'uns objectes amb els altres pot ser important ja que la distància entre ells és petita. Podem pensar en tres tipus d'interacció: la interacció d'una estrella d'alta massa amb el seu entorn, l'impacte dels fluxos moleculars en el medi circumdant, i la col·lisió de nuclis densos.

Suposant que en un nucli dens s'ha format una estrella d'alta massa ($\geq 8\ M_\odot$), l'estrella començarà a emetre radiació ultraviolada, que ionitza el medi circumdant creant una regió HII en expansió (Dyson & Williams 1997; Garay & Lizano 1999) i que a més exerceix una pressió de radiació sobre els grans de pols (Kahn 1974). A més, l'estrella massiva tindrà associat un vent estel·lar potent (Shull 1980; Garay et al. 1986). Tant a través del front the ionització, com per la pressió de radiació, o pel vent estel·lar, una estrella d'alta massa pot crear un front de compressió que anirà empenyent cap a fora el material que inicialment envoltava l'estrella, fins que el núvol original sigui completament dispersat (Megeath et al. 1996). S'ha suggerit en alguns estudis que el front de compressió podria induir la formació estel·lar en algun nucli dens del material circumdant (Hester & Desch 2005).

Un altre tipus d'interacció ve dels fluxos molecular impulsats pels objectes estel·lars joves (YSOs). Els fluxos moleculars produeixen gas d'alta velocitat, injectant moment i energia cinètica en el medi circumdant, i obren cavitats a mesura que avancen en el medi interestel·lar (Lefloch et al. 1998; Quillen et al. 2005). En algunes

regions s'ha trobat que el flux molecular ha impactat en material més dens (Bachiller & Pérez Gutiérrez 1997; Beltrán et al. 2002), i fins i tot en alguns casos s'ha proposat que la formació estel·lar ha estat induïda per l'impacte d'un flux molecular (Yokogawa et al. 2003).

Finalment, un altre tipus d'interacció en un cúmul és la col·lisió entre dos nuclis densos. Aquest tipus d'interacció podria induir també la formació estel·lar en els nuclis, com s'ha proposat pel cas de L723 (Girart et al. 1997).

Sobre aquest treball

Tal com s'ha vist, en medis de formació estel·lar en cúmul la interacció entre els diferents YSOs pot ser important, i fins i tot pot induir la formació estel·lar en alguns nuclis. L'objectiu d'aquest treball és doncs *caracteritzar differents medis de cúmuls en les primeres etapes de formació, per tal d'aclarir si la interacció entre els diferents YSOs és important per la formació estel·lar en aquests medis.*

L'estratègia a seguir serà la següent. Donat que es pretén estudiar medis de cúmuls en les primeres etapes de la seva formació, les regions estaran immerses en grans quantitats de gas i pols del núvol original, a una temperatura de 10–20 K. Per tant, l'emissió dels YSOs, principalment radiant a l'infraroig, serà absorbida i reemesa a longituds d'ona mil·limètriques (mm) i submm. Així doncs, farem el nostre estudi en aquests rangs de longituds d'ona. Ara bé, per tal de poder identificar els diferents YSOs de les regions que volem estudiar, situades la majoria a distàncies > 1 kpc, necessitem ser capaços de resoldre escales espacials de ~ 5000 AU, que és un tamany raonable per a l'embolcall d'una protostrella, i de ser sensibles a masses $\leq 1\ M_\odot$. Per a detectar nuclis amb masses $\leq 1\ M_\odot$, cal que les regions que estudiem no estiguin més lluny de ~ 3 kpc. Per tant, la resolució angular que necessitem és $2''$–$5''$, la qual cosa requereix l'ús d'interferòmetres. Així doncs, per a observar els medis de cúmuls utilitzarem interferòmetres que observin en el rang mm i/o submm.

De tota la instrumentació que s'ha utilitzat per a elaborar aquest treball hi ha un interferòmetre que és especialment interessant: el Submillimeter Array (SMA). Mentre que la resta d'instruments fa anys que estan en funcionament, el SMA es va inaugurar a finals del 2003. A més, el SMA és l'únic interferòmetre al món que observa a longituds d'ona submm, un rang on en molts casos les regions de formació estel·lar tenen el màxim d'emissió. Així doncs, l'ús del SMA és interessant per la

seva novetat i pel rang de longituds d'ona que permet estudiar.

La present tesi és el resultat de diferents treballs duts a terme entre el 2003 i el 2005. Durant aquest període, hem observat i estudiat quatre medis en cúmul, un que conté objectes de baixa massa, i tres que contenen a més estrelles de massa intermitja/alta. En el capítol 2 presentem els resultats per a la regió de baixa massa, HH 211, observada amb el SMA (Mauna Kea, Hawaii), i estudiem el medi que l'envolta a partir de treballs buscats a la literatura. En el capítol 3 mostrem el procés que s'ha dut a terme per tal de seleccionar les altres tres regions, pel qual ha estat necessari fer observacions amb el telescopi IRAM 30 m (Pico Veleta, Espanya) i amb l'interferòmetre Very Large Array (VLA, New Mexico, US). En els capítols 4, 5 i 6 presentem els resultats de les tres regions de massa intermitja/alta que s'han observat amb els interferòmetres Plateau de Bure Interferometer (PdBI, Alpes, France), SMA, i Berkeley-Illinois-Maryland Array (BIMA, Hat Creek, California), respectivament. Finalment, en el capítol 7 fem una discussió global dels resultats obtinguts en aquestes quatre regions i donem les conclusions generals d'aquest treball pel que fa a la formació estel·lar en cúmuls.

HH211: un cas simple the formació estel·lar en cúmul

HH 211 és una regió de formació estel·lar que pertany al cúmul IC 348, localitzat al núvol fosc de Perseus, on la formació estel·lar té lloc en mode de cúmul (Hatchell et al. 2005). IC 348 és un cúmul on la majoria d'estrelles que el formen són pre-seqüència principal. Està estructurat en un subcúmul central, i vuit subcúmuls més petits a les afores del subcúmul central (Lada & Lada 1995). Eislöffel et al. (2003) va trobar que un d'aquests subcúmuls més petits té un contingut estel·lar més jove que la resta de subcúmuls. Aquest subcúmul especialment jove es troba al sudoest de IC 348, i conté almenys dues fonts Classe 0: IC348 MMS i HH211 mm. IC348 MMS sembla ser la font impulsora d'un jet trobat a gran escala, i el seu lòbul sud passa a prop del flux molecular de HH 211 (Eislöffel et al. 2003). Entre mig d'aquestes dues fonts Classe 0 hi ha vàries fonts infraroges, la més brillant de les quals és IC348 IR, d'unes 4 $M_\odot$, i associada amb una petita nebulosa de reflexió vermella (Strom et al. 1974; Boulard et al. 1995).

En aquest treball hem estudiat amb més profunditat la font HH211 mm, i la seva interacció amb el medi circumdant. Hem observat l'emissió del continu submm a 850 μm i l'emissió de les transicions de CO(3–2) i SiO(8–7) amb el SMA. La font impulsora del jet s'ha detectat en el continu submm i hem trobat que té una morfologia allargada, perpendicular a la direcció del jet. El tamany deconvolucionat de la font impulsora és de 510×200 AU, i la seva massa està entre 0.02 i 0.06 $M_\odot$ (assumint la llei d'opacitats de Beckwith et al. (1990), un índex d'emissivitat de la pols igual a 1 i una temperatura de la pols entre 20 i 40 K).

L'emissió del gas d'alta velocitat tant pel CO(3–2) com pel SiO(8–7) mostra una estructura molt col·limada i amb nusos. Pel que fa al gas de baixa velocitat del CO(3–2), hem trobat que traça les parets de la cavitat excavada pel flux molecular. En canvi, el SiO(8–7) no presenta emissió de baixa velocitat. Hem calculat els paràmetres del flux molecular a partir de l'emissió del CO(3–2) seguint Yang et al. (1990) i sense corregir l'efecte de la inclinació del jet en el pla del cel. En general els paràmetres són típics de fluxos moleculars molt joves associats a fonts de baixa massa.

A la base del flux molecular, és a dir, molt a prop de la font impulsora, el SiO(8–7) cobreix un rang de velocitats molt ample, des de -20 fins a 40 km s^{-1}. Això suggereix que un vent d'angle ample podria ser el mecanisme que impulsa el flux molecular. Per a distàncies $\geq 5''$ (~ 1500 AU) de la font impulsora, l'emissió tant del SiO(8–7) com del CO(3–2) s'observa a velocitats més elevades a mesura que ens allunyem de la font, amb el SiO(8–7) arribant a velocitats sistemàticament més altes que el CO(3–2). Això indica que l'emissió de SiO(8–7) segurament traça material arrossegat que es troba més a prop del jet primari, mentre que el CO(3–2) traça gas arrossegat menys dens i per tant més lluny del jet primari. A més, també s'ha trobat que els nusos de SiO(8–7) es troben localitzats sistemàticament una mica més a prop de la font impulsora que els nusos de CO(3–2). Aquest fet suggereix que la diferenciació química és important al llarg del jet. Finalment, també s'ha comparat l'emissió del SiO(8–7) amb la del SiO(5–4) de Hirano et al. (2006), i s'ha trobat que el quocient de la temperatura de brillantor de SiO(8–7)/SiO(5–4) decreix per nusos que es troben més lluny de la font impulsora. Això és consistent amb el fet que la densitat decreix al llarg del jet, des de $(3$–$10)\times 10^6$ cm^{-3} a 500 AU fins $(0.8$–$4)\times 10^6$ cm^{-3} a 5000 AU de la font impulsora.

Per tant, es veu com la formació de la font HH211 mm és un cas senzill de for-

mació estel·lar en cúmul, on el jet de HH 211 interacciona amb el medi bàsicament arrossegant el material circumdant i creant una cavitat. Hem considerat la possibilitat que altres fonts del subcúmul de HH 211 estiguin interaccionant amb HH 211, però no n'hem trobat cap evidència a partir de les observacions de la línia d'emissió de H_2 a 2.12 μm (Eislöffel et al. 2003) i del continu submm (Hatchell et al. 2005). Així doncs, amb les dades de què es disposa actualment la formació de HH211 mm es pot dir que té lloc de forma aïllada, constituint el cas més simple de formació estel·lar en un cúmul. Per a continuar el nostre estudi de medis on hi ha cúmuls hem triat regions on es formen estrelles de massa intermitja/alta.

Una mostra de regions de formació estel·lar d'alta massa candidates a tenir cúmuls molt joves

Per tal de seleccionar medis molt joves de formació estel·lar en cúmul amb estrelles de massa intermitja/alta hem partit de tres llistes de candidats a protostrelles d'alta massa. D'aquestes llistes estem interessats només en aquelles regions on la detecció dels membres de baixa massa serà factible, i això implica un límit superior en la distància de les regions que triem. Fem notar que la majoria d'estudis fets amb interferometria mm/submm cap a regions d'alta massa (e. g., Molinari et al. 1998; Wyrowski et al. 1999; Ward-Thompson et al. 2000; Beuther et al. 2002a; Furuya et al. 2002; Molinari et al. 2002; Gómez et al. 2003; Shepherd et al. 2003; Fontani et al. 2004; Shepherd et al. 2004) no arriben a sensibilitats prou bones com per a detectar els possibles membres de baixa massa (normalment l'objectiu d'aquests treballs és estudiar l'estrella massiva en si, i per tant no hi ha necessitat d'assolir sensibilitats més grans).

Hem compilat una llista de regions amb candidats a protostrelles d'alta massa a partir de les llistes de Molinari et al. (1996), Mueller et al. (2002), i Sridharan et al. (2002), seleccionant només aquelles regions que compleixen els criteris següents:

1. *La lluminositat bolomètrica IRAS ha de ser* > 1000 $L_\odot$.

2. *La distància ha de ser* < 3.5 *kpc.*

   En la taula 3.4 (pàgines 48–51) presentem la llista de 99 regions que resulten d'aplicar aquests dos criteris de selecció a les tres llistes de candidats a

protostrelles d'alta massa citades més amunt. Per a seleccionar les fonts més prometedores per a observar amb un interferòmtre, hem adoptat dos criteris de selecció més:

3. *L'emissió mm en telescopis d'antena única ha de ser intensa, amb una intensi-tat de pic a 1.2 mm més gran que 100 m*Jy beam^{-1}*:* Aquest criteri és necessari perquè amb l'interferòmetre detectarem només una part de l'emissió detectada amb antena única, ja que els interferòmetres no són sensibles a l'emissió a gran escala i a més són capaços de resoldre la contribució de diferents fonts.

4. *L'emissió cm ha de ser feble, < 10 mJy a 3.6 cm, i d'un tamany < 0.1 pc:* Aquest criteri és necessari per assegurar que no hi ha una regió HII suficient-ment desenvolupada com per què hagi dispersat la major part del núvol original en un radi comparable al tamany del cúmul, que és d'uns ~ 0.4 pc. Per això rebutjarem aquelles regions on l'emissió cm sigui > 0.1 pc.

Per a les 99 regions de la llista hem recopilat de la literatura la informació referent a cada criteri de selecció, junt amb informació addicional que ens ajuda a confirmar o no l'estat evolutiu de les regions. Per a dues fonts que semblaven prometedores es va aconseguir temps d'observació als interferòmetres de SMA i BIMA, i els resultats es presenten en els capítols 5 i 6 respectivament.

Per a poder decidir els dos últims criteris en algunes regions que semblaven in-teressants però que no tenien observacions mm amb antena única o els hi faltava observacions cm, es va proposar d'observar 9 regions amb el telescopi IRAM 30 m, i 9 regions (algunes coincidint amb les regions del IRAM 30 m) amb el VLA. De les observacions amb IRAM 30 m, hem trobat que 5 de les 9 regions observades tenen emissió massa extensa com per ser detectada amb un interferòmetre, mentre que la resta de regions semblen bones candidates. Pel que fa a les observacions amb el VLA, ens han permès descartar dues regions perquè mostren emissió cm extensa, i les altres 7 semblen bones candidates. Com a resultat d'aquestes noves observa-cions trobem que hi ha dues fonts especialment interessants: IRAS 00117+6412 i IRAS 04579+4703. Vam proposar d'observar-les amb el PdBI i se'ns va concedir temps per a IRAS 00117+6412.

IRAS 00117+6412: primers resultats amb el PdBI d'una regió seleccionada a partir de les noves dades mm i cm

La regió IRAS 00117+6412 té unes 1400 $L_\odot$ i es troba a 1.8 kpc de distància (Molinari et al. 1996). Aquesta regió mostra emissió mm intensa i parcialment extensa i emissió cm compacta. La font cm coincideix amb la font infraroja més brillant de la regió, i té associats dos màsers d'aigua (Comoretto et al. 1990). A més, cap a aquesta regió s'ha detectat un flux molecular bipolar en CO(2–1) (Zhao et al. 2003; Zhang et al. 2005). A partir de l'emissió cm estimem un flux de fotons ionitzants de $3.6 \times 10^{44}\,\mathrm{s}^{-1}$, que correspon a una estrella de tipus espectral B2, i assumim que la font cm traça una regió UCHII.

Vam observar amb el PdBI l'emissió a 1 i 3 mm, així com l'emissió de les transicions N_2H^+(1–0) i CS(5–4), traçadores de gas dens. L'emissió del continu a 3 mm mostra dues fonts compactes dins del feix primari de 54″, i no presenta emissió mm associada a la regió UCHII. La més intensa d'elles, mm1, es troba a 15″ cap a l'oest de la regió UCHII, i és allargada en la direcció est-oest. L'altra font mm, mm2, es troba a uns 20″ cap al sud de mm1 (veure Fig. 4.1). A 1 mm hem detectat mm1, mentre que mm2 cau fora del feix primari. Les masses que derivem per mm1 i mm2 es troben al voltant de 1 $M_\odot$. L'emissió més intensa de gas dens traçada pel N_2H^+ està associada a mm1 i és allargada en la direcció est-oest. També trobem N_2H^+ associat a mm2, i una tercera condensació a uns 20″ cap a l'oest de mm2 (Fig. 4.3). Cap a mm1 hem detectat CS(5–4). Finalment, hem trobat gradients de velocitat associats amb mm1 i mm2.

D'aquests resultats preliminars ja es pot fer una primera aproximació de l'estat evolutiu de les fonts detectades a la regió. Primer, la regió UCHII no té associada ni emissió del continu mm ni emissió de gas dens traçat pel N_2H^+, cosa que suggereix que l'estrella ionitzant ha acabat la fase d'acreció de matèria i està dispersant el material del seu voltant. Aquest no és el cas, clarament, de mm1 i mm2. En aquestes dues fonts trobem tant emissió del continu mm com emissió de N_2H^+, i per tant aquestes fonts encara estan immerses en el material original d'on s'han format. Ara bé, mentre que mm1 coincideix espacialment amb dues fonts infraroges del 2MASS relativament intenses, mm2 es troba en una zona on l'emissió infraroja és

totalment inexistent, almenys a partir de la imatge de la banda K del 2MASS. Això porta a pensar que mm1 es troba en un estat evolutiu més avançat que mm2. La no detecció d'emissió infraroja cap a mm2 podria indicar que mm2 traça un objecte sense una font d'escalfament intern important, i per tant que és un nucli dens on encara no s'hi ha format una protostrella, o bé és una protostrella extremadament jove. Recordem aquí que la massa de pols de mm1 i mm2 són molt semblants, i per tant els diferents estats evolutius trobats per mm1 i mm2 probablement ens indiquen que aquestes dues fonts no s'han format simultàniament.

IRAS 20343+4129: una regió de formació estel·lar massiva enigmàtica

IRAS 20343+4129 és una regió de formació estel·lar que ha estat inclosa en la llista de candidats a protostrelles d'alta massa de Sridharan et al. (2002). La regió, d'unes 3200 $L_\odot$ i a uns 1.4 kpc de distància, es troba al nord-est de l'associació Cygnus OB2, i té gas dens associat (Richards et al. 1987; Miralles et al. 1994; Fuller et al. 2005). En l'infraroig proper Kumar et al. (2002) hi troba tres estrelles brillants: IRS 1 i IRS 3 que estan dins l'el·lipsoide d'error de la font IRAS, i IRS 2 més al nord. A més, Kumar et al. (2002) troba emissió de la línia de H_2 a 2.12 μm traçant una estructura amb forma de ventall que s'estén al sud de IRS 1 i que té al centre IRS 3. Observacions cm mostren que hi ha una font associada amb IRS 3 (Miralles et al. 1994; Carral et al. 1999). Per una altra banda, Comerón et al. (2002) fa un estudi de les estrelles massives de l'associació Cygnus OB2 i proposa que IRS 1 és una de les fonts més brillants de tota l'associació. A més, IRS 1 és una de les fonts de l'associació amb un excés infraroig més gran i no es detecta en el visible, la qual cosa fa pensar que si és una estrella d'alta massa, encara està molt immersa en grans quantitats de gas i pols. En canvi, observacions a longituds d'ona mm amb antena única no mostren un pic d'emissió de la pols associat a IRS 1 (Beuther et al. 2002b). Això planteja la qüestió de quina és la massa de IRS 1 realment. Amb antena única també es va trobar emissió d'almenys dos fluxos moleculars, però no està clar quines són les seves fonts impulsores. Nosaltres hem observat amb alta resolució angular l'emissió en el continu a 1 mm, així com l'emissió de CO(2–1), fent servir el SMA.

L'emissió del continu mostra tres condensacions principals de pols dins del feix primari de 45″ (Fig. 5.2). Dues d'aquestes condensacions queden a l'est i a l'oest de

IRS 3, mentre que la tercera es troba associada amb IRS 1. La condensació a l'oest de IRS 3 conté diferents subcondensacions, i entre elles hi ha les condensacions més intenses de tota la ragió, fins a 18σ. Cap a la condensació de l'est el SMA filtra gairebé tota l'emissió detectada amb antena única. La condensació associada amb IRS 1 té una massa de 0.2–0.5 $M_\odot$, amb una incertesa d'un factor quatre segons les propietats de la pols (llei d'opacitat i índex d'emissivitat de la pols). Cap a IRS 3 no hi detectem emissió de la pols, però en canvi IRS 3 és l'única font de la regió que té emissió cm associada.

Pel que fa a l'emissió de CO(2–1), hem descobert un flux molecular bipolar d'alta velocitat, allargat en la direcció est-oest, i IRS 1 és clarament la seva font impulsora (veure Fig. 5.6). Hem calculat els paràmetres del flux molecular i trobem valors comparables als valors dels fluxos associats amb estrelles de baixa massa. L'emissió de CO(2–1) de baixa velocitat també està associada a IRS 1, i a més presenta dues estructures febles, allargades més o menys en la direcció nord-sud, als dos costats de IRS 3.

L'emissió a gran escala del lòbul blau del flux molecular de CO trobat en antena única per Beuther et al. (2002c) és completament filtrat pel SMA, i per tant el lòbul no conté emissió compacta. Trobem que les nostres observacions són consistents amb un escenari en què el lòbul blau a gran escala traça una cavitat en expansió creada per IRS 3, i on les condensacions de pols trobades amb el SMA als dos costats de IRS 3 són el resultat de l'acumulació de massa en les parets d'aquesta cavitat en expansió. La cavitat en expansió podria ser impulsada o bé pel vent estel·lar de IRS 3, o bé radiativament, suposant que IRS 3 és una estrella B2 (tal com deduïm a partir de l'emissió cm, si assumim que l'emissió traça una regió HII fotoionitzada).

Pel que fa a la massa associada amb IRS 1, les nostres observacions de continu i de CO(2–1) suggereixen que IRS 1 és una font de baixa massa. Tot i amb això, aquest resultat no és consistent amb el tipus espectral anterior a B0 que Comerón et al. (2002) troben per IRS 1, basant-se en fotometria de 2MASS. Aquest tipus espectral tampoc és consistent amb la lluminositat bolomètrica IRAS, que correspon a tipus espectrals més tardans. Suggerim que IRS 1 és una protostrella variable de baixa massa, semblant a un objecte FU Ori, que va tenir un increment fort del flux després de les observacions fetes per IRAS, però anterior a les observacions fetes per 2MASS.

Finalment, hem trobat objectes amb diferents propietats i estats evolutius que s'han format en el mateix núvol original. A més, aquests objectes no es troben

distribuïts de forma aleatòria, sinó que la seva distribució sembla que està determinada per les condicions inicials del núvol juntament amb la inducció de la formació estel·lar pel front de compressió impulsat per una de les fonts formades dins del núvol.

IRAS 20293+3952: interacció i formació estel·lar contínua en un cúmul

IRAS 20293+3952 és una regió de formació estel·lar massiva a 2.0 kpc de distància (Beuther et al. 2004c) i que es troba a la part sud-oest de l'associació Cygnus OB2. La seva lluminositat bolomètrica és de 6300 $L_\odot$. Aquesta regió forma part de la llista de candidats a protostrelles d'alta massa compilada per Sridharan et al. (2002). La font IRAS està associada a una font cm que molt probablement traça una regió UCHII (Beuther et al. 2002d), i que es troba al centre d'un anell circular d'emissió en la línia de H_2 a 2.12 μm (Kumar et al. 2002). Observacions mm amb alta resolució angular fetes per Beuther et al. (2004b) mostren una font compacta i intensa, mm1, a $\sim 15''$ cap al nord-est de la regió UCHII, i que està associada amb un màser d'aigua (Beuther et al. 2002d). A més, Beuther et al. (2004b) detecten dues fonts mm més, mm2 i mm3, situades $10''$ cap a l'est de la regió UCHII, així com múltiples fluxos moleculars, alguns d'ells molt col·limats. Observacions posteriors a 2.6 i 1.3 mm fetes per Beuther et al. (2004c) mostren emissió de CN(1–0) molt a prop de mm1, mm2 i mm3. Nosaltres vam dur a terme observacions del continu a 3 mm i de l'emissió de gas dens traçat per N_2H^+, $NH_3(1,1)$ i $NH_3(2,2)$ cap a IRAS 20293+3952, juntament amb observacions de vàries transicions de $CH_3OH(2-1)$. El continu a 3 mm, l'emissió de N_2H^+, i de CH_3OH es van observar amb BIMA, mentre que l'emissió de $NH_3(1,1)$ i $NH_3(2,2)$ es va observar amb el VLA.

L'emissió de gas dens traçada per N_2H^+ i NH_3 mostra essencialment dos núvols, un cap a l'est de la regió UCHII (núvol principal), de ~ 0.5 pc de tamany, i un altre núvol cap al nord-oest (núvol oest) de la regió UCHII, de ~ 0.15 pc (veure Fig. 6.2). El núvol oest apareix corregut cap al vermell ~ 1 km s^{-1} respecte el núvol principal. Pel que fa a l'emissió del continu a 3 mm, hem trobat dues components intenses al nord del núvol principal, BIMA 1 i BIMA 2, i dues components més febles a la part sud, BIMA 3 i BIMA 4, juntament amb emissió extensa formant com un embolcall comú (Fig. 6.1). Referent a l'emissió de CH_3OH, hem trobat emissió intensa en

estructura de forquilla associada al flux molecular B, així com dues condensacions de CH_3OH formant com una cresta associats al flux molecular A (Fig. 6.2).

Hem obtingut els espectres de N_2H^+(1–0), NH_3(1,1) i NH_3(2,2) en una xarxa de $2'' \times 2''$ cobrint el núvol principal i el núvol oest, i hem ajustat l'estructura hiperfina per a cada espectre pel cas de N_2H^+(1–0) i NH_3(1,1), i una gaussiana pel cas NH_3(2,2). A partir dels resultats dels ajustos als espectres de NH_3(1,1) i NH_3(2,2) hem calculat mapes de temperatura rotacional i de densitat columnar de NH_3 i de N_2H^+. Per la temperatura rotacional hem seguit els procediments estàndard (Ho & Townes 1983; Sepúlveda 1993), per la densitat columnar de NH_3 hem seguit Anglada et al. (1995), i per la densitat columnar de N_2H^+, hem seguit Benson et al. (1998).

El mapa de temperatura rotacional obtingut mostra que la temperatura és més alta al nord del núvol principal, al voltant de 22 K, que al sud, al voltant de 16 K. Hem trobat tres màxims locals de temperatura que semblen estar associats a YSOs immersos, un d'ells associat a una font 2MASS i els altres dos, el Màxim Local Nord, i el Màxim Local Sud, associats amb emissió feble en el continu a 2.12 μm.

La distribució de densitats columnars de N_2H^+ és semblant a l'emissió de la pols, que és intensa al nord i feble al sud del núvol principal. En canvi, el mapa de densitat columnar de NH_3 té els valors més alts al sud del núvol principal. Amb l'objectiu de comparar l'emissió de NH_3 amb la de N_2H^+, hem convolucionat els mapes de canals de N_2H^+, NH_3(1,1) i NH_3(2,2) per tal de tenir la mateixa resolució angular de $7''$ (l'eix més gran dels feixos de N_2H^+ i NH_3). Hem ajustat espectres a cada posició en una xarxa de $4'' \times 4''$ en els mapes convolucionats, i hem derivat la densitat columnar pel N_2H^+ i pel NH_3, corregint per l'atenuació del feix primari de cada interferòmetre (BIMA i VLA). El mapa del quocient NH_3/N_2H^+ de densitats columnars mostra una forta diferenciació química en la regió. En particular, trobem un gradient molt clar des del nord-oest del núvol principal, amb un quocient ~ 50, fins al sud-est, on el quocient creix fins a ~ 300. Aquests valors tan alts també s'assoleixen al núvol oest. Notem que els valors baixos del quocient NH_3/N_2H^+ es troben a la part del núvol principal on hi ha més activitat de formació estel·lar, a diferència dels valors alts, que es troben associats a nuclis on gairebé no trobem signes d'activitat estel·lar. Això és consistent amb el fet que el NH_3 sigui realçat respecte el N_2H^+ per a densitats moderades ($\sim 10^5$ cm^{-3}), mentre que per a densitats al voltant de 10^6 cm^{-3}, el NH_3 podria començar a dipositar-se en grans de pols, mentre que el

N_2H^+ es mantindria en fase gasosa fins a densitats encara més altes.

Hem indentificat tres nuclis de NH_3 amb temperatures relativament baixes i sense emissió infraroja associada, de forma similar als nuclis 'sense estrella' trobats en regions de formació estel·lar de baixa massa, però amb temperatures lleugerament més altes, ~ 15 K, possiblement degut a escalfament extern del núvol, ja sigui per la regió UCHII i/o per estrelles OB properes de l'associació Cygnus OB2. Aquests nuclis estan associats a BIMA 3, BIMA 4 i el núvol oest.

La interacció entre les diferents fonts de la regió és important. Primer, la regió UCHII està interaccionant amb el núvol principal, escalfant-lo i realçant l'emissió de CN(1–0) a les vores del núvol que queden en front de la regió UCHII. Segon, el flux molecular A sembla que estigui excavant una cavitat i escalfant les seves parets. Tercer, el flux molecular B sembla estar interaccionant amb el nucli de NH_3 associat a BIMA 4, sent aquesta la causa segurament de la deflexió observada en el flux molecular B en la posició de BIMA 4. La radiació emesa per l'impacte del flux molecular B amb BIMA 4 sembla que estigui il·luminant una condensació on hi hem trobat línies de CH_3OH estretes, situada a ~ 0.2 pc cap al nord-est de la posició d'impacte. A més, hem trobat que el Màxim Local Nord molt probablement és la font impulsora del flux molecular B.

Hem indentificat al voltant d'uns vuit YSOs en el gas dens al voltant de la regió UCHII. Aquests YSOs tenen masses circumstel·lars entre < 0.4 i ~ 4 $M_\odot$, i semblen estar en estats evolutius diferents, fins i tot tenint en compte només les fonts de baixa massa. Per tant, en aquesta regió sembla que les estrelles no s'estan formant simultàniament.

Mentre que no podem descartar que la interacció entre les diferents fonts hagi induït la formació estel·lar en algun cas particular, la formació estel·lar induïda no pot explicar la distribució global dels diferents YSOs, suggerint que aquesta distribució queda essencialment determinada per les condicions inicials en el núvol molecular.

Discussió general i Conclusions

En aquest treball s'ha fet un estudi amb alta resolució angular i alta sensibilitat de quatre medis de formació estel·lar en mode de cúmul a longituds d'ona mm i submm, amb l'objectiu de caracteritzar aquests cúmuls i estudiar la interacció entre els diferents objectes estel·lars joves (YSOs) del cúmul. Les conclusions principals són:

1. En les quatre regions estudiades s'ha trobat estats evolutius diferents no només entre les fonts d'alta massa i les fonts de baixa massa, sinó també entre les fonts de baixa massa, la qual cosa indica que els membres en el cúmul no es formen simultàniament.

2. S'ha fet la primera llista de regions de formació estel·lar d'alta massa que s'han observat amb suficient sensibilitat per a detectar les fonts de baixa massa al voltant de l'estrella massiva a longituds d'ona mm i submm. A partir de la llista (que inclou les regions estudiades en aquest treball i dues regions més de la literatura) s'ha trobat que la *mediana* de fonts mm/submm al voltant d'un YSO massiu és més baixa que la *mediana* de fonts infraroges al voltant d'una estrella d'alta massa. Tot i que aquest resultat d'ha de confirmar amb més observacions, suggerim que el nombre més petit de fonts mm/submm és degut al fet que els membres en un cúmul no es formen simultàniament i que el temps típic en què un YSO és brillant a longituds d'ona mm/submm és més petit que el temps típic en què un YSO és brillant a l'infraroig.

3. Per a les quatre regions estudiades s'ha trobat grups de fonts predominantment en un estat evolutiu particular associat amb una escala espacial de 0.1–0.3 pc, semblant al tamany dels cúmuls i dels nuclis densos. Això suggereix que la formació estel·lar en mode de cúmul té lloc en nuclis densos, i que cada nucli comença a formar estrelles independentment dels altres nuclis.

4. En les tres regions de formació estel·lar de massa intermitja/alta la interacció entre les fonts sembla ser important, i podria induir formació estel·lar en alguns casos. De totes maneres, la distribució global dels YSOs en el cúmul no es pot explicar únicament per formació estel·lar induïda, i les condicions inicials en el núvol poden ser també importants.

5. A partir de l'experiència adquirida en aquest treball, s'ha trobat que les futures observacions de regions molt joves de formació estel·lar d'alta massa s'han de dur a terme amb sensibilitats fins a $\sim 0.1~M_\odot$, i amb molt bon recobriment u-v. A més, s'ha trobat que la construcció d'imatges a partir del continu mm/submm i la construcció de mapes de temperatura de les regions, per exemple a través de la molècula de NH_3, són eines complementàries per a indentificar fonts immerses de baixa massa. Finalment, s'ha trobat que la diferenciació química juga un paper important en les regions joves de formació estel·lar en cúmul, i que per tant s'ha d'utilitzar diferents molècules traçadores de gas dens per tal de caracteritzar degudament aquestes regions.

Figure: View of the Submillimeter Array at the end of 2003, when all eight telescopes were operating on Mauna Kea in Hawaii.

Chapter 1

Introduction: the relevance of cluster environments in star formation

1.1 Why studying cluster environments

1.1.1 The sites of star formation

The observation of the night sky with naked eye reveals the white path of the Milky Way crossing the full sky, where stars seem to be closely packed. Even with a small telescope, a high number of star clusters are visible, each one containing a number of stars close to each other that seem to have a common origin. One may think that this is the case for most of the stars. But, why should stars preferently form 'closely packed' rather than in isolation? This work is an attempt to answer this question or, at least, to find some clues that can give us an answer.

These intuitive results arising from the simple observation of the sky with naked eye have been deeply investigated during many years, by many scientists and by making use of the most advanced instruments available. Stars in the Galaxy are formed in the spiral arms as well as near the center of the Galaxy. In particular, their birth sites are condensations of gas where hydrogen is in molecular form, called 'molecular clouds'. Molecular clouds are the densest parts of the interstellar medium,

and are surrounded by less dense gas with hydrogen in the atomic form. Their interior is inhomogeneous, and contains regions of enhanced density called 'clumps'. Throughout these work, dense clumps that may collapse to form a star or a group of stars will be called 'cores', following the terminology of Larson (2003).

Molecular clouds are usually classified in two main categories, according to their mass. Molecular clouds of low mass ($< 10^4 \, M_\odot$) are traditionally called 'dark clouds', because they are abundant and, thus, some are found near the Sun, and are seen as a dark shape in contrast with the background field stars because their dust absorbs the radiation from the stars behind. These 'dark clouds' typically have sizes of 0.5–1 pc, masses $\sim 10^3 \, M_\odot$, and temperatures around 10 K. Molecular clouds of high mass ($> 10^4 \, M_\odot$) are less abundant, and are found in large complexes, the so called Giant Molecular Clouds (GMCs). GMCs have masses up to $10^6 \, M_\odot$ and sizes of ~ 50 pc , much larger than those of dark clouds. The internal structure of GMCs is hierarchichal, with smaller clumps inside larger ones, and clumps may have filamentary morphologies. In addition to having higher masses than dark clouds, GMCs have associated high-mass stars, while in dark clouds only low-mass stars are formed.

Among the best studied star forming regions near the Sun, we can find molecular clouds of both categories. One of the molecular clouds closest to the Sun (~ 140 pc) is the Taurus-Auriga complex. This complex is composed of several dark clouds forming low-mass stars, and the dense cores which already contain stars typically have only one to a few stars per core (Benson & Myers 1989). The cores are widely distributed in the molecular cloud, and ~ 100 young stellar objects (YSOs) have been counted in a area of 15 pc $\times$ 20 pc, implying a stellar surface density of ~ 0.3 stars pc^{-2} (Lada et al. 1993b). Another example of a nearby molecular cloud is Perseus, at a distance of ~ 315 pc. Perseus is associated with two clusters of stars and one OB association, and thus it is forming stars more massive than Taurus. In the outer parts of one of the clusters, Lada & Lada (1995) find eight other 'subclusters', each one having between 5 and 20 stars inside a diameter of 0.2–0.4 pc, yielding a surface stellar density $\gtrsim 100$ pc^{-2}, and thus stars in Perseus are formed in groups, tighter than in Taurus. There are however molecular clouds where stars are formed still more densely packed. The Orion Molecular Cloud contains the GMC nearest to the Sun, at ~ 450 pc. Mapping in CO of the large-scale gas distribution shows that the molecular material is concentrated in two large clouds, Orion A and Orion B, and both are associated with regions of active star formation

(Maddalena et al. 1986; Lada et al. 1993b). While star formation in Orion A is found distributed, with single stars forming from individual cores, and also in clusters (like the Trapezium cluster), in Orion B 96% of the sources associated with the cloud are found in three rich clusters, and these clusters constitute a small fraction (2%) of the total area of the CO cloud (Lada et al. 1991a; Lada 1999). This leads to the conclusion that star formation in Orion B is a higly localized process for both high-mass and low-mass stars. The Orion Molecular Cloud is the closest cloud forming high-mass stars, and most sites of high-mass star formation are located at distances higher than 1 kpc from the Sun.

From observational studies it appears that star formation takes place in two modes: the isolated or distributed mode, and the clustered or closely-packed mode. In the isolated mode, stars form in loose aggregates, typically forming one star (or a multiple system) per dense core, like in the Taurus-Auriga complex, and stars are more or less uniformly distributed in the cloud. Since the stellar surface density is low, the gravitational collapse occurs independently for individual small cores to form single stars. The first detailed theories of formation of single stellar systems assume this isolated mode (e. g., Shu et al. 1987). In this context, the dense core is initially turbulent and magnetically supported, and turns out to be dynamically unstable through ambipolar diffusion of magnetic fields. The core collapses from the inside-out, and the inner regions form a protostar. Assuming that the core was initially slightly rotating, a disk is formed around the protostar, while the material in the outer envelope continues infalling spherically onto the star-disk system. At some point, a strong wind or outflow developes along the polar axis and progressively clears up the surrounding material. Once the protostar has accreted most of its surrounding material, it becomes visible at optical wavelengths as a young star-disk system.

In the clustered mode of star formation, a single massive clump of dense gas, containing closely-packed cores, produces a group of stars, which may or may not evolve to form a bound cluster (Lada et al. 1993b; Nikolić 2004). The clustered mode of star formation is characterized by high stellar surface densities, and by a distribution of stars in tight groups. Perseus and Orion are examples of this mode of star formation, with stars forming not in isolation but in a densely-packed environment, or 'cluster environment'.

Star formation in a cluster environment may differ from isolated star formation

in different aspects. For example, fragmentation seems to play an important role in the formation of a cluster because the separation of stars in clusters is smaller than the size of cores forming stars in isolation (Lada & Lada 2003). However, the physical mechanism producing fragmentation is not well understood yet (see, e. g.,Vázquez-Semadeni 2004 and references therein). Another aspect which may differ from isolated star formation is the role of magnetic fields. Magnetic diffusion is not likely regulating the formation of stellar groups (it can regulate only the formation of individual stars), because star formation in clusters is finished in a timescale about three times shorter than the magnetic diffusion time through all the cloud (Elmegreen et al. 2000). Still another aspect concerns the way the YSO gains mass. In a cluster environment, the collapsing fragments may gain mass not only from their own envelope (as in the case of an isolated star) but also from the reservoir of gas shared with the other collapsing fragments in the group, or even through collisions with other YSOs (e. g., Bonnell et al. 2001). Finally, because stars form 'closely-packed' in a cluster, interaction between the different objects is more likely than in the isolated mode. Overall, physics governing the star formation in the clustered mode may be different from the physics governing the isolated mode. Theories of star formation in cluster environments appeared recently (e. g., Mac Low & Klessen 2004) but these are not so well consolidated as theories for star formation in isolation. Therefore, detailed observations of cluster environments in the first stages of star formation are needed to contrast with model predictions.

1.1.2   Most stars are born in cluster environments

The isolated mode of star formation in Taurus is not the common mode of star formation in the Galaxy, since most stars in the Galaxy of all masses seem to form in clusters (Clarke et al. 2000). First, most star formation takes place in GMCs rather than in dark clouds (Zinnecker et al. 1993; Williams et al. 2000). Second, inside GMCs, most stars are formed in clusters. This has been studied by carrying out near-infrared and/or submm surveys in the Orion B cloud (Lada et al. 1991b; Li et al. 1997; Carpenter 2000), in Mon OB1 (Lada et al. 1993a), in the Rosette cloud (Phelps & Lada 1997), in Gem OB1 (Carpenter et al. 1995), and in Perseus (Hatchell et al. 2005). These works suggest that the fraction of stars formed in clusters is around 70–90% (Lada & Lada 2003), and thus that the clustered mode of star formation is the dominant mode in GMCs, and hence in the Galaxy.

In addition, clusters with more massive stars have been found to have higher stellar densities. For example, loose goups of stars, with stellar densities around a few stars per cubic parsec, contain typically low-mass stars (Gómez et al. 1993), while clusters with higher stellar densities (around 10^4 stars pc^{-3}) contain both high-mass and low-mass stars (Hillenbrand & Hartmann 1998). Filling the gap between the loose groups and the richest clusters are the clusters studied at near-infrared wavelengths around Herbig Ae/Be stars (Hillenbrand 1995; Testi et al. 1997, 1998, 1999) and intermediate-mass Class I sources (Massi et al. 2000; 2003), with stellar densities around 10^3 stars pc^{-3}. These studies also find a dependence of the richness of the cluster on the mass of the intermediate-mass star, fitting well the trend observed between low-mass and high-mass star-forming regions. Therefore, while the majority of stars seem to form in clusters, these studies show that high-mass stars form *only* in clusters (although this is not definitively stablished, e. g., Gerhard et al. 2002).

This relation between the mass of the most massive star in the cluster and the richness of the cluster additionally suggests that the formation of a (massive) star is related to its surrounding medium. At present, it is not well understood if this relation arises because the final properties of the stars are determined by the medium or because the stars interact with the medium and determine its properties. Possibly, both 'stars' and 'medium' influence each other, and thus one could think that initial conditions and/or interaction between the different sources play an important role in cluster environments.

1.1.3 The role of interactions in cluster environments

Let us consider the scenario in which closely-packed cores in a high-density clump of a molecular cloud are active sites of star formation. We have seen above that the physics involving star formation in clusters may differ from that in isolated environments. In particular, the interaction between the different objects may play a role. In this section we consider three types of interaction: first, interaction of a high-mass star with the surrounding medium; second, impact of outflows on the surrounding medium; third: mergers of cloud cores.

Interaction of high-mass stars with the surrounding medium

We briefly summarize first how a high-mass star is supposed to form, under the different points of view which are currently in debate. Any theory for high-mass star formation must be consistent with the main observational facts found for high-mass stars. Among the most important observational results, there is first that high-mass stars are closely related to clusters (e.g., Lada & Lada 2003; Kumar et al. 2006) and that mass segregation has been observed in some clusters (Hillenbrand & Hartmann 1998). A second result recently found is that outflows, some of them collimated (Beuther et al. 2002c; Gibb et al. 2003a; Beuther et al. 2004b; Zhang et al. 2005), and disk-like structures (Cesaroni et al. 1997, 1999a; Zhang et al. 2002; Kumar et al. 2003; Sandell et al. 2003; Beltrán et al. 2004; Patel et al. 2005) have been detected in massive protostars, suggesting that there is disk-mediated accretion in high-mass stars. However, for the highest luminosity sources flattened accretion flows not forming an accretion disk have been found (Sollins & Ho 2005).

High-mass star formation faces basic theoretical problems, due to the fact that massive stars start to burn hydrogen while still accreting mass (e.g., Bernasconi & Maeder 1996), producing a large luminosity and intense flux of ionizing photons. The first problem is that spherically symmetric accretion models for high-mass stars show that the radiation pressure reverts the accretion flow before the star has acquired its final mass (Kahn 1974; Wolfire & Casinelli 1987). The problem is loosened, but not fully solved, when considering nonspherical accretion (Nakano 1989; Jijina & adams 1996). The second problem is related with the ionizing photons from the massive star. When UV photons ionize the surrounding medium they create an HII region (or ultra compact HII (UCHII) region when its size is $\lesssim 0.1$ pc and its density is $\gtrsim 10^4$ cm^{-3}), that expands and could stop further accretion of material onto the star. If the HII region is quenched close enough to the star, then accretion may continue. Today, two models for the formation of high-mass stars are proposed: the 'competitive accretion' models and the 'high mass accretion rate' models.

In the 'competitive accretion' model, stars in a clump are formed with low masses, $\sim 0.5\ M_\odot$, and grow their mass through accretion from unbound gas in the clump and through collisions (Bonnell, Bate & Zinnecker 1998; Stahler, Palla & Ho 2000). In the center of the clump the stellar densities may be as high as 10^8 stars pc^{-3}, and hence merging of low-mass stars is possible. While this model can account for the observational fact that high-mass stars are found in the center of rich clusters, it

finds difficulties in explaining the collimated outflows observed toward massive stars. Furthermore, the high stellar densities predicted are about 3 orders of magnitude higher than the stellar densities observed (Hillenbrand & Hartmann 1998). Still, theoretically it is not clear whether these models can successfully solve the radiation pressure problem, as well as the confinement of the UCHII region, since competitive accretion rates are as small as $\sim 10^{-7}$ $M_\odot$ yr^{-1} (McKee & Tan 2002; Edgar & Clarke 2004). Finally, theoretical work shows that for typical properties of clumps, competitive accretion within them cannot be effective (Krumholz et al. 2005b).

The 'high-mass accretion rate' models are the models in which the high-mass star is built up in a massive core through a high mass accretion rate, which is achieved by the high pressure of the environment and/or by the influence of an external trigger (e. g., Hennebelle et al. 2003). Massive cores inside a molecular cloud may arise from turbulent fragmentation (Padoan & Nordlund 2002), and cannot be thermally supported (because the thermal Jeans mass is ~ 1 $M_\odot$ for the temperature of star-forming regions), they are likely supported by turbulence. In the 'turbulent core' model of McKee & Tan (2003), the high pressure of the environment in which the massive cores form yields high densities for the cores, and hence high mass accretion rates, around 10^{-3} $M_\odot$ yr^{-1}, which form a high-mass star in 10^5 yr. Such rates have been recently observed toward massive stars (e. g., Keto & Wood 2006). The results of the 'turbulent core' model were compared with models of infalling envelopes heated by a central massive star by Osorio et al. (1999), who fit the spectral energy distributions of hot molecular cores and find the best fits for mass accretion rates slightly higher than those predicted by the turbulent core model. While in the 'turbulent core' model the initial massive cores are only twice as massive as the mass of the final star, in the models of Osorio et al. (1999) the massive cores contain hundreds of solar masses (González-Avilés et al. 2005). Whatever is the mechanism by which the high mass accretion rates are achieved, the consequent ram pressure by the infalling material confines the stellar wind and chokes off the HII region from the massive star. When a small amount of rotation is considered in the modeling, a circumstellar disk is formed and the radiation pressure problem is still loosened through the 'flashlight effect' (radiation reverses infall along the poles while accretion goes on through the equatorial disk, Yorke & Sonnhalter 2002). In addition, the incorporation of outflows in the models reduces the effects of radiation pressure because the outflow cavity collimates the radiation (Krumholz et al. 2005a). Thus, it seems likely that in these models the effects of radiation pressure are reduced significantly so that accretion can build massive stars. The ionization problem is

solved in these models because the mass accretion rates ($\sim 10^{-3}$ $M_\odot$ yr^{-1}) are high enough to trap the ionizing photons near te stellar surface, where the sound speed of the ionized material remains smaller than the escape velocity of the gravitational field of the central star (Walmsley 1995; Keto 2002, 2003). Observational evidences of accretion through an UCHII region (Sollins et al. 2005) support these models of trapped HII regions. Eventually the mass accretion rate will decrease and/or the radiation from the central star will be high enough to reverse the infall, allowing the stellar wind to blow out, and allowing the HII region to expand into the surrounding medium.

Thus, when a high-mass star is formed it will interact with the surrounding medium through the developement of an HII region, through its powerful stellar winds and through radiation pressure (and at the end of its life, through the explosion of the star as a supernova, but in this work we focus only on the first stages of star formation).

The developement of an HII region starts when the ionizing photons are no longer trapped close to the stellar surface, photodissociating and ionizing the gas in its surroundings until the flux of ionizing photons equals the rate of recombinations. Such a region of ionized gas will have temperatures around 10^4 K, producing a difference in pressure between the ionized gas and the surrounding gas, and the consequent expansion of ionized gas pushing forward the surrounding material (see, e. g., Dyson & Williams 1997; Garay & Lizano 1999). The ionization front, which is preceeded by a compression front, increases the pressure in the medium and can transfer momentum and energy into it.

Another source of input of energy and momentum into the interstellar gas by the massive star is its stellar wind. Assuming that the stellar wind and the UCHII region are both present from the begining of the nuclear burning, the stellar wind interacting with the surrounding medium produces a shell of circumstellar gas, expanding away from the massive star, that is partially ionized because it is exposed to the UV radiation from the ionizing star. The shell is driven by the pressure of the hot bubble of shocked stellar wind. Shull (1980) investigates under which conditions a stellar wind will be dynamically more important than the expansion by thermal pressure of the UCHII region, and find a relation between the mechanical luminosity of the wind, the flux of ionizing photons and the initial density of the ionized gas. For typical luminosities of winds (Garay et al. 1986) and for the fluxes

of ionizing photons of B stars it seems possible that the wind will be dynamically more important than the expansion of the UCHII region.

Radiation pressure on dust grains also may transfer energy and momentum in the surrounding medium, and can also produce, as stellar winds and HII regions, shell-like morphologies. Kahn (1974) studies the problem and find that a shell of circumstellar material will be driven away from the massive star if the luminosity to mass ratio is higher than a critical value that depends on the abundance of dust grains in the interstellar gas. However, it seems that radiation pressure is less important than stellar winds (Turner & Matthews 1984).

Therefore, either through the expansion of an UCHII region, either by the effects of a stellar wind or through radiation pressure, it seems that the momentum input to the interstellar gas from a massive protostar is able to put into motion significant amounts of the surrounding gas, which will be led by an advancing compression front ahead of a shell-like structure. Compression fronts have been observed in different massive star-forming regions (see Hester & Desch 2005 and references therein). A point in which we are particularly interested is that compression fronts driven by massive stars may trigger star formation. As seen above, massive stars are formed in cluster environments, surrounded by cores which are possible sites of star formation. These cores, if evolve on their own, may finally form stars or may be transient cores (Morata et al. 2003; Garrod et al. 2005) which will be dispersed with time. How does affect the passage of the compression front to these cores surrounding the massive star? Since the mass of a core required for collapse decreases with increasing pressure (e.g., Larson 2003), it is likely that cores that may have never formed stars, do undergo collapse when the compression front reaches them increasing their pressure. Some observations seem to corroborate this triggered star formation by compression fronts (e.g., Wilking et al. 1984; Redman et al. 2003; Healy et al. 2004; Thompson et al. 2004; Deharveng et al. 2005; Lee et al. 2005; Zavagno et al. 2006). After the passage of the compression front the parental cloud will be completely disrupted and a cluster of infrared/optical sources will emerge. The destruction of the parental cloud occurs on a timescale of ~ 0.1 Myr (Megeath et al. 1996).

Impact of outflows on the surrounding medium

In addition to the interaction of a high-mass star, another type of interaction in cluster environments is produced by the outflows from the YSOs formed in the cloud. Even in regions of small stellar densities, such as L1551 in Taurus, outflows seem to play an important role in neighboring star formation (Yokogawa et al. 2003). Thus, one would expect that in more crowded environments the impact of outflows on the medium will be noticeable. Recent high-angular resolution observations of high-mass star-forming regions reveal multiple outflows associated with the cloud forming the high-mass star (e. g., Beuther et al. 2002a; Beuther et al. 2003; Gibb et al. 2003a; Kumar et al. 2004; Sandell et al. 2005).

Outflows and winds from YSOs inject momentum and kinetic energy into the surrounding gas, and create cavities in their parental cloud (e. g., Arce & Goodman 2002). Toward NGC 1333, Quillen et al. (2005) identify up to 20 cavities of ~ 0.1 pc in the ^{13}CO maps, and interpret them as remnants of past outflow activity (see also Lefloch et al. 1998). This suggests that the structure seen in NGC 1333 is the result of excavations by the outflows from the YSOs in the cloud. Thus, outflows may determine the internal structure of cloud cores, and even may disrupt the surrounding molecular cloud (Reipurth et al. 1997; Reipurth & Bally 2001).

Considering the interaction of an outflow with a medium where cores are closely packed, it seems likely that while the outflow is excavating a cavity in the medium it may find a pre-existing core in the way. The impact of an outflow on a core compresses and heats the gas in the core, producing a 'shock chemistry' that increases the abundance of some molecular species (e. g., L1157: Bachiller & Pérez Gutiérrez 1997; IRAS 21391+5802: Beltrán et al. 2002). In some cases star formation in a dense core is proposed to have been triggered by the swept-up shell of an outflow impacting on it. For example, Yokogawa et al. (2003) considered the scenario in which the outflow from L1551 IRS5 has triggered the formation of a Class 0 object deeply embedded in the redshifted lobe of the outflow. Thus, while the creation of cavities by outflows has been observed in different cases, the possibility that outflows induce the collapse on pre-existing cores is also plausible, especially in a cluster environment.

Mergers of cloud cores and/or protostars

In the inside of a molecular cloud that has undergone fragmentation into densely packed cores one may expect to find cores collapsing at different times and evolving at different rates (Bally & Zinnecker 2005), and thus this environment may contain a mixture of cores without stars (starless), protostellar cores (cores that already contain a YSO), and possibly young stars. Encounters of two (starless) cores must be low-energy events, because cores are diffuse, while encounters between protostellar cores and stars are more energetic but less likely. We consider here whether there is observational evidence of mergers between cores without stars and/or protostellar cores. Note that on larger spatial scales high-velocity cloud-cloud collisions have been studied as the mechanism triggering the formation of a cluster of stars (Usami et al. 1995, and references therein), but we concentrate here on the collisions which may occur inside a molecular cloud.

Signs of interaction between protostellar cores have been found in the massive clump NGC 2264-C. Peretto et al. (2005) interpret a sharp velocity discontinuity of ~ 2 km s^{-1} observed in different dense gas tracers as a strong dynamical interaction between two protostellar cores which could be possibly merging. On the other hand, interaction of cloud cores with no signs of star formation has been proposed as a possible mechanism for triggering the formation of the Class 0 source in L723 (Girart et al. 1997). This scenario is suggested by the morphology and kinematics of the dense gas, while the free-fall time for the formation of the low-mass source is consistent with the timescales involved in the merging process. Other cases of possible collision of two cloud cores are IRAS 2306+1451 (Vallée 1995), and OMC-1 IRc2 (Wiseman & Ho 1996). In spite that in most of these cases the merging of cores are only possible scenarios and that regions where merging has been demonstrated are scarce, it seems reasonable to think that merging of cores in cluster environments is feasible.

Overall, star formation in cluster environments may be affected by interaction between the different sources. The interaction of a high-mass star with the surrounding medium is likely leaving a clear footprint in the surrounding material, which should show more evolved YSOs closer to the high-mass star, and the younger, farther away.

The impact of outflows on cores and merging of two cloud cores might produce star formation localized in the parts of the cloud affected by this triggering. Studying in detail particular cluster environments may help elucidate the relevance of all these processes in star formation in clustered mode.

1.2   About this work

1.2.1   Goal of the thesis

In the paragraphs above, we have seen that in a cluster environment there may be different types of interaction between the members of the cluster.

The goal of this thesis is *characterizing different cluster environments in their first stages of formation, in order to elucidate whether interaction between the members plays an important role for star formation in these environments.*

For this, we will select individual cluster environments. The characterization will consist in identifying the members of the cluster, even the low-mass members if possible, and estimating their main properties. Interaction will be addressed through the study of molecules tracing outflows and shocks.

1.2.2   Approach and strategy: why mm and submm interferometry

Most of the studies of clusters have been carried out in the infrared, since instrumentation did not allow to perform large surveys in the mm and submm range. However, our goal is studying different cluster environments with the members *in their first evolutionary stages*, and hence YSOs in these environments will be still deeply embedded in the molecular cloud and may not be detectable in the infrared, since the cold surrounding gas will absorbe and reemit at longer wavelengths the infrared radiation of the YSOs. In addition, there may be cloud cores not intrisically emitting in the infrared because they do not harbor any YSO that heats them. Therefore, because we aim at observing the first stages of star formation, we will carry out our observations in the mm/submm range.

There are several ways to identify possible sites of star formation in a star-forming region. One way is the study of the thermal radiation of dust, observing the continuum at mm/submm wavelengths. Another way is studying the emission of dense gas tracers with lines detectable in the mm range, such as CS, HCO^+, NH_3, and N_2H^+. These molecules (with critical densities $\gtrsim 10^4$ cm^{-3}), reveal cores with higher density in a molecular cloud, and thus the possible sites of future or current star formation. The study through dense gas tracers must be carried out by observing different molecules, since the effects of chemical differentation (such as depletion onto dust grains, and photon-dissociation by UV radiation) affect differently each molecule. The cores traced by mm/submm continuum or dense gas tracers may harbor already protostars or not yet any, but describe well the possible sites of future or on-going star formation as a first approximation. Finally, in order to study the interaction of the different members in the region we will observe the emission of shock/outflow tracers, such as CO, SiO or CH_3OH, which reveal the interaction of YSOs with the cloud.

Most of the cluster environments studied in this work harbor an intermediate/high-mass protostar. In order to properly characterize the medium around a massive protostar, it is necessary to be sensitive to small ($\lesssim 5000$ AU) and low-mass (≤ 1 $M_\odot$) cores of gas and dust. In order to detect cores of low masses we should observe relatively nearby (< 3 kpc) massive star-forming regions, while most high-mass stars are at distances ≥ 1 kpc. Therefore, it will be necessary to achieve angular resolutions between $2''$–$5''$, which requires using interferometers and not single-dish telescopes. In conclusion, for the study of the individual cluster environments we need to use mm/submm interferometers.

1.2.3   The new instrumentation used: the Submillimeter Array, the first submm interferometer

The instrumentation used in this work involves one single-dish telescope and four interferometers. While three of the interferometers have been operating during years and are well known instruments, the Submillimeter Array (SMA) is an interferometer that was opened to do science at the end of 2003, and thus is a new instrument. A detailed description of the SMA is given in Ho et al. (2004) and references therein. The array is located on the top of Mauna Kea (Hawaii, see the figure introducing this chapter), one of the best astronomical sites in the world, and currently has

receiver bands at 230, 345, and 690 GHz. Bands at 460 and 850 GHz are planned to be available in the future. The capability of observing at submm wavelengths makes this interferometer unique in the world. The array consists of 8 telescopes of 6 m of diameter, and can be configured to reach a maximum angular resolution of $0\rlap{.}''1$–$0\rlap{.}''5$. The primary beam is $17''$–$52''$.

Depending on the configuration used for the observations, the SMA antennas are placed in different pads. There are 24 pads distributed in four nested rings. The location of the pads has been chosen to achieve a maximum uniform sampling of the u-v plane spacings within a circular boundary. There are three possible configurations: compact (inner and second ring), extended (up to the third ring), and very extended (up to the fourth ring). Transport of the antennas from one pad to another is done by means of a special transporter (not by rails), which picks up and moves the 50 ton telescopes.

Each antenna contains currently a helium cryostat with the receivers for the 230, 345, and 690 GHz bands, and has space for five additional receivers. Observing simultaneously with two receivers is possible with the SMA (at the moment, the possible combinations are 230/690 and 345/690, and more combinations will be possible in the future).

The SMA correlator is very flexible and can be configured in many ways, yielding unique capabilites of spectral line imaging. The intermediate-frequency band is 2 GHz, and the separation between sidebands is 10 GHz. Each sideband is broken up into six blocks of 328 MHz, and each block splits up into four chunks or basebands of 104 MHz (usable bandwith of 82 MHz). In the configuration of the correlator that provides uniform spectral resolution accross the 2 GHz bandwidth, each baseband has 128 spectral channels, yielding a spectral resolution of 0.812 MHz accross the full 2 GHz band. This makes the SMA an extremely efficient instrument to perform imaging spectral line surveys, as has been shown in the work of Beuther et al. (2004d). Correlator configurations with higher spectral resolution for particular basebands can currently be achieved by reducing the spectral resolution in other basebands.

Calibration at submm wavelengths faces the problem that the number of strong quasars is lower than at mm and cm wavelengths because quasar fluxes decrease rapidly toward shorter wavelengths. In addition, instrumental noise is higher toward shorter wavelengths. Planets are used to do passband calibration and flux

calibration, for which the effects of absorption lines and the variation of the flux with baseline length are taken into account in the calibration process. Flux calibration can be done also with strong quasars. For phase calibration one must find a relatively strong quasar nearby the target source. In spite the challenges of observing in the submm range, the SMA allows to investigate with high-angular resolution many astrophysical objects that radiate strongly in the submillimeter range, like high-mass protostars and clusters in the first stages of formation. The only instruments observing in the submm prior to the construction of the SMA were single-dish telescopes with an angular resolution around $10''$. The SMA is providing up to 2 orders of magnitude higher angular resolution, and thus it is a clue instrument for the research in astrophysics.

1.2.4 Outline of the thesis and status of the different works constituting the thesis

This thesis is the result of different works carried out between 2003 and 2005. During this period, we have observed and studied four cluster environments, one of low-mass stars and the other three containing intermediate/high-mass stars. In the following, we outline the different parts of the thesis and explain which is the status of each work.

In chapter 2 we show the results for the low-mass region, HH 211, observed with the SMA, and study its environment from works in the literature. This work, entitled *Submillimeter emission from the hot molecular jet HH 211*, and authored by A. Palau, P. T. P. Ho, Q. Zhang, R. Estalella, N. Hirano, H. Shang, C.-F. Lee, T. L. Bourke, H. Beuther, and Y.-J. Kuan, appeared in the Astrophysical Journal Letters, 2006, volume 636, page 137.

In chapter 3 we describe the selection process carried out to choose the other three massive star-forming regions. In the selection process we first compiled a list of 99 massive star-forming regions which are well suited to detect an embedded cluster, and we used a mm single-dish telescope, the IRAM 30 m Telescope (Pico Veleta, Spain), to observe the large-scale continuum emission of dust in different promising regions. We additionally used the Very Large Array (VLA, New Mexico, US) to search for emission from ionized gas toward some regions which lacked cm observations.

In chapter 4 we present the preliminary results of an intermediate-mass region selected from the observations described in chapter 3, which was observed with the Plateau de Bure Interferometer (PdBI, Alpes, France). The reduction process was carried out in Grenoble in 2005 April, and this work is still in progress. These first results already reveal that this is an active star forming region.

In chapter 5 we show the results of an intermediate/high-mass star-forming region observed with the SMA. This work has been presented as a poster in the Conference *Submillimeter Astronomy in the era of the SMA* held in Cambridge (Massachusetts, US) in June 2005, and is currently in preparation for a publication.

In chapter 6, we show the results for an intermediate/high-mass star-forming region observed with the Berkeley-Illinois-Maryland Array (BIMA, Hat Creek, California). This work is finished, and will be submitted to Astronomy and Astrophysics as soon as the final comments of the coauthors will be incorporated in the paper.

Finally, in chapter 7 we discuss the global results from these four cluster environments and summarize the main conclusions derived from this work.

HH 211

IC348 IR +
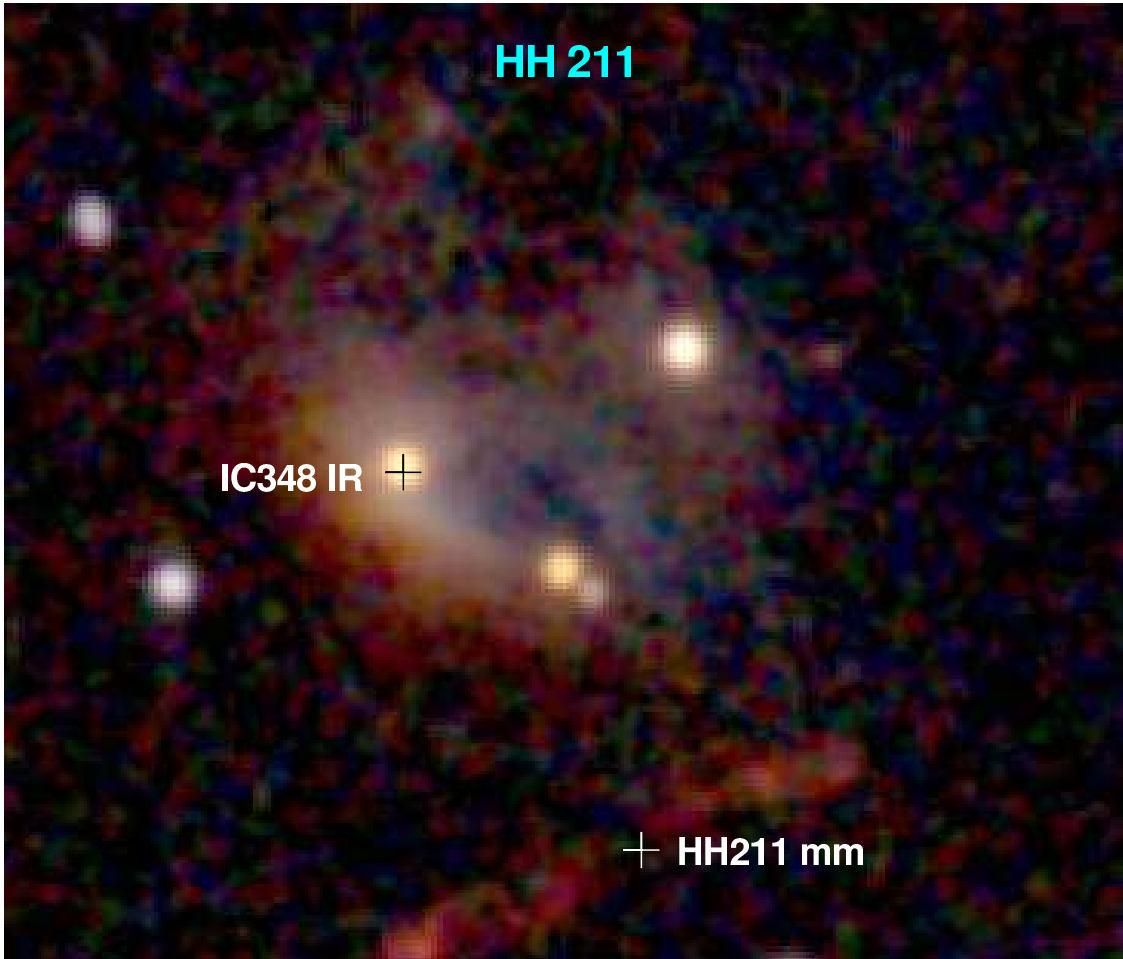
+ HH211 mm

Figure: 2MASS composite image of J, H, and K filters of the HH 211 region. Red objects in the image are sources with high H–K color (more embedded objects). Note that HH211 mm is not visible at these wavelengths.

Chapter 2

HH211: a simple case of star formation in a cluster

2.1 The medium where HH211 mm is forming

In this chapter we study the formation of a low-mass protostar, HH 211 mm, which belongs to the young open cluster IC 348, located in the Perseus dark cloud. Perseus is associated with two clusters of pre-main-sequence stars (IC 348 and NGC 1333), and the Per OB2 association containing one B0.5 star. Observations with the JCMT at 450 and 850 μm toward Perseus reveal that more than 80% of the dust cores detected belong to a cluster of submm cores, and thus star formation in Perseus is taking place in clustered mode (Hatchell et al. 2005).

IC 348 contains hundreds of stars found in the optical, infrared and in X-rays (see references in Eislöffel et al. 2003), most of them being pre-main-sequence stars. The structure of IC 348 consists of one central subcluster and eight small subclusters in the outskirts of the central one, as found by Lada & Lada (1995). Eislöffel et al. (2003) find that one of the small subclusters, located in the southwest of the main subcluster, seems to be in very early evolutionary stages, younger than in other parts of IC 348. The size of this subcluster is $\sim 4'$ (~ 0.35 pc at 315 pc), and the two youngest sources known to date are IC348 MMS and HH211 mm. In Figure 2.1 we show a view of this young subcluster. IC348 MMS is a compact millimeter source found at 1.3 mm with the IRAM-30m Telescope by Eislöffel et al. (2003). The authors suggest that this millimeter source is driving a large scale

jet, oriented roughly in the north-south direction (marked with a straight line in the figure), and classified this source as a Class 0 source. About $2'$ to the south of IC348 MMS there is HH211 mm, a compact millimeter source driving the jet HH 211 (McCaughrean et al. 1994). This source, similarly to IC348 MMS, is not seen in the infrared at 2 μm, and has been detected at 3 mm and 1 mm (Gueth & Guilloteau 1999), suggesting that it is also a Class 0 source. Half-way between IC348 MMS and HH211 mm there are different 2MASS sources, the most prominent being the intermediate-mass source IC348 IR, associated with a small red reflection nebula (Strom et al. 1974; Boulard et al. 1995).

The study of Hatchell et al. (2005) shows that there are about 18 submm cores with masses larger than 0.4 $M_\odot$ associated with the southwestern subcluster of IC 348 (some of them are shown in Fig. 2.1). From the infrared population, Hatchell et al. (2005) derive a star formation rate in IC 348 which is consistent with the number of submm cores found, suggesting that the star formation rate has been constant in the southwest of IC 348. Therefore, star formation is still going on in the IC 348 cluster, but it is localized in the southwestern subcluster, that is, around HH 211.

2.2 The interaction of HH211 mm with the surrounding medium

HH211 mm was found after the discovery of the HH 211 outflow. HH 211 is a warm and energetic molecular outflow located in the IC 348 complex at 315 pc, which was discovered by McCaughrean et al. (1994) from observations of H_2 (at 2.12 μm). The inclination from the plane of the sky is supposed to be small, around $10°$ (Hirano et al. 2006). The outflow in the CO(2–1) transition shows a well collimated structure at high velocities, and traces the outflow cavity walls at low velocities (Gueth & Guilloteau 1999). On the other hand, the SiO emission has been detected with single-dish telescopes up to the 11–10 transition, indicative of gas densities $> 10^6$ cm^{-3} along the jet (Nisini et al. 2002; Chandler & Richer 2001). Recently, Hirano et al. (2006) observed HH 211 in the SiO(5–4) transition and found a highly collimated structure consisting of a chain of knots. The innermost knots likely trace the primary jet launched at the close vicinity of the protostar. In order to study the interaction of the HH 211 outflow with the surrounding material, we have carried
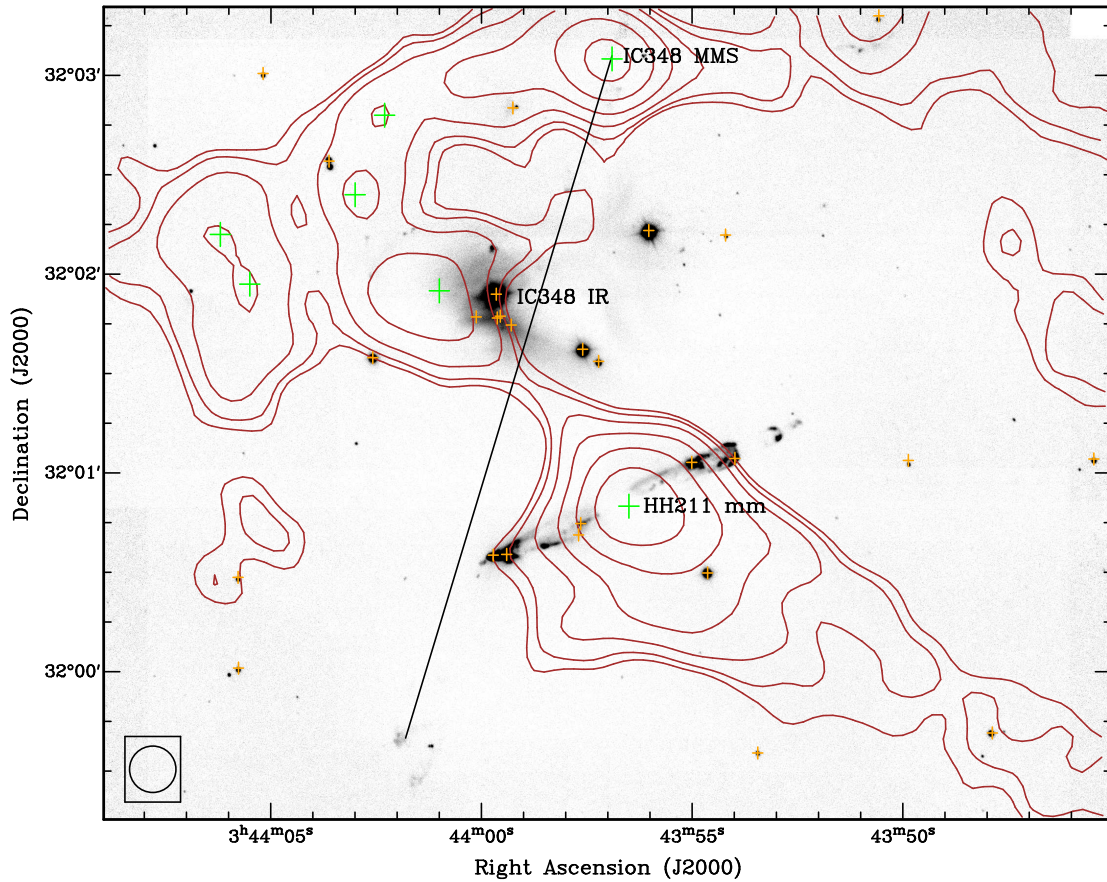
Figure 2.1: Continuum emission (contours) at 850 μm by Hatcell et al. (2005) overlaid on the H$_2$ image of the southwestern side of IC 348 (Hirano et al. 2006). Contours are 25, 50, 100, 200, 400, and 800 mJy beam^{-1}. Orange crosses are 2MASS sources, and green crosses indicate the center of the submm cores identified by Hatchell et al. (2005). The straight line indicates the direction of the north-south outflow discovered by Eislöffel et al. (2003). The beam of the 850 μm continuum emission, $14''$, is indicated in the bottom left corner.

out observations of the high-J transitions CO(3–2) and SiO(8–7) with high-angular resolution.

2.2.1　Observations

Observations of HH 211 with the Submillimeter Array[1] (SMA; Ho et al. 2004) in the 345 GHz band were carried out on 2004 October 4 and October 18, with seven antennas for each day in the compact configuration. The phase reference center of the observations was α(J2000) = $03^h43^m56^s.8$, δ(J2000) = $+32°00'50''.4$, and the projected baselines ranged from 14.7 to 127 m. The half-power width of the SMA primary beam at 345 GHz is $\sim 36''$. During each track, we observed 3 pointing fields, separated from the central pointing by $26''$ (to southeast) and $21''$ (to northwest) along the axis of the jet. The correlator was configured in the standard mode, providing a uniform spectral resolution across the full 2 GHz IF band in each sideband of 0.8125 MHz (or 0.7 km s^{-1}). The frequency range covered by the lower and upper sidebands was 335.58–337.55 GHz, and 345.59–347.56 GHz, respectively. The passband of each dataset was calibrated in MIR-IDL[2] by using both sidebands of Saturn for the Oct 4 dataset, and the lower sideband of Venus for the Oct 18 dataset (lower sideband of Venus was used to calibrate the lower sideband and the upper sideband). The maximum error due to passband calibration across the full 2 GHz sideband was about $\sim 20\%$. Gain calibration of the visibility phases and amplitudes and flux calibration was performed in the Multichannel Image Reconstruction Image Analysis and Display (MIRIAD) software package (Sault et al. 1995) using 3C 84 as the gain and flux calibrator, for which we set the flux to be 1.7 Jy (value independently measured with the SMA at 345 GHz within 15 days from our observations). The typical rms of the gain phases was $\sim 65°$, and the overall flux uncertainty is estimated to be about 15%.

Imaging of data cubes was made in MIRIAD by combining the data from the 3 pointings in the visibility plane, and cleaning in a box covering the full extent of the jet. The final maps include both Oct 4 and Oct 18 datasets, and have a

---

[1]The Submillimeter Array is a joint project between the Smithsonian Astrophysical Observatory and the Academia Sinica Institute of Astronomy and Astrophysics, and is funded by the Smithsonian Institution and the Academia Sinica.

[2]MIR-IDL was developed originally for the Owens Valley Radio Obsevatory and was adapted for the SMA. For a description of MIR, see Qi 2006 at http://cfa-www.harvard.edu/ cqi/mircook.html.

synthesized beam of $1''94 \times 0''97$ (P.A.= $67°2$), with an rms noise level per channel (of 2 km s^{-1} wide) of 0.30 and 0.25 Jy beam^{-1} for the CO(3–2) and SiO(8–7), respectively. Although weather conditions were not very good on Oct 4 ($\tau_{230} \simeq$ 0.1, compared with $\tau_{230} \simeq 0.04$ for Oct 18), the combination of Oct 4 and Oct 18 datasets improved the S/N for the line emission. Continuum emission at 345 GHz was obtained by averaging the spectral channels free of line emission. The continuum image shown in this letter is the result of combining the upper and lower sideband data of the Oct 18 dataset only, with natural weighting of the u-v data and without spatial restrictions in the image cleaning process. The synthesized beam of the continuum map was $2''04 \times 1''02$ (P.A.= $63°9$), and the rms noise level was 7 mJy beam^{-1}.

2.2.2   Results

CO(3–2) and SiO(8–7) emission

The systemic velocity of HH 211 is 9.2 km s^{-1} (velocities in this work are Local Standard of Rest). CO(3–2) emission is detected up to -14 km s^{-1} for the blue side of the outflow, and up to 40 km s^{-1} for the red side. In Fig. 2.2a we show an overlay of the low-velocity CO(3–2) emission on the H$_2$ emission at 2.12 μm from Hirano et al. (2006). We find CO(3–2) low-velocity emission associated with the brightest infrared knots, as well as weak emission tracing a shell-like structure, similar to the CO(2–1) emission in the same velocity range (Gueth & Guilloteau 1999).

The CO(3–2) high-velocity emission ('high-velocity' refers to velocitites lower than 0 km s^{-1} and higher than 20 km s^{-1}) traces a very well collimated and knotty jet-like structure, and is very close to the axis of the cavity traced by the low-velocity CO and the H$_2$ emission (see Fig. 2.2b).

The SiO(8–7) emission is very weak for velocities close to the systemic velocity, but is detectable up to -20 and 42 km s^{-1} (see spectrum in Fig. 2.2c). The high-velocity SiO(8-7) emission (Fig. 2.2c) is also very well collimated and clumpy. However, the SiO is found much closer to the protostar than the CO for the high-velocity emission. We have adopted the same nomenclature for the knots as Hirano et al. (2006). Toward the strongest H$_2$ features, there is no significant high-velocity CO(3–2) or SiO(8–7) emission (for a discussion on H$_2$ excitation and a comparison

Table 2.1: Physical Parameters[a] of the HH 211 Outflow from CO(3–2)

Age (yr)	N_{12} (cm^{-2})	Mass ($M_\odot$)	$\dot{M}$ ($M_\odot$ yr^{-1})	P ($M_\odot$ km s^{-1})	$\dot{P}$ ($M_\odot$ km s^{-1} yr^{-1})	E_{kin} (erg)	L_{mech} ($L_\odot$)	L_{bol} ($L_\odot$)
1400	6.0×10^{16}	0.0013	9.3×10^{-7}	0.022	1.6×10^{-5}	3.8×10^{42}	0.015	3.6[b]

[a] The parameters were obtained as follows: age $= t_{\mathrm{dyn}}$ (see main text); rate of the outflow mass: $\dot{M} = M/t_{\mathrm{dyn}}$; momentum: $P = MV_{\mathrm{range}}$ (V_{range} is the range for which we integrated the emission for each lobe, see main text); momentum rate (or mechanical force): $\dot{P} = P/t_{\mathrm{dyn}}$; energy of the outflow: $E = 1/2\, M\, V_{\mathrm{range}}^2$; mechanical luminosity: $L_{\mathrm{mech}} = E/t_{\mathrm{dyn}}$.

[b] From Froebrich (2005).

with SiO emission in HH 211, see Chandler & Richer 2001). Regarding the medium in which the HH 211 jet is propagating, the emission from NH$_3$ and H^{13}CO$^+$ reveals an elongated condensation of ~ 1 $M_\odot$, located on the red side of the jet, as shown in Fig. 2.2b (Bachiller et al. 1987; Gueth & Guilloteau 1999; Wiseman et al. 2001).

We estimated the physical parameters of the outflow from the CO(3–2) emission (Table 2.1) assuming optically thin emission in the wing, and an excitation temperature of ~ 12 K (derived from the line intensity). The age or dynamical timescale t_{dyn} was derived by dividing the size of each lobe ($25'' \times 3''$) by the maximum velocity reached in the outflow with respect to the systemic velocity (30.8 km s^{-1} for the red lobe, and 23.2 km s^{-1} for the blue lobe; the value given in the table is the average of the dynamical timescales derived for the red and for the blue lobes). See the Appendix for the expressions used to derive the column density of CO and the mass of the lobes. The values shown in the table are not corrected for the inclination effect. The derived age and mass are consistent with those obtained by Gueth & Guilloteau (1999) from CO(1–0) and CO(2–1) with the PdBI.
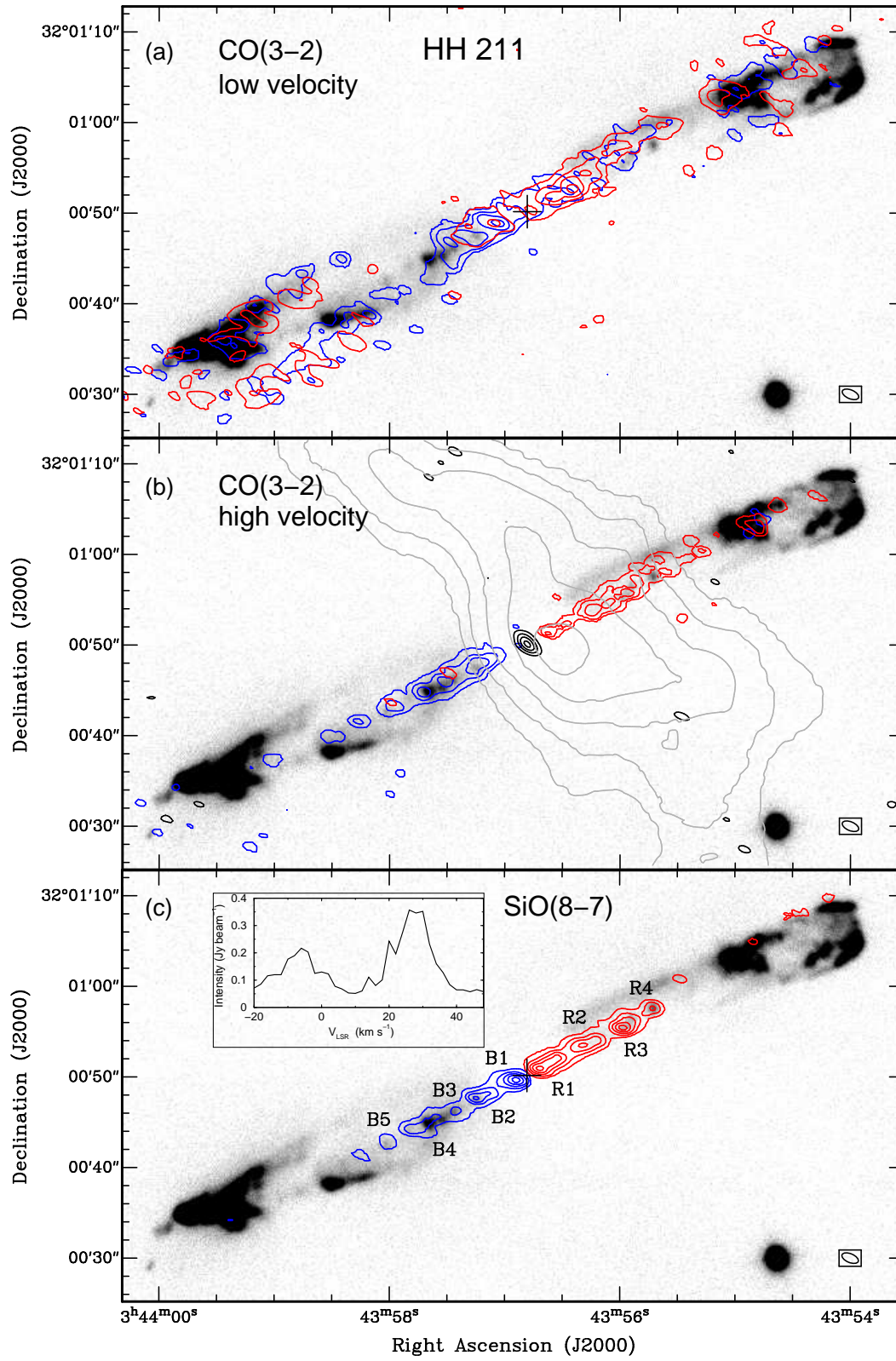
Figure 2.2: (see behind)

Figure 2.2: *(a)* Contours: CO(3–2) emission integrated for low velocities (2 to 8 km s^{-1}, blue, and 10 to 18 km s^{-1}, red). Blue and red contours start at 15% of the peak intensity (blue: 26.34 Jy beam^{-1} km s^{-1}; red: 33.44 Jy beam^{-1} km s^{-1}), and increase in 25% intervals. The cross marks the position of the submillimeter continuum source (as in the bottom panel). *(b)* Color contours: CO(3–2) emission integrated from -14 to 0 km s^{-1} (blue) and from 20 to 40 km s^{-1} (red). Blue and red contours start at 10% of the peak intensity (blue: 25.31 Jy beam^{-1} km s^{-1}; red: 18.36 Jy beam^{-1} km s^{-1}), and increase in steps of 30%. Black contours: submillimeter continuum emission. Contours start at 0.03 Jy beam^{-1} and increase in steps of 0.03 Jy beam^{-1}. Grey contours: zero-order moment map of the NH$_3$(1,1) emission from Wiseman et al. (2001). Contours start at 10% of the peak intensity, 94.9 Jy beam^{-1} km s^{-1}, and increase in steps of 20%. *(c)* Contours: SiO(8–7) emission integrated from -20 to 0 km s^{-1} (blue) and from 20 to 42 km s^{-1} (red). Blue and red contours start at 10% of the peak intensity (blue: 41.75 Jy beam^{-1} km s^{-1}; red: 49.09 Jy beam^{-1} km s^{-1}), and increase in 20% intervals. Knots labeling is the same as Hirano et al. (2006). An inlay of the SiO(8–7) spectrum averaged over the central 10$''$ of the jet is also shown (1 Jy beam^{-1} corresponds to 5.4 K). In all panels, the grey scale is the deep image of the H$_2$ emission at 2.12 μm from Hirano et al. (2006), and the clean beam, shown in the bottom-right corner, is 1$.''$94 $\times$ 0$.''$97, P.A.= 67$.°$2.

Continuum emission

In Fig. 2.2b, we show the continuum emission overlaid on the high-velocity CO(3–2) emission. We detected the source at the center of the outflow with $S/N = 18$. The position for the source derived from a Gaussian fit is α(J2000) = $03^\mathrm{h}43^\mathrm{m}56\overset{\mathrm{s}}{.}8$, δ(J2000) = $+32°00'50\overset{''}{.}2$. The deconvolved size of the source is $(1\overset{''}{.}6 \pm 0\overset{''}{.}2) \times (0\overset{''}{.}6 \pm 0\overset{''}{.}1)$, corresponding to 510×200 AU, and the deconvolved position angle (P.A.) is $26° \pm 4°$. The P.A. of the large-scale jet in the integrated SiO emission has been determined to be $116\overset{\circ}{.}2 \pm 0\overset{\circ}{.}2$. Thus, we find that the submillimeter continuum source, which is likely tracing the disk, is exactly perpendicular to the large-scale collimated jet emanating from it, to within the measurement error.

The peak intensity of the source is 0.13 ± 0.02 Jy beam^{-1}, and the flux density is 0.22 ± 0.02 Jy. Assuming that the dust emission is optically thin and well described by a modified black body law, we can estimate the mass of the disk, for a given dust emissivity index and dust temperature. We assumed the opacity law of Beckwith et al. (1990), and an emissivity index $\beta \simeq 1$. The uncertainty in the mass due to uncertainties in the opacity law and in the dust emissivity index is estimated to be a factor of four. For dust temperatures of 20–40 K, we derive a mass for the disk ranging from 0.02 to 0.06 $M_\odot$, only $\sim 5\%$ of the mass of the large-scale NH$_3$ condensation (see above). The derived mass is 3 times lower than the value obtained at 230 GHz by Gueth & Guilloteau (1999) for the same opacity law, dust emissivity index and dust temperature, indicating that our measurements at 345 GHz could be tracing only the warmer part of the dusty disk.

2.2.3   Discussion and Conclusions

SiO(8–7) versus SiO(5–4)

Observations toward HH 211 in the SiO(5–4) transition at 217 GHz were carried out by Hirano et al. (2006), with similar angular resolution. In order to compare the maps from both transitions, we convolved the moment-zero maps (integrated over all velocities) with a Gaussian to achieve a final beam of $1\overset{''}{.}95$, the largest major axis of the SiO(8–7) and SiO(5–4) beams.

We computed the SiO(8–7)/SiO(5–4) brightness temperature ratio map after
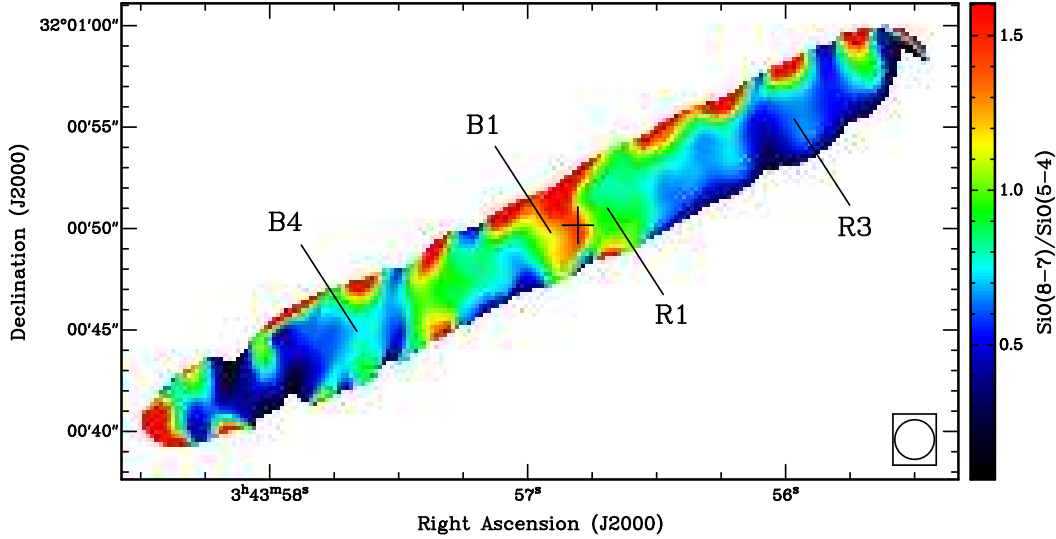
Figure 2.3: Map of the ratio SiO(8–7)/SiO(5–4), performed using the task MATHS in MIRIAD on the images of SiO(8–7) and SiO(5–4) integrated over all the velocity range, and smoothed to the same angular resolution of $1.''95$. The ratio is made by shifting the SiO(5–4) map $(+0.''19, +0.''07)$, the offset between the positions of the continuum source at 217 GHz and 345 GHz.

correcting for the offset found in the position of the continuum source of both images ($\sim 0.2''$ in declination), and the result is shown in Fig. 2.3. The uncertainty in the ratio is $\sim 20\%$. While the value for the ratio at the position of the innermost knots, B1 and R1, is ~ 1, far away from the protostar the ratio decreases down to ~ 0.5. Comparing the ratio with the results of LVG modeling of Nisini et al. (2002), we set ranges for the density. Note that the SiO(8–7)/SiO(5–4) ratio is not very sensitive to temperature variations for $T \gg 100$ K, since the SiO(8–7) upper level energy is ~ 75 K. At the position of B1 and R1 (~ 500 AU) we estimate that, for temperatures in the range 100–1000 K, the density must be $(3–10) \times 10^6$ cm^{-3}. On the other hand, $\sim 15''$ (or 5000 AU) away from the center of the jet the ratio is 0.5, and this yields a density of $(0.8–4) \times 10^6$ cm^{-3}. This is consistent with the density derived by Hirano et al. (2006) from the SiO(5–4) jet and by Nisini et al. (2002) from the single-dish data. Therefore, the density of the innermost knots seems to be about 1 order of magnitude higher than that of the knots farther out along the jet.

SiO(8–7) versus CO(3–2)

Position-velocity (p-v) plots were computed for both CO(3–2) and SiO(8–7) emission from 0.7 km s^{-1} wide channel maps along the axis of the jet, P.A.= 116°. Since the CO emission is somewhat extended in the direction perpendicular to the jet axis, we have smoothed the image with a gaussian twice the beam of the observations, and with a position angle perpendicular to the axis of the jet, in order to enhance the S/N of the CO emission in the p-v plot. An overlay of SiO on the CO p-v plot is presented in Fig. 2.4.

First of all, there is a distinct gap in CO emission from 7 to 8 km s^{-1}, affecting all positions along the jet. CO(3–2) and (1–0) observations of low angular resolution ($\sim$ 15″; Hirano et al., in preparation) show an absorption feature at the same velocity. The gap is probably due to an intervening cold cloud along the line of sight.

In the CO(3–2) p-v plot, one can see a low-velocity component, extending along all positions and tracing the shell structure seen in the low-velocity map from Fig. 2.2a, and a second component tracing the high-velocity material, with velocities increasing with distance from the protostar (Hubble-law), up to velocities of ~ -14 km s^{-1} (blue side) and ~ 40 km s^{-1} (red side). Note that for CO no high-velocity emission comes from the positions close to the protostar. As for SiO(8–7), the p-v plot shows several features. Contrary to the CO case, only very weak SiO emission is coming from the low-velocity material. The SiO emission resembles the CO emission at distances greater than $\sim 5″$, with velocities increasing with distance. However, the most remarkable characteristic of the SiO p-v plot is that the emission close to the protostar has the widest range of velocities, including the highest, up to -20 km s^{-1} in the blue side and up to 40 km s^{-1} in the red side. This is a striking feature of the SiO jet, that is, that very high velocities are found very close (~ 500 AU) to the protostar.

A possible explanation for the wide range of velocities found for SiO at the spatial scales of the disk would be that SiO close to the protostar is tracing a protostellar wind, with a large opening angle, and thus yielding a maximum spread of velocities. This interpretation favors a wide-angle wind as the mechanism for driving the outflow (e. g., Shu et al. 1991), since a pure jet model, in which velocity vectors point only in the polar direction, cannot produce this feature (e. g., Masson & Chernin 1993; Smith et al. 1997). However, the overall structure of the SiO
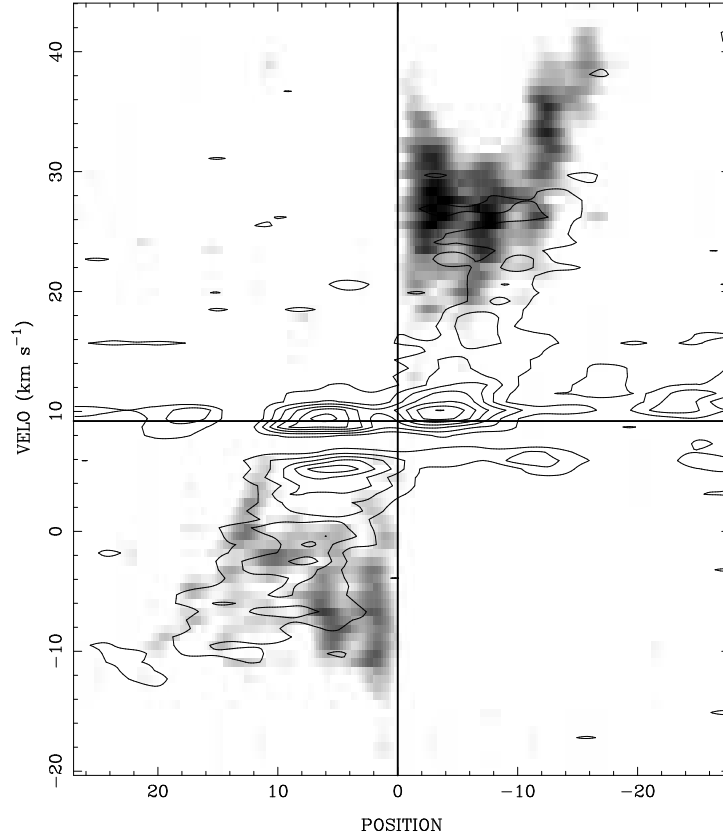
Figure 2.4: CO(3–2) position-velocity (p-v) plot (contour) overlaid on the SiO(8–7) (grey scale). Velocity resolution is 0.7 km s^{-1}. Position is in units of arcsec. The CO(3–2) plot was computed by smoothing the channel maps with a Gaussian of $4'' \times 2''$ and P.A.$= 26°$. The range of the grey scale is from 0.6 to 2.8 Jy beam^{-1}, and contours start at 0.55 Jy beam^{-1} and increase in steps of 0.55 Jy beam^{-1}. The straight lines indicate the position of the continuum source and the systemic velocity.

emission is highly collimated, and is very reminiscent of a pure jet (see Fig. 2.2b,c). In the wind-driven model, such a collimated structure would be the densest portion of a wide-angle wind. In this model, at distances ~ 500 AU (the position of the innermost SiO knots), the density decreases steeply with distance perpendicular to the axis of the jet, while the velocity vectors still span a wide angle around the jet axis (see e. g., Shang et al. 1998; Shu et al. 2000). Note that the SiO emission close to the driving source is not due to mixing with entrained material. The highly collimated morphology, together with the observed high velocity (up to 40 km s^{-1}), and the derived high density ($> 10^6$ cm^{-3}) and high temperature (> 300 K, Hirano et al. 2006) for the SiO gas very close to the center are strongly suggestive of material

from the primary jet, and not of ambient material being entrained.

Finally, we also see from the p-v plot that for distances larger than $\sim 5''$ (1500 AU), the velocity of both CO and SiO emission increases with distance. This is consistent with high-velocity CO and SiO tracing entrained material, dragged by the primary jet. However, the velocities reached by SiO are ~ 5 km s^{-1} higher than those of CO, especially on the red side. This feature is also seen when superposing the SiO(5–4) p-v plot on the CO(2–1) (Hirano et al. 2006). Presumably, SiO at distances larger than $\sim 5''$ from the protostar comes from entrained material with higher density than CO. This is consistent with the critical density of SiO(8–7) being higher than that of CO(3–2). Such higher-density material would be likely closer to the primary jet, resulting in entrained SiO showing higher velocities than entrained CO.

In order to compare the peak positions of the high-velocity SiO emission with those of the CO emission, we cross correlated the map of high-velocity SiO with that of high-velocity CO. The cross correlation function on the blue side of the jet has a single maximum at $3''\!.8$, meaning that the SiO knots are on average $\sim 4''$ closer to the protostar than the CO knots on the blue side. For the red side, the cross correlation function had two maxima, one at $\sim 1''$, and the other one at $\sim 6''$, with the SiO knots closer to the protostar. Thus, for both sides of the jet, the SiO knots are found closer to the driving source than the CO knots. This suggests that chemical differentiation can be important in the jet.

In particular, we measured (in the high-velocity maps) the distance to the center for the SiO knots B1 and R1, and found that the peak is at $\sim 1''\!.5$ (470 AU) from the center. Since B1 and R1 are only slightly resolved by the beam (even if we include the low-velocities), no significant emission of SiO is closer to the protostar than the peak of the innermost knots.

In summary, from the comparison of SiO(8–7) with SiO(5–4) and CO(3–2), it seems that the SiO(8–7) emission close to the protostar has contributions from the primary jet, which could be driven by a wide-angle wind. At projected distances ≥ 1500 AU from the protostar, the SiO(8–7) shows velocities increasing with distance, likely tracing entrained gas. For the same distances, the CO(3–2) also shows velocities increasing with distance, but reaching systematically lower velocities than the SiO(8–7). We interpret this feature as SiO(8–7) tracing entrained gas which is denser, and therefore closer to the primary jet, than the entrained CO(3–2) gas.

2.3   Are other nearby protostars interacting with HH211 mm?

In the previous section we have seen a simple case of star formation in a cluster. The compact submm emission from the Class 0 protostar HH211 mm, which is driving a highly collimated jet, is likely tracing a disk perpendicular to the jet. The outflow is interacting with the surrounding medium, essentially through the entraining of the ambient gas, and the data suggest that a wide-angle wind model could be the driving mechanism of the outflow. In this section we consider whether it is likely that other YSOs are/have been interacting with HH211 mm.

The first source which should be considered for a possible interaction with HH211 mm is IC348 MMS. This source is driving a north-south large-scale outflow whose southern lobe passes very close to the southeastern lobe of HH 211 (see Fig. 2.1). Eislöffel et al. (2003) propose that the emission found at 8.2 km s^{-1} in the southeastern bow of HH 211 by Gueth & Guilloteau (1999) could be due to the north-south outflow from IC348 MMS. However, this is affecting only the ends of the outflow. Thus, even the proximity of the two lobes of the outflows, there is no clear evidence of interaction.

Other sources which could be interacting with HH 211 are the sources found halfway between IC348 MMS and HH211 mm. Next to IC348 IR there is a group of knots along the east-west direction (Eislöffel et al. 2003), thus not intersecting the HH 211 dust core. There is no evidence from the H$_2$ images of shocked gas associated with the other sources halfway between IC348 MMS and HH211 mm.

Finally, there is a group of knots about 2′ to the northwest of HH211 mm and another group of knots about 4′ to the southeast of HH211 mm (not shown in Fig. 2.1: see Eislöffel et al. 2003). These knots are on a line that passes very close by HH 211 mm. If HH211 mm was the driving source of this large-scale jet, it should be a binary. Eislöffel et al. (2003) resolve HH211 mm as a double point-like source in the mm continuum maps from IRAM 30 m, but we did not find with the SMA any sign of a secondary source. In addition, the group of knots to the southeast of HH211 mm could be part of the large scale north-south jet emanating from IC348 MMS. From the available data it is not clear to which source are related these groups of knots.

Therefore, we conclude that there is no clear evidence of interaction of the different sources of the subcluster with HH211 mm, and thus HH211 mm could be understood as a low-mass protostar forming in isolation, although belonging to a cluster environment, constituting thus an example of the simplest case of star formation in a cluster.

Cluster environments in which interaction between the different members might be very important are found in intermediate/high-mass star-forming regions, since the stellar density is higher than in low-mass regions, and the influence of high-mass stars on the surrounding medium is much more noticeable. We will focus now our attention on cluster environments associated with intermediate/high-mass stars at the first stages of their formation.

Top Figure: View of the IRAM 30 m Telescope after a snow storm; *Bottom Figure:* View of the VLA in its most compact configuration.

Chapter 3

A sample of massive star-forming regions to search for deeply embedded clusters

3.1 Why a new list of massive star-forming regions

In order to study cluster environments in intermediate/high-mass star-forming regions, we will select our targets from lists of candidates to high-mass protostars. From these lists, we are most interested in those regions where the detection of the low-mass sources is feasible, and thus the regions must be located at relatively small distances from the Sun. In this chapter we show the process of selecting the regions observed in this work, and in chapters 4, 5, and 6 we show the results of the interferometric observations carried out toward each selected region.

We first consider under what observational conditions we can expect detecting the low-mass members of an embedded cluster. Studies of clusters around intermediate/high-mass stars at optical and near-infrared wavelengths, for an angular resolution of ~ 2–$3''$ and for minimum *stellar* masses of $\sim 0.2\ M_\odot$ have revealed a number of ~ 15 sources around the intermediate/high-mass star (Hillenbrand 1995; Testi et al. 1999; Massi et al. 2000). Thus, if we map a field of view encompassing all the cluster (expected to be around 0.4 pc, Hillenbrand 1995; Testi et al. 1998, 1999),

and if we reach enough resolution and sensitivity to detect minimum masses for the condensations of ~ 0.2 $M_\odot$, we could expect to detect a number of mm sources of the same order. This is a very broad approach since the minimum masses observed in the optical and infrared are *stellar* masses, while the masses of gas and dust estimated from the mm continuum emission are envelope/disk masses. However, as a first approach we consider that the masses derived from the mm continuum will be of the same order to the final stellar masses. Thus, our interferometric observations should have high-angular resolution and should be sensitive enough to detect masses down to ~ 0.2 $M_\odot$, approximately.

A few studies have been addressed to very young massive stars at mm wavelengths with high-angular resolution. However, the rms noise level achieved was not low enough to detect condensations with masses < 1 $M_\odot$ at the distance of the source (e. g., Molinari et al. 1998b; van der Tak et al. 2000; Furuya et al. 2002; Molinari et al. 2002; Gibb et al. 2003a; Gómez et al. 2003; Shepherd et al. 2003; Felli et al. 2004; Fontani et al. 2004; Shepherd et al. 2004b; Sollins et al. 2004; Su et al. 2004). Even with such high noise levels, in some cases the central millimeter peak splits up into several sources (e. g., Wyrowski et al. 1999; Ward-Thompson et al. 2000; Beuther et al. 2002a), suggesting that a cluster would be detected if observed with high sensitivity. Only very few works have been performed at millimeter wavelenghts with high sensitivity and high resolution toward massive protostars which are not too distant to detect low-mass sources, and one of them has succeeded in the detection of the cluster, that of Beuther & Schilke (2004). This work has revealed that the cluster mass function can be explained via fragmentation of the initial massive cores. Another region that was observed with enough resolution and sensitivity to detect low-mass sources was IRAS 20126+4104 (Cesaroni et al. 1999a). However, no other sources different from the high-mass protostar were detected at mm wavelengths, raising thus the fundamental question of why this high-mass protostar seems to be forming with no embedded sources around it.

Recently, other samples of high-mass protostar candidates have been published, but these were subsequent to the compilation of the list presented here. For example, Beltrán et al. (2006) compiled a list of high-mass candidates in the Southern Hemisphere, studied with SEST at mm wavelengths. Another work is that from Sridharan et al. (2005), who compiled a list of high-mass starless cores candidates from a comparison between observations at 1.2 mm and observations at mid-infrared wavelengths, and observed the regions of the sample in NH_3 with the Effelsberg-100m

Telescope. Finally Klein et al. (2005) compiled a list of FIR-bright IRAS sources, observed them in the mm continuum by using single-dish telescopes, and compared the mm emission with the infrared and cm emission. From these recent samples new regions could be selected to study clusters in the first stages of formation.

3.2 Selection criteria

We have collected a list of massive protostar candidates essentially from the lists compiled by Molinari et al. (1996), Mueller et al. (2002), and Sridharan et al. (2002), by selecting those targets where the detection of a protocluster is feasible with the current interferometers. Selection criteria were basically the following:

1. *The IRAS bolometeric luminosity must be* $> 1000\ L_\odot$: This is necessary to select intermediate/high-mass targets.

2. *The distance must be* $< 3.5\ kpc$: This is required in order to be sensitive to masses of $\lesssim 1\ M_\odot$. Otherwise, it is not possible to properly characterize the low-mass population of the forming cluster with the current interferometers.

   In Table 3.4 we present the compiled list resulting from these two selection criteria, which resulted in 99 sources. Two additional criteria were adopted in order to select the targets to observe.

3. *Millimeter emission in single-dish telescopes must be strong, with a peak intensity at 1.2 mm higher than 100 mJy beam^{-1}:* In addition to the fact that the first stages of star formation are characterized by strong millimeter emission, this is important for two other reasons. First, the large-scale structure will be resolved out by the interferometer, and, second, we expect that there will be contribution from several millimeter sources. These two facts imply that the peak intensity detected with the interferometer will be substantially lower than the peak intensity detected in the single-dish, and thus strong mm emission is required in single-dish observations.

4. *Centimeter emission must be weak, fainter than 10 mJy at 3.6 cm and smaller than 0.1 pc in size:* This criterion is required to assure that there is no HII

region which has already disrupted the surrounding material in a radius comparable to the size of the cluster, about 0.4 pc. Thus, we will accept targets with UCHII regions of size < 0.1 pc.

The resulting list has constituted a tool to select the regions studied in this work, and contains, for each region, the information concerning each selection criteria, together with some comments that may give further light on the nature of the region. For example, the association with dense gas, masers, or outflows supports the high-mass nature and young evolutionary stage of the region. All this information has been compiled from the literature (see references in the table). We note that the list does not contain all the studies made for each region, only those which are relevant to properly select our targets.

3.3   New observations to complete the list

Out of the 99 sources resulting from the two first selection criteria, 39 could already be discarded. The main reasons are: too strong or extended cm emission, too weak mm emission, association with an IR/optical cluster at the position of the IRAS source, ambiguity in the determination of the distance, and signs of a more evolved object, like a Herbig Ae/Be star.

We note that in order to properly select our targets it is necessary to have the mm single-dish and cm *images*, not being enough with the flux densities alone. The images are required to judge how compact/extended are the mm and cm emission.

Some of the remaining sources had enough gathered data to consider the observation of the region with an interferometer, while others lacked mm single-dish or cm images. We selected two of the regions which already were good candidates, and observed them with the SMA and BIMA. The results are presented in chapters 5 and 6, respectively.

Regarding the regions for which there were no mm single-dish images, we proposed to observe 9 of them with the IRAM 30 m Telescope. We also proposed to observe with the VLA 9 regions (most coinciding with the sources proposed to the IRAM 30 m) not imaged at cm wavelengths in the literature, and that could be promising targets to observe with an interferometer. The IRAM 30 m and VLA

Table 3.1: Parameters of the sources at 1.2 mm from the observations with IRAM 30 m

Source	Number of Clumps[a]	I_ν^{peak} (mJy beam^{-1})	S_ν[b] (mJy)	Rms (mJy beam^{-1})
00117+6412	3	108	1160	8
04579+4703	> 2	92	386	7
18123−1203	1	68	444	15[c]
18172−1548	2	74	2180	16[c]
18212−1320	-	< 56	-	14[c]
19045+0813	1	100	394	9
20293+4007	4	55	573	9
22187+5559	3	86	392+176	7
23448+6010	3	63	1630	11

[a] Clump considered when at least one closed contour at levels $\geq 4\sigma$ is found.

[b] Flux density inside an aperture of 80″ of diameter, except for IRAS 22187+5559, where the aperture was 50″ for the strong source and 30″ for the faint source.

[c] High rms noise due to observing at low elevations.

observations completed the missing information for those promising sources of Table 3.4. Below we show the results of these new observations with the IRAM 30 m and the VLA.

3.3.1   IRAM 30 m observations

The MPIfR 117-element bolometer array MAMBO at the IRAM 30 m Telescope was used to map the 1.2 mm dust continuum emission toward the 9 selected high-mass protostar candidates. The observations were carried in the 'pool dynamic scheduling' from 2004 January 23 to 25. We used the on-the-fly mapping mode, in which the telescope scans in azimuth along each row in such a way that all pixels see the source once. The sampled area was typically $320'' \times 80''$, and the scanning speed was $6''$ s^{-1}. Each scan was separated by $8''$ in elevation. The secondary mirror was wobbling at a rate of 2 Hz in azimuth with a wobbler throw of $70''$. The average zenith opacity was between 0.3–0.4. The overall uncertainty in calibration is estimated to be 20%. Data reduction was performed with the MOPSIC software package, which is complete with all necessary scripts for reduction (distributed by R. Zylka).

Figure 3.1 shows the 1.2 mm emission toward 8 of the 9 regions proposed to
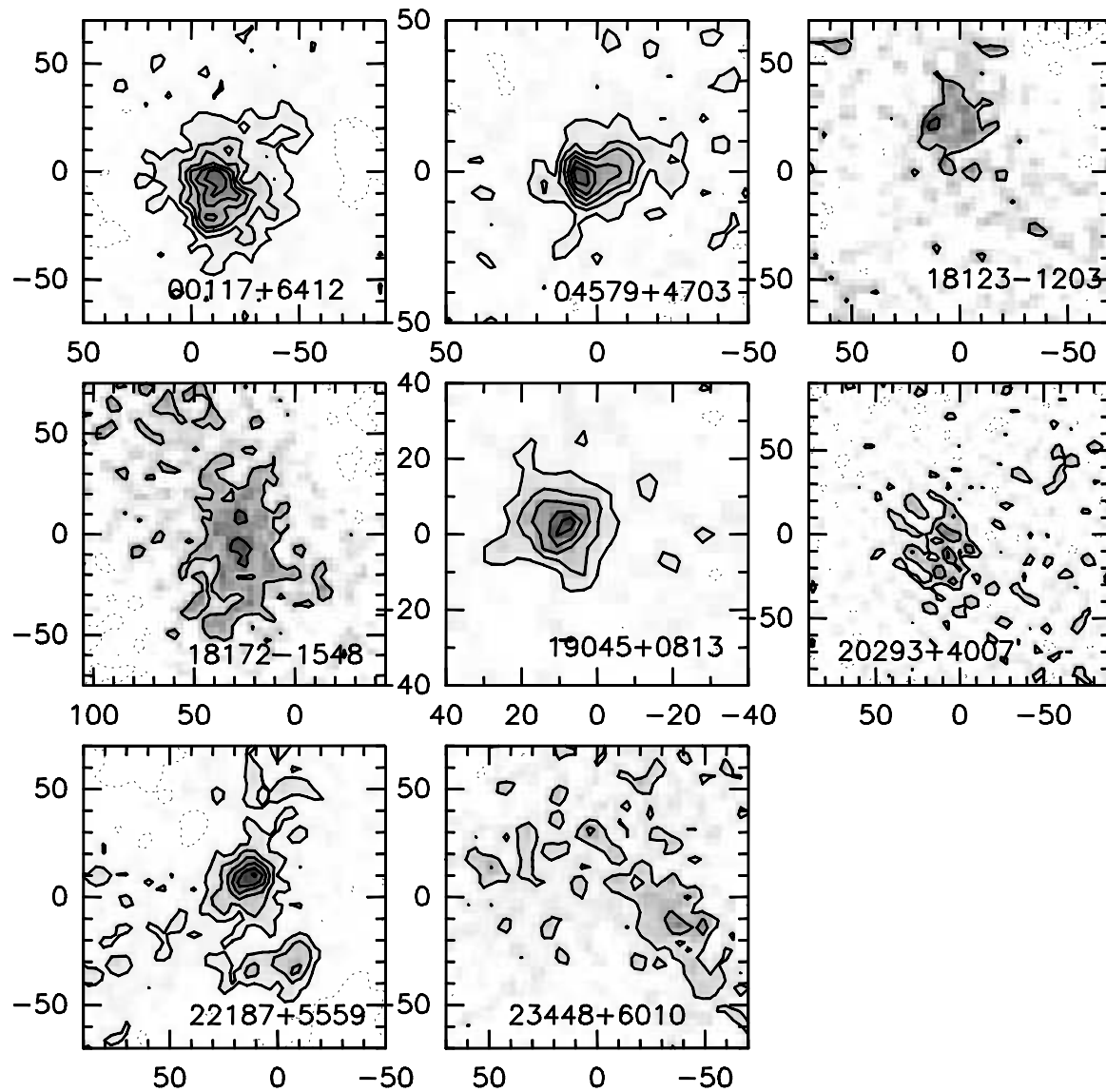
Figure 3.1: MAMBO (IRAM 30 m) 1.2 mm continuum maps. The axes show offsets in arcseconds from the absolute IRAS position given in Table 3.4. Contours are multiples of 2 times the rms of the map, listed in Table 3.1.

Table 3.2: Parameters of the observations at 3.6 cm with the VLA

Source	Phase Cal.	Bootstrapped Flux (Jy)	Beam (arcsec)	P.A. (°)	Rms (μJy beam^{-1})
00117+6412	0102+584	1.811 ± 0.003	13.9×7.5	78	92
04579+4703	0423+418	1.986 ± 0.003	10.6×9.4	49	28
18123−1203	1822−096	1.321 ± 0.002	13.1×8.7	7.4	42
18172−1548	1822−096	1.321 ± 0.002	13.9×8.8	3.6	148
19045+0813	1922+155	0.665 ± 0.002	12.4×8.8	45	75
20293+4007	2025+337	1.820 ± 0.002	9.3×9.0	50	60
22187+5559	2148+611	0.968 ± 0.002	9.8×8.7	17	360
22198+6336	2148+611	0.968 ± 0.002	10.4×8.8	6.6	31
23448+6010	0102+584	1.811 ± 0.003	10.0×8.7	4.2	74

observe. One region, IRAS 18024−2231, could not be observed due to dynamic scheduling. In Table 3.1 we summarize the main results, in particular the number of clumps detected, and the peak intensity and flux density for each region.

Most of the regions observed with the IRAM 30 m do not show a point-like morphology. On the contrary, five regions (IRAS 18123-1203, IRAS 18172-1548, IRAS 20293+4007, and IRAS 23448+6010) have very extended emission, with no clear peak. We then exclude these regions as good targets to observe with high angular resolution, since most of this large scale emission would be resolved out by the interferometer. The other regions have a clear peak of emission and show some substructure, being thus good candidates to observe with high-angular resolution. However, note that the peak intensities listed in Table 3.1 are around 100 mJy beam^{-1} or lower, which is just the limit of our third selection criterion.

3.3.2 VLA observations

We observed the 3.6 cm continuum emission of the 9 star-forming regions selected from Table 3.4 with the Very Large Array of the NRAO[1] in the D configuration. The observations were carried out during 2004 July 10–13. The regions observed, the phase calibrators used and their bootstrapped fluxes, as well as the parameters of the synthesized beam, and the rms noise of the maps for each source are given in Table 3.2. The positions of the phase centers correspond to the position of the

---

[1]The National Radio Astronomy Observatory is a facility of the National Science Foundation operated under cooperative agreement by Associated Universities, Inc.

Table 3.3: Parameters of the Sources at 3.6 cm from the observations with the VLA

| Source | Position | | I_ν^{peak} | S_ν | Size[a] | P.A.[a] |
	α(J2000)	δ(J2000)	(mJy beam^{-1})	(mJy)	($''\times''$)	($°$)
00117+6412	00:14:27.99	+64:28:44.7	1.38	2.61	12.1 × 4.9	58
04579+4703	05:01:39.93	+47:07:21.1	16.5	20.7	6.8 × 2.4	180
18123−1203	18:15:09.38	−12:05:10.0	1.14	1.23	2.3 × 0.0	176
18172−1548	18:20:06.84	−15:46:44.6	1.54	3.50	15.2 × 12.0	60
19045+0813	19:06:59.82	08:19:03.3	0.53	1.57	32.6 × 2.3	58
20293+4007	20:31:07.22	+40:17:22.8	1.03	3.37	14.1 × 12.3	57
22187+5559	22:20:35.61	+56:14:45.5	8.83	138	-	
22198+6336	22:21:26.71	+63:51:38.2	0.48	0.43	1.4 × 0.0	177
23448+6010	-	-	< 0.3			

[a] Deconvolved size and P.A.

IRAS source listed in Table 3.4. Absolute flux calibration was achieved by observing 0137+331, with an adopted flux density of 3.15 Jy. CLEANed maps were made using the task IMAGR of the Astronomical Image Processing System (AIPS) software of NRAO. All sources were cleaned setting the robust parameter to 4 (close to natural weighting), except for 00117+6412, for which robust was set to 0.

The maps for each region at 3.6 cm are shown in Fig. 3.2, overlaid on the dust continuum emission from the IRAM 30 m observations (when available). In Table 3.3 we give the peak intensity, the flux density, the position, and the deconvolved size of the cm sources detected toward each region. For almost all the regions, we found a cm source in the center, roughly coinciding with the position of the mm peak. For IRAS 18123-1203, the emission is very weak and extended, following the edge of the mm emission detected with the IRAM 30 m. For IRAS 22187+5559, the cm emission is very extended, and thus we discarded this source for our study. Toward the source IRAS 23448+6010 we did not detect any cm emission above the 4σ level of 0.3 mJy beam^{-1}. The regions that show a compact cm source or where cm emission has not been detected could be good targets for our purposes.

From these new observations with the IRAM 30 m and the VLA, we found several regions, like IRAS 00117+6412 and IRAS 04579+4703, with strong dust and with a compact and faint cm source which deserve high-angular resolution observations. In the next chapter we show the prelimanary results for IRAS 00117+6412, observed with the PdBI.
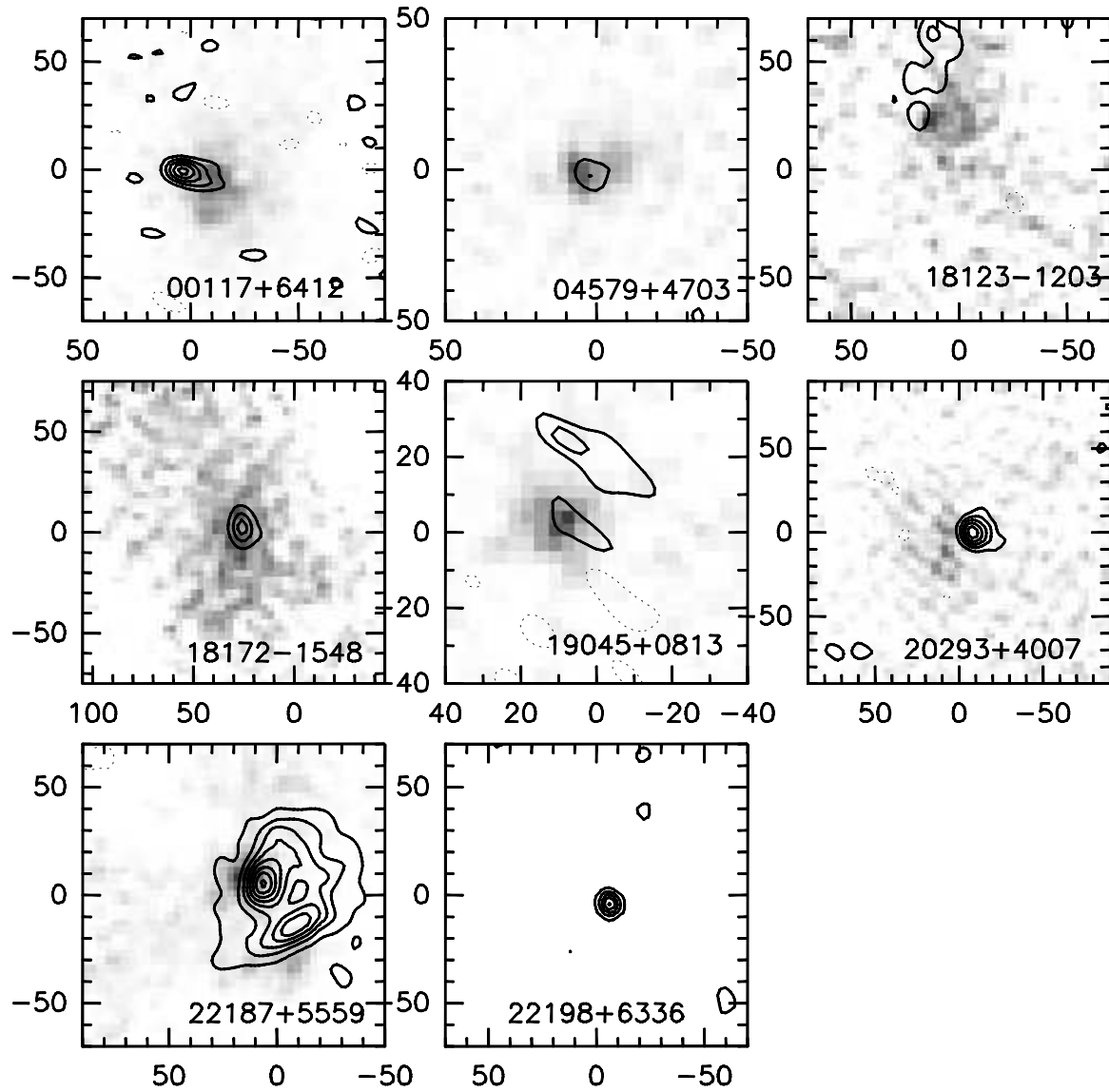
Figure 3.2: VLA 3.6 cm continuum maps. The axes show offsets in arcseconds from the absolute IRAS position given in Table 3.4. Contours are multiples of 3 times the rms of the map, listed in Table 3.2.

Table 34. List of intermediate/high-mass star-forming regions to search for deeply embedded clusters

Source	ref.cat.[a]	Position α(J2000)	δ(J2000)	D[b] (kpc)	L_bol log($L/L_\odot$)	mm/submm single-dish map λ (mm)	I_{peak}[c] (Jy beam^{-1})	clumps	ref.	cm emission λ (cm)	Flux (mJy)	size/morphology ('')	ref.	Comments[d]
00117+6412	M96	00:14:27.7	+64:28:46	1.80	3.1	1.2	0.11	> 3	100	3.6	2.61	7	100,59	outf.(1,97); maser (1,6,97); CS (60); PdBI: M_{min} = 0.41 $M_\odot$ (100)
00338+6312	M02	00:36:47.5	+63:29:01	0.85	-	0.35	160	1	M02	3.6	0.35	extended	25	L1287, RNO1B; IR Cl (28)
						0.85	17	1	10	6	< 0.3		19	
						1.1	5.6	1	19					
G123.07-6.31	M02	00:52:25.2	+56:33:53	2.2	-	0.35	160	1	M02					NGC281-W; dense gas (4); maser (30); HII (SIMBAD)
02219+6152	M02	02:25:40.6	+62:05:51	2.3	5.2	0.35	30	3	M02,48	6	10.7	UCHIIs	48,84	W3-IRS5; maser (27); IR Cl (35)
02232+6138	M02	02:27:04.7	+61:52:26	2.4	4.3	0.35	400	1	M02	6	1.5	radiojet,UCHII	26,48,87	W3(OH); PdBI: M_{min} = 6 $M_\odot$ (26)
03236+5836	M02	03:27:38.5	+58:46:58	0.90	3.3	0.35	80	1	M02,48	6	3.2		48	GL490; IR Cl (28); BIMA: M_{min} = 1.4 $M_\odot$ (83)
04579+4703	M96	05:01:39.7	+47:07:23	2.47	3.6	1.2	0.093	> 1	100	3.6	20.7	4,no HII	100,50	
										6	< 0.6		2	
05274+3345	M96	05:30:45.6	+33:47:52	1.55	3.6	0.85	21	2	10	3.6	0.8	5	24,31,91	AFGL 5142; dense gas (79,4); maser (30, 91) outf. (97); IR Cl (51)
05345+3157	M02	05:37:47.8	+31:59:24	1.80	3.1	0.85	0.31	> 3	15	2	< 1.4		2	IR Cl (5); OVRO: M_{min} = 4.5 $M_\odot$ (5)
						-				3.6			5	outf. (97)
						-				6	14.3	3	2	
05358+3543	M02,S02	05:39:10.4	+35:45:19	1.8	3.8	0.35	190	1	M02	3.6	< 1		S02	S233, S231; outf. (13); dense gas (4); maser (30,80) IR Cl (11); PdBI: M_{min} = 2.6 $M_\odot$
						1.2	0.890	4	12					
S235A-B	M02	05:40:53.3	+35:41:49	1.6	-	0.35	50	2	M02			HII	86	dense gas (4); maser (30); PdBI: M_{min} = 1.5 $M_\odot$ (85)
						0.45	11	1	85					
						0.85	5	1	15,85					
05490+2658	S02	05:52:12.9	+26:59:33	2.1	3.5	1.2	0.19	2	12	3.6	< 1		S02	S242; IR/opt Cl (11,18)
05553+1631	M96,S02	05:58:13.9	+16:32:00	2.5	3.8	1.2	0.32	1	12	3.6	1.3		S02	AFGL 5173; outf. (72); IR/opt Cl (11,18); dense gas (69)
06053-0622	M02	06:07:43.3	−06:23:08	0.9	-	0.35	150	5	M02			UCHII	64,88	MonR2; dense gas (4); maser (30); IR Cl (29)
						0.85	21	4	10					
S252A	M02	06:08:35.4	+20:39:03	1.5	-	0.35	130	1	M02					HII (SIMBAD)
06056+2131	M96	06:08:41.0	+21:31:01	1.50	3.8	1.2	0.33	2	15	6	1.6		23	AFGL6366-S; outf., NH$_3$ (M96); IR Cl (11); no opt Cl (18)
06105+1756	M96	06:13:28.3	+17:55:29	3.38	4.2					6	18		36	IR Cl (37)
06291+0421	M96	06:31:48.1	+04:19:31	1.96	3.6	0.85	< 5.4		10					IR Cl (46)
						2.7	< 0.057		9					
06308+0402	M96	06:33:31.1	+04:00:07	2.02	3.9	2.7	< 0.24		9	2	69	extended	9	IR Cl (46)
										6	45	extended	9	
RCW 142	M02	17:50:14.6	−28:54:32	2.0	-	0.35	530	1	M02			UCHII	89	
17527-2439	M96	17:55:49.1	−24:40:20	3.23	4.2					6		extended HII	20	
17574-2403	M02	18:00:30.4	−24:03:58	2.6	5.1	0.35	950	1	M02	6	2100	4,UCHII	48,88	W28A2; masers, outf. (53,61); SMA: M_{min} = 4.2 $M_\odot$ (63)
18014-2428	M96	18:04:29.3	−24:28:47	2.87	4.2	1.1	0.15	1	3	2	< 1		2	opt Cl (38)
										6	< 0.6		2	
18018-2426	M96,M02	18:04:53.9	−24:26:41	1.50	3.8	0.35	210	1	M02	2	7.0	< 2	2	M8E; outf. (97), NH$_3$ (M96)
										6	5.0	< 2	2	
18024-2231	M96	18:05:30.6	−22:31:36	2.92	3.7	e				2	< 1		2	
										6	< 0.6		2	
										11	0.66		39	
G12.42+0.50	M02	18:10:51.8	−17:55:56	2.1	-	0.35	210	1	M02			1,UCHII	90	3.8 kpc (68)
18089-1732	M96,M02,S02	18:11:51.3	−17:31:29	3.6	4.5	0.35	220	1	M02	0.7	1.0	6	78	G12.89+0.49; maser (80); SMA: M_{min} = 6 $M_\odot$ (81,82); mm (10)
						0.85	11	1	47,10	3.6	0.9	~ 2	S02,80	
						1.2	2.1	4	12					
18102-1800	S02	18:13:12.2	−17:59:35	14–(2.6)	5.3–(3.8)	1.2	0.32	1	12	3.6	44	~ 10	S02,80	maser (80); 12.8 kpc (68)

Table 34. Cont.

Source	ref.cat.[a]	Position α(J2000)	δ(J2000)	D[b] (kpc)	L_{bol} log($L/L_\odot$)	λ (mm)	I_{peak}[c] (Jy beam^{-1})	clumps	ref.	λ (cm)	Flux (mJy)	size/morphology ('')	ref.	Comments[d]
18123-1203	M96	18:15:07.3	−12:02:42	3.09	3.9	1.2	0.068	2	100	3.6	1.23	2	100	
										6	< 0.6		20	
18134-1942	M96	18:16:22.3	−19:41:20	1.62	3.9	0.85	5.1	1	47	3.6	0.32	5	20,21	
18151-1208	M96,S02	18:17:57.1	−12:07:22	3.0	4.3	1.1	2.8	1	19	3.6	< 1		S02	outf. (13); maser (80); NIR imaging (73)
						1.2	0.67	4	12	6	< 0.3		19	
18156-1343	M96	18:18:28.7	−13:42:22	2.5	4.7					11	1680		39	opt Cl (40)
18159-1648	M96,M02	18:18:53.5	−16:47:39	2.50	4.5	0.35	440	1	M02			UCHII	99	G14.33-0.64; outf. (14)
18172-1548	M96	18:20:04.6	−15:46:47	2.56	3.9	1.2	0.074	> 3	100	3.6	3.50	14	100	
GL2136	M02	18:22:26.4	−13:30:08	2.0	4.8	0.35	240	1	M02,48					13.6 kpc (68); OVRO: M_{min} = 6.6 $M_\odot$ (48)
18212-1320	M96	18:24:04.7	−13:19:16	2.18	3.2	1.2	< 0.056		100					
18236-1205	M96	18:26:24.3	−12:03:47	2.51	4.0	0.85	3.8	1	47					maser (M96,47); 12 kpc (68)
18256-0742	M96	18:28:20.5	−07:40:22	2.90	4.0					2	< 1.1		2	
										6	4.1	0.4	2	
18258-0737	M96	18:28:34.1	−07:35:31	2.97	4.5					6		extended	22	
18264-1152	S02	18:29:14.3	−11:50:26	12.5–3.5	5.1–4.0	1.2	1.77	1	12	0.7	1.30		78	outf. (13); maser (80);
										3.6	< 0.2		78	SMA: M_{min} = 5 $M_\odot$ (66); 12.0 kpc (68)
18272-1217	S02	18:30:02.7	−12:15:27	2.9	4.0	1.2	0.14	2	12	3.6	110		S02	12.7 kpc (68)
18316-0602	M96	18:34:19.8	−05:59:44	3.17	4.6	0.85	9.2	1	47	3.6	3.8	3,HII	10,56	GL7009S; maser (M96)
						1.1	7.5	1	19,22	6	2.7		19	
18317-0513	M96	18:34:25.9	−05:10:59	3.13	4.5					6		extended	22	
G24.49-0.04	M02	18:36:05.3	−07:31:23	3.5	-	0.35	190	1	M02					6.4 kpc (68); HII (SIMBAD)
18372-0541	M96,S02	18:39:56.0	−05:38:49	13.4–1.8	5.3–3.5	1.2	0.26	1	12	3.6	80	∼ 3	S02,80	maser, outf. (53)
18385-0512	S02	18:41:12.0	−05:09:06	13.1–(2.0)	(5.3)–3.7	1.2	0.72	3	12	3.6	29	∼ 3	S02,80	maser (80)
18424-0329	M96	18:45:03.3	−03:26:49	3.36	3.7					2	< 1.1		2	
										6	8.81	0.7	2	
18454-0136	S02	18:48:03.7	−01:33:23	11.9–2.7	4.8–3.5	1.2	0.30	2	12	3.6	42		S02	
18472-0022	S02	18:49:50.7	−00:19:09	11.1–3.2	4.9–3.8	1.2	0.28	3	12	3.6	110		S02	
18517+0437	M96,S02	18:54:13.8	+04:41:32	2.9	4.1	1.1	5.0	1	19	3.6	< 1		S02	maser, NH$_3$ (M96)
						1.2	0.81	2	12	6	< 0.3		22	
18537+0749	M02	18:56:10.4	+07:53:14	2.1	-	0.35	240	1	M02					G40.50+2.54; HII (SIMBAD)
						0.85	33	2	10					
G35.58-0.03	M02	18:56:22.6	+02:20:28	3.5	-	0.35	110	1	M02	3.6	197	< 1	56	maser (53)
18540+0220	S02	18:56:35.6	+02:24:54	10.6–3.3	4.9–3.9	1.2	0.069	1	12	3.6	97		S02	
18567+0700	M96	18:59:29.5	−06:56:25	2.16	3.9	1.1	0.45	1	3	2	6.92	< 8	2	
										6	2.73	0.6	2	
18586+0106	M96	19:01:10.6	+01:11:16	2.71	3.7					2	< 1.1		2	
										6	34.75	11	2	
19012+0505	M96	19:03:43.5	+05:09:49	2.89	4.2					2	< 1.0		2	
										6	48.38	3.6+halo	2	
19035+0641	S02	19:06:01.1	+06:46:35	2.2	3.9	1.2	0.31	1	12	3.6	4.0	∼ 1	S02,80	outf. (13); maser (57,80)
19045+0813	M96	19:06:59.8	+08:18:43	1.6	3.2	1.2	0.10	3	100	3.6	1.57	32	100	maser (M96,50)
19282+1814	M96,S02	19:30:28.1	+18:20:53	8.2–1.9	4.9–3.6	1.2	0.27	1	12	3.6	< 1	UCHII	S02,56	maser (80); outf. (97)
19403+2258	S02	19:42:27.2	+23:05:12	6.3–2.4	4.7–3.8	1.2	0.090	1	12	3.6	< 1		S02	
19410+2336	S02	19:43:11.4	+23:44:06	(6.4)–2.1	5.0–4.0	1.2	0.85	2	12	0.7	< 1.5		24	outf. (13); maser (80); PdBI: M_{min} = 0.63 $M_\odot$, mm Cl (93)
										3.6	0.7	< 2	24	

Table 34. Cont.

Source	ref.cat.[a]	Position α(J2000)	Position δ(J2000)	D[b] (kpc)	L_bol log($L/L_\odot$)	λ (mm)	I_peak[c] (Jy beam^{-1})	clumps	ref.	λ (cm)	Flux (mJy)	size/morphology ('')	ref.	Comments[d]
19411+2306	S02	19:43:18.1	+23:13:59	5.8–2.9	4.3–3.7	1.2	0.22	2	12	3.6	< 1		S02	outf. (13)
19413+2332	S02	19:43:28.9	+23:40:04	6.8–1.8	4.4–3.3	1.2	0.14	2	12	3.6	< 1		S02	
19442+2427	M02	19:46:20.5	+24:35:34	2.3	-	0.35	140	2	M02			1,UCHII	53,56	S87
						0.85	17	2	10					
S88B	M02	19:46:47.7	+25:12:56	2.0	-	0.35	150	1	M02			1,UCHII	53,88	outf. (53); 4.1 kpc (68)
19471+2641	S02	19:49:09.9	+26:48:52	2.4	3.6	1.2	0.17	2	12	3.6	?		S02	
20028+2903	M96	20:04:53.3	+29:11:37	1.55	3.7									IC4955; IR Cl (37)
20051+3435	S02	20:07:03.8	+34:44:35	3.7–1.6	4.0–3.3	1.2	0.17	1	12	0.7	< 1.5		24	
										3.6	0.8	10	24	
20056+3350	M96	20:07:31.5	+33:59:39	1.67	3.6	0.8	6.2	1	10	3.6	0.93	extended	10	outf. (97)
20106+3545	M96	20:12:31.3	+35:54:46	1.64	3.3					2	< 1		2	NH$_3$ (M96); OVRO: M_{min} = 2.4 $M_\odot$ (5)
										6	< 0.6		2	outf. (97)
20126+4104	M96,S02	20:14:26.0	+41:13:32	1.7	3.9	1.2	1.09	1	12	3.6	0.3		92	outf. (13,97); masers (30,76,80); dense gas (4,M96);
										6	< 0.3		2,19	PdBI: M_{min} = 0.34 $M_\odot$ (17); no IR Cl (11)
20216+4107	S02	20:23:23.8	+41:17:40	1.7	3.3	0.8	4.6	2	19	3.6	1.4		S02	outf. (13)
						1.2	0.26		12					
20275+4001	M02	20:29:24.4	+40:11:18	1.0	-	0.35	230	1	M02,48	3.6	4.7	UCHII	30	GL2591
						0.85	19	1	10	6	0.4		48	
20293+4007	M96	20:31:07.9	+40:17:23	3.41	3.9	1.2	0.055	4	100	3.6	3.37	13	100	pre-UCHII region (42)
20293+3952	S02	20:31:10.7	+40:03:10	2.0–1.3	3.8–3.4	1.2	0.35	2	12	3.6	7.6	4.5	S02	outf. (13); maser (80); BIMA (100);
														PdBI: M_{min} = 0.87 $M_\odot$ (94)
20319+3958	S02	20:33:49.3	+40:08:45	1.6	3.8	1.2	0.21	1	12	3.6	25	9	S02,67	
20343+4129	S02	20:36:07.1	+41:40:01	1.4	3.5	1.2	0.31	3	12	3.6	1.8	1.5	S02,67	outf. (13);
														SMA: M_{min} = 0.21 $M_\odot$ (100)
20444+4629	M96	20:46:08.3	+46:40:41	2.42	3.5					6	2.88	< 5	2	
21078+5211	M96	21:09:25.2	+52:23:44	1.49	4.1	0.85	18	1	9,10	2	31		67	maser, NH$_3$ (M96), outf. (97)
										6	263.72	11+halo	2,67	
21418+6552	M02	21:43:06.7	+66:07:04	2.0	-	0.35	40	1	M02					BFS11-B, LkHa234; IR Cl (28)
						0.85	3.4	1	10					
22134+5834	S02	22:15:09.1	+58:49:09	2.6	4.1	1.2	0.23	1	12	3.6	3.7		S02	outf. (13); NH$_3$ (95)
22172+5549	M96	22:19:09.0	+56:04:45	2.87	3.7					3.6		50	5	outf. (97); OVRO: M_{min} = 11.6 $M_\odot$ (5)
22176+6303	M02	22:19:18.2	+63:18:47	0.90	-	0.35	350	2	M02,48	3.6	5.5	UCHII	56	S140-IRS1; IR Cl (28)
										6	5.8		48	
22187+5559	M96	22:20:34.9	+56:14:39	2.93	3.9	1.2	0.086	3	100	3.6	138	40	100	
22198+6336	M96	22:21:27.6	+63:51:42	1.28	3.1	0.85	5.2	1	9,10	6	< 0.8		20	L1204-G; outf. (97); maser (M96,30);
										3.6	0.43	1	100	dense gas (M96,4); no IR Cl (11); mm (9)
22272+6358A	M96	22:28:52.2	+64:13:43	1.23	3.3	2	0.11	1	33	2	< 1.1		9	BRC 44 (33); IR Cl (11,28)
						2.7	0.067	1	9	6	< 0.8		9	
22457+5751	M96	22:47:46.5	+58:07:19	2.28	4.0									HAe/Be star
CEP A	M02	22:56:18.1	+62:01:46	0.73	-	0.35	430	1	M02			UCHIIs	56,96	IR Cl (28); BIMA: M_{min} = 0.9 $M_\odot$ (83)
22551+6221	M96,S02	22:57:05.2	+62:37:44	1.3–0.7	4.0–3.2	1.2	0.1	1	12	3.6	4.5	UCHII	S02,56	outf. (14)
22570+5912	M96,S02	22:59:06.4	+59:28:28	5.1–2.92	4.7–4.3	1.2	0.21	4		12				
23033+5951	S02	23:05:25.7	+60:08:08	3.5	4.0	1.2	0.63	1	12	3.6	1.7	~ 1	S02,80	outf. (13); maser (80); CS (60); IR Cl (49)
S158-NGC7538 S	M02	23:13:44.8	+61:26:51	2.8	-	0.35	250	1	M02	6	2.8		31	BIMA (31)

Table 34. Cont.

Source	ref.cat.[a]	Position α(J2000)	δ(J2000)	D[b] (kpc)	L_{bol} log($L/L_\odot$)	mm/submm single-dish map λ (mm)	I_{peak}[c] (Jy beam^{-1})	clumps	ref.	cm emission λ (cm)	Flux (mJy)	size/morphology ('')	ref.	Comments[d]
23116+6111	M02	23:13:45.4	+61:28:12	2.8	5.1	0.35	150	1	M02,48	1.3	600	UCHII	32,88	NGC7538-IRS1; O6.5 ZAMS star (32)
										2	420	1	32,55	JCMT (75)
										6	120	2	32,55,88	
23118+6110	M02	23:14:01.7	+61:27:20	2.8	4.6	0.35	130	1	M02,48	1.3	< 20		32	NGC7538-IRS9; OVRO: M_{min} = 6.5 $M_\odot$ (48);
										3.6	0.44	1	74	JCMT (75); BIMA: M_{min} = 38 $M_\odot$ (74)
										6	0.32	2	74	
S157	M02	23:16:04.4	+60:01:41	2.5	-	0.35	70	1	M02	3.6	101	9,CHII	56	maser (53)
						0.85	5.9	2	10					
23152+6034	M96	23:17:25.8	+60:50:45	1.67	3.2					2	< 0.32		34	MWC1080; IR Cl (43,44); Herbig Ae/Be (34)
										6	0.21		34	
23314+6033	M96	23:33:44.4	+60:50:30	2.78	4.0	0.85	3.9	1	10	2	< 1		2	outf. (97)
										3.6	< 0.3		10	
										6	< 0.6		2,34	
23448+6010	M96	23:47:20.1	+60:27:21	2.02	3.4	1.2	0.063	> 2	100	3.6	< 0.3		100	
23545+6508	M96,S02	23:57:05.2	+65:25:11	1.3–0.8	3.6–3.0	1.2	0.15	2	12	3.6	1		S02,54	NH$_3$ (M96)

[a] Reference catalog: M96: Molinari et al. (1996); S02: Sridharan et al. (2002); M02: Mueller et al. (2002).

[b] Distances from the corresponding catalog listed in column 2.

[c] Flux density for sources from M02 catalog in Jy. Note that all sources (but 18517+0437) from S02 have additional maps at 450 and 850 μm (Williams et al. 2004), and additional observations of dense gas (Fuller et al. 2005).

[d] In this column we list other names of the sources, signposts of star formation such as outflows (outf.) or masers, association with dense gas, association with optical or IR clusters ("Cl" stands for "cluster"), comments on the distance, and observations carried out with a mm/submm interferometer and the mass sensitivity achieved (M_{min}).

[e] Proposed to observe with the IRAM 30 m, but observation was not possible due to dynamic scheduling.

References: 1: Zhao et al. (2003); 2: Molinari et al. (1998a); 3: Molinari et al. (2000); 4: Cesaroni et al. (1999b); 5: Molinari et al. (2002); 6: Comoretto et al. (1990); 7: Beuther et al. (2002a); 9: Wilking et al. (1989); 10: Jenness et al. (1995); 11: Hodapp (1994); 12: Beuther et al. (2002b); 13: Beuther et al. (2002c); 14: Wu et al. (2005); 15: Klein et al. (2005); 17: Cesaroni et al. (1999a); 18: Carpenter et al. (1993); 19: McCutcheon et al. (1995); 20: Hughes & MacLeod (1994); 21: van der Walt et al. (2003); 22: McCutcheon et al. (1991); 23: Carpenter et al. (1990); 24: Carral et al. (1999); 25: Rodríguez et al. (2002); 26: Wyrowski et al. (1999); 27: Wilson et al. (2003); 28: Porras et al. (2003); 29: Carpenter et al. (1997); 30: Tofani et al. (1995); 31: Sandell et al. (2003); 32: Zheng et al. (2001); 33: Sugitani et al. (2000); 34: Girart et al. (2002); 35: Megeath et al. (1996); 36: Fich et al. (1993); 37: Dutra et al. (2001); 38: Sung et al. (2000); 39: Fürst et al. (1990); 40: Belikov et al. (1999); 42: Setia Gunawan et al. (2003); 43: Bica et al. (2003); 44: Testi et al. (1998); 46: Phelps & Lada (1997); 47: Walsh et al. (2003); 48: van der Tak et al. (2000); 49: Kumar et al. (2002); 50: Codella & Felli (1995); 51: Hunter et al. (1997); 53: Codella et al. (2004); 54: Anglada et al. (2002); 55: Franco-Hernández et al. (2004); 56: Kurtz et al. (1994); 57: Pestalozzi et al. (2004); 59: Palla et al. (1993); 60: Bronfman et al. (1996); 61: Kim et al. (2003); 62: Ojha et al. (2004); 63: Sollins et al. (2004); 64: Jaffe et al. (2004); 66: Su et al. (2004); 67: Miralles et al. (1994); 68: Sewilo et al. (2004); 69: Shepherd et al. (2004a); 70: Boogert et al. (2004); 72: Jones et al. (2004); 73: Davis et al. (2004); 74: Sandell et al. (2005); 75: Reid et al. (2005); 76: Moscadelli et al. (2005); 78: Zapata et al. (2006); 79: Zhang et al. (2002); 80: Beuther et al. (2002d); 81: Beuther et al. (2005b); 82: Beuther et al. (2004a); 83: Gibb et al. (2003b); 84: Tieftrunk et al. (1997); 85: Felli et al. (2004); 86: Israel et al. (1978); 87: Wilner et al. (1995); 88: Wood et al. (1989); 89: Walsh et al. (1998); 90: Jaffe et al. (1984); 91: Torrelles et al. (1992a); 92: Hofner et al. (1999); 93: Beuther & Schilke (2004); 94: Beuther et al. (2004c); 95: Sepúlveda (2001); 96: Garay et al. (1996); 97: Zhang et al. (2005); 98: Wu et al. (2004); 99: Shirley et al. (2003); 100: this work.
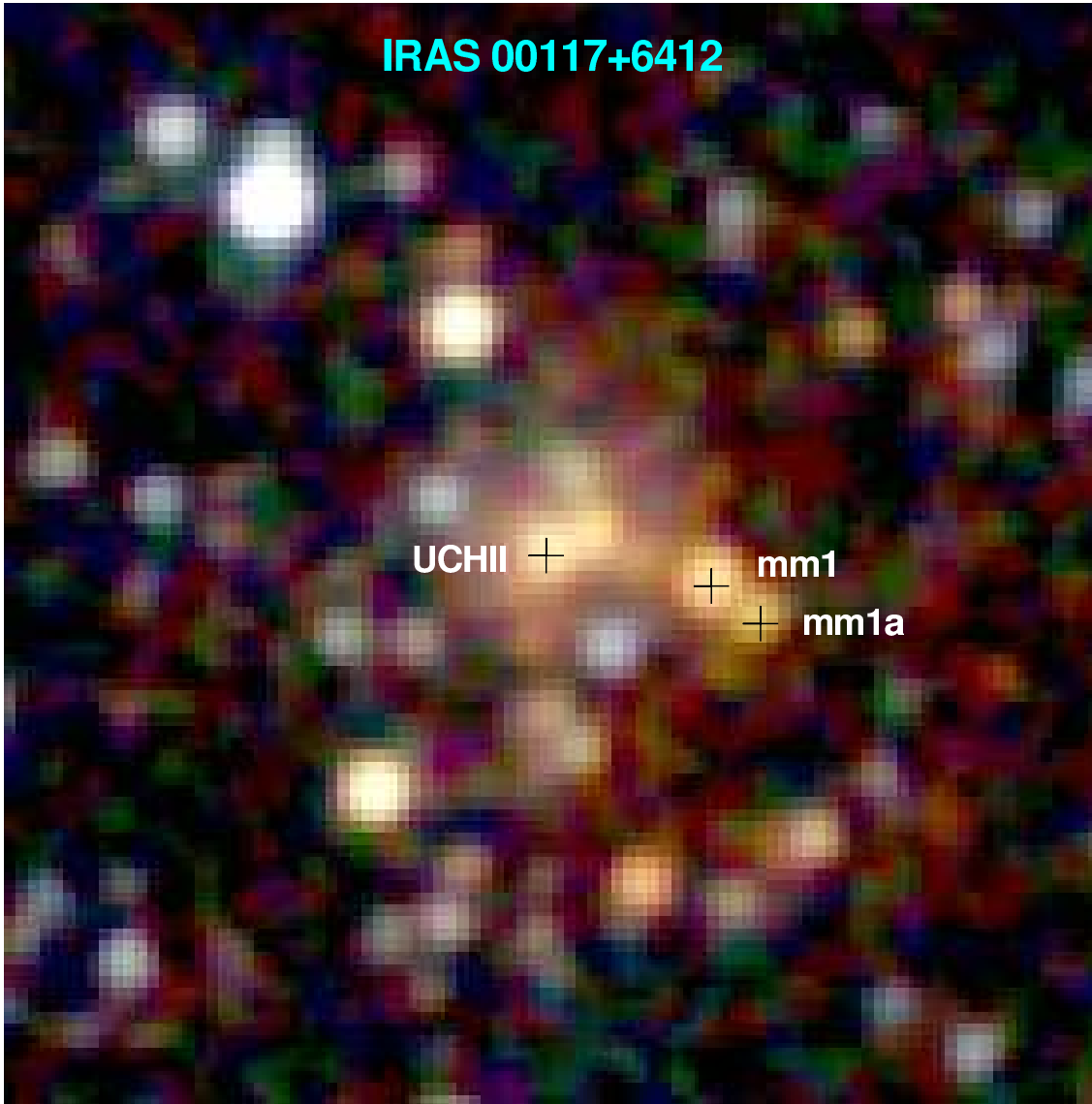
Figure: 2MASS composite image of J, H, and K filters of the IRAS 00117+6412 region. Red objects in the image are embedded objects.

Chapter 4

IRAS 00117+6412: first results with the PdBI of a region selected from new mm and cm data

4.1 Introduction

In the previous chapter we showed the process of compiling a sample of regions candidate of harboring embedded clusters and, in order to complete the sample, we observed some of the regions with the IRAM-30m and the VLA, being IRAS 00117+6412 among them. IRAS 00117+6412 has a bolometric luminosity of 1400 $L_{\odot}$ and is located at a distance of 1.8 kpc (Molinari et al. 1996). The mm single-dish image shows strong emission with some substructure, and the cm emission reveals one compact cm source. The mm peak lies $\sim 15''$ to the west of the compact cm source, which is spatially coinciding with the brightest infrared source in the 2MASS Point Source Catalogue (PSC). The cm source is also associated with two H_2O masers (Zhao et al. 2003). This suggests that the cm and infrared emission are tracing an intermediate/high-mass (proto)star different from the source traced by the mm peak. In addition, a bipolar outflow has been detected in CO(2–1) toward this region (Zhao et al. 2003; Zhang et al. 2005).

We thus conducted high-sensitivity observations with the PdBI in order to study the different mm sources embedded in this region, as well as the distribution of

dense gas through the observation of some molecular transitions. We present here the preliminary results obtained from these observations.

4.2   Observations

The continuum emission at 3 and 1 mm was observed simultaneously together with the $N_2H^+(1-0)$, and CS(5–4) molecular transitions with the PdBI. The observations were carried out during 2004 October 17 and December 7, with the array in the D (5 antennas) and C (6 antennas) configurations, respectively. The phase center was α(J2000) = $00^h14^m25^s.8$, δ(J2000) = $+64°28'43''.00$, and the projected baselines ranged from 24.0 to 229.0 m. The system temperatures were ~ 300 K for the receiver at 3 mm, and ~ 2000 K for the receiver at 1 mm for both days, and atmospheric phase correction based on the 1 mm total power was applied. The receiver at 3 mm was tuned to 93.17378 GHz (lower sideband) to cover the $N_2H^+(1-0)$ transition, for which we used a correlator unit of 20 MHz of bandwidth and 512 spectral channels, providing a spectral resolution of 0.04 MHz (0.13 km s^{-1}). The receiver at 1 mm was tuned to 244.93556 GHz (upper sideband), covering the CS(5–4) transition, and we also used a unit of 20 MHz and 512 channels (spectral resolution of 0.05 km s^{-1}). In addition, we placed two units of 40 MHz and 512 channels (spectral resolution of 0.078 MHz or 0.1 km s^{-1}) in the lower sideband of the receiver at 1 mm, in order to cover a few transitions of $CH_3OH(5-4)$. For the continuum measurements we used two correlator units of 320 MHz in each band for both receivers. The FWHM of the primary beam was $\sim 54''$ at 3 mm, and $\sim 20''$ at 1 mm.

The calibration and reduction of the data was carried out at the IRAM offices in Grenoble during April 2005. Bandpass calibration was performed by observing 3C454.3 for Oct 17 and 2145+067 for Dec 7. We used the source 0212+735 to calibrate the phases and amplitudes of the antennas for both days. The rms of the phases was $< 50°$ for the data at 3 mm and $< 60°$ for 1 mm. The absolute flux density scale was determined from MWC 349 for Oct 17 and from 2145+067 for Dec 7, with an estimated uncertainty around 15%. Data were calibrated, imaged and cleaned using MAPPING of the GILDAS software package. Imaging was performed using natural weighting. The synthesized beam at 3 mm was $4''.30 \times 3''.39$, with P.A.= $60°.8$, and $1''.50 \times 1''.18$, with P.A.= $58°.3$ at 1 mm. The rms noise was 0.2 mJy beam^{-1} and 1.1 mJy beam^{-1} at 3 mm and 1 mm respectively. For the CS(5–4) emission we

tapered the u-v data at 50 kλ, in order to increase the S/N, and the synthesized beam was $2\rlap{.}''89 \times 2\rlap{.}''43$, with P.A.=49°.

Additional observations at 1.3 cm were carried out with the VLA in the D configuration in 2004 July 10, using 0137+331 as flux calibrator, with an adopted flux of 1.12 Jy. The phase calibrator was 0102+584, with a bootstrapped flux density of 2.24 Jy. CLEANed maps were made using the task IMAGR of the Astronomical Image Processing System (AIPS) software of NRAO. In order to increase the S/N ratio we tapered the u-v data at 50 kλ. The resulting synthesized beam was $5\rlap{.}''2 \times 4\rlap{.}''6$, with P.A.= 47°, and the rms noise of the map was 0.2 mJy beam^{-1}.

4.3   Results

4.3.1   Continuum emission

The 3.6 cm continuum emission shown in Figure 4.1 consists essentially of one point-like source that is coincident with the brightest infrared source in the field. The 3.6 cm flux density is 2.6 mJy, and the deconvolved size is $12\rlap{.}''1 \times 4\rlap{.}''9$ (0.1 pc $\times$ 0.04 pc). If this cm emission is free-free emission from a photoionized HII region, the observed flux density yields to an ionizing flux of 3.6×10^{44} s^{-1}, which corresponds to a B2 star (Panagia 1973). The expected luminosity for a B2 star (Panagia 1973) is compatible with the bolometric luminosity of IRAS 00117+5412, and we thus interpret the cm emission as arising in an UCHII region produced by a B2 star. Figure 4.2 shows the 1.3 cm emission, which is elongated in the north-south direction and associated with the peak of emission at 3.6 cm. The flux density in an aperture including the extended emission is 2.5 mJy, and thus the spectral index between 3.6 and 1.3 cm is -0.03, consistent with optically thin free-free emission.

In Fig. 4.1 we show the 3 mm continuum emission in the region overlaid on the K-band image of 2MASS. There are two compact sources, the strongest source, mm1, lying $\sim 15''$ to the west of the UCHII region, and the other source, mm2, being located about $20''$ to the south of mm1. The peak of mm1 is associated with an infrared source, and is partially extended to the southwest, also spatially coinciding with an infrared source. We label this extension, which is likely associated with the infrared source, mm1a. Note that toward mm2 the K-band image from 2MASS
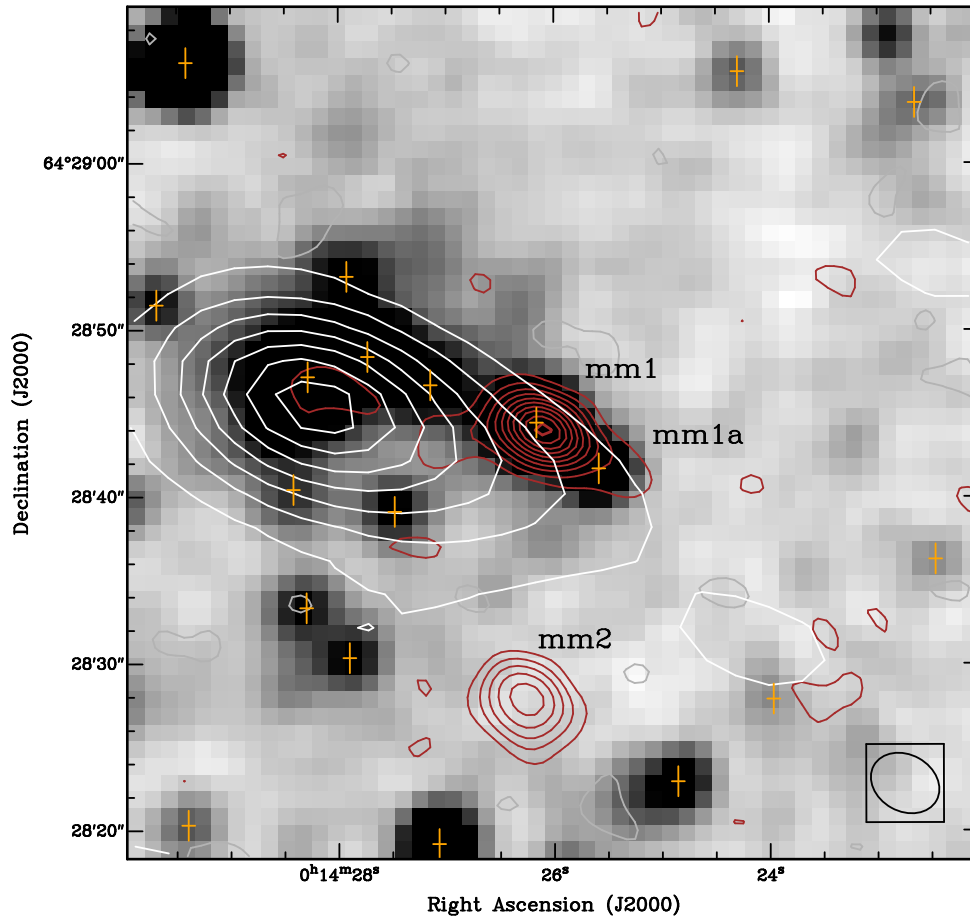
Figure 4.1: Brown contours: PdBI continuum emission at 3 mm toward IRAS 00117+6412. Contour levels are -2, 2, 4, 6, 8, 10, 12, 14, 16, 18, and 20 times the rms of the map, 0.2 mJy beam^{-1}. White contours: VLA continuum emission at 3.6 cm. Contour levels are -4, -2, 2, 4, 6, 8, 10, 12, and 14 times the rms of the map, 0.092 mJy beam^{-1}. The synthesized beam of the 3 mm observations, shown in the bottom right corner, is $4''30 \times 3''39$, P.A.= $60°8$, and the synthesized beam at 3.6 cm (not shown) is $13''9 \times 7''5$, P.A.= $78°$. Grey scale: K-band 2MASS image. The crosses indicate the position of 2MASS sources.

shows no infrared emission at all. The continuum emission at 1 mm, shown in Fig. 4.2, is strong toward mm1, and is also slightly elongated to the southwest. At 1 mm, the faint emission toward mm2 is affected by the primary beam attenuation.
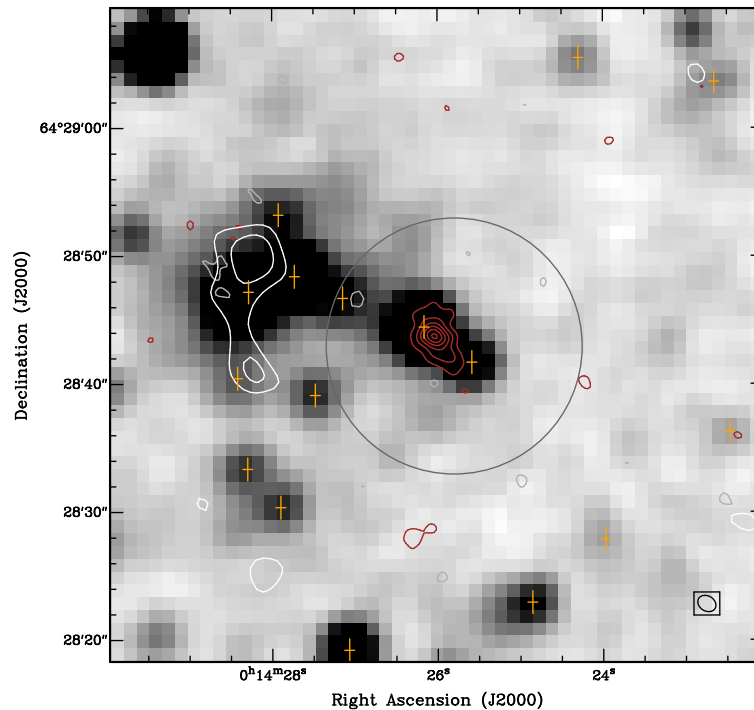
Figure 4.2: Brown contours: PdBI continuum emission at 1 mm toward IRAS 00117+6412. Contour levels are -3, 3, 6, 9, 12, 15, and 18 times the rms of the map, 1.0 mJy beam^{-1}. White contours: VLA continuum emission at 1.3 cm. Contour levels are -4, -3, 3, and 4 times the rms of the map, 0.2 mJy beam^{-1}. The synthesized beam of the 1 mm observations, shown in the bottom right corner, is $1''50 \times 1''18$, with P.A.$= 58°3$, and the synthesized beam at 1.3 cm (not shown) is $5''2 \times 4''6$, P.A.$= 47°$. Grey scale: K-band 2MASS image. The crosses indicate the position of 2MASS sources, and the circle indicates the primary beam of the PdBI observations at 1 mm.

Table 4.1 summarizes the properties of the continuum emission for each detected source. Intensities and flux densities at 3 and 1 mm have been corrected for the primary beam attenuation. Both mm1 and mm2 have masses of $\sim 1~M_\odot$. Note that for deriving the masses we assumed a lower dust temperature for mm2 than for mm1, since mm2 has no infrared emission associated.

Table 4.1: Parameters of the mm and cm sources detected in the I00117 region

Source	Position α(J2000)	δ(J2000)	λ (mm)	$I_\nu^{\mathrm{peak\,a}}$ (mJy beam^{-1})	S_ν^{a} (mJy)	Mass$^{\mathrm{b}}$ ($M_\odot$)
mm1	00:14:26.10	+64:28:44.0	3	4.2	5.1	1.1
			1	21.3	71.4	1.0
mm2	00:14:26.27	+64:28:28.1	3	2.8	2.9	1.0
			1	19.3	59.3	1.4
UCHII	00:14:27.99	+64:28:44.7	36	1.4	2.6	
			13	1.0	2.5	

$^{\mathrm{a}}$ Corrected for the primary beam response.

$^{\mathrm{b}}$ Masses derived assuming a dust emissivity index of 1, the opacity law of Beckwith et al. (1990), and a dust temperature of 30 K for mm1 and of 20 K for mm2 (see main text). The uncertainty in the masses due to the opacity law and the dust emissivity index is estimated to be a factor of 4. Note that we did not estimate the dust emissivity index from our measurements at 3 and 1 mm because the different u-v coverages filter out different amounts of flux.

4.3.2 Molecular emission

The zero-order moment map integrated for the hyperfine $F_1 = 0$–1 of N_2H^+ is shown in Figure 4.3. The N_2H^+ emission shows three main clumps, one associated with mm1 and mm1a, and elongated in the northeast-southwest direction; another clump is associated with mm2, and is elongated in the northwest-southeast direction; the third clump falls at the southwestern edge of the field, where there is very faint mm and cm continuum emission.

The zero-order moment map for the CS(5–4) emission is shown in Figure **??**. The CS emission is associated only with mm1. Since $\sim 10''$ away from mm1 the intensity is attenuated by the primary beam by more than a factor of 2, we cannot properly judge whether there is no CS emission associated with mm2, or the emission has just been strongly attenuated.

Toward mm1 we additionally found CH_3OH emission from the 5_0–4_0 A+ and 5_{-1}–4_{-1} E transitions. In particular, the emission from the 5_0–4_0 A+ transition is very elongated in the northeast-southwest direction, starting at mm1 and ending at mm1a (Figure 4.4).

Spectra for N_2H^+(1–0), CS(5–4), and CH_3OH(5–4) are shown in Figure 4.5.
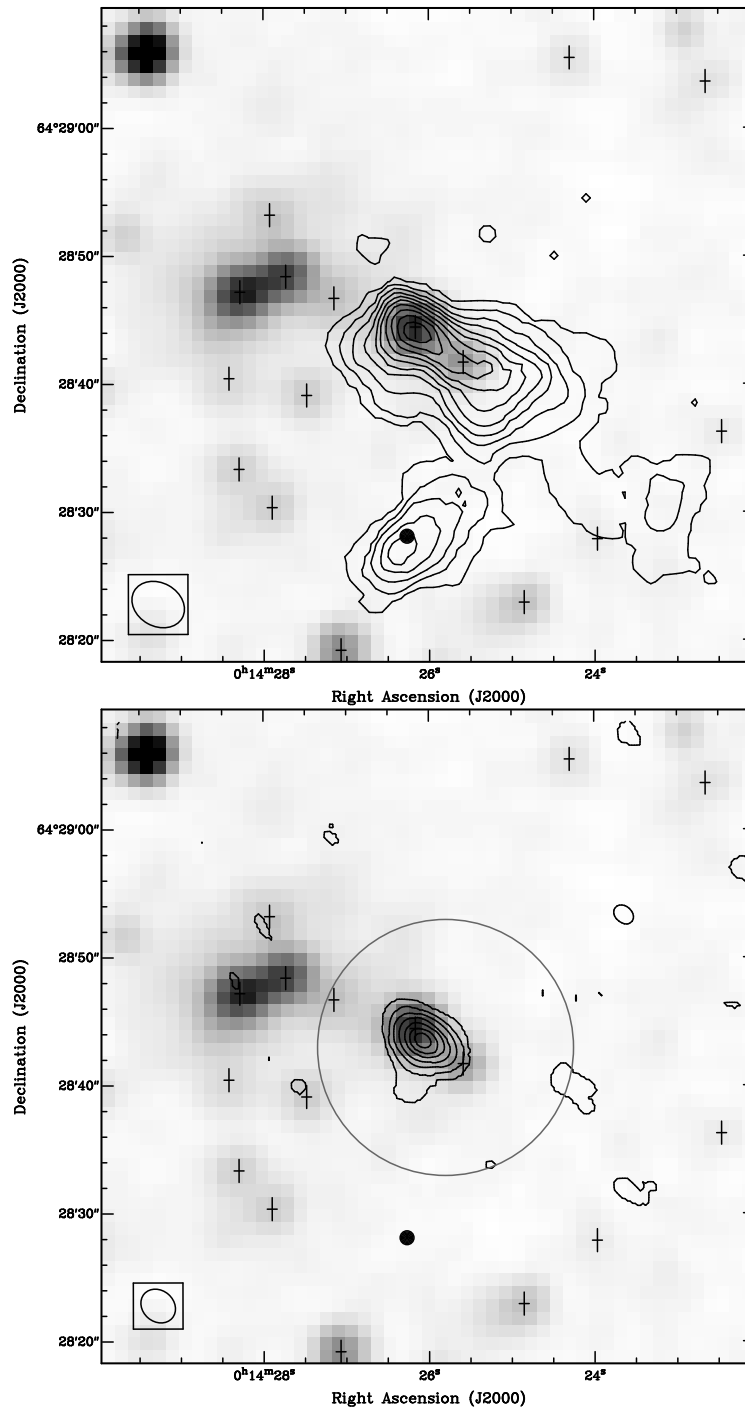
Figure 4.3: *Top:* Contours: zero-order moment for the hyperfine $F_1 = 0 - 1$ line of N_2H^+ toward IRAS 00117+6412. Contour levels range from 1 to 91% of the peak intensity, 0.358 Jy beam^{-1} km s^{-1}, increasing in steps of 10%. *Bottom:* Contours: zero-order moment for the CS(5–4) line. Contour levels range from 3 to 93% of the peak intensity, 4.07 Jy beam^{-1} km s^{-1}, increasing in steps of 15%. In both figures, the synthesized beam is shown in the bottom left corner. Grey scale: K-band 2MASS image. The crosses indicate the position of 2MASS sources, and the black dot marks the position of mm2. For the bottom figure, the circle indicates the primary beam at 1 mm.
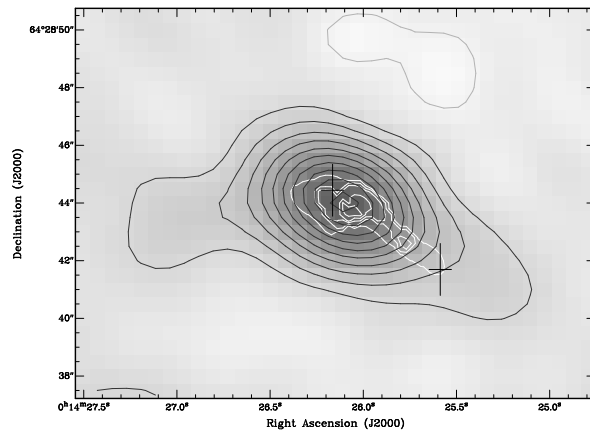
Figure 4.4: White contours: zero-order moment for the CH_3OH 5_0–4_0 A+ transition toward IRAS 00117+6412. Contour levels range from 5 to 95% of the peak intensity, 0.507 Jy beam^{-1} km s^{-1}, increasing in steps of 20%. The synthesized beam, is $1''50 \times 1''18$, P.A.= $58°3$. Grey scale and grey contours: 3 mm continuum emission shown in Fig. 4.1. The crosses indicate the position of the 2MASS sources associated with mm1 and mm1a.
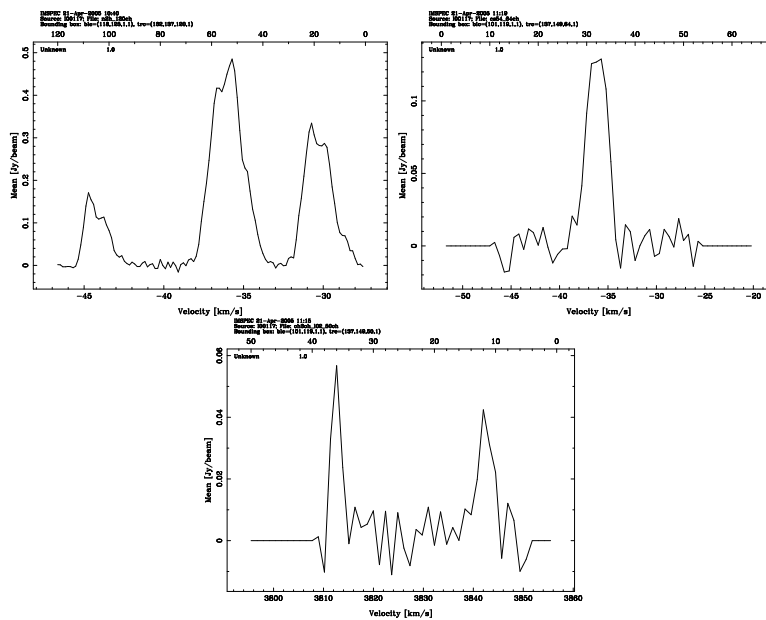
Figure 4.5: Spectra toward mm1 for N_2H^+ (top left), CS(5–4) (top right), and CH_3OH(5–4) (bottom) transitions. In the CH_3OH(5–4) spectrum, the strongest line is the 5_0–4_0 A+ transition, and the fainter is the 5_{-1}–4_{-1} E transition, and velocities are relative to the CS(5–4) transition.

4.4   Brief Discussion

We have shown the first results obtained with the PdBI toward IRAS 00117+6412. Further analysis must be carried out in order to properly interpret the results. For example, the first-order moment map made integrating only the hyperfine $F_1 = 0$–1 of $N_2H^+(1$–$0)$ reveals velocity gradients in the N_2H^+ clump associated with mm1 and also in the clump associated with mm2 (Figure 4.6). In addition, the N_2H^+ clump to the southwestern edge of the field shows an abrupt change in velocity of about 1 km s^{-1}. Note that the velocity gradients observed toward mm1 and mm2 have the blueshifted velocities toward the northwest and the redshifted velocities toward the southeast, while the bipolar outflow observed by Zhang et al. (2005) with lower angular resolution ($\sim 30''$) has the blue lobe to the north and the red lobe to the south. We should further investigate whether these gradients are consistent with infall/rotation, or are tracing the outflow motions.

From these preliminary results we can make a rough estimation of the evolutionary stage of the detected sources. First, the cm source is associated with the brightest 2MASS source and it is likely tracing a B2 star which has developed an UCHII region. The fact that we do not detect dust emission nor emission from dense gas tracers toward the cm source seems to support the idea that the underlying star has already cleared up most of the parental material. This is not the case, however, for mm1 that, although bright in the infrared, is the strongest mm source in the field and has dense gas associated with it traced by N_2H^+ and CS. Thus, mm1 is still deeply embedded in the molecular cloud, being likely in an earlier evolutionary stage than the UCHII region. Finally, mm2, which is also associated with dust emission and dense gas tracers, shows no infrared emission at all. Therefore, mm2 seems to be still more embedded than mm1, and thus could be a cold YSO that is completely dark in the infrared, or could be a starless core. Given that the masses derived from the dust emission are very similar for mm1 and mm2, the different evolutionary stages in these two sources is possibly an indication that they have not formed simultaneously.

Observations of outflow and shock tracers, such as CO, SiO and HCO$^+$ with high-angular resolution would allow us to study the interaction between the sources, and would possibly reveal the sources driving molecular outflows. In particular, if an outflow associated with mm2 is found, this would imply that mm2 is not a starless
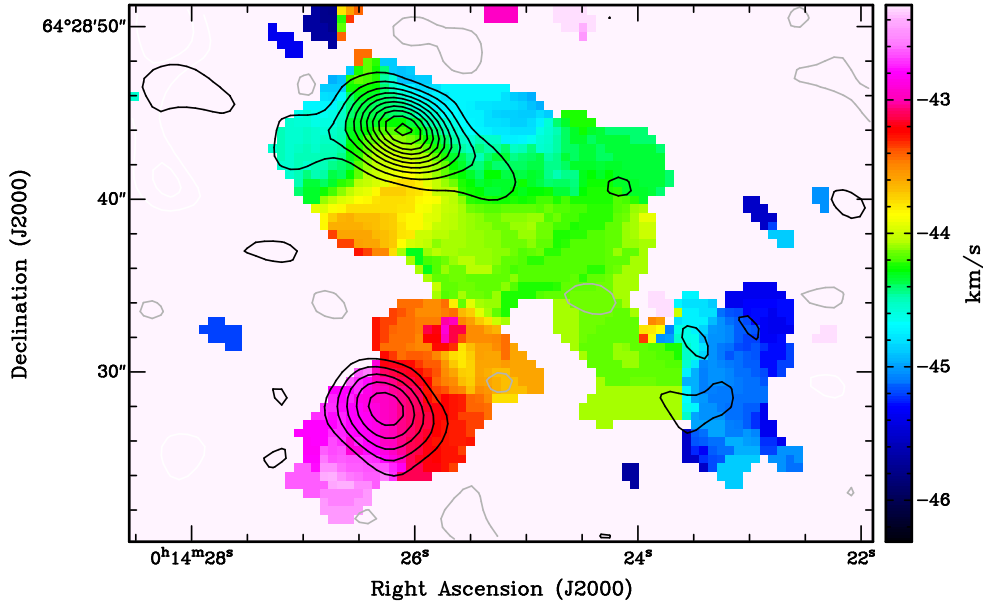
Figure 4.6: Color scale: first-order moment for the hyperfine $F_1 =$0–1 of N_2H^+(1–0) toward IRAS 00117+6412. Contours: 3 mm continuum emission shown in Fig. 4.1. Note that the systemic velocity of IRAS 00117+6412 is -36.3 km s^{-1} (Molinari et al. 1996; Zhang et al. 2005), and that the velocities in the first-order moment map correspond to the hyperfine $F_1 = 0 - 1$, which is shifted by -8.0 km s^{-1} from the hyperfine line taken as the reference line, the $F_1 = 2 - 1$, $F = 3 - 2$ transition. Blueshifted velocities are those smaller than -44.3 km s^{-1}, and redshifted velocities are those larger than -44.3 km s^{-1}.

core but a protostar in the very first stages of formation.

The results obtained toward IRAS 00117+6412 show that different sources formed in the same cloud are in different evolutionary stages. One of the sources seems to be an intermediate/high-mass YSO associated with an UCHII region, and the other two are of low mass. The low-mass source in the earliest evolutionary stage is found farther away from the UCHII region than the other low-mass source, raising the question of whether the low-mass sources have been triggered by the UCHII or not. Observations of molecules excited in photon-dissociated regions (like CN) and determination of the temperaure in the region (for example, through NH_3) would provide new light on the interaction of the UCHII region with the surrounding sources.
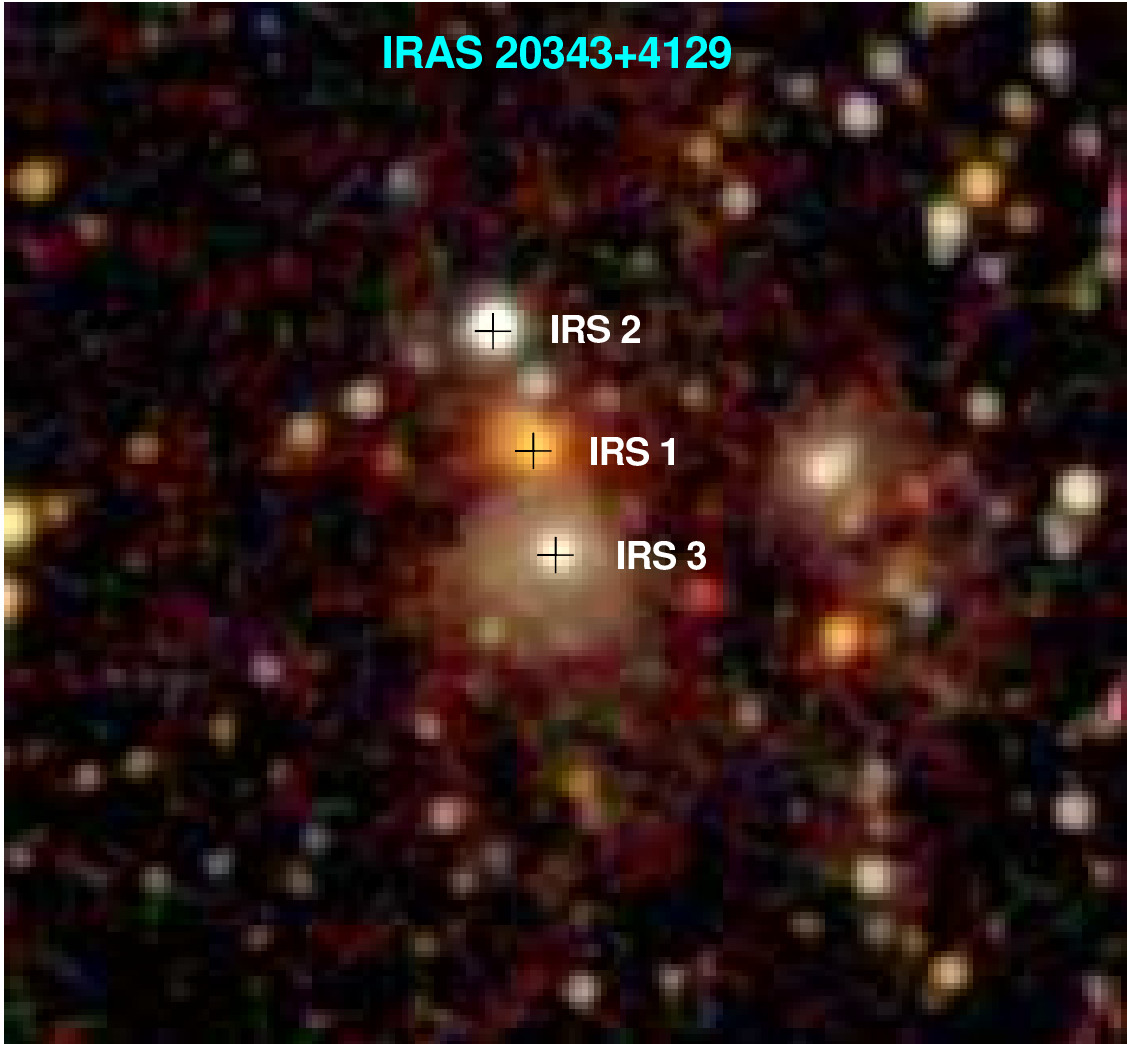
Figure: 2MASS composite image of J, H, and K filters of the IRAS 20343+4129 region. Note that IRS 1 is much redder than IRS 3, and that both IRS 1 and IRS 3 are surrounded by extended emission.

Chapter 5

IRAS 20343+4129: a puzzling massive star-forming region

5.1 Introduction

IRAS 20343+4129 is a star-forming region in the northeast of the Cygnus OB2 association. This region has been selected as a massive protostar candidate by Sridharan et al. (2002), has a kinematic distance of 1.4 kpc, and a luminosity of 3200 $L_\odot$. About $1'$ to the west of the IRAS source, there is a rimmed feature (see Figure 5.1) bright at centimeter wavelengths (Miralles et al. 1994; Carral et al. 1999), and in the H$_2$ (2.12 μm) emission line (Kumar et al. 2002). This arched morphology, which is facing the center of the Cygnus OB2 association, is reminiscent of high-mass cometary globules. Dense gas tracers such HCO$^+$, H^{13}CO$^+$, NH$_3$ and N$_2$H$^+$ have been detected toward the IRAS source (Richards et al.1987; Miralles et al. 1994; Fuller et al. 2005), suggesting this region is embedded in gas and dust.

In the near-infrared, Kumar et al. (2002) find three bright nebulous stars: IRS 1 and IRS 3 lying inside the IRAS error ellipsoide, and IRS 2 located toward the north. Extending southward from IRS 1 and surrounding IRS 3, there is line emission in a fan-shape structure (see Fig. 5.1). Centimeter observations carried out toward this region revealed an unresolved source associated with IRS 3 that was interpreted as an UCHII region ionized by a B2 star (Miralles et al. 1994; Carral et al. 1999).

A study of the red and massive objects in the entire Cygnus OB2 association was
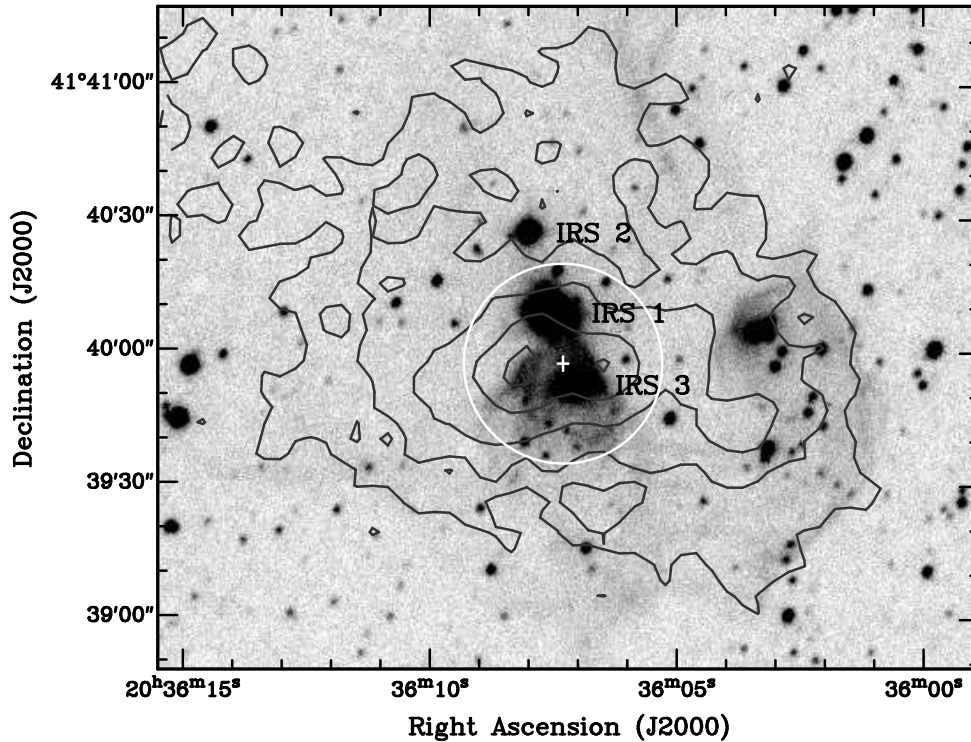
Figure 5.1: Continuum dust emission (contours) at 1.2 mm from single-dish (Beuther et al. 2002b) overlaid on H_2 emission (continuum plus line) at 2.12 μm (grey scale) from Kumar et al. (2002). Contours are 25, 50, 100, 200, and 300 mJy $beam^{-1}$. The beam from the 1.2 mm emission is $11''$. Note the H_2 emission surrounding IRS 3, in a fan-shape structure and coincident with two peaks of millimeter emission. Also note the cometary arch toward the west, matching very well the first continuum contour level. The circle and the cross indicate the primary beam of the SMA and the phase center of the observations presented in this chapter.

carried out through JHK photometry from 2MASS and spectroscopy in the range 1.5–2.4 μm by Comerón et al. (2002), concluding that this object may be one of the most luminous and embedded members of the Cygnus OB2 association. Thus, one would expect detecting a significant amount of dust toward IRS 1. However, single-dish observations revealed that none of the millimeter peaks detected in the region (see Fig. 5.1) were associated with IRS 1. No mm peak was associated with IRS 3 either (Beuther et al. 2002b; Williams et al. 2004). This raises the puzzling question of which is the massive source of the region, and which is the nature of the dust emission. In addition, Beuther et al. (2002c) found CO(2–1) outflow emission coming at least from two different sources, but the driving sources of these outflows

remain unidentified.

In this chapter we present the results of observations of the inner $1'$ around the IRAS source. Since previous studies at millimeter wavelengths have been carried out through single-dish observations, they provided large-scale properties of the region, but no concluding results on the nature of the embedded sources associated with the IRAS source and no clues regarding the nature of the CO features found in the region. Here we report on SMA observations of continuum at 1.3 mm and CO(2–1) which provide an angular-resolution four times better than that of single-dish observations, allowing us to gain light on the nature of each source of the region.

5.2   Observations

The SMA was used to observe the 1.3 mm continuum and the CO(2–1) emission toward IRAS 20343+4129. The observations were carried on 2003 August 3, with 6 antennas on the array. We note that this was one of the first days that the SMA was working with 6 antennas. The phase center was α(J2000) = $20^{\mathrm{h}}36^{\mathrm{m}}07\overset{s}{.}3$, δ(J2000) = $+41°39'57''{.}20$, and the projected baselines ranged from 119.8 to 13.1 m. The pads of the antennas were 1, 4, 5, 8, 11, and 16, which corresponds to an hybrid between compact and extended configuration. System temperatures were around 200 K. The full bandwidth for each sideband at that time was 0.984 GHz, and each sideband was divided into three blocks with four basebands each block. The correlator was set to the standard mode, which provided a spectral resolution of 0.8125 MHz (or 1.06 km s^{-1} per channel) accross the full bandwidth of 1 GHz. The tunning was set to 230.53796 GHz to observe CO(2–1). The FWHM of the primary beam at 230 GHz was $\sim 45''$.

The raw visibility data were flagged and calibrated with the MIR-IDL package. The passband response was obtained from observations of Uranus, which provided flat baselines when applied to Neptune. The baseline-based calibration of the amplitudes and phases was performed by using 2015+371. Typical rms of the phases was $\sim 60°$. Flux calibration was set by using Uranus, and the uncertainty in the absolute flux density scale was $\sim 20\%$.

Imaging was conducted using the standard procedures in MIRIAD (Sault et al. 1995). The continuum map has been made using only the lower sideband (the upper

sideband was more noisy and combining both sidebands did not result in a higher
S/N), without any tapering. For cleaning we used three boxes, one box in each
condensation detected with single-dish, and the other box toward IRS 1. Cleaning
with these boxes is the way that gives less negative lobes in the final cleaned map.
The final synthesized beam was $3''.47 \times 2''.64$, with P.A.$= -38°.0$, and the rms noise
of the continuum map was 2 mJy beam^{-1}. The rms noise of the 2 km s^{-1} wide
channel maps is 0.08 Jy beam^{-1}.

5.3 Results

5.3.1 Continuum

In Figure 5.2 we show the continuum emission observed with the SMA at 230 GHz
for the lower sideband. The continuum emission is found basically toward three
positions in the field: to the west of IRS 3 (where we find the strongest condensa-
tions, detected up to 18σ), to the east, and to the north of IRS 3 (where we find
condensations at a 6σ level). The condensations to the west and to the east of
IRS 3 are coincident with the single-dish peaks of emission (Beuther et al. 2002b),
and are not associated with any infrared source. The emission to the west of IRS 3
contains four condensations, mm1 to mm4, with a total flux density of 230 mJy
(correcting for the primary beam response). Since the integrated flux toward the
western condensation from single-dish is 1 Jy (Beuther et al. 2002b), 77% of the
flux has been filtered out by the interferometer. On the other hand, the eastern
condensation, mm7, detected at a 6σ level with a flux density of 28.0 mJy, corre-
sponds to a single-dish peak of 1.6 Jy (Beuther et al. 2002b), that is, almost all the
emission picked up with the single-dish is resolved out by the SMA for the eastern
condensation. Thus, this eastern peak detected in single-dish is not constituted by
compact sources but rather extended emission, while the western single-dish peak
contains more compact millimeter emission. In Table 5.1 we list the position, peak
intensity, flux density and mass for each mm condensation detected above 5σ. In
the derivation of the masses, we assumed that the dust emission is optically thin,
and adopted a dust temperature of 20 K, a dust emissivity index of 1 and the opac-
ity law of Beckwith et al. (1990). There is a factor of four in the uncertainty of
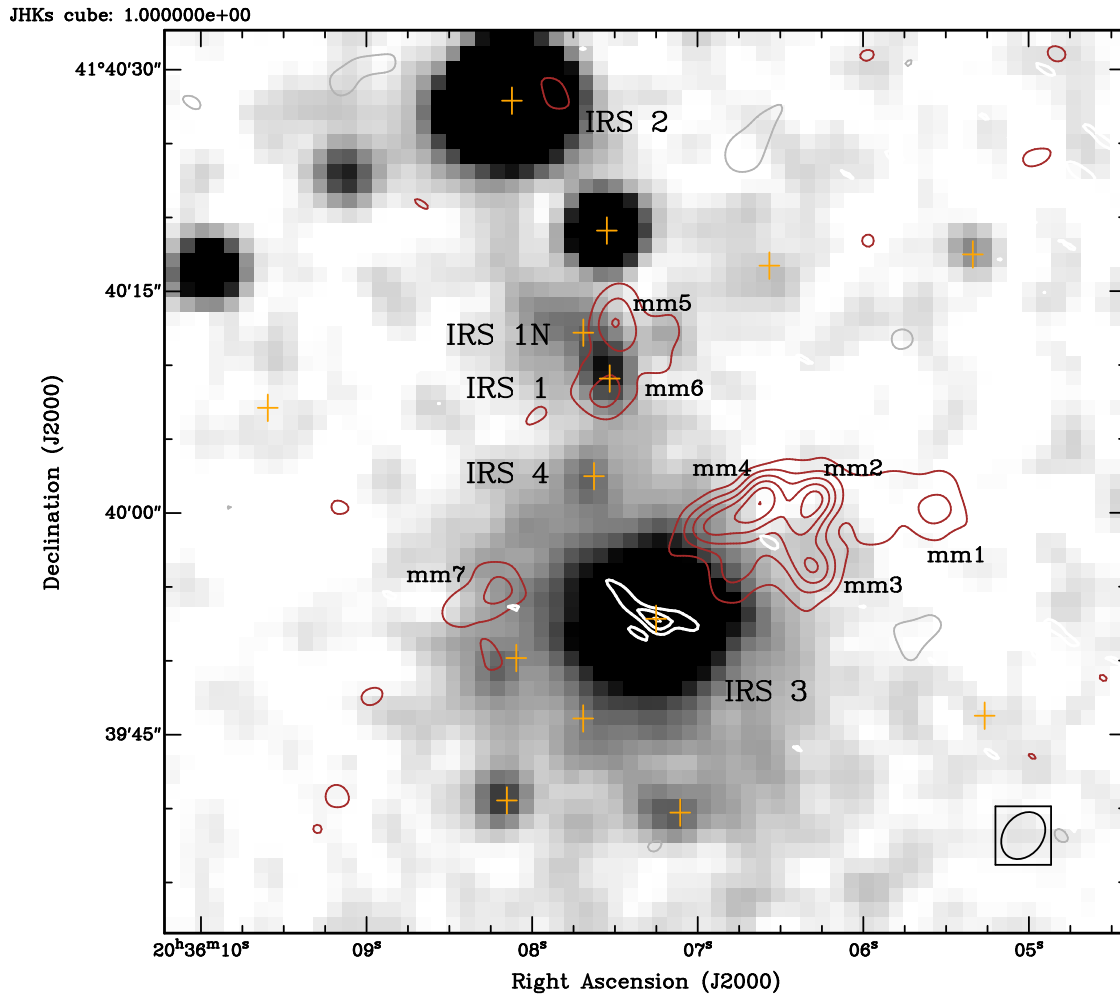these masses due to uncertainties in the opacity law and the dust emissivity index.

Figure 5.2: Brown contours: SMA continuum emission at 230.5 GHz obtained with natural weighting. Contours are -3, 3, 6, 9, 12, 15, and 18 times the rms of the map, 2 mJy beam^{-1}. The synthesized beam, shown in the bottom right corner, is $3''\!.5 \times 2''\!.6$, at P.A. $= -38°\!.0$. White contours: 3.6 cm emission obtained with the VLA (Sridharan et al. 2002). Contours are 3, 6, and 9 times the rms of the map, 0.2 mJy beam^{-1}. Grey scale: 2MASS J-band image from Extended Source Catalog. The crosses correspond to IR sources from 2MASS PSC.

Table 5.1: Parameters of the mm sources detected at 1.3 mm in the I20343 region

| Source | Position[a] | | $I_\nu^{\mathrm{peak}\,\mathrm{b}}$ | $S_\nu{}^{\mathrm{b}}$ | Mass[c] |
	α(J2000)	δ(J2000)	(mJy beam^{-1})	(mJy)	($M_\odot$)
mm1	20:36:05.56	+41:40:00.2	26.8	44.8	0.74
mm2	20:36:06.30	+41:40:00.7	40.5	40.5[d]	0.64
mm3	20:36:06.31	+41:39:56.4	29.9	34.0	0.57
mm4	20:36:06.62	+41:40:00.6	39.7	45.3	0.75
mm5	20:36:07.49	+41:40:12.8	25.8	34.8	0.58
IRS1/mm6	20:36:07.56	+41:40:08.0	16.9[e]	31.5[e]	0.52
mm7	20:36:08.19	+41:39:54.8	16.7	28.0	0.47

[a]   Positions correspoding to the peak intensity.

[b]   Corrected for the primary beam response.

[c]   Masses derived assuming a dust emissivity index of 1, and a dust temperature of 20 K. The uncertainty in the masses due to the opacity law and the dust emissivity index is estimated to be a factor of 4.

[d]   Unresolved source.

[e]   Intensity and flux density derived from a Gaussian fit.

The four mm sources associated with the western single-dish condensation result in a mass of $\sim 4\ M_\odot$. This is consistent with the masses derived by Beuther et al. (2002b) if we take into account the fraction of flux density resolved out by the SMA, and the different parameters of dust temperature and dust emissivity index used by Beuther et al. (2002b). In addition, the masses reported in Beuther et al. (2002b) are a factor of two lower, as explained in the erratum of Beuther et al. (2005a).

The dust condensation to the north of IRS 3, mm6, is associated with IRS 1. The integrated flux density of mm6 is 31.5 mJy, correcting for the primary beam response. Taking a dust temperature from NH_3 of ~ 20 K (Miralles et al. 1994), this flux density corresponds to 0.52 $M_\odot$. For a dust temperature T_{d} of 44 K (derived from the spectral energy distribution, Sridharan et al. 2002), the mass is 0.20 $M_\odot$. Then, for the adopted opacity law and dust emissivity index the mass of gas and dust toward IRS 1 is 0.2–0.5 $M_\odot$.

There is one condensation, mm5, $5''$ to the north of IRS 1 which is slightly offset ($\sim 2''$) to the west of the infrared source IRS 1N (Fig. 5.2). Since we estimate an absolute position accuracy of $\sim 1''$, it is not clear from our data whether mm6 is associated with IRS 1N or it is tracing a different source. However, the association of some dust emission with IRS 1N is expected because IRS 1N is the infrared source

with highest infrared excess in the region (see § 5.4.4 and Figure 5.10).

Fig. 5.2 also shows the centimeter emission at 3.6 cm from Sridharan et al. (2002). The only centimeter source in the field is found toward IRS 3. From our millimeter observations we can only set an upper limit of $4\sigma = 8$ mJy for the emission at 1.3 mm. The nature of the cm source associated with IRS 3 is discussed in § 5.4.2.

5.3.2 CO(2–1)

Channel maps of the CO(2-1) emission are displayed in Figure 5.3. CO(2–1) emission extends from -8 up to 38 km s^{-1}, being the systemic velocity 11.5 km s^{-1}. The negative lobes seen at ambient velocities are produced by the missing short-spacings of the interferometer. The strongest CO(2–1) feature is associated with IRS 1, and spans several channels for blue and red velocities. Figure 5.4 shows the spectrum of the CO(2–1) emission toward IRS 1, with wings extending up to ±15 km s^{-1} from the systemic velocity.

The map of the low-velocity emission, integrated from 8 to 14 km s^{-1}, is shown in Figure 5.5, and reveals two filamentary structures at both sides of IRS 3, possibly associated with the fan-shape structure found in H$_2$ by Kumar et al. (2002). From the low-velocity map, it is also clear the association of CO(2–1) with IRS 1, as well as the presence of weak low-velocity components westwards of the CO(2–1) main emission.

Regarding the high velocities, these are present only in the immediate surroundings of IRS 1. Fig. 5.6 plots the integrated high-velocity emission toward IRS 1. Blue velocities have been integrated from -4 to 6 km s^{-1}, and red velocities from 16 to 38 km s^{-1}. The high-velocity CO(2–1) emission has a bipolar structure, with the center at the position of IRS 1, and elongated in the east-west direction. Note that the red emission has two knots.

A position-velocity (p-v) plot obtained toward IRS 1 in the east-west direction is shown in Figure 5.7. At low velocities, the emission extends over all positions, and has negative lobes, as already seen in the channel maps (Fig. 5.3). Up to $\pm8''$ from the zero offset position, the emission shows a bipolar morphology, reaching high-velocities which are blueshifted for positive offsets (to the east), and redshifted for negative offsets (to the west). The distance from IRS 1 where we find high
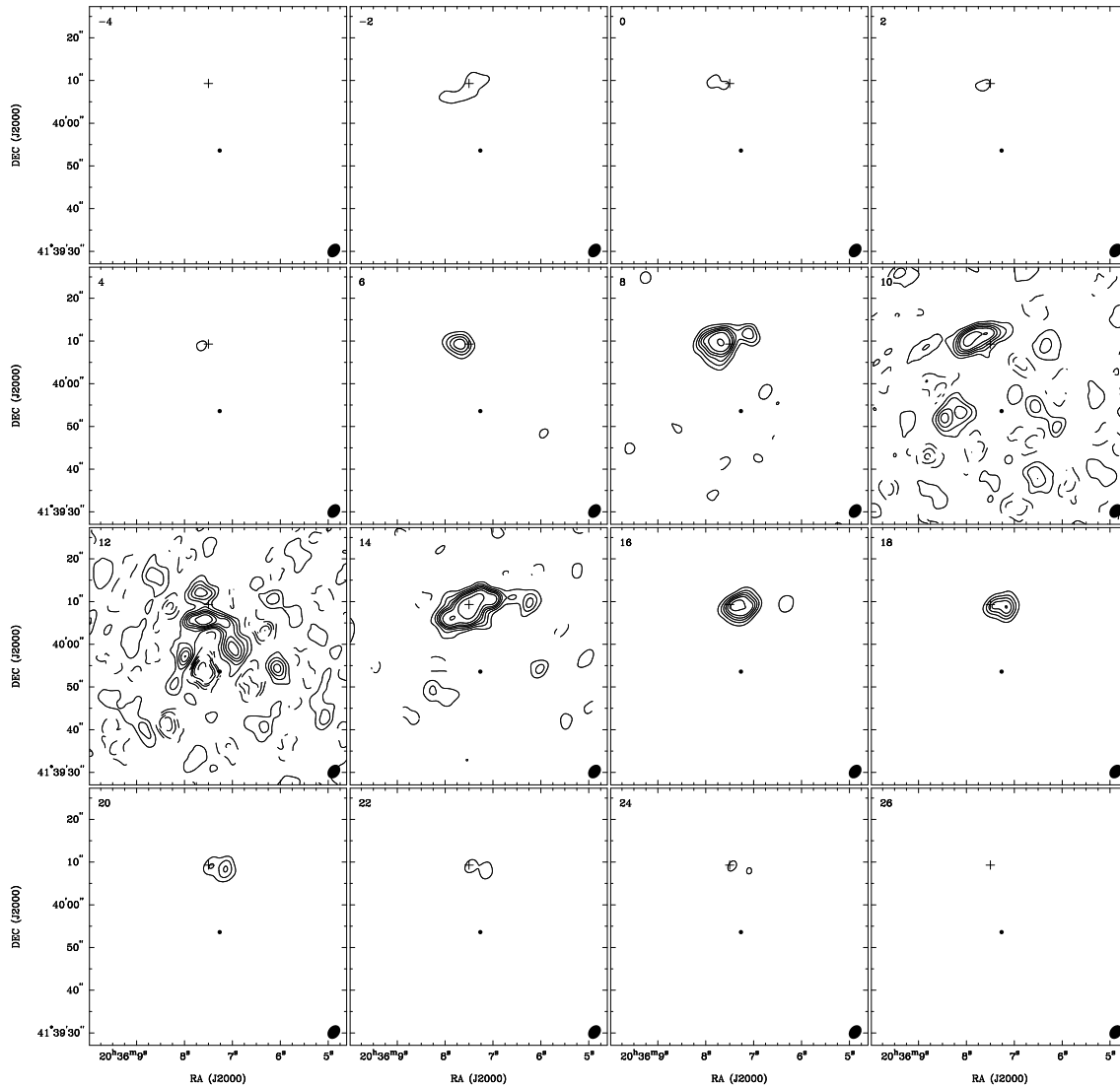
Figure 5.3: Channel maps of the CO(2–1) emission, averaged over 2 km s^{-1} wide velocity intervals. The central velocity of each channel is indicated in the upper left corner of each panel, and the systemic velocity is 11.2 km s^{-1}. The cross and the circle indicate the position of IRS 1 and the centimeter source, respectively. The synthesized beam, shown in the lower right corner, is $3.''5 \times 2.''7$, at P.A.$= -37.°8$. Contours are -30, -20, -15, -12, -9, -6, -3, 3, 6, 9, 12, 15, 20, and 30 times 0.4 Jy beam^{-1}.
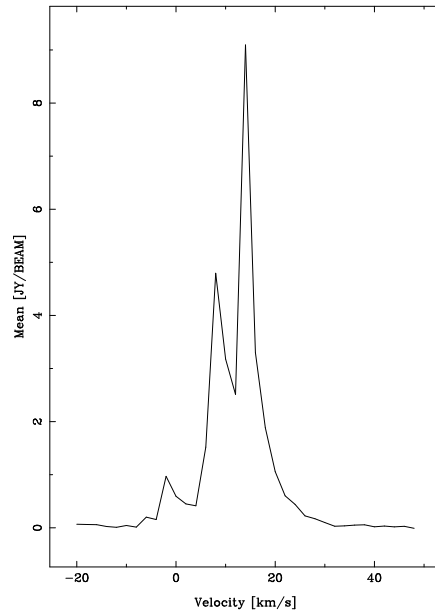
Figure 5.4: Spectrum of the CO(2–1) emission toward the position of IRS 1, from the 2 km s^{-1} wide channel maps. The conversion factor from Jy beam^{-1} to K is 2.46.

velocities allows us to constrain whether such velocities are due to gravitationally bound motions. We find weak high-velocity gas at ~ 12 km s^{-1} from the systemic velocity at position offsets up to 8″, or 10000 AU. Such velocities at these distances would imply an extremely high central mass of ~ 1000 $M_\odot$ to be gravitationally bound, and hence the bipolar structure seen in CO(2–1) toward IRS 1 is tracing an outflow motion.

Additionally, we computed the p-v plot toward IRS 1 in the north-south direction (Figure 5.8). For low velocities we find again negative lobes due to large scale emission. For this reason, we are not very confident about the weak clumps at offset positions 12″ and −35″. The only clear CO feature along the north-south direction is the clump at the offset position zero, and does not seem related to any other CO feature in the south, as one would expect judging from the single-dish CO map from Beuther et al. (2002c). The CO emission at position zero arises from IRS 1, with the high-velocity component coming from outflow motions (see above). The low-velocity emission toward IRS 1 has a ring structure in the p-v plot, covering positions from −3″ to 3″, and ranging from −8 to 14 km s^{-1}. This could be tracing a ring (seen edge-on and oriented in the north-south direction, perpendicular to the direction of the outflow) in contraction or expansion. Assuming this is tracing a
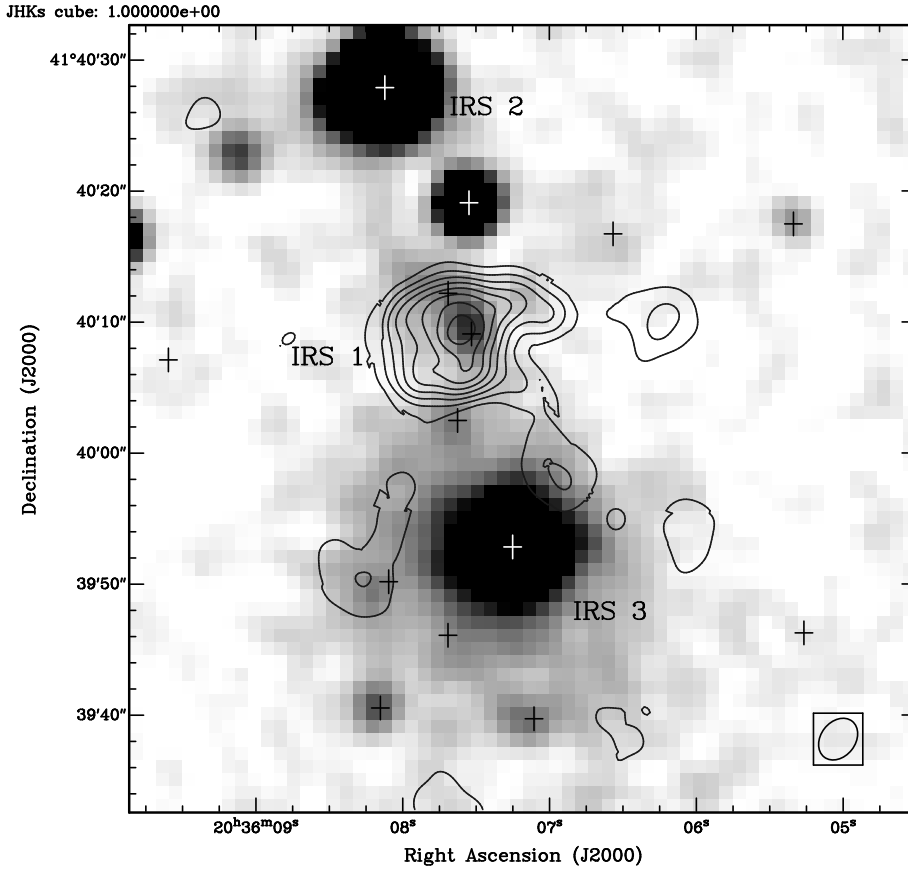
Figure 5.5: Contours: Moment zero map for the low velocity CO(2–1) emission. Velocities have been integrated from 8 to 14 km s^{-1}. Contours range from 8 to 64 Jy beam^{-1} km s^{-1}, increasing in steps of 8 Jy beam^{-1} km s^{-1}. Grey scale: same as Fig. 5.2.

ring in contraction, the central mass which could account for such gravitationally bound motions should be $\sim 40\ M_\odot$. However, it is unlikely that IRS 1 is harboring such a massive star (see § 5.4.3 for a discussion on the mass of IRS 1). Thus, if this structure is really tracing a ring, it should be an expanding ring in the equatorial plane of the protostar. Alternatively, this structure could be produced by self-absorption of the foreground quiescent material, which seems a more plausible possibility. Observations of ^{13}CO would allow us to determine the CO opacity and thus confirm or discard the possibility of self-absorption.

Finally, we calculated the energetics of the outflow associated with IRS 1 for each lobe separately, and we list the values in Table 5.2. The expressions used for

JHKs cube: 1.000000e+00
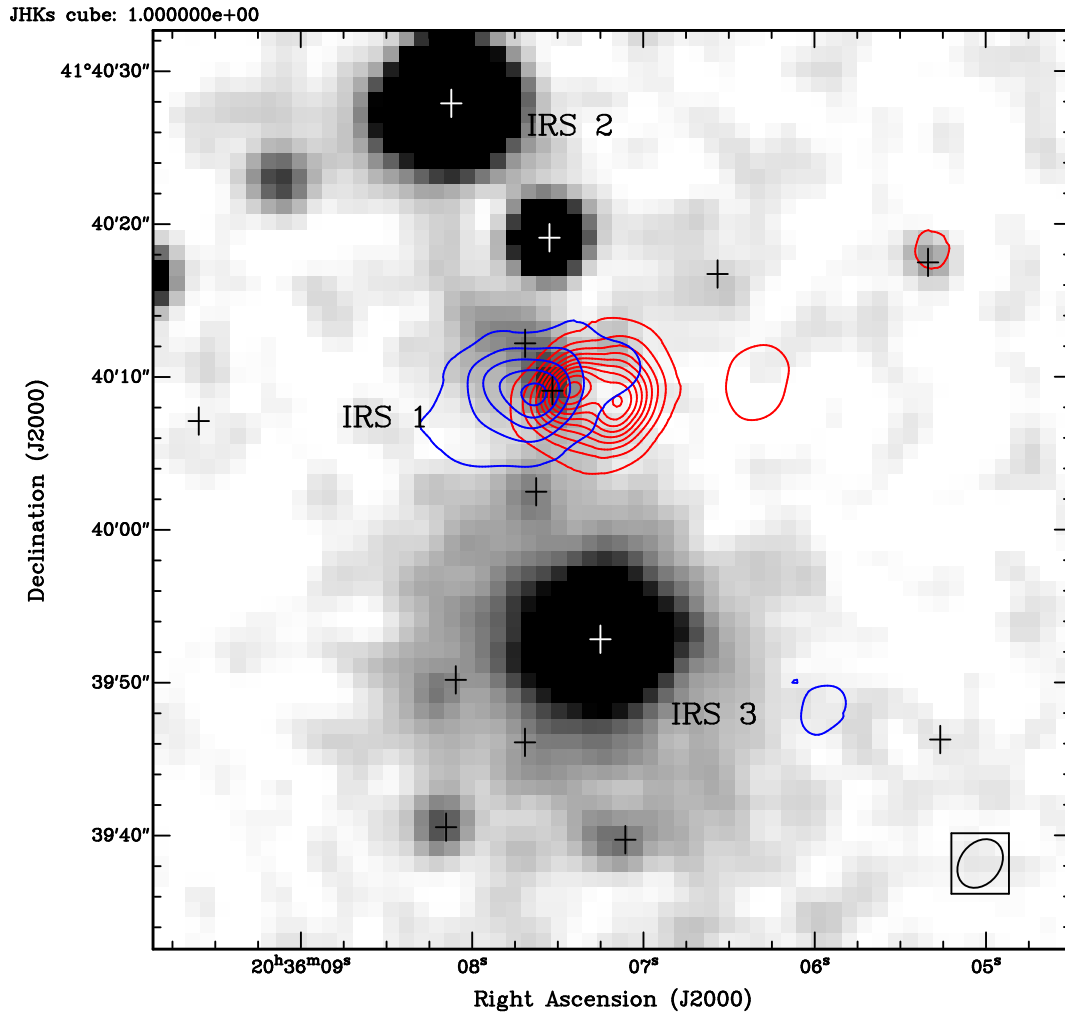
Figure 5.6: Red and blue integrated CO(2–1) emission overlaid on the 2MASS J-band image from Extended Source Catalog (grey scale). Red contours, corresponding to a velocity range from 16 to 38 km s^{-1}, range from 2 to 49 Jy beam^{-1} km s^{-1}, increasing in steps of 5 Jy beam^{-1} km s^{-1}; blue contours correspond to -4 to 6 km s^{-1}, and range from 2 to 23 Jy beam^{-1} km s^{-1}, increasing in steps of 5 Jy beam^{-1} km s^{-1}. Crosses mark the positions of IR sources from 2MASS PSC.
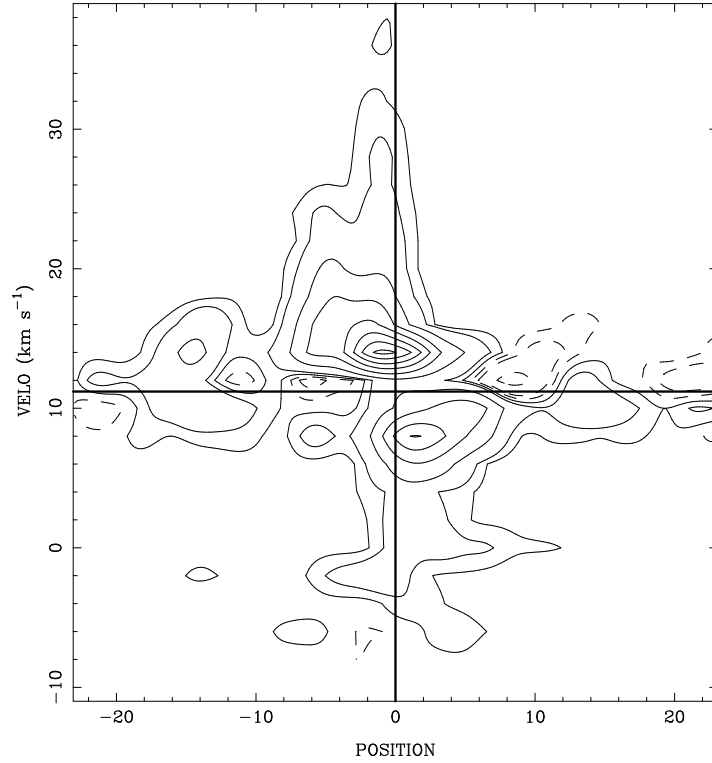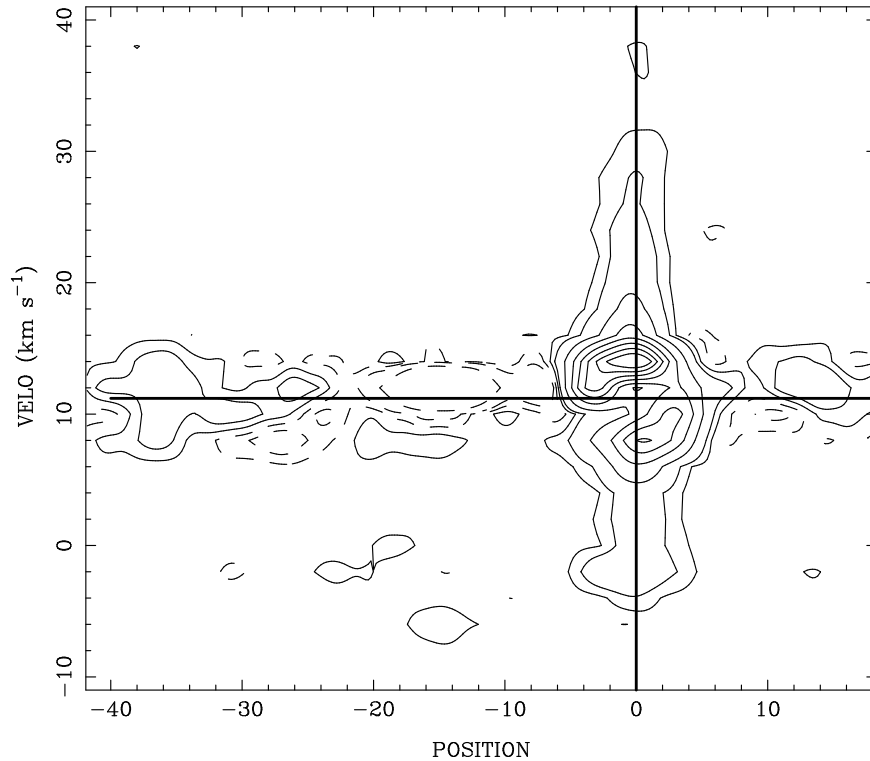
Figure 5.7: Position-velocity plot along the east-west direction centered on IRS 1. Contours are -30, -9, -3, 3, 9, 30, 60, 90, 120, 150, and 180 times 0.1 Jy beam^{-1}. The straight lines mark the position of IRS 1 and the systemic velocity, 11.2 km s^{-1}.

calculating the outflow parameters are listed in the Appendix. We assumed optically thin emission in the wing, and an excitation temperature of ~ 25 K, derived from the spectrum in Fig. 5.4. For the red lobe we integrated from 16 to 30 km s^{-1}, and for the blue lobe from -6 to 8 km s^{-1}. The age or dynamical timescale t_{dyn} was derived by dividing the size of each lobe (from the first contour shown in Fig. 5.6) by the maximum velocity reached in the outflow with respect the systemic velocity (measured in the spectrum: 18.5 km s^{-1} for the red lobe, and 17.5 km s^{-1} for the blue lobe). We did not correct for the inclination angle, since this parameter is not well known.

Figure 5.8: Position-velocity plot along the north-south direction centered on IRS 1. Contours are -30, -9, -3, 3, 9, 30, 60, 90, 120, 150, and 180 times 0.08 Jy beam^{-1}. The cross marks the position of IRS 1 and the systemic velocity, 11.2 km s^{-1}.

5.4 Discussion

5.4.1 The young high-velocity bipolar outflow toward IRS 1

Small scale outflow discovered toward IRS 1: The high-velocity bipolar out-flow found toward IRS 1 has a short dynamic timescale compared with typical values for other outflows, and the mass, the rate of the outflow mass, the momentum, momentum rate, kinetic energy, and mechanical luminosity are similar to those of low-mass outflows (Bontemps et al. 1996; Wu et al. 2004), and are about 2 orders of magnitude smaller than the parameters of high-mass outflows (Beuther et al. 2002c; Wu et al. 2005; Zhang et al. 2005). This suggests that the driving source is a low/intermediate-mass protostar. However, all the mentioned studies of high-mass

Table 5.2: Physical Parameters[a] of the Outflow Driven by IRAS 20343+4129-IRS1

Lobe	Age (yr)	N_{12} (cm^{-2})	Mass ($M_\odot$)	$\dot{M}$ ($M_\odot$ yr^{-1})	P ($M_\odot$ km s^{-1})	$\dot{P}$ ($M_\odot$ km s^{-1} yr^{-1})	$E_{\rm kin}$ (erg)	$L_{\rm mech}$ ($L_\odot$)
Red	3600	2.4×10^{16}	0.014	3.9×10^{-6}	0.20	5.5×10^{-5}	2.8×10^{43}	0.048
Blue	3800	2.9×10^{16}	0.016	4.3×10^{-6}	0.23	6.1×10^{-5}	3.2×10^{43}	0.056

[a] The parameters were obtained as follows: age $= t_{\rm dyn}$ (see main text); rate of the outflow mass: $\dot{M} = M/t_{\rm dyn}$; momentum: $P = M V_{\rm range}$ ($V_{\rm range}$ is the range for which we integrated the emission for each lobe, see main text); momentum rate (or mechanical force): $\dot{P} = P/t_{\rm dyn}$; energy of the outflow: $E = 1/2\, M\, V_{\rm range}^2$; mechanical luminosity: $L_{\rm mech} = E/t_{\rm dyn}$.

outflows were based on single-dish observations, picking up the large-scale structure and considering thus larger areas of outflow emission, which yield much larger values. We compared thus the parameters of the outflow with results toward high-mass protostars from interferometric observations. Sandell et al. (2005) observed with BIMA the NGC 7539-IRS 9 region and found parameters about three-four orders of magnitude higher than those found for IRS 1. The authors derived the parameters correcting for inclination and opacity, but these effects may contribute only about one order of magnitude. If we compare with the outflow toward S235A-B observed with the PdBI by Felli et al. (2004), the values toward IRS 1 are still about 2 orders of magnitude smaller. This supports that the outflow parameters for IRS 1 are comparable to those of a low-mass protostar. We estimated the luminosity of the driving source from the rate of the outflow mass following the relation by Churchwell (1997) derived for YSOs between 1 and 10^6 $L_\odot$, and obtained a luminosity of 2–9 $L_\odot$, depending on whether we adopt the correction for opacity of Bontemps et al. (1996) or not.

By plotting the momentum rate versus the mass of the envelope of IRS 1, following Bontemps et al. (1996), we find that the momentum rate of the IRS 1 outflow is comparable to those of low-mass Class 0 sources. Thus, if IRS 1 is a low-mass protostar, it is likely a Class 0 source. Given that for Class 0 sources the mass of the envelope is larger than the accreted mass (André et al. 1993), if IRS 1 is an intermediate/high-mass protostar, then the classification of a Class 0 source will not be valid (see § 5.4.3 for a discussion on the mass of IRS 1).

We additionally considered the cm luminosity which should be observed given the momentum rate of the outflow, assuming the cm emission is produced by shock ionization. Anglada (1995) study the relation between these two quantities for a

sample of low-mass and intermediate-mass YSOs, and fit the data assuming an efficiency (fraction of stellar wind that is shocked) of 0.1. The value of the momentum rate of the outflow from IRS 1 yields a cm luminosity of 0.07–0.4 mJy kpc^2, for efficiencies between 0.1 and 1. These cm luminosities are undetectable with the sensitivity of our observations, which is of 0.4 mJy kpc^2. Then, the momentum rate derived for the outflow of IRS 1 is not able to produce a detectable amount of cm emission, consistent with our observations.

Large scale CO emission: Single-dish observations of CO(2–1) toward IRAS 20343+4129 show a blue lobe with two subcondensations around IRS 3, and a red single-peaked lobe around IRS 1 (Beuther et al. 2002c). H$_2$ emission in a fan-shape structure is found to be associated with the blue CO large-scale lobe (see Fig. 5.1). This seems to suggest the existence of an outflow in the north-south direction. However, from the SMA data shown in this work we find no evidence of such an outflow (see Fig. 5.8).

We compared the SMA CO(2–1) channel maps with the single-dish CO(2–1) channel maps provided by H. Beuther. The blue lobe observed with single-dish results from integrating only from 8 to 9 km s^{-1}, an interval very close to the systemic velocity, because for velocities smaller than 8 km s^{-1} the single-dish observations were affected by an OFF-position problem, making unusable the channels with velocities smaller than 8 km s^{-1}. In the SMA channel maps from Fig. 5.3, we do not detect emission at 8 km s^{-1} at the position of the blue lobe seen in single-dish. Considering that the large-scale blue lobe arises from extended emission, we find that no emission could have been detected by the SMA. The intensity detected in single-dish toward the blue lobe is 24.6 K km s^{-1}, and the size of the blue lobe is $\sim 30'' \times 10''$. If all the CO emission detected with single-dish is uniformly distributed over the entire area of 300 arcsec^2, then beam dilution implies that with the SMA we should detect only 0.75 K km s^{-1}, or 0.3 Jy beam^{-1} km s^{-1}. The noise in the channel maps (of 1 km s^{-1}) is ~ 0.11 Jy beam^{-1}, and thus the large scale lobe seen in single-dish should be barely detectable with the SMA if there is no contribution from compact emission.

Regarding the red single-dish lobe, this was obtained integrating from 13 to 15 km s^{-1} (Beuther et al. 2002c). We estimated the contribution of the SMA redshifted emission to the single-dish redshifted emission. The SMA integrated intensity of the red lobe for the same range of velocities as Beuther et al. (2002b) is

34.8 K km s^{-1} (obtained from the spectrum toward IRS 1), and the size of the lobe is $\gtrsim 10''$. This size is similar to the beam of the IRAM-30m, and thus the red lobe seen with the SMA was filling almost all the single-dish beam (filling factor ~ 1). Beuther et al. (2002c) obtained an integrated intensity of 33.4 K km s^{-1}, implying that the SMA redshifted emission can account for all the redshifted emission detected with single-dish. Therefore, the main contribution to the redshifted large-scale lobe is, contrary to the blueshifted lobe, the compact emission detected with the SMA. This suggests that the red and blue lobes seen in single-dish do not come from the same material.

At this point, it seems reasonable to think that if we reobserved with single-dish the blueshifted emission with velocities smaller than 8 km s^{-1}, we would detect the blue compact high-velocity lobe seen with the SMA to the east of IRS 1. In fact, some hints of blueshifted emission can be seen to the east of IRS 1 in the Beuther et al. (2002c) integrated intensity maps. In order to definitively confirm that the single-dish and the interferometric observations are consistent, we should reobserve this region with single-dish.

5.4.2   Is IRS 3 driving a cavity around it?

As seen above, the CO(2–1) emission from single-dish shows a sligthly blueshifted large-scale lobe with two subcondensations at both sides of IRS 3 (Beuther et al. 2002c). This CO blueshifted large-scale lobe matches well the fan-shape structure seen in H$_2$ emission (Kumar et al. 2002). In addition, from the SMA data of this work, we found an elongated low-velocity CO(2–1) filament at each side of IRS 3, as well as dust condensations also at each side of IRS 3. All these observational features seem to suggest that IRS 3 is interacting with the surrounding medium and producing a shell of circumstellar gas expanding away from IRS 3.

The cm emission shown in Fig. 5.2 reveals a compact source associated with IRS 3. We assume that the high luminosity of the IRAS source is produced by IRS 3 and that the UV photons from IRS 3 have ionized the surrounding gas creating an UCHII region. The flux density at 3.6 cm is 1.8 mJy, and the deconvolved size of the source is $2''4 \times 0''9$ (0.02 pc $\times$ 0.006 pc). We estimate a flux of ionizing photons of 1.8×10^{44} s^{-1}, which corresponds to a B2 star (Panagia 1973), consistent with the spectral type found by Miralles et al. (1994) from observations at 6 cm. We consider

now whether a B2 star is able to produce an expanding shell by radiation pressure. Given the mass and the luminosity of a star, one can calculate the lower limit of the luminosity to mass ratio for the ejection by radiation pressure of an optically thin cloud of material surrounding the star (e. g., Kahn 1974), which depends on the average mass absorption coefficient of the dust surrounding the star. Anglada et al. (1995) estimate this absorption coefficient as the Planck mean of a mixture of dust grains typical for molecular clouds by assuming the same opacity contributors and monochromatic opacities as in Calvet et al. (1991), and list the calculated values of the absorption coefficient (which are independent of dust temperature and gas density) for different effective temperatures of the central star. Thus, the lower limit value for the luminosity to mass ratio sets an upper limit to the mass of the central star, given its luminosity and the absorption coefficient of the surrounding dust. For a typical B2 star, we adopt a luminosity of 2900 $L_\odot$, and an effective temperature of 20000 K (Panagia 1973), yielding an absorption coefficient of ~ 300 cm^2 g^{-1}, from Table 3 of Anglada et al. (1995). We derive an upper limit for the mass of IRS 3 of 68 $M_\odot$. If the mass of IRS 3 is smaller than 68 $M_\odot$, then the ejection of a shell of surrounding material is possible, given its luminosity and the assumed properties of the dust around it. Young stars with the luminosity of the IRAS source, around 3000 $L_\odot$, have typically masses between 5–10 $M_\odot$ (e. g., Palla & Stahler 1994), and thus IRS 3 could be radiatively driving a cavity around it.

Alternatively, we considered that the cm source associated with IRS 3 is tracing an ionized stellar wind. If this was the case, we may estimate the mass loss rate of the ionized material, $\dot{M}_{\rm ion}$, by following Beltrán et al. (2001). Assuming that the half-width of the jet is constant with the distance from the star, which yields a spectral index of 0.6, a velocity for the wind of 200 km s^{-1}, a turnover frequency of ~ 10 GHz, an inclination angle (onto the plane of the sky) equal to 0°, and a jet injection opening angle for the wind of $\sim 60°$, we obtained $\dot{M}_{\rm ion} = 3.9 \times 10^{-7}$ $M_\odot$ yr^{-1}. Anglada et al. (1995) considered a wind-driven cavity model and derived several relations between the characteristics of the cavity, $\dot{M}_{\rm ion}$ and the velocity of the wind. In particular, we have observed the radius of the shell and its velocity. We adopted as radius of the shell $\sim 10''$, the distance between IRS 3 and the walls traced by H$_2$ and CO, and a velocity of the shell of ~ 2 km s^{-1}, since Beuther et al. (2002c) observed the CO(2–1) material around IRS 3 to be blueshifted by ~ 2 km s^{-1} (see § 5.4.1). The external pressure that the ambient cloud is producing on the expanding shell can be derived from the line width of the CO(2–1) line in the walls of the cavity, traced by the elongated low-velocity structures found with

the SMA (see Fig. 5.5), which is ~ 3.3 km s^{-1}. The unknowns are the density of the medium, ρ_0, which we consider to be uniform, and the time during which the wind has been blowing up and pushing the material out. From equations (17) and (18) of Anglada et al. (1995), we derive $\rho_0 = 2300$ cm^{-3}, and $t = 11000$ yr. This value for the density of the medium is comparable to typical densities of molecular clouds (e. g., Benson & Myers 1989). For this case, the maximum radius that the cavity will reach, R_{max}, can be calculated , and we found $R_{max} = 0.08$ pc, which is slightly larger than the size of the cavity observed. We note that the time during which the wind has been blowing is not the age of the star. Rather, this can be interpreted as IRS 3 having episodic mass loss rates. Therefore, if the cm emission arises from an ionized stellar wind from IRS 3, this wind could be driving a cavity of swept up material that is in agreement with the observational features found around IRS 3.

Thus, either we interpret the cm emission as an UCHII region, or as an ionized stellar wind, IRS 3 can create a cavity of swept up material around it. In order to distinguish between both scenarios, it would be very useful having the spectral energy distribution in the cm range for IRS 3. In addition to the 3.6 cm measurement from Sridharan et al. (2002), shown in this work, there are other observations at 6, 3.6 and 2 cm (Miralles et al 1994; Carral et al 1999). The flux densities for each wavelength are plotted in Figure 5.9, together with the 3σ upper limits at 1.3 mm of 6 mJy beam^{-1} (this work), and at 7 mm of 9 mJy beam^{-1} (K. Menten, private communication). The only simultaneous measurements are those at 6 and 2 cm (observed in 1989), which result in a spectral index of ≤ -0.1, consistent with an optically thin UCHII region. However, the other observations at 3.6 cm (carried out 5 and 9 years later than the observations at 6 and 2 cm) are not consistent with this flat spectral index. With the measurements at 3.6 and 6 cm, the spectral index ranges from 0.3 to 0.9 (depending on the epoch of the observations at 3.6 cm). This spectral index is consistent with emission from an ionized wind (e. g., Reynolds 1986). Thus, from the current data it is not clear if the source is variable with time, and what is the value of the spectral index of the cm source associated with IRS 3. New observations at 6, 3.6, 2, and 1.3 cm toward IRS 3 would give insight into which mechanism, a stellar wind or radiation pressure, is driving the cavity.
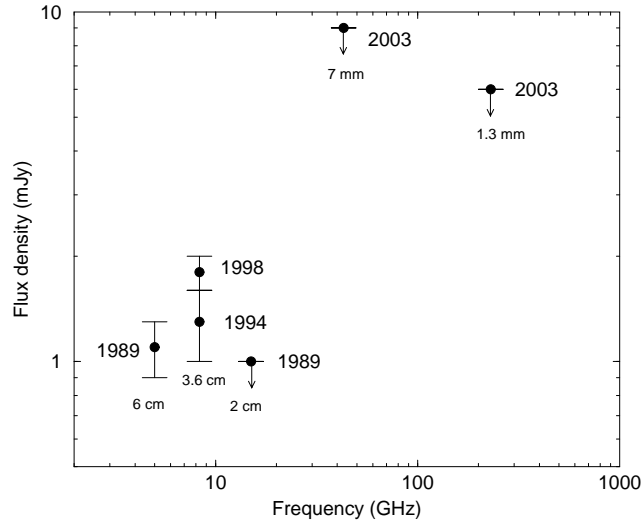
Figure 5.9: Spectral Energy Distribution at centimeter wavelenghts for IRAS 20343+4129-IRS3. Next to each measurement there is the year of the observations. 1989: Miralles et al. (1994); 1994: Carral et al. (1999); 1998: Sridharan et al. (2002); 2003: Menten et al., in prep. and Palau et al., in prep.

5.4.3 On the mass of IRS 1

The source IRAS 20343+4129 could be associated with IRS 1 and IRS 3, since both sources fall inside the IRAS error ellipsoide. Both IRS 1 and IRS 3 may contribute then to the IRAS fluxes. From evolutionary tracks for the formation of intermediate-mass stars, we find that the total amount of mass which can account for the IRAS luminosity, 3200 $L_\odot$, is $\sim$ 7 $M_\odot$ (see, e. g., Palla & Stahler 1994), and from the 'turbulent core' models for high-mass stars of McKee & Tan (2002), we derive a mass of 5–8 $M_\odot$, given the IRAS luminosity. Thus, from the IRAS fluxes we conclude that the most massive star in this region likely has a mass between 5 and 10 $M_\odot$. If there are two sources of $\sim$ 1600 $L_\odot$, each source would have around 6 $M_\odot$. High-angular resolution observations in the FIR should be carried out in order to disentangle the contribution of IRS 1 and IRS 3 to the IRAS fluxes.

The nature of the cm emission associated with IRS 3 constrains the mass of IRS 3. On one hand, if the cm source is tracing an UCHII region, then IRS 3 must be a B2 star with a bolometric luminosity of $\sim$ 2900 $L_\odot$, very similar to the IRAS bolometric luminosity. On the other hand, if the cm emission comes from an ionized

stellar wind, then IRS 3 is not necessarily of high mass, and IRS 1 could be the massive source of the region.

IRS 1 has been proposed to be one of the most luminous objects in the entire Cygnus OB2 association by Comerón et al. (2002), from a comparison of the high-mass stars of the association in color-magnitude diagrams made from the 2MASS database. In the K, $(H - K)$ diagram, IRS 1 is the reddest object of the association, and dereddening along the extinction vector yields a very bright K magnitude compared with the other massive stars. However, these plot sets an upper limit to the intrinsic brightness because in the K band there may be contribution from circumstellar material. For this reason, Comerón et al. (2002) use the H, $J - H$ diagram, which is not that affected by circumstellar emission, to estimate the brightness of the members of the association, and find again that IRS 1 was among the brightest. Since the color-magnitude diagrams were made by using the Second Incremental Release of the 2MASS Point Source Catalog (PSC), and this release is by now obsolete, we redid the diagrams with magnitudes from the current release of 2MASS PSC, and found the same values except for the J magnitude, yielding $(J - H) = 3.26$ instead of 4.23 given by Comerón et al. (2002). Thus, dereddening along the extinction vector in the H, $(J - H)$ diagram does not set IRS 1 among the brightest members of the association, but IRS 1 is still intrinsically brighter than stars with spectral type B0. Such spectral type corresponds to a luminosity of 25000 $L_\odot$ (Panagia 1973), setting thus a lower limit for the luminosity of IRS 1. This is not consistent with the bolometric luminosity derived from IRAS, and is suggestive of IRS 1 showing variability.

In addition to the inconsistency between the IRAS bolometric luminosity and the brightness of IRS 1 in the infrared, we found from the data shown in this work that IRS 1 seems to be a low-mass source. We discussed in § 5.4.1 the properties of the outflow driven by IRS 1, and found that it had parameters typical of outflows associated with low-mass protostars. From the continuum emission of this work we found a circumstellar mass of $\sim 0.3\ M_\odot$ (§ 5.3.1), and furthermore no cm emission is detected above the 3σ level of 0.2 mJy beam^{-1}. Thus, the mass of IRS 1 is somewhat puzzling. If IRS 1 is a low-mass star, there is some trouble to explain the bright magnitudes derived from 2MASS photometry. If IRS 1 is a high-mass star of spectral type earlier than B0, one would expect detecting cm emission from ionized gas, and detecting the star at optical wavelengths, while IRS 1 does not appear in the POSSII plates. If IRS 1 is a high-mass *protostar*, deeply embedded and still

accreting most of its mass, one would expect observing a massive envelope, with a mass of the order of the accreted mass, surrounding the protostar. Such a massive envelope would be also required to explain the lack of cm emission. But we do not detect a massive envelope toward IRS 1, at least from the mm continuum emission.

At this point we consider whether the continuum emission is really tracing all the dust surrounding IRS 1. Let us consider different possibilities. First, the SMA could be filtering out large-scale emission. We estimated, from the shortest baseline of the observations, the largest angular scale to which the SMA is sensitive, and found this is $\sim 20''$, as seen from the size of the CO low-velocity emission in Fig. 5.5. Thus, the faint continuum emission is not due to filtering the large scale emission by the interferometer. Second, the dust could be optically thick. Assuming the flux density at 1.3 mm arises from optically thick dust, that is, the continuum emission can be described by a pure blackbody, and adopting a deconvolved size for the source of $\sim 3''$ (derived from a Gaussian fit), the temperature of the dust should be 2.3 K, smaller than the background temperature, which is not possible. Third, the dust could be sublimated. Since dust sublimates at ~ 1500 K (van der Tak & Menten 2005), if we had a considerable amount of gas (say, around 5 $M_\odot$, to be associated with a massive protostar) at such high temperature we should detect this at optical wavelengths, since the maximum of a blackbody at this temperature is at ~ 3 μm. Fourth, toward some multiple systems CO emission has been detected with no continuum emission, and it has been proposed that a circumbinary disk with a central gap could explain the lack of continuum emission (e.g., Andrews & Williams 2005). However, this has been observed toward low-mass systems of Class II sources, and this should be investigated for the case of IRS 1, which would be a binary system with a high-mass star. Thus, none of these explanations is convincing to explain the observations toward IRS 1. In order to estimate the mass of the envelope surrounding IRS 1 independently from dust emission, observations of different dense gas tracers such as CS, NH_3, N_2H^+, HCO^+ with high-angular resolution should be carried out (different dense gas tracers are needed to resolve effects of chemical evolution and chemical differentiation).

There is still another piece in the puzzle that is worth noting. The image of the H_2 line at 2.12 μm (1–0 S(1)) reveals strong emission very close to IRS 1 (Kumar et al. 2002), being elongated in the east-west direction, and thus coincident with the direction of the outflow detected in this work. This would suggest that the H_2 emission at 2.12 μm close to IRS 1 arises from shocks in the outflow. However,

Comerón et al. (2002) detected line emission at 2.225 μm, which could be due to the 1–0 S(0) line of H$_2$. This H$_2$ line at 2.225 μm is found associated with outflows (Everett et al. 1995; Davis & Smith 1999; Caratti o Garatti et al. 2006) and with photon-dissociated regions (Ramsay et al. 1993; Luhman et al. 1998), but usually the H$_2$ line at 2.225 μm is much fainter than the H$_2$ line at 2.12 μm, while this is clearly not the case for IRS 1 (see Fig. 7 of Comerón et al. 2002). Therefore, this is suggestive of H$_2$ being excited by fluorescence rather than in shocks. Ratios of different intensities of H$_2$ lines are used to discriminate between these two mechanisms, and this should be further investigated.

In an attempt to interpret all these observational features, we considered that IRS 1 could be a protostar showing variability, similar to FU Ori objects. These objects are eruptive low-mass pre-main-sequence stars that have disks with high mass accretion rates (10^{-5}–10^{-4} $M_\odot$ yr^{-1}), and powerful stellar winds (see, e. g., Hartmann et al. 1985; Hartmann & Kenyon 1996). Thus, the low amount of continuum emission would be naturally explained because the central star would not be of high mass, while the CO outflow we have observed, with a mass loss rate of 2×10^{-5} $M_\odot$ yr^{-1}, is consistent with the typical mass accretion rates for these objects, which are about 1 order of magnitude higher than the mass loss rate (Hartmann & Kenyon 1996), and hence the mass accretion rate for IRS 1 would be $\sim 10^{-4}$ $M_\odot$ yr^{-1}. FU Ori objects are usually discovered by an increase in optical of 3–6 magnitudes over timescales of months. If the IRAS and the POSSII observations were made before the increase in flux, which was detected by 2MASS, this would explain why the 2MASS magnitudes suggest IRS 1 is an O star while the IRAS bolometric flux is only of 3200 $L_\odot$. The outburst would have occurred between years 1983 (IRAS) and 2001 (2MASS). In addition, FU Ori objects have spectral types similar to F-G supergiants in the optical, show reflection nebulae, large UV and IR excesses of radiation, wavelength dependent spectral types, and 'double-peaked' absorption line profiles at optical and infrared wavelengths (e. g., Kenyon et al. 1993). Reflection nebulae and infrared excess are seen in IRS 1. However, FU Ori objects have been modeled through viscous accretion disks, and the models predict that FU Ori should display strong 2.3 μm CO absorption features which do not seem to be present in the low-resolution spectrum of IRS 1 (Comerón et al. 2002). This lack of the CO absorption features does not rule out the possibility of IRS 1 being a FU Ori object, since these features were *not* identified in one case (V346 Nor: Graham & Frogel 1985), and were weak in another case (Z CMa: Hartmann et al. 1989).

Finally, we propose observations which should be carried out toward IRS 1 in order to elucidate its nature. While optical and infrared spectrophotometry and broadband photometry would help to determine its spectral type at these wavelengths, and to compare with that for FU Ori objects, high resolution spectra between 2.290 and 2.315 μm would be very useful to search for signs of the first-overtone CO absorption bands. In addition, further high spectral resolution observations of the Balmer lines would serve to look for P Cygni optical profiles, which have been found toward all FU Ori objects (Hartmann & Kenyon 1996). Finally, the high resolution spectra would also reveal if IRS 1 has double-peaked line profiles. These are possible tests to assess the validity of the classification of IRS 1 as a FU Ori object.

5.4.4 Evolutionary stage of the different sources in the region

Selection of 2MASS sources associated with the region: We extracted a sample of stars in a field of $2'$ of diameter centered on IRS 3 from the 2MASS All-Sky Catalog of Point Sources (Cutri et al. 2003) with the aim of finding the possible 2MASS sources associated with the cloud of gas and dust studied in this work, and plotted a $(J - H)$, $(H - K)$ diagram (Figure 5.10). In the diagram, there is a group of sources with small colors, being IRS 3 among them, which are unreddened stars. There is another group of sources with high infrared excess, $(H - K) > 2$, and thus these could be 2MASS sources embedded in the cloud. Among these sources with infrared excess, it is remarkable the large $H - K$ color of IRS 1N, IRS 1 and IRS 4. The other two sources with $(H - K) > 2$ do not fall close to the dust and gas emission detected in this work, and will not be taken into account.

IRS 1: Given that IRS 1 shows a high $H - K$ color (see Fig. 5.10), has dust emission associated and is the driving source of a molecular outflow, IRS 1 must be still accreting material onto the central protostar.

IRS 1N: This 2MASS source also has, as IRS 1, a bright K magnitude, and a very high $H - K$ color. When these values are plotted in a K, $H - K$ diagram and are dereddened along the extinction vector, IRS 1N is placed among the most luminous sources in the Cygnus OB2 association. However, unlike IRS 1, this does not happen
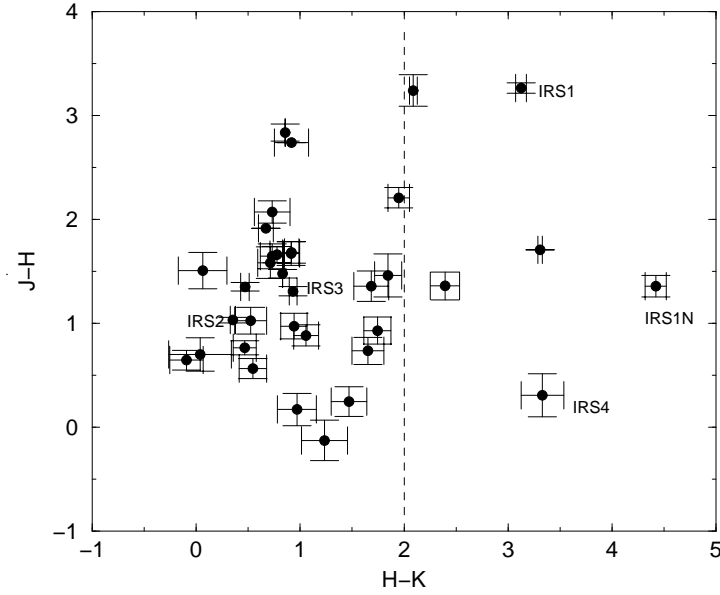
Figure 5.10: $(J-H)$, $(H-K)$ diagram of 2MASS sources in a field of $2'$ of diameter centered on IRS 3 in the IRAS 20343+4129 region. Note that IRS 3 has no infrared excess, while IRS 1 and IRS 1N are among the most embedded sources.

when one plots IRS 1N in the magnitude-color diagram H, $J-H$, which is supposed to be less affected of circumstellar emission than the K, $H-K$ diagram. In the H, $J-H$ diagram, IRS 1N is well below the B0 stars, and thus our observations, which reveal that this source has CO and possibly faint dust associated, are in agreement with IRS 1N being a low-mass YSO.

IRS 3: Since IRS 3 is visible at optical wavelenghts, it does not show infrared excess, and has no CO(2–1) and dust emission associated, it seems that this object is a YSO in the final stages of accretion, or is already a main sequence star, and thus in a more advanced evolutionary stage than IRS 1 and IRS 1N. If the cm emission associated arises from an UCHII region, IRS 3 is a B2 star of 5–10 $M_{\odot}$ (see § 5.4.3).

IRS 4: IRS 4 shows a high $H-K$ color and thus could belong to the same cloud forming IRS 1 and IRS 3. However, given that we find no CO nor dust associated, IRS 4 could be a background object as well.

Dust condensations: Regarding the dust condensations detected in this work (see Fig. 5.2), these are located ahead of the walls of CO and H_2. We interpreted these walls as tracing an expanding shell driven by IRS 3 (§ 5.4.2). These dust condensations have no infrared emission associated and lie, specially those to the west, in a region where there is no infrared emission at all. In addition, we do not find any sign of star formation such as outflow emission, and thus we classify them as starless cores. We especulate that these starless cores are the result of the expanding cavity driven by IRS 3, which has compressed the material around it.

5.4.5 An overall view of the region

In IRAS 20343+4129 we find objects with very different properties and evolutionary stages which have been born in the same parental cloud. In addition, we find that star formation is localized, that is, to the north of IRS 3 there are YSOs which are already bright in the infrared, while to the east and to the west there are mm sources that seem to be starless cores. This suggests that either the initial conditions of the cloud were very different, or that there is a triggering agent, like the cavity produced by IRS 3, which is determining the distribution of the stars in the cloud. Note that since IRS 1 and IRS 1N are farther away than the starless cores but are likely more evolved objects, these infrared sources may not have been triggered by IRS 3, and likely reflect an initial condition of high-density of the cloud at the position of IRS 1.

H_2 emission shows a cometary arch about $1'$ to the southwest of IRS 3, which is also detected in cm emission (Kumar et al. 2002; Carral et al. 1999; see Fig. 5.1). There are at least two scenarios to explain this arched feature. First, the arched morphology is produced by the stellar wind or the radiation from IRS 3. However, in this scenario IRS 3 should have undergone two events, the first associated with this arched morphology and the second associated with the cavity studied in § 5.4.2, and we expect that the first would have cleared up most of the surrounding material. In this scenario, it is not easy to explain the detected amounts of dust and gas. Second, the cometary arch could be produced by the ionization front from a nearby OB star. In fact, the arch is facing the center of the Cygnus OB2 association. The cometary arch in this case would be similar to the bright-rimmed clouds facing HII regions, such as IC1396N (Sugitani et al. 1991; Beltrán et al. 2002). Evidences of sequential star formation have been found in these bright-rimmed clouds, suggesting that star formation in these clouds has been triggered by the ioinzing stars (Sugitani 1989,

1995). This scenario suggests that IRS 3 has been triggered by an OB star from Cygnus OB2, but a detailed study of all the YSOs in the cloud with distance to the cometary arch should be carried out to test this hypothesis.

5.5 Conclusions

We have observed the dust continuum emission at 1.3 mm with the SMA as well as the CO(2–1) emission toward the high-mass protostellar candidate IRAS 20343+4129, in order to study the properties of the different protostars in the region. Two bright infrared sources, IRS 1 in the north and IRS 3 in the south, lie inside the SMA primary beam, and IRS 3 is associated with cm emission. Our main conclusions can be summarized as follows:

1. The dust continuum emission reveals three main condensations, to the north (associated with IRS 1), to the east, and to the west of IRS 3, being the western condensation the strongest one and consisting of different slightly extended subcondensations. Toward the eastern condensation the SMA has likely filtered out most of the emission. Assuming the opacity law of Beckwith et al. (1990) and a dust emissivity index of 1, the mass of the condensation associated with IRS 1 is 0.2–0.5 $M_\odot$.

2. We have discovered a bipolar high-velocity CO outflow, elongated in the east-west direction, and identify IRS 1 as its driving source. The parameters of the outflow agree with IRS 1 being a low-mass protostar. The low-velocity CO emission is also associated with IRS 1, and shows in addition two elongated faint structures at both sides of IRS 3.

3. The emission from the blueshifted lobe of the large-scale CO outflow seen in single-dish by Beuther et al. (2002c) has been filtered out by the SMA, and the lobe does not have compact emission. A scenario in which the blue large-scale CO lobe traces a cavity blown up by IRS 3 and in which the dust condensations at both sides of IRS 3 are the result of accumulation of mass in the walls of the expanding cavity is consistent with the observations. The expanding cavity could be either driven by a stellar wind from IRS 3, or driven radiatively if we assume IRS 3 is a B2 star.

4. Regarding the mass associated with IRS 1, our continuum and CO(2–1) observations suggest this is a low-mass YSO. However, this is not consistent with the spectral type earlier than B0, i.e. O, derived by Comerón et al. (2002) for IRS 1 from the 2MASS database. This spectral type is not consistent with the bolometric luminosity from IRAS. We suggest that IRS 1 is a variable protostar, similar to FU Ori objects, which had a burst between 1983 and 2001. This naturally explains why we find that IRS 1 has properties of a low-mass source.

5. We find objects with very different properties and evolutionary stages which have been born in the same parental cloud. In addition, these objects are not randomly distributed in the cloud, but their distribution seems to be determined by the initial conditions in the cloud together with triggering by a compression front driven by one of the sources formed inside the cloud.
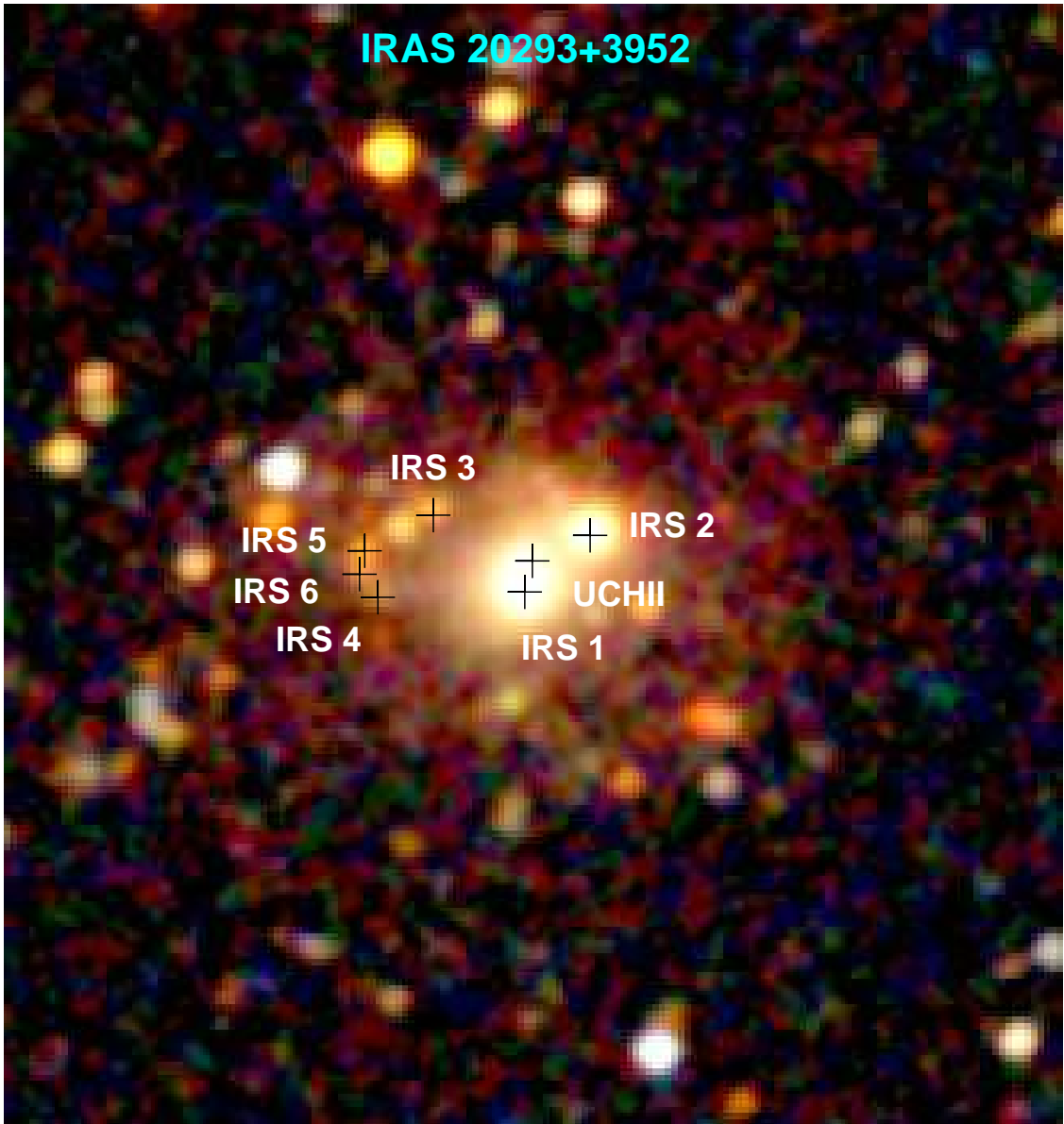
Figure: 2MASS composite image of J, H, and K filters of the IRAS 20293+3952 region. Red objects in the image are embedded objects.

Chapter 6

IRAS 20293+3952: interaction and on-going star formation in a closely-packed environment

6.1 Introduction

In this chapter we report on observations of one intermediate/high-mass star-forming region, IRAS 20293+3952, located at 2.0 kpc of distance (Beuther et al. 2004c) in the southwestern edge of the Cygnus OB2 association, and with a luminosity of 6300 $L_\odot$. This region has been included in a sample of high-mass protostars candidates by Sridharan et al. (2002). The IRAS source is associated with the only centimeter source detected in the region, which is likely tracing an UCHII region (Beuther et al. 2002d). A study of H_2 emission in the region shows two near-infrared stars (IRS 1 and IRS 2) associated with the IRAS source, and a circular ring of H_2 emission surrounding IRS 1 (Kumar et al. 2002). Beuther et al. (2002b) observed the region with the IRAM-30m telescope and find some substructure at 1.2 mm around the UCHII region. The strongest millimeter peak, very close to the position of a H_2O maser, is located $\sim 15''$ north-east of the IRAS source, and observations with high-angular resolution by Beuther et al. (2004b) reveal a compact and strong millimeter source, mm1, associated with the H_2O maser. Two other fainter compact millimeter sources, mm2 and mm3, are located $10''$ to the east of the UCHII region. Beuther et al. (2004b), from observations of CO(2–1) and SiO(2–1), suggest the

presence of four molecular outflows in the region, with two of them, outflow A and outflow B, associated with two chains of H_2 knots (Kumar et al. 2002). Subsequent observations with the PdBI were carried out at 2.6 and 1.3 mm by Beuther et al. (2004c), who find CN emission close to mm1, mm2 and mm3. The different mm sources detected, the presence of multiple outflows, and the existence of an UCHII region makes this region a good choice to study star formation and interaction in a closely-packed environment.

We carried out BIMA and VLA observations of the continuum at 3 mm and the dense gas traced by N_2H^+(1–0), NH_3(1,1), and NH_3(2,2) toward IRAS 20293+3952, together with observations of several CH_3OH(2–1) transitions. The continuum and the dense gas tracers allow us to determine properties for the different sources in the field, while the CH_3OH emission is useful for studying the interaction between them. These new data allow us to gain insight into the formation of stars that are not isolated but in the cluster environment found very close to an intermediate/high-mass star.

6.2   Observations

6.2.1   BIMA

The N_2H^+(1–0) and CH_3OH(2–1) lines and continuum at 95 GHz were observed towards the IRAS 20293+3952 region with the BIMA array[1] at Hat Creek. The observations were carried out in 2003 September 28 with the C configuration, and in 2004 March 24, with the B configuration, with 10 antennas in use. The phase center of the observations was chosen to be $\alpha(J2000) = 20^{\mathrm{h}}31^{\mathrm{m}}12\overset{s}{.}70$; $\delta(J2000) = +40°03'13''\!\!.4$ (position of the millimeter peak detected with the IRAM 30 m telescope by Beuther et al. 2002b). The full range of projected baselines, including both configurations, was 9.4–240 m. The FWHM of the primary beam at the frequency of observations was $\sim 120''$. Typical system temperatures were ~ 500 K for Sep 28 and 500–1500 K for Mar 24.

The digital correlator was configured to observe simultaneously the continuum

---

[1]The BIMA array was operated by the Berkeley-Illinois-Maryland Association with support from the National Science Foundation.

Table 6.1: Parameters of the BIMA and VLA observations

Observation	Telescope	Config.	Robust Weight[a]	Beam (arcsec)	P.A. (°)	Spec. resol. (km s^{-1})	Rms[b] (mJy beam^{-1})
Continuum	BIMA	B+C	+0.3	4.5×4.2	58.9	–	0.8
CH$_3$OH(2–1)	BIMA	B+C	+5	6.1×5.7	−6.2	0.31	80
N$_2$H$^+$(1–0)	BIMA	B+C	+5	6.2×5.9	−4.1	0.31	70
NH$_3$(1,1)	VLA	D	+5	6.9×3.0	71.5	0.62	3
NH$_3$(2,2)	VLA	D	+5	6.6×3.1	71.4	0.62	3

[a] Robust= +5 is equivalent to natural weight, and robust= −5 is equivalent to uniform weight

[b] Rms noise per channel in the case of line emission

emission and the N$_2$H$^+$(1–0) group of hyperfine transitions (93.17631 GHz, in the lower sideband), and the CH$_3$OH(2–1) 2_1–1_1 E, 2_0–1_0 E, 2_0–1_0 A$^+$, and 2_{-1}–1_{-1} E transitions (96.74142 GHz, in the upper sideband). For the continuum, we used a bandwith of 600 MHz in each sideband, and for the lines we used a bandwidth of 25 MHz with 256 channels of 100 KHz width, providing a spectral resolution of 0.31 km s^{-1}.

Phase calibration was performed with 2013+370, with typical rms in the phases of 12° and 43° for C and B configurations, respectively. The absolute position accuracy was estimated to be around 0.″5. We used 2013+370 for flux calibration, and the error in the flux density scale was assumed to be $\sim$ 30%. Data were calibrated and imaged using standard procedures in MIRIAD (Sault et al. 1995). We combined the data from B and C configurations. In order to improve the angular resolution of the continuum emission, we weighted the visibility data with a robust parameter of +0.3. For the line emission, which is more extended than continuum, we used natural weight. The continuum and N$_2$H$^+$ emission were cleaned using a box around the emitting region. The resulting synthesized beams and the final rms noises are listed in Table 6.1.

6.2.2 VLA

Observations of the $(J, K) = (1, 1)$ and $(2, 2)$ inversion transitions of the ammonia molecule were carried out with the Very Large Array (VLA) of the NRAO[2] in the

---

[2]The National Radio Astronomy Observatory is a facility of the National Science Foundation, operated under cooperative agreement by the Associated Universities, Inc.

D configuration on 2000 September 3. The phase center was set to $\alpha(J2000) = 20^{\mathrm{h}}31^{\mathrm{m}}10\overset{s}{.}70$; $\delta(J2000) = +40°03'10''\!.7$ (position of the IRAS source). The FWHM of the primary beam at the frequency of observations was $\sim 110''$, and the range of projected baselines was 37.9–708 m. The absolute flux calibration was performed by using 3C48, adopting a flux density at 1.3 cm of 1.05 Jy. The phase calibrator was 2013+370, with a bootstrapped 1.3 cm flux density of 3.84 Jy, and 3C 84 was used as bandpass calibrator.

The $NH_3(1,1)$ and $NH_3(2,2)$ lines (with 2 polarizations for each line) were observed simultaneously in the 4 IF correlator mode of the VLA, providing 63 channels with a spectral resolution of 0.62 km s^{-1} across a bandwith of 1.56 MHz, plus an additional continuum channel containing the central 75% of the total bandwith. The bandwidth was centered at a systemic velocity v_{LSR} of 6.3 km s^{-1} for the $NH_3(1,1)$ line, and at $v_{\mathrm{LSR}} = 11.3$ km s^{-1} for the $NH_3(2,2)$ line (for $NH_3(2,2)$ the main hyperfine component was shifted by 5 km s^{-1} from the band center to cover the main and one of the satellite hyperfine component). Data were calibrated and imaged using standard procedures of the Astronomical Imaging Processing System (AIPS) of the NRAO. Channel maps were cleaned using a different box for each channel, and using natural weighting of the visibility data. Table 6.1 summarizes the parameters of the observations.

6.3   Results

6.3.1   Continuum emission

Figure 6.1 shows the continuum map at 3.15 mm overlaid on the continuum infrared emission at 2.12 μm from Kumar et al. (2002). The millimeter continuum emission has two strong components, BIMA 1 and BIMA 2, both spatially resolved. While BIMA 1 is elongated in a northeast-southwest direction (roughly P.A.$\simeq 45°$), BIMA 2 is somewhat flattened in the east-west direction, and is surrounded by a very elongated structure of $\sim 30''$ (0.3 pc), which is tracing a dust ridge. There is an extended clump $10''$ to the southeast of the dust ridge, which we label BIMA 3. Note that in this southeastern region there are very few infrared sources. At $10''$ to the east of the ridge, there is another faint feature, BIMA 4, extending for $10''$ in the northwest-southeast direction. Very weak continuum emission is detected
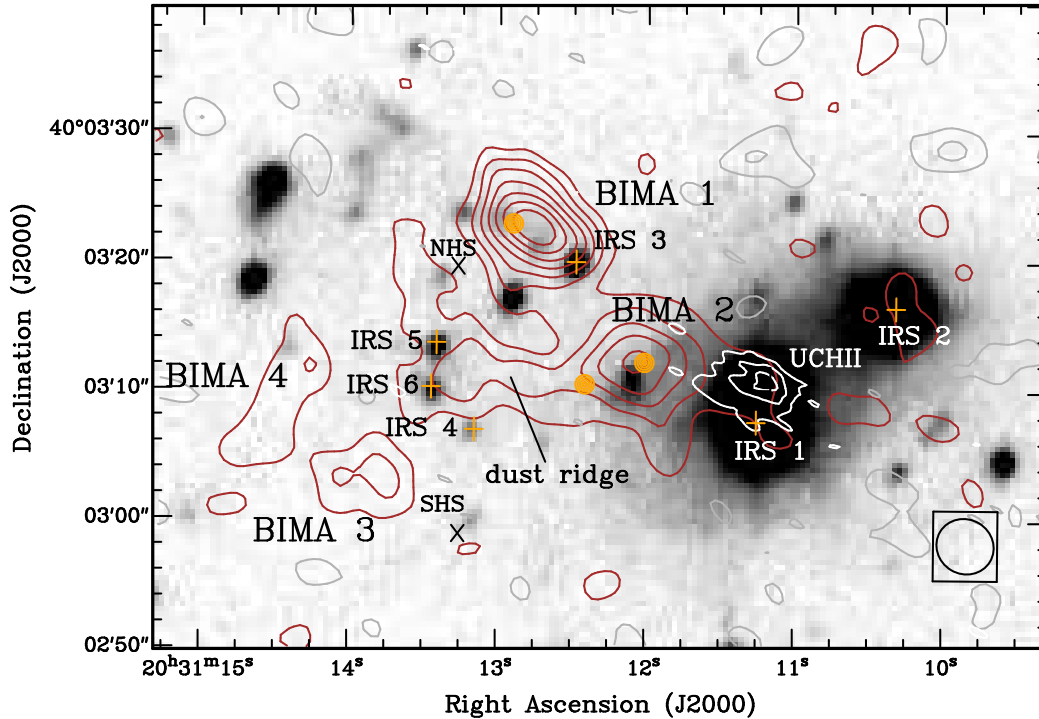
Figure 6.1: Contours: Map at 3.15 mm obtained with BIMA in B and C configurations and using an intermediate weight between uniform and natural, robust= $+0.3$. The contour levels are -4, -2, 2, 4, 6, 8, 10, 12, 14, and 16 times the rms noise of the map, 0.8 mJy beam^{-1}. The synthesized beam, shown in the bottom right corner, is $4''5 \times 4''2$, at P.A. $= 58.9°$. White contours correspond to the centimeter emission at 3.6 cm, and trace the UCHII region (Sridharan et al. 2002, Beuther et al. 2004b). Contours are -3, 3, 6, and 9 times the rms of the map, 70 μJy beam^{-1}. Grey scale: Continuum image at 2.12 μm from Kumar et al. (2002). Main clumps of dust emission appear labeled as BIMA 1 to BIMA 4. Circles indicate the compact millimeter sources detected by Beuther et al. (2004c) at 2.6 mm with the PdBI. These are, from west to east, mm2, mm3, and mm1. Orange crosses mark the sources from 2MASS with infrared excess, and the green tilted crosses mark the position of the Northern Hot Spot (NHS) and the Southern Hot Spot (SHS).

Table 6.2: Parameters of the continuum sources at 95 GHz

	Position		I_ν^{peak}	Flux[a]	Mass[b]	Assumed T_d[c]
	α(J2000)	δ(J2000)	(mJy beam^{-1})	(mJy)	($M_\odot$)	(K)
BIMA 1	20:31:12.755	40:03:22.61	13.0	28	6.4	34
BIMA 2	20:31:12.065	40:03:12.35	8.3	19	4.4	34
BIMA 2+ridge	-	-	-	37	12	25
BIMA 3	20:31:13.759	40:03:03.28	3.9	5.3	2.6	17
BIMA 4	20:31:14.263	40:03:11.78	3.4	6.0	2.9	17

[a] Flux density inside the 5σ contour level for BIMA 1 and BIMA 2, and the 3σ level for BIMA 2+ridge, BIMA 3, and BIMA 4.

[b] Masses of gas and dust derived assuming a dust emissivity index $\beta = 1$ (Beuther et al. 2004c). The uncertainty in the masses due to the opacity law and the dust emissivity index is estimated to be a factor of 4.

[c] T_d is estimated by correcting the rotational temperature derived from NH_3 (see § 6.4.2) to kinetic temperature, following Tafalla et al. 2004.

toward the position of the UCHII region, at a level of 3σ. Beuther et al. (2004c) observed the same region at 2.6 mm with the PdBI at higher angular resolution ($1''5 \times 1''2$), but with a smaller primary beam ($44''$). The authors find a very strong compact source, mm1, toward the position of BIMA 1 and elongated in the same northeast-southwest direction as BIMA 1. Besides this strong component, a weak subcomponent was resolved in the direction of the elongation (to the southwest of mm1), and was labeled mm1a. Beuther et al. (2004c) find two compact millimeter sources associated with BIMA 2, mm2 and mm3 (see Fig. 6.1 to see the positions of these compact millimeter sources).

In Table 6.2 we show the position, peak intensity, flux density and masses associated with BIMA 1 and BIMA 2, the entire dust ridge (including BIMA 2), BIMA 3 and BIMA 4. We discuss these results in section 6.4.1.

6.3.2   CH$_3$OH

Figure 6.2a shows the zero-order moment map of the CH$_3$OH emission, integrated from -1.5 to 21 km s^{-1}, including the two strongest transitions 2_0–1_0 A$^+$, and 2_{-1}–1_{-1} E. Figure 6.3 shows the CH$_3$OH spectrum at selected positions. The channel maps corresponding to the lines 2_0–1_0 A$^+$ and 2_{-1}–1_{-1} E are shown in Figure 6.4.
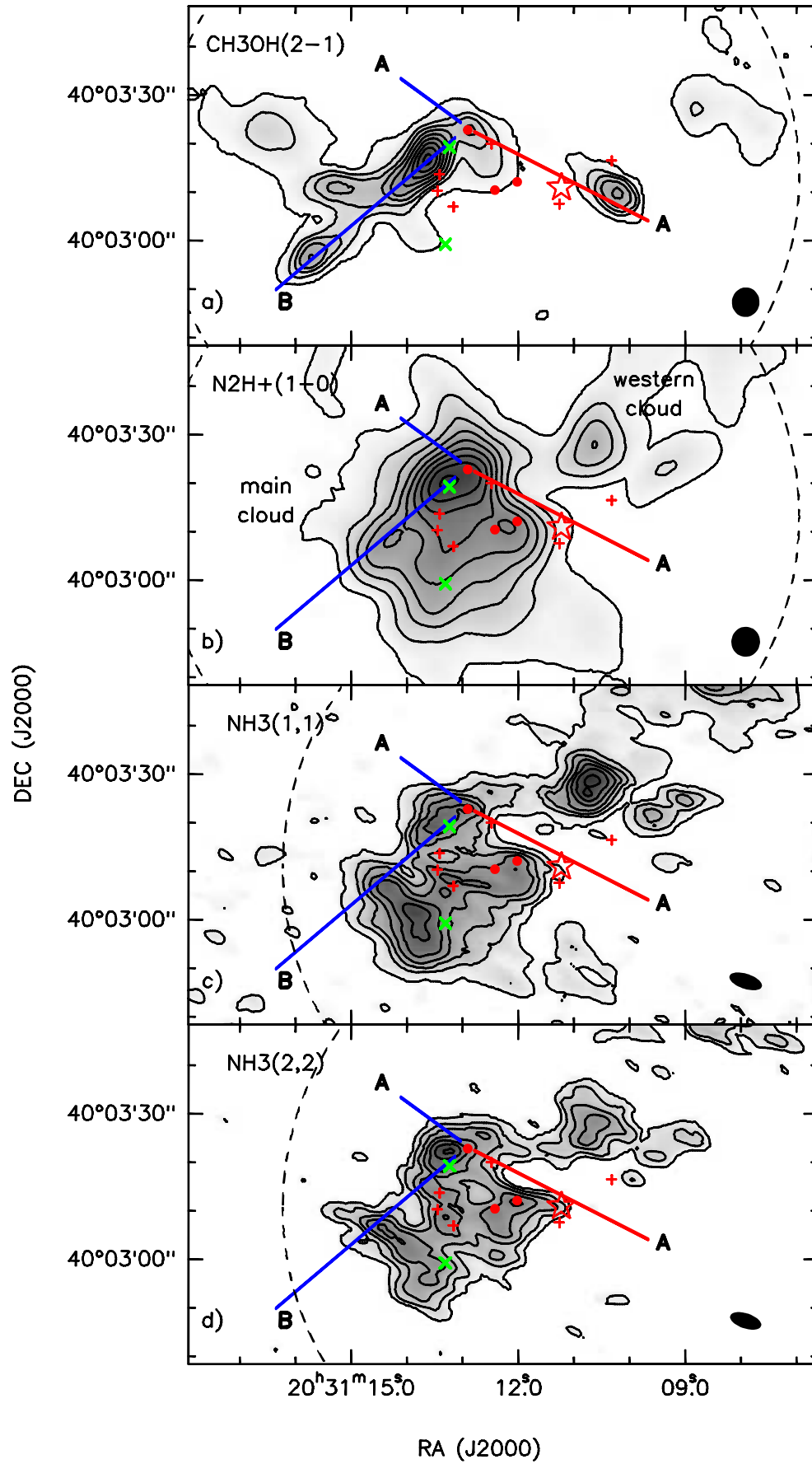
Figure 6.2: (see behind)

Figure 6.2: *a)* Zero-order moment for the CH_3OH 2_0–1_0 A^+, and 2_{-1}–1_{-1} E lines. Contours start at 1%, increasing in steps of 12% of the peak intensity, 10.7 Jy beam^{-1} km s^{-1}. *b)* Zero-order moment for the hyperfine F_1 =0–1 line of N_2H^+. Contours start at 2%, increasing in steps of 12% of the peak intensity, 21.9 Jy beam^{-1} km s^{-1}. *c)* Contours: zero-order moment for the $NH_3(1,1)$ line. Contours start at 5%, increasing in steps of 15% of the peak intensity, 0.240 Jy beam^{-1} km s^{-1}. *d)* Zero-order moment for the $NH_3(2,2)$ line. Contours start at 7%, increasing in steps of 15% of the peak intensity, 0.0892 Jy beam^{-1} km s^{-1}. In all panels, the first level is about the 3 times the rms noise of the map. Symbols are the same as in Fig. 6.1. The synthesized beams for each transition are shown in the bottom right corner, and are listed in Table 6.1. The dashed curve indicates the primary beam of BIMA (panels a and b) and VLA (panels c and d) observations.
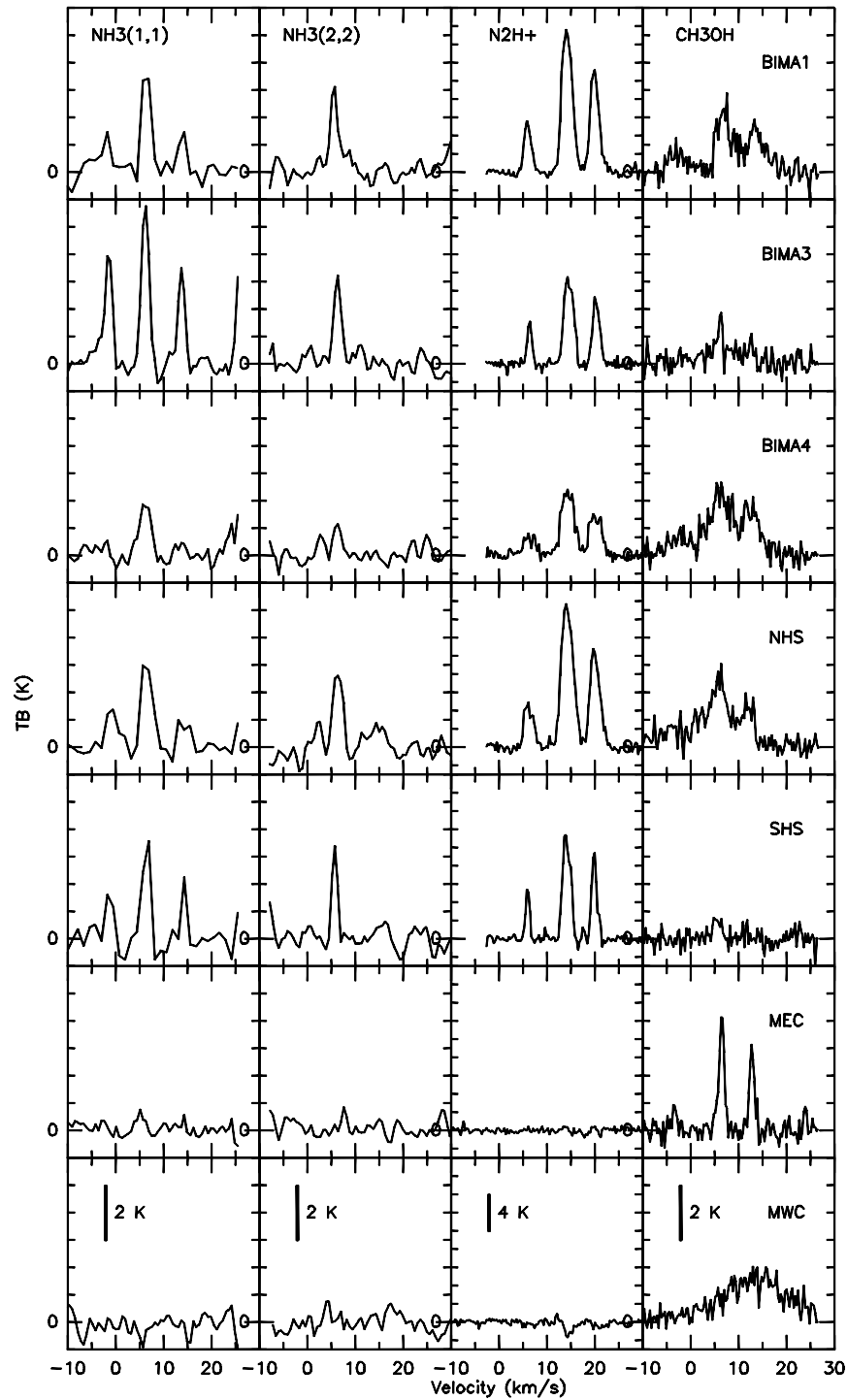
Figure 6.3: Spectra toward seven positions of the I20293 region for the four transitions studied in this work, from left to right, $NH_3(1,1)$, $NH_3(2,2)$, $N_2H^+(1-0)$, and $CH_3OH(2-1)$. The seven positions are labeled on the right panel of each row, and are, from top to bottom, BIMA 1, BIMA 3, BIMA 4, NHS (Northern Hot Spot), SHS (Southern Hot Spot), MEC (methanol eastern clump), and MWC (methanol western clump). The vertical scale is indicated for each transition in the bottom row. For CH_3OH we show, in order of increasing velocity, the 2_0-1_0 E, 2_0-1_0 A^+, and $2_{-1}-1_{-1}$ E lines (velocities are referred to the 2_0-1_0 A^+ line). For N_2H^+, velocities are referred to the $F_1 = 0-1$ hyperfine.

The strongest emission of CH_3OH is found to the southeast of BIMA 1, elongated in the southeast-northwest direction, and covering a spatial extension of $\sim 55''$ (0.6 pc). The emission has a fork-like structure (this is well observed in the 7.7 km s^{-1} velocity channel of Fig. 6.4), and extends several channels. This structure is associated with high-velocity SiO(2–1) and CO(2–1) emission of outflow B (Beuther et al. 2004b). We label this structure as 'ridge B'. The position-velocity (p-v) plot along this ridge is shown in Figure 6.5a. The most prominent feature in the plot is a blue wing, ~ 6 km s^{-1} wide, spanning from $0''$ to $15''$ offset positions. Interestingly, at negative offsets the CH_3OH emission is dominated by a weak red wing (this is better seen for the 2_{-1}–1_{-1} E line). Farther away than $\sim 25''$ (which corresponds to the southeasternmost clump of ridge B), the emission has contributions from both redshifted and blueshifted CH_3OH. This change of behaviour starts at the position of BIMA 4, at an offset position of $20''$.

A clump to the east of ridge B that can be seen in the integrated intensity map shows narrow lines and appears only at systemic velocities (see Figs. 6.3 and 6.4). We label this clump, which has not been previously detected, 'methanol eastern clump'.

In addition, there are two redshifted clumps, one associated wiht BIMA 1, and the other close to the UCHII region (see, e. g., velocity channels from 13 to 16 km s^{-1}), which probably are part of the redshifted CO(2–1) lobe of outflow A (Beuther et al. 2004b). We label these two clumps 'ridge A', and the clump close to the UCHII region 'methanol western clump'. In Figure 6.6, showing the p-v plot along ridge A, we find that there is a velocity gradient, from 4 km s^{-1} at a position of $7''$, to 8 km s^{-1} at $-10''$, clearly seen in the two lines. This velocity gradient is centered around the zero offset position (corresponding to mm1). The methanol western clump, seen at $\sim -35''$, is highly redshifted (line 2_0–1_0 A$^+$ is at ~ 9 km s^{-1}) and shows broad red wings, spreading ~ 5 km s^{-1}.

6.3.3 N_2H^+

The zero-order moment map integrated for all the hyperfine transitions is presented in Figure 6.2b. Fig. 6.3 shows the N_2H^+ spectra at selected positions.

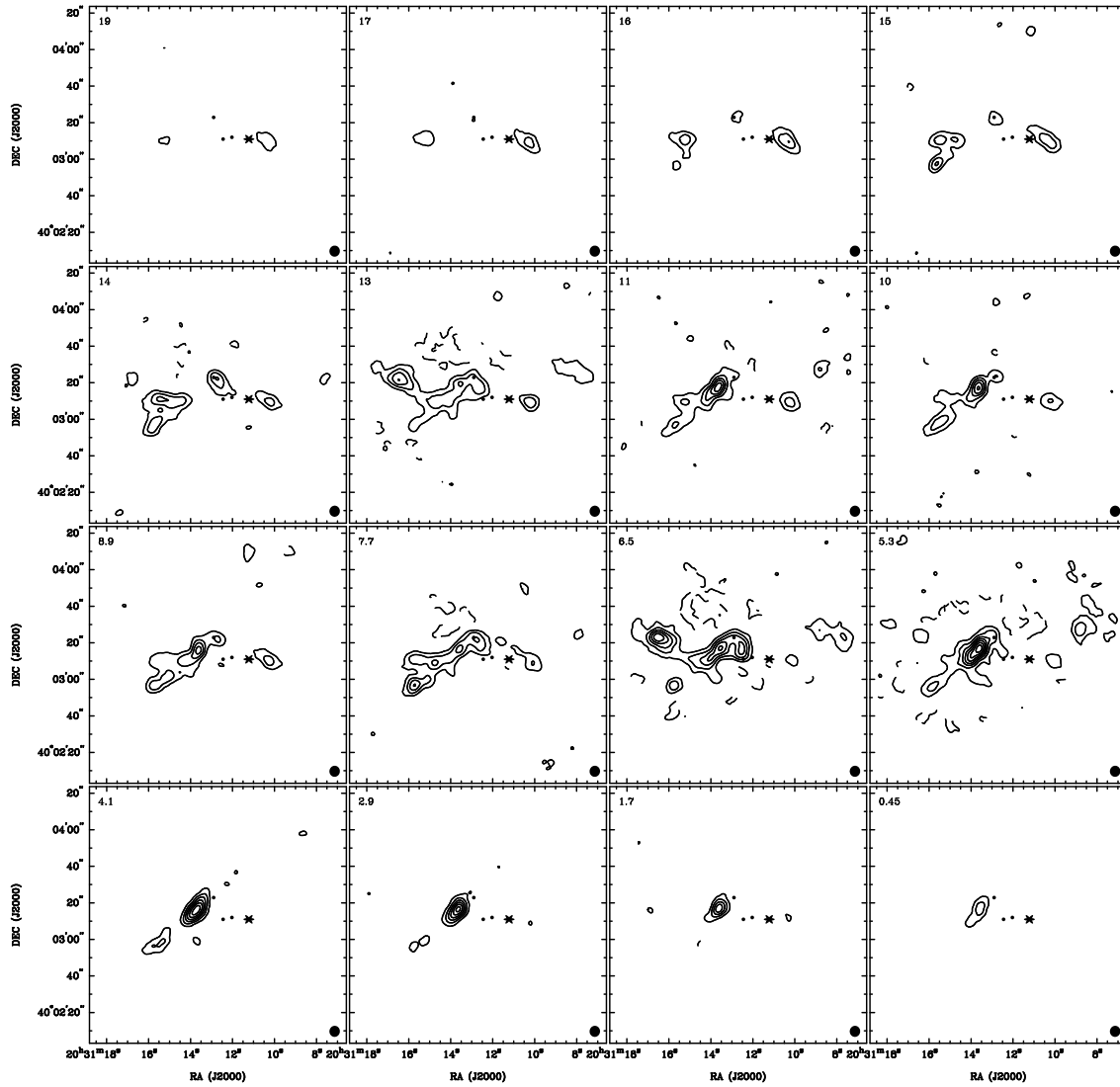The integrated N_2H^+ emission consists of a main cloud and a smaller and weaker

Figure 6.4: Channel maps for 2_0–1_0 A^+ (around 6.3 km s^{-1}, the systemic velocity), and 2_{-1}–1_{-1} E (around 13 km s^{-1}) lines of CH$_3$OH, averaging every 4 channels. Contours are -16, -12, -8, -4, 4, 8, 12, 16, 20, 24, 28, and 32 times the rms of the map, 0.04 Jy beam^{-1}. Symbols are the same as Fig. 6.7. The synthesized beam is shown in the bottom right corner (see Table 6.1).
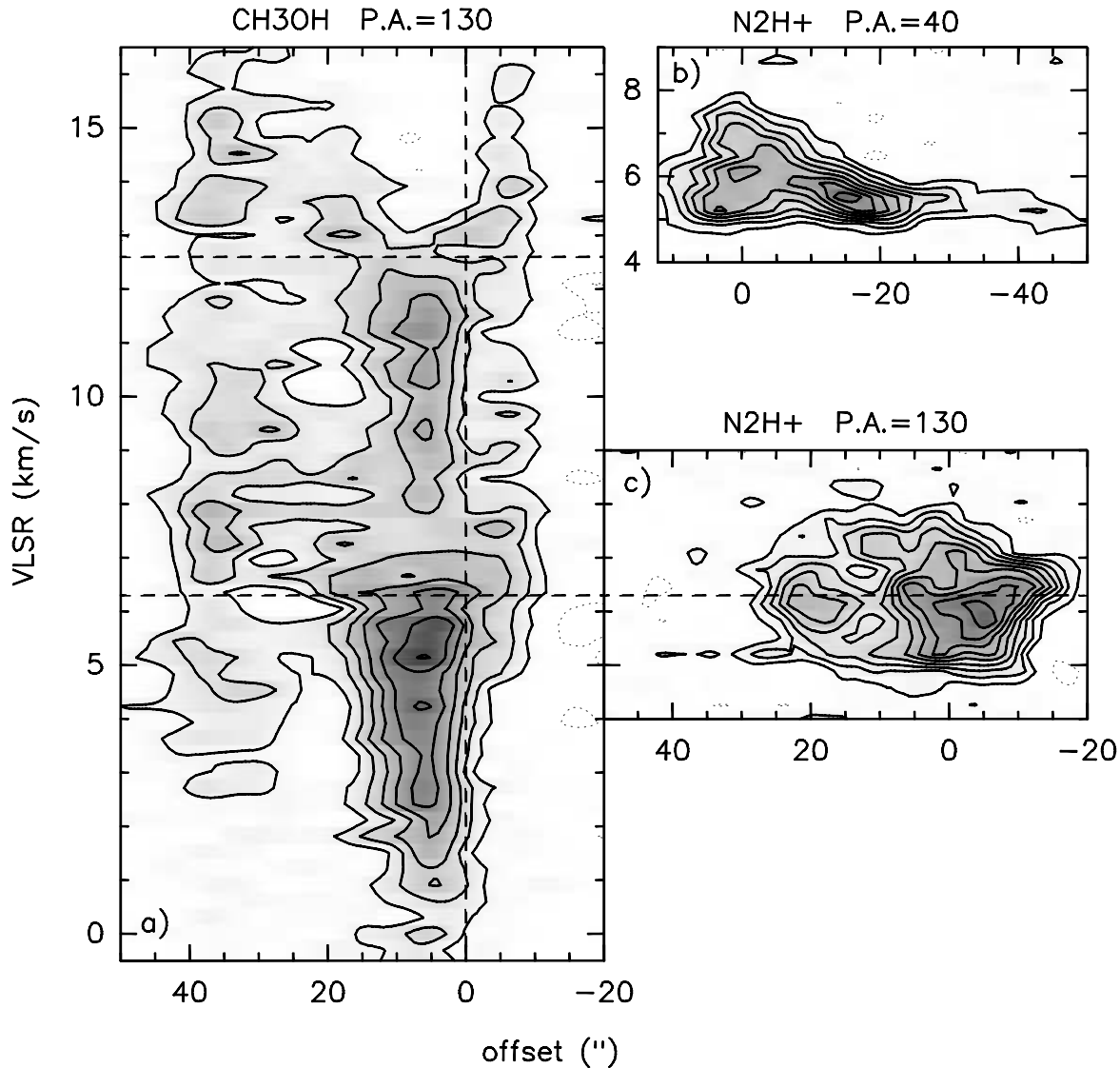
Figure 6.5: *a)* Position-velocity (p-v) plot of CH_3OH along ridge B (cut of P.A.= $130°$). Channel maps have been convolved with a beam of $5'' \times 2''$, with P.A. perpendicular to the direction of the cut. Contours start at 0.17 Jy beam^{-1}, and increase in steps of 0.17 Jy beam^{-1}. *b)* p-v plot of N_2H^+ emission accross ridge B and the main cloud (cut of P.A.= $40°$). Positive positions are toward the northeast. Contours start at 0.2 Jy beam^{-1}, increasing in steps of 0.2 Jy beam^{-1}. *c)* p-v plot of N_2H^+ emission along ridge B (cut of P.A.= $130°$). The velocity scale is placed matching the velocity scale of the CH_3OH emission. Contours start at 0.15 Jy beam^{-1}, increasing in steps of 0.15 Jy beam^{-1}. For N_2H^+, we did not convolve the channel maps. In all panels, the central position corresponds to the Northern Hot Spot (see Table 6.4), and is marked by a vertical dashed line in panel a). The bottom dashed line indicates the systemic velocity for line 2_0–1_0 A^+ (taken as the reference line), at 6.3 km s^{-1}. The top dashed line indicates the systemic velocity for line 2_{-1}–1_{-1} E, at 12.6 km s^{-1}.
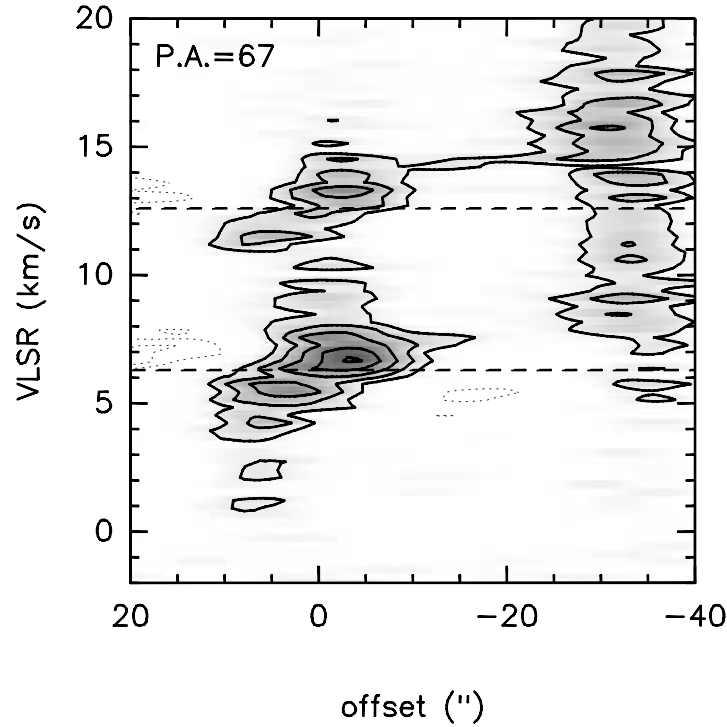
Figure 6.6: p-v plot along ridge A, with a P.A.= $67°$. Contours are -0.35, -0.25, -0.15, 0.15, 0.25, 0.35, 0.45, and 0.52 Jy beam^{-1}. The velocity resolution is 0.30 km s^{-1}, and the channel maps have been convolved with a beam of $10'' \times 5''$, with P.A. perpendicular to the direction of each cut, in order to recover the maximum emission in each position. The velocity range includes two lines: 2_0–1_0 A$^+$ (at 6.3 km s^{-1}) and 2_{-1}–1_{-1} E (at 12.6 km s^{-1}). The zero position corresponds to mm1, and positive values go to the northeast.

cloud to the west of the main cloud (western cloud). The size of the main cloud and the western cloud are $\sim 50''$ (0.5 pc), and $\sim 15''$ (0.15 pc), respectively. The four BIMA sources are located in the main cloud with BIMA 1 close to the N$_2$H$^+$ emission peak. Marginal N$_2$H$^+$ emission is detected towards the UCHII region.

The hyperfine F_1 =0–1 was used for the analysis of the kinematics of the N$_2$H$^+$ emission because it is not blended with the other hyperfines. In Figures 6.7 and 6.8 we show the channel maps and the first and second-order moments for this hyperfine. The channel with maximum intensity for the hyperfine F_1 =0–1 was found at the systemic velocity, 6.3 km s^{-1} (Sridharan et al. 2002).

The first-order moment map shows a small velocity gradient in the main cloud with increasing velocities roughly from the southwest to the northeast. In addition,
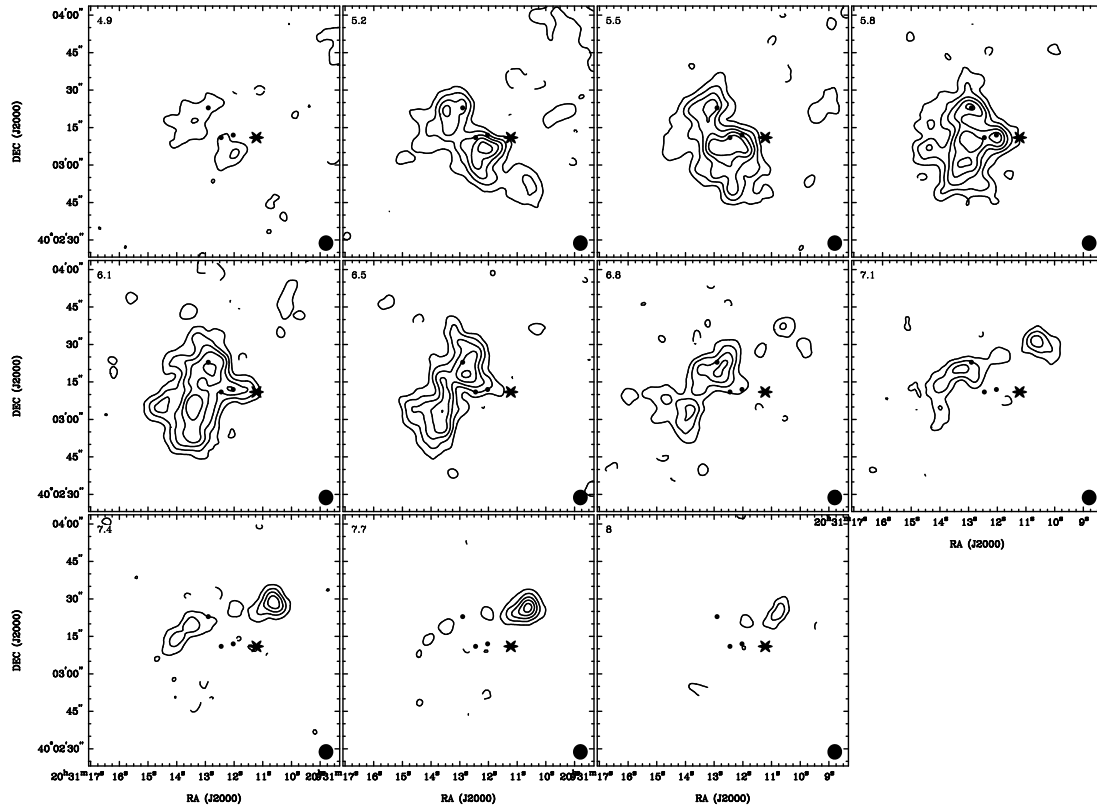
Figure 6.7: Channel maps for the hyperfine $F_1 = 0$–1 line of N_2H^+. Contour levels are -4, 4, 8, 12, 16, and 20 times the rms noise of the maps 0.07 Jy beam^{-1}. Filled circles are the compact millimeter sources detected by Beuther et al. (2004c), and the star marks the position of the UCHII region. The synthesized beam is shown in the bottom right corner (see Table 6.1).

there is a sligthly redshifted filament spatially coincident with ridge B (see also Fig. 6.7), which has very broad lines associated, as seen in the second-order moment map (Fig. 6.8b). The p-v plot calculated accross ridge B and within the main cloud (Figure 6.5b) shows the aforementioned velocity gradient in the main cloud and the line broadening toward ridge B (at offset position zero). The p-v plot along ridge B (Figure 6.5c) shows clearly line broadening all along the ridge, but without the wing emission component found in the CH_3OH emission.

The western cloud appears redshifted, at ≥ 7 km s^{-1}, and has narrow lines (Fig. 6.7). At these velocities, there is weak emission connecting the western cloud with ridge B. Figure 6.9 shows the p-v plot along a cut at P.A.= 110°, picking up partially the ridge and the western cloud. From this plot, it seems that the western
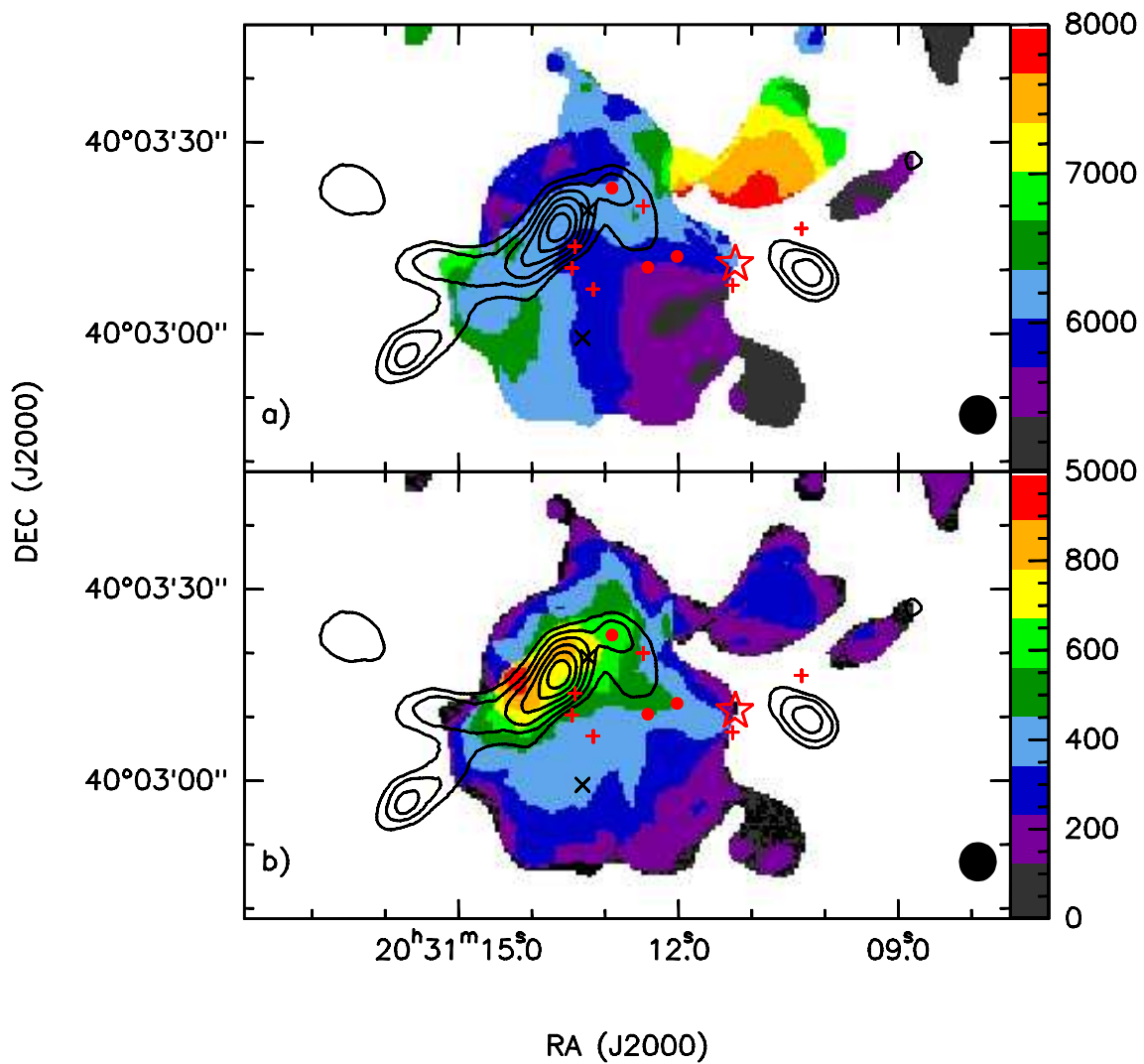
Figure 6.8: *a)* Color scale: first-order moment map for the hyperfine $F_1 = 0-1$ line of N_2H^+. *b)* Color scale: second-order moment map for the hyperfine $F_1 = 0-1$ line of N_2H^+. In both figures, black contours are the same as Fig. 6.2a, showing the $CH_3OH(2-1)$ emission, with contours starting at 13%, and increasing in steps of 15% of the peak intensity. Color scales are in ms^{-1}. The synthesized beam is shown in the bottom right corner, and symbols are the same as Fig. 6.2. Note that the second-order moment gives the velocity dispersion, and must be multiplied by the factor $2\sqrt{2\ln 2} \simeq 2.35$ to have line widths.
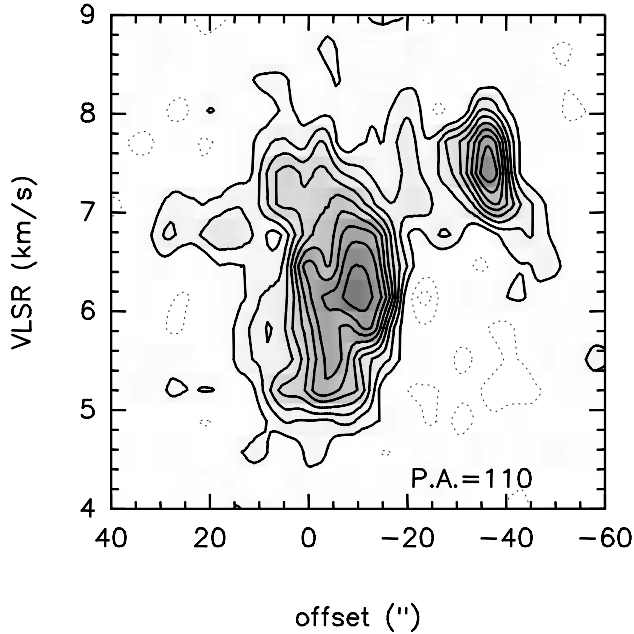
Figure 6.9: Position-velocity (p-v) plot of N_2H^+ at P.A.$= 110°$, that is, along the western cloud and the northern side of the main cloud. Central position is $\alpha(J2000) = 20^h31^m13^s63$; $\delta(J2000) = +40°03'16''7$ (methanol peak). Positive positions are toward southeast. Contours start at 0.15 Jy beam^{-1}, increasing in steps of 0.15 Jy beam^{-1}.

cloud extends $\sim 1'$ (0.6 pc) toward the east, intersecting the main cloud.

6.3.4 NH_3

The zero-order moment map of the $NH_3(1,1)$ emission (integrated including the main line and the inner satellites) is shown in Figure 6.2c. The overall structure of $NH_3(1,1)$ resembles roughly the emission of the dust and the emission of N_2H^+. $NH_3(1,1)$ emission is also associated with the main cloud and the western cloud. There is another $NH_3(1,1)$ clump to the northwest (not shown in Fig. 6.2), which is very weak in N_2H^+ (in part due to the primary beam attenuation). A difference between N_2H^+ and $NH_3(1,1)$ emission is that whereas N_2H^+ peaks close to the mm continuum sources, the strongest $NH_3(1,1)$ emission in the main cloud lies in the southeastern part. In addition, the strongest $NH_3(1,1)$ emission over the entire region comes from the western cloud, not from the main cloud. $NH_3(1,1)$ emission toward the UCHII region is weak.

Figure 6.2d shows the zero-order moment map of the $NH_3(2,2)$ emission. $NH_3(2,2)$ emission resembles closely that of the $NH_3(1,1)$. However, the main difference with $NH_3(1,1)$ is that the strongest emission of the $NH_3(2,2)$ in the entire region is found very close to BIMA 1. The $NH_3(2,2)$ emission in the western edge of the main cloud matches very well with the position of the UCHII region.

Note that the dense gas traced by NH_3 and N_2H^+ is morphologically very different from the gas traced by CH_3OH.

6.4 Analysis

6.4.1 Dust

We compared the positions of BIMA 1 with the mm source found by Beuther et al. (2004b) at 3.5 mm at similar angular resolution. The peak of BIMA 1 is shifted $\sim 1''$ to the west of mm1. The values of the peak intensities (Table 6.2) are in very good agreement with Beuther et al. (2004b), and the flux densities from Table 6.2 are about 50% larger than those reported in Beuther et al. (2004b). The offset in positions and the larger flux densities detected in this work could be produced by the different spatial filtering of the BIMA and PdBI arrays, being the BIMA array more sensitive to large scale structures.

The continuum emission at 3.15 mm is probably due to thermal dust emission for most positions of the region, since free-free emission from ionized gas, traced by the continuum emission at 3.6 cm (Fig. 6.1), is detected only at the western edge of the main cloud. However, Beuther et al. (2004c) find a spectral index between 1.3 and 2.6 mm toward mm1a (the subcomponent to the west of mm1) of 0.8, and suggest that the collimated ionized wind from outflow A could account for such a spectral index. The contribution of the possible free-free emission from mm1a to BIMA 1 is small, given that the intensity of mm1 is five times larger than the intensity of mm1a, and thus essentially all continuum emission at 3 mm is due to thermal dust emission.

To derive masses from the flux densities at 3.15 mm, we corrected the rotational temperature, between 15 and 25 K (calculated from $NH_3(1,1)$ and $NH_3(2,2)$, see

section 6.4.2), to kinetic temperature by following Tafalla et al. (2004), yielding kinetic temperatures in the range 17–34 K. The masses (Table 6.2) are 2 times larger than those obtained by Beuther et al. (2004b) from observations at 3.5 mm. The difference arises because BIMA is detecting more flux than PdBI observations, and to the different dust temperatures assumed. While Beuther et al. (2004b) assumed a dust temperature (derived from a graybody fit to the spectral energy distribution in the entire region) of 56 K, we adopted the temperatures obtained from the NH_3 observations (correcting from rotational temperature to kinetic temperature), which allowed us to separate the contribution from each source, thanks to the high angular resolution.

6.4.2   Rotational Temperature and Column Density Maps

We obtained N_2H^+ and NH_3 spectra for positions in a grid of $2'' \times 2''$ in the main cloud and the western cloud, and fitted the hyperfine structure to each spectrum, or a single Gaussian for $NH_3(2,2)$. We performed the fits only for those spectra with an intensity greater than 5σ for the $NH_3(1,1)$, and greater than 4σ for the $NH_3(2,2)$. We set a higher cutoff for $NH_3(1,1)$ to ensure that not only the main line is detected but also the satellites. The results from the fits indicate that the entire main cloud is essentially optically thin for N_2H^+ ($\tau_{\mathrm{main}} \leq 0.4$), but optically thick for $NH_3(1,1)$. In both cases, the highest opacities are reached in the southeastern side of the cloud.

From the results of the fits to the $NH_3(1,1)$ and the $NH_3(2,2)$ spectra we computed the rotational temperature and NH_3 column density maps. We derived the rotational temperature following the standard procedures (Ho & Townes 1983; Sepúlveda 1993), and assuming that the excitation temperature and the intrinsic line width were the same for both $NH_3(1,1)$ and $NH_3(2,2)$. For the NH_3 column density derivation, we followed the expression given in Table 1 of Anglada et al. (1995), and assumed that the filling factor was 1 (see Appendix for more details).
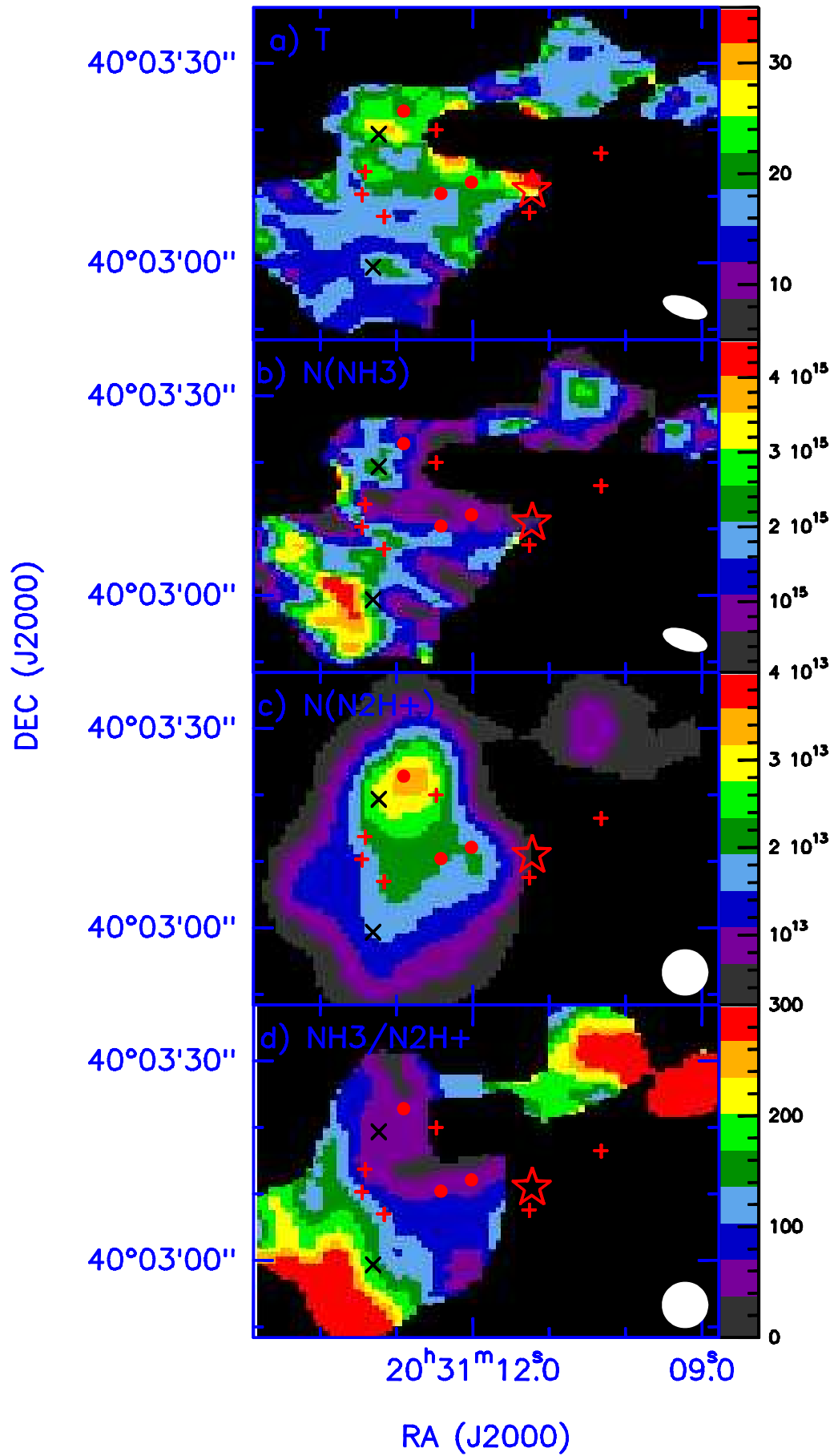
Figure 6.10: (see behind)

Figure 6.10: *a)* Rotational temperature map from $NH_3(1,1)$ and $NH_3(2,2)$. Scale units are in K. *b)* NH_3 column density map. Scale units are in cm^{-2}. *c)* N_2H^+ column density map convolved to an angular resolution of $7''$. Scale units are in cm^{-2}. *d)* $N(NH_3)/N(N_2H^+)$ ratio map after convolving the NH_3 column density map from panel b) to a final angular resolution of $7''$. Symbols are the same as in Fig. 6.2. Beams are shown in the bottom right corner, and are $6\rlap{.}''9 \times 3\rlap{.}''0$, with P.A.=$71\rlap{.}°5$ for panels a and b, and $7''$ for panels c and d.

Table 6.3: Local temperature enhancements

Position		$T_{\rm rot}$	$\Delta T^{\rm a}$	Possible
α(J2000)	δ(J2000)	(K)	(K)	Counterparts
20:31:12.22	40:03:01.9	23 ± 7	14 ± 9	-
20:31:13.26	40:02:58.9	20 ± 2	10 ± 3	2.12 μm faint emission (SHS$^{\rm b}$)
20:31:13.27	40:03:19.6	29 ± 6	14 ± 9	2.12 μm faint emission (NHS$^{\rm b}$)
20:31:13.44	40:03:13.4	24 ± 3	9 ± 6	IRS 5
20:31:14.96	40:03:03.4	23 ± 4	9 ± 5	H$_2$ knot c $^{\rm c}$

[a] ΔT is the temperature enhancement, defined by the difference between the minimum and the maximum values inside a box of twice the beam size.

[b] NHS: Northern Hot Spot; SHS: Southern Hot Spot

[c] from Kumar et al. (2002).

The map of the rotational temperature is presented in Figure 6.10a. The maximum value, 38 ± 15 K, is reached at the position of the UCHII region. Interestingly, around the apparent dense gas cavity west to BIMA 1, NH$_3$ shows high temperatures, with a maximum of 34 ± 9 K (the fits to the NH$_3$(1,1) and NH$_3$(2,2) at these positions are reasonably good, so this heating is most probably real). Toward the western cloud we find that temperature is essentially constant, around 16 K, slightly decreasing toward the center of the cloud.

There are some local maxima of rotational temperature in the map. In order to test the significance of these local maxima, we estimated the maximum and minimum values in a box with a size of about twice the beam size. In Table 6.3 we list the positions of the local maxima, the temperature, and the temperature enhancement (defined by the difference between the minimum and the maximum inside the box). There is a local maximum which is spatially coincident (the offset in positions is only of $0''\!.5$) with IRS 5, with a value of 23 ± 2 K. The warmest local maximum is located $\sim 5''$ to the southeast of mm1 (labeled as 'Northern Hot Spot'), reaching 29 ± 5 K, and is apparently associated with faint continuum emission at 2.12 μm (see Fig.6.1). There is another local maximum associated also with faint emission at 2.12 μm, which is found $10''$ to the southwest of BIMA 3, with 20 ± 3 K (labeled as 'Southern Hot Spot'). Another local maximum is associated with the H$_2$ knot c (Kumar et al. 2002), and lies in the axis of outflow B. There is also some heating about $20''$ to the southeast of the Northern Hot Spot, but we did not consider this

heating as a local maximum because it falls in the edge of the region where we fitted the spectra. Finally, the local maximum located $\sim 10''$ to the west of the Southern Hot Spot has no clear counterparts.

Figure 6.10b shows the resulting column density map for NH_3, corrected for the primary beam response. An obvious feature from the column density map is that the highest values are found to the southeast of the main cloud, where we found the lowest rotational temperatures in the rotational temperature map (Fig. 6.10a). In the northern part of the cloud the column density is higher around the Northern Hot Spot. It is worth noting that the NH_3 column density decreases toward IRS 5. Note that in the western cloud the column density increases toward the center.

We calculated the N_2H^+ column density by following the expression given in Benson et al. (1998), which takes into account the opacity effects. In the expression for the column density, the value for T_{ex} was derived from the hyperfine fit made with CLASS to the spectrum (CLASS gives as output parameter $A\tau_m$, with $A = f(J(T_{ex}) - J(T_{bg}))$, and f the filling factor, assumed to be 1). The resulting map is shown in Figure 6.10c. Contrary to NH_3, the map of the N_2H^+ column density has the maximum value very close to the position of the Northern Hot Spot and BIMA 1, and not in the southern side of the main cloud.

6.4.3   The NH_3/N_2H^+ column density ratio map

We convolved the NH_3 and N_2H^+ channel maps to obtain a final beam of $7''$ (the major axis of the NH_3 and N_2H^+ beams) in order to compare the NH_3 emission with the N_2H^+ emission. We fitted the spectra in each position of a grid of $4'' \times 4''$ in the convolved maps, and derived the column density for NH_3 and N_2H^+ following the same procedures outlined above, and correcting for the primary beam of each interferometer. We computed the NH_3/N_2H^+ column density ratio map, and the result is shown in Figure 6.10d. From the NH_3/N_2H^+ ratio map, one can see a clear gradient from the northwest, with a ratio around 50, to the southeast, where the ratio reaches values up to ~ 300. Such high values are also reached in the western cloud.

6.5   Discussion

6.5.1   General properties of the dense gas

Rotational temperature

The temperature distribution in the main cloud can be clearly separated into two parts: the northern side, with an average temperature of ~ 22 K, and the southern side, with an average temperature of ~ 16 K. It is interesting to note that almost all the young stellar objects in the region (see § 6.5.3), are associated with the northern side of the cloud, while in the cold southern side we found very few hints of active star formation. Thus, the higher temperature in the northern side could be due to internal heating from the embedded YSOs, whereas in the southern side internal heating is probably less important. However, the mean temperature in the south of the main cloud is higher than the mean temperature for low-mass externally heated starless cores, which show temperatures around 10 K (e. g., Tafalla et al. 2002, 2004). A similar result was found by Li et al. (2003), who derived temperatures of ~ 15 K toward massive (with masses similar to the mass derived for the main cloud, see next paragraph) quiescent cores, with no signs of star formation, in Orion. Li et al. (2003) find that the temperatures of the massive quiescent cores can be well explained by the dust being heated by the external UV field from the Trapezium, at a distance of ~ 1 pc from the massive cores. In our case, the B1 star associated with the UCHII region could be the source of heating of the southern side of the main cloud, at ~ 0.5 pc from the UCHII region. Alternatively, the heating could be produced by the nearby O and B stars of the Cygnus OB2 association (Le Duigou & Knödlseder 2002).

Column density and mass

The average NH_3 column density for the main cloud, 1.45×10^{15} cm^{-2}, is similar to the values derived by Jijina et al. (1999) for starless regions, and the derived N_2H^+ column densities, $(0.9–3) \times 10^{13}$ cm^{-2}, are in agreement with those obtained by Pirogov et al. (2003) for molecular cloud cores with massive stars and star clusters. The mass estimated for the main cloud from NH_3 is ~ 340 $M_\odot$, assuming an

abundance for NH_3 of 10^{-8}, and the mass derived from the N_2H^+ column density map is 75–190 $M_\odot$ for N_2H^+ abundances in the range $(2$–$5)\times10^{-10}$ (Pirogov et al. 2003; Tafalla et al. 2004). We compared these masses with that obtained from the dust emission, integrating in a region including all the BIMA sources, and obtained a total amount of gas and dust of ~ 102 $M_\odot$ (assuming $T_d = 25$ K, and $\beta = 1.5$). Thus, although the uncertainty in the abundances is certainly affecting the estimation of the mass from NH_3 and N_2H^+ (we found strong chemical differentiation across the main cloud, see § 6.4.3), we obtained similar masses from the dense gas tracers and the dust emission.

The mass derived from NH_3 arises mainly from the southern side of the cloud, while the main contribution to the mass derived from N_2H^+ comes from the northern side, as for the dust emission case. Thus the N_2H^+ column density distribution resembles the dust emission much more than NH_3.

Effects of chemical abundance and density

The NH_3/N_2H^+ ratio map of Fig. 6.10d shows a clear gradient in the NH_3/N_2H^+ ratio accross the cloud, from northwest, with low values, to southeast, with the highest values. In particular, there seems to be an anticorrelation between the NH_3/N_2H^+ ratio and the evolutionary stage of the sources embedded in the cloud. On one hand, in the north of the main cloud we found almost all the YSOs in the field, where the value of the ratio is < 100. On the other hand, the ratio rises up to ~ 300 in the southeastern side of the main cloud and in the western cloud, where we found cores with no signs of star formation (see below). The values of the ratio in the entire region are consistent with those derived for low-mass star forming regions by other authors (Caselli et al. 2002; Hotzel et al. 2004), who also find the same trend of low values (about 60–90) associated with YSOs, and high values (140–190) associated with starless cores.

A possible explanation for the higher NH_3/N_2H^+ ratio toward starless cores may be given in terms of abundance and density. For (sufficiently evolved) cores with moderate densities ($\leq 10^5$ cm^{-3}), there is a 'golden period' for NH_3 (Aikawa et al. 2003; Hotzel et al. 2004), while N_2H^+ keeps a constant abundance, as has been seen toward starless cores (e. g., Tafalla et al. 2004). This is consistent with the NH_3/N_2H^+ ratio being high in the southern side of the main cloud, where we

find starless cores with faint dust emission, indicating that the volume density is moderate. For higher densities ($\sim 10^6$ cm^{-3}), the NH$_3$ may start to freeze out onto dust grains, while N$_2$H$^+$ remains unaffected up to densities of $\sim 10^7$ cm^{-3} (Aikawa et al. 2003; Hotzel et al. 2004). In the main cloud, the highest densities are likely reached in the northern side, where there is the strongest dust emission. We did a rough estimation of the average volume density toward BIMA 1, from the derived mass and the size (at the 5σ contour level) of BIMA 1 (see Table 6.2), and obtained an average volume density toward BIMA 1 of 5×10^5 cm^{-3}. Thus we find low values of the ratio where there is the highest volume densities, where most of the YSOs in the main cloud are found.

It should be noticed that in the south of the main cloud and in the western cloud we find unusual high values for the NH$_3$/N$_2$H$^+$ ratio, up to 300. In addition, toward these positions the dust emission is faint compared with the dust emission in the north of the main cloud. Such high values for the NH$_3$/N$_2$H$^+$ ratio in combination with faint continuum emission could be explained from chemical models if the clumps are long-lived and have low densities, around 3×10^4 cm^{-3}, assuming a visual extinction of 100 (comparable to the visual extinction estimated for BIMA 3) and reasonable amounts of depletion (S. Viti, private communication). This would explain the differences found between the dust emission (strong in the north) and the NH$_3$ emission (strong in the south). A higher density in the north of the main cloud would lead to 'short-lived' cores, which did not have enough time to produce an amount of NH$_3$ comparable to the southern cores.

Starless cores

As seen above, the highest NH$_3$ column density in the region is reached in the south of the main cloud, around BIMA 3. The average rotational temperature toward BIMA 3 is ~ 16 K, which is among the lowest temperatures in the cloud, and there is no infrared emission associated and no signs of outflow emission. These properties suggest that BIMA 3 could be tracing a starless core. The NH$_3$ core associated with BIMA 3 is elongated in the northeast-southwest direction, and has a secondary maximum in the southern side of BIMA 4 (Fig. 6.10b). This secondary maximum has also associated low rotational temperatures, around 14 K, and no infrared emission, suggesting again a starless nature for the south of BIMA 4. Finally, we found that the ratio of NH$_3$ emission versus dust emission is very high toward the western

cloud, since the NH_3 emission shows a high-density clump and we did not detect any dust emission. An overabundance of NH_3 has been found toward other starless cores (Tafalla et al. 2002, 2004). In addition, Fig. 6.10a shows that the western cloud seems to be externally heated, and no 2MASS sources with infrared excess are associated with this cloud, indicating it is also likely a starless core. Note that these temperatures for starless cores, which are higher than the temperatures found toward low-mass starless cores, can be due to external heating from nearby OB stars, as has been found in massive quiescent cores in Orion by Li et al. (2003, see discussion about the temperature in the first paragraph of this section).

It is worth noting that, for these three starless cores, line widths derived from NH_3 and N_2H^+ hyperfine fits are around 1.2 km s^{-1} (Table 6.4), which are considerably larger than typical line widths measured toward starless cores in low-mass star-forming regions, $\sim$ 0.2 km s^{-1} (see, e.g., Crapsi et al. 2005). For the massive quiescent cores studied by Li et al. (2003) the NH_3 line widths were between 0.6 and 0.9 km s^{-1}, similar to what we find. Since the thermal component is around $\sim$ 0.2 km s^{-1} at 15 K, the line widths that we find suggest that these cores are dominated by turbulence, as Li et al. (2003) stated, or that there are important systematic motions.

6.5.2   Interaction of the YSOs with the surrounding gas

The UCHII region:

In Figure 6.11 we overlay the CN(1–0) emission (contours) from Beuther et al. (2004c) on the NH_3(1,1) emission (grey scale). The morphology of the CN emission next to the UCHII region is following the edge of the dense cloud traced by NH_3(1,1), and is facing the UCHII region. CN emission is often found in photon-dominated regions, tracing the part of the molecular cloud which is exposed to an intense flux of FUV photons from a nearby young OB star (see, e.g., Fuente et al. 1993; Simon et al. 1997; Boger & Sternberg 2005). Moreover, H_2 emission at 2.12 μm (Kumar et al. 2002; Beuther et al. 2004b) reveals a ring-like structure around the UCHII region, of radius $\sim$ 8″, reaching the edge of the main cloud. In addition, we found heating toward this edge of the cloud (Fig. 6.10a), with rotational temperature progressively increasing when approaching the UCHII region. All this is indicating that the UCHII region is interacting with the main cloud. On one hand, the interaction comes from

the radiation of the ionizing star, enhancing the CN emission and producing the heating seen in the rotational temperature map. On the other hand, there are strong H_2 knots in the ring that could be tracing a mechanical interaction of the compression front from the UCHII region with the surrounding medium.
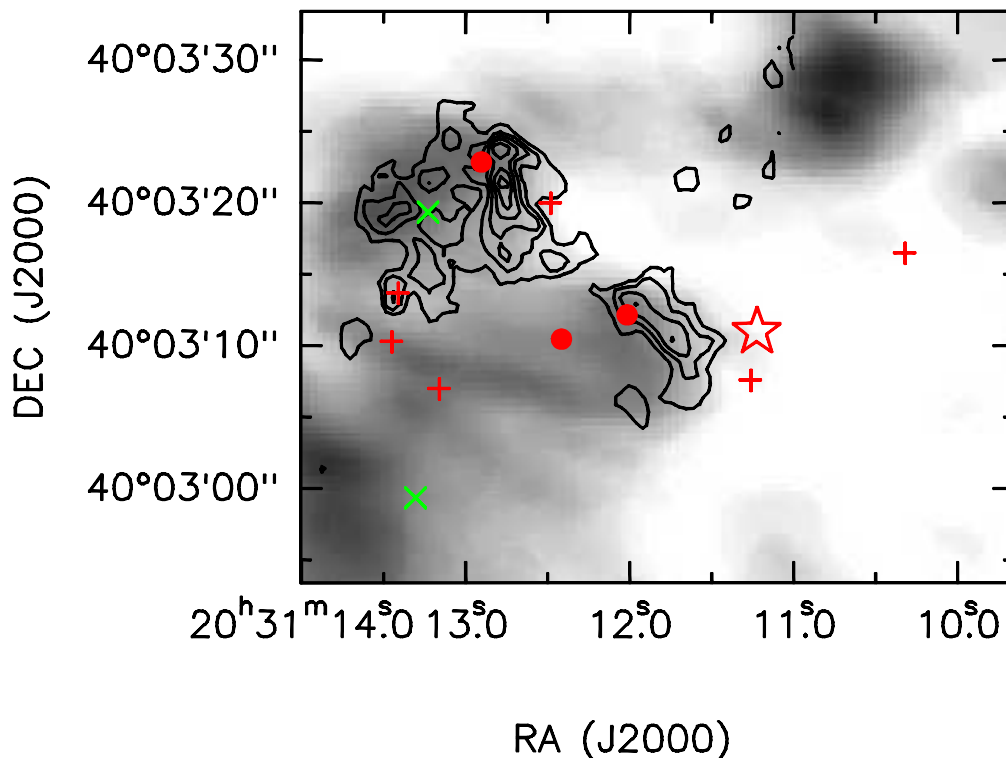
Figure 6.11: Grey scale: $NH_3(1,1)$ emission shown in Fig. 6.2c. Contours: zero-order moment map of the CN(1–0) emission from Beuther et al. (2004c), integrated from 4 to 12 km s^{-1}. Contours start at 15% of the peak intensity, 273 Jy beam^{-1} km s^{-1}, increasing in steps of 15%. Symbols are the same as Fig. 6.2. Beams are $6''9 \times 3''0$, with P.A.$= 72°$ for $NH_3(1,1)$, and $1''46 \times 1''21$, with P.A.$= 32°$ for CN(1–0).

Outflow A:

Beuther et al. (2004b) discovered a highly collimated outflow in CO(2–1) (outflow A), elongated in the northeast-southwest direction, and with mm1 being its driving source. The axis of the outflow is shown in Fig. 6.2.

The velocity gradient seen in CH_3OH toward mm1 (see § 6.3.2 and Fig. 6.6) is consistent with tracing material entrained by ouflow A. In addition, the p-v plot

shows a clump $\sim -35''$ to the west of mm1, the methanol western clump, with wide redshifted wings (see Figs. 6.3 and 6.6), and matching well the red lobe of CO(2–1) and the redshifted clump of SiO(2–1) from Beuther et al. (2004b). Thus, the methanol western clump emission may have originated in a shock between the redshifted lobe of the outflow and the ambient material, producing the wide redshifted wings observed in CH_3OH.

The red lobe of outflow A, which starts at mm1, propagates through the cavity apparent in the N_2H^+ and NH_3 zero-order moment maps (see Fig. 6.2). The rotational temperature and column density maps of Fig. 6.10 show that the walls of this cavity are characterized by remarkably high temperatures and low column densities. In addition, the NH_3 gas of the walls of the cavity is redshifted (as the lobe of outflow A), and shows line broadening. Thus, this cavity could have been excavated by outflow A, and the high temperatures could arise from the shock interaction of outflow A with the walls of the cavity. This has been observed toward other outflows driven by high-mass stars (AFGL 5142: Zhang et al. 2002).

Outflow B:

Outflow B was first identified by Beuther et al. (2004b) in SiO(2–1), which shows a very strong blue lobe elongated in the northwest-southeast direction, and in CO(2–1), with faint high-velocity blueshifted emission. Ridge B is morphologically very similar to the SiO(2–1) blue lobe and also splits up into two lobes at the position of BIMA 4. In addition, we found some heating in the northern part of BIMA 4 (see Fig. 6.10a), and we also found that the kinematics of the outflow changed at this position (see § 6.3.2). Moreover, the N_2H^+ second-order moment map shows a clear line broadening associated with the first $20''$ of ridge B (Fig. 6.8b). This line broadening is also observed in the $NH_3(1,1)$ emission. Interestingly, in the south of BIMA 4, there is a secondary maximum in the NH_3 column density map, for which we found properties suggestive of starless cores (§ 6.5.1). Thus, it seems evident from these observations that outflow B is interacting with the starless core in the south of BIMA 4, and that the heating found in the north could be the result of this interaction. Downstream of the starless core, there is heating (see Fig. 6.10a) associated with the H_2 knot c by Kumar et al. (2002), likely as a result of the interaction of outflow B with the ambient medium.

The scenario in which outflow B is interacting with a starless core naturally explains the morphology of the CH$_3$OH emission splitting into two clumps at the position of BIMA 4. One of the clumps follows the same direction of the outflow, and the other clump is deflected to the east, elongated in the east-west direction, and has broad lines. The deflection of an outflow due to the interaction with a dense quiescent clump has been found toward other star-forming regions (e. g., IRAS 21391+5802, Beltrán et al. 2002).

In addition, the properties of the methanol eastern clump, which is found to the northeast of the deflected clump, at ambient velocities, and with narrow lines (around 1 km s^{-1}, Fig. 6.3), are easily explained in this scenario. These properties are consistent with the methanol eastern clump being illuminated by the UV radiation coming from the interaction of outflow B with the starless core in the south of BIMA 4. The illumination of the UV radiation from shocks has been proposed as the mechanism of enhancement of the emission of some species in clumps ahead of shocks, in particular of CH$_3$OH and NH$_3$ (see e. g., Torrelles et al. 1992b; Girart et al. 1994, 2002). With the present observations, we were not very sensitive to the NH$_3$ emission toward the methanol eastern clump because the clump is located beyond the VLA primary beam (see Fig. 6.2c,d). Typically, such illuminated clumps in low-mass star-forming regions have sizes of 0.05–0.1 pc, and are located at distances to the shock of the order of 0.1 pc (Girart et al. 1998). This is consistent with the methanol eastern clump, which has a size of $\sim$ 0.15 pc, and is located about 0.2 pc from BIMA 4.

Regarding the driving source of outflow B, a possible candidate is mm1, as Beuther et al. (2004b) proposed. If this was the case, mm1 would be a binary system, since outflow A is clearly associated with mm1. The Northern Hot Spot found in this work is aligned with outflow B, and is located at the begining of the blue lobe of CH$_3$OH. Furthermore, we found a clear symmetry with respect to the Northern Hot Spot in the p-v plot of Fig. 6.5 (see § 6.3.2), strongly suggesting that the Northern Hot Spot could be the driving source of outflow B. In § 6.5.3 we estimate a circumstellar mass < 0.4 $M_\odot$ for the Northern Hot Spot.

Finally, the interaction of outflow B with the starless core next to BIMA 4 tempts one to speculate that outflow B could be triggering the collapse in this core in a future, as has been proposed in other regions (e. g., Yokogawa et al. 2003). This would draw a nice picture in which a YSO in the north of the main cloud is

'responsible' for star formation in the south, but should be further investigated by studying in more detail the morphology and kinematics across the core.

6.5.3   Very YSOs in the region

Selection of 2MASS sources associated with the region

In order to study the different sources associated with the dense gas found around the UCHII region, we extracted a sample of stars within the BIMA primary beam from the 2MASS All-Sky Catalog of Point Sources (Cutri et al. 2003), and plotted a $(J-H)$,$(H-K)$ diagram (Figure 6.12). The total amount of infrared sources inside the BIMA primary beam is 43. The color-color diagram shows that there is a bulk of infrared stars at low-to-moderate values of the color indices, which likely occupy the position of the unreddened stars (see, e. g., Comerón et al. 2002), and a group of stars with high $(H-K)$ and low $(J-H)$ colors. We took the criteria of $(H-K) > 2$, $(J-H) < 3$ and spatial coincidence with emission detected in this work to select those 2MASS sources which are possibly (but not necessarily) associated with the dense gas around the UCHII region. The selected 2MASS sources are labeled as IRS 1, IRS 2 (following the nomenclature of Kumar et al. 2002), and IRS 3 to IRS 6 (increasing RA). These infrared sources (with the exception of those which seem to be background objects, see below) are listed in Table 6.4 together with the compact millimeter sources from Beuther et al. (2004c), and the sources found in this work. For each source we show the main properties derived in this work.

Individual YSOs

IRS 1 and the UCHII region: From the 2.12 μm image provided by Kumar et al. (2002), IRS 1 is a binary system, the fainter component being associated with the UCHII region. The UCHII region has a flux density of 7.6 mJy beam^{-1} at 3.6 cm (Sridharan et al. 2002; Beuther et al. 2004b), and a deconvolved size of $4''5$ (0.04 pc). This corrresponds to an ionizing flux of $\sim 1.5 \times 10^{45}$ s^{-1}, typical of stars of spectral type B1 (Panagia 1973). Toward the UCHII region, we found the highest rotational temperature in the main cloud, and very low column densities, as expected for gas after the passage of an ionization front (see, e. g., Dyson & Williams 1997).

Table 6.4: List of sources in the IRAS 20293+3952 region

	Position[a]		Outf[b]	$I_\nu^{\text{peak c}}$	T_{rot}	$N(\text{NH}_3)$	Ratio[d]	Line width (km s^{-1})[e]	
	α(J2000)	δ(J2000)		(mJy beam^{-1})	(K)	(10^{15} cm^{-2})		NH$_3$(1,1)	N$_2$H$^+$
YSOs									
IRS 1[f]	20:31:11.26	+40:03:07.6	NN	< 2.4	-	-	-	-	0.9
UCHII	20:31:11.22	+40:03:11.0	NN	< 2.4	38 ± 15	0.14	-	2.4	1.0
IRS 2[f]	20:31:10.32	+40:03:16.5	NN	< 2.4	-	-	-	-	
IRS 3[f]	20:31:12.48	+40:03:20.0	YN	6.3	-	-	-	-	
IRS 5[f]	20:31:13.41	+40:03:13.7	?N	2.6	24 ± 3	0.59	42	1.5	1.5
mm1	20:31:12.9	+40:03:22.9	YY	10.8	24 ± 3	1.1	37	1.4	1.6
mm2	20:31:12.01	+40:03:12.2	YN	8.1	23 ± 4	0.88	46	1.1	1.1
mm3	20:31:12.41	+40:03:10.5	YN	3.9	19 ± 1	0.66	57	1.2	1.1
NHS[f]	20:31:13.27	+40:03:19.6	NY	< 2.4	29 ± 6	1.8	56	2.0	1.9
SHS[f]	20:31:13.26	+40:02:58.9	YN	< 2.4	20 ± 2	1.3	150	1.0	0.9
Starless Cores									
BIMA 3	20:31:13.90	+40:03:03.3	NN	< 2.4	14 ± 2	5.4	290	1.2	1.2
SBIMA 4[f]	20:31:14.41	+40:03:11.8	YY	< 2.4	14 ± 2	3.8	180	1.3	1.7
WCloud	20:31:10.71	+40:03:30.3	NN	< 2.4	15 ± 3	2.8	280	1.0	0.8

[a] Positions correspond to those in the 2MASS Point Source Catalog for IRS 1 to IRS 5; the centimeter source given by Beuther et al. (2002d) for the UCHII region; the positions given by Beuther et al. (2004c) for mm1 to mm3; the peak in the rotational temperature map of Fig.6.10a for the NHS and the SHS, and the position of the peak in the NH$_3$ column density map of Fig.6.10b for the starless cores.

[b] High-velocity outflow associated (Y=yes; N=No): the first character refers to CO from Beuther et al. (2004b), the second character refers to high-velocity CH$_3$OH from this work.

[c] Intensities from this work, at 3.15 mm.

[d] Ratio of $N(\text{NH}_3)$ over $N(\text{N}_2\text{H}^+)$.

[e] Line widths derived from the hyperfine fits (see main text).

[f] The 2MASS PSC names are IRS 1: J20311125+4003076; IRS 2: J20311031+4003164; IRS 3: J20311247+4003199; IRS 5: J20311341+4003136; NHS: Northern Hot Spot; SHS: Southern Hot Spot; SBIMA 4 stands for the core found in NH$_3$ to the south of BIMA 4 (see § 6.5.1).
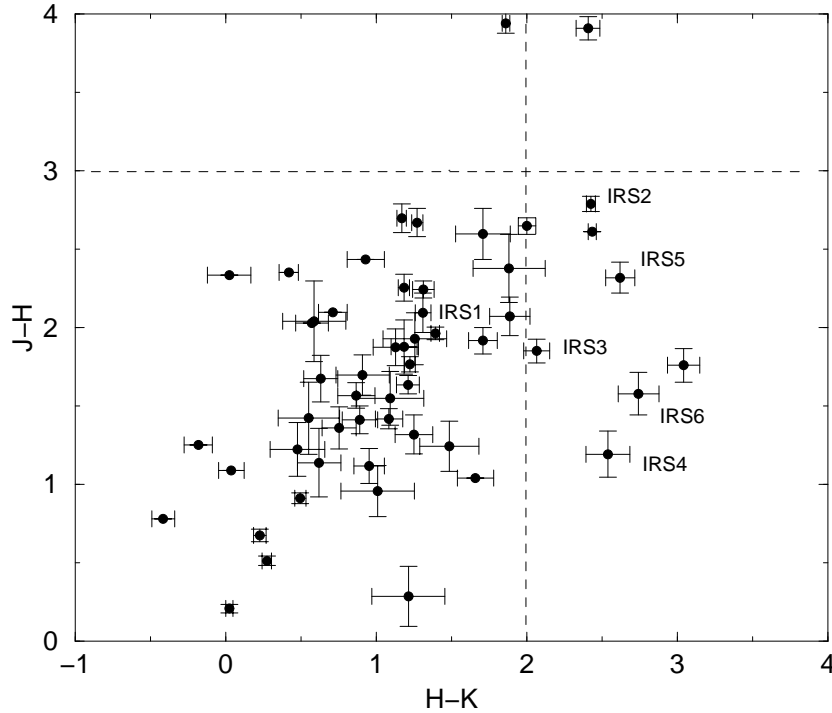
Figure 6.12: $(J - H)$, $(H - K)$ diagram for the 2MASS sources in the IRAS 20293+3952 region lying within the BIMA primary beam.

IRS 2: About $10''$ to the northwest from the UCHII region, there is the second brightest source in the field, IRS 2, which shows much more infrared excess than IRS 1, as already stated by Kumar et al. (2002). We could not determine a temperature and column density from NH_3 toward IRS 2 due to low S/N of the NH_3 emission.

IRS 3: IRS 3 is the only infrared source with infrared excess falling inside the 2σ contour level of BIMA 1. The high-angular resolution observations of Beuther et al. (2004c) reveal a weak extension of mm1 toward the southwest and reaching the position of IRS 3. From our data, the dense gas emission was too weak to derive a temperature and column density toward this source. Thus, IRS 3 shows strong infrared emission and weak mm emission, indicating that IRS 3 is likely a YSO which has cleared up most of the material in its surroundings.

IRS 5: IRS 5 falls inside the 2σ contour level of the dust ridge (see Fig. 6.1), in its eastern edge. We found heating associated with IRS 5 (§ 6.4.2 and Table 6.3), indicating that this source is physically associated with the main cloud. In addition, the NH_3 column density is low (Fig. 6.10b), and thus IRS 5 could be a protostar in the process of clearing up the surrounding material. Alternatively, the low NH_3 column density could be due to depletion of NH_3 onto dust grains.

mm1: mm1 is likely the main contribution to the emission of BIMA 1, since it is the strongest compact mm source in the region, and is the driving source of outflow A, which is highly collimated (Beuther et al. 2004b) and elongated in the same direction as BIMA 1 (Fig. 6.1). In addition, the infrared emission at 2.12 μm associated with mm1 is faint and arises mainly from shocked gas (see Fig. 2 of Kumar et al. 2002). The rotational temperature toward mm1 is 24 ± 3 K (Table 6.4), and the NH_3 column density is rather low, possibly due to depletion of NH_3 onto dust grains. From the flux density of Beuther et al. (2004c) at 2.6 mm, we obtain a mass for mm1 of 4.0 $M_\odot$, assuming $\beta = 1$ (value calculated by Beuther et al. 2004c), and $T_d = 32$ K (T_d estimated from the rotational temperature derived in this work and following Tafalla et al. 2004). All this indicates that mm1, in contrast with IRS 3, is deeply embedded in a massive and not very hot envelope, suggesting that it is an intermediate/high-mass protostar.

mm2 and mm3: Beuther et al. (2004b) detected two compact millimeter sources inside the 5σ contour level of BIMA 2, mm2 and mm3, each one likely driving a molecular high-velocity CO(2–1) outflow, suggesting that mm2 and mm3 are truly protostars, and not heated clumps of dust without any star yet. Taking the flux density from Beuther et al. (2004c) at 2.6 mm, a dust emissivity index $\beta = 1$, and $T_d = 30$ K and $T_d = 23$ K for mm2 and mm3 respectively (T_d derived as in the case of mm1), we estimate circumstellar masses of 1.3 $M_\odot$ for mm2 and 0.8 $M_\odot$ for mm3.

The Northern Hot Spot: The Norhtern Hot Spot is located about $5''$ (10000 AU) to the southeast of mm1, and is near a local maximum in NH_3 and N_2H^+ column densities (see Fig. 6.10b and c). Very close to the hot spot, $1''3$ to the east, there is faint infrared continuum emission at 2.12 μm, which is not detected in the J and H band images of 2MASS, indicating that the source has strong infrared excess. In addition, there is no H_2 line emission at 2.12 μm tracing shocked gas (see

Fig. 2 of Kumar et al. 2002). Therefore, the infrared emission could be tracing a deeply embedded protostar, heating the dense gas around it. The mm continuum sets an upper limit to the mass of 0.4 $M_\odot$ (taking an upper limit of 3σ, and assuming $\beta = 1$ and $T_d = 44$ K, T_d estimated as in the case of mm1), suggesting that the source associated with the Northern Hot Spot is a low-mass protostar. Thus, these properties support that the Northern Hot Spot is the driving source of outflow B.

The Southern Hot Spot: A similar case to the Northern Hot Spot is that found $\sim 10''$ to the southwest of BIMA 3 (see §6.4.2). At this position, the temperature enhancement is very significant (see Table 6.3), and we also found faint infrared emission associated, again present only in the K filter of 2MASS, and with no H_2 line emission associated. The emission from the continuum at 3.15 mm is below 3σ, implying a circumstellar mass $\lesssim 0.8$ $M_\odot$ (assuming $T_d = 25$ K, estimated as in the case of mm1). Furthermore, there is high-velocity blueshifted CO(2–1) emission spatially coincident with the Southern Hot Spot (Beuther et al. 2004b). All this indicates that possibly the heating in the Southern Hot Spot is due to a deeply embedded low-mass YSO.

Background objects: In addition to IRS 5, we find two 2MASS sources with infrared excess, IRS 4 and IRS 6, spatially coincident with the dust ridge. IRS 6 is the source with the highest infrared excess among the 2MASS sources in the main cloud, suggesting that it is embedded in gas and dust. The faint source IRS 4 is located only $4''$ to the southwest of IRS 6, and also shows infrared excess. However, the association of IRS 4 and IRS 6 with the dense gas is not clear from the rotational temperature and NH_3 column density maps (Fig. 6.10), and thus these two infrared sources could be background stars or YSOs highly extincted by the foreground dust of the main cloud.

Summary: As seen above, there is a variety of YSOs in the region. The most massive source seems to be a binary system (the UCHII region and IRS 1). To the east of the most massive source, there is the main cloud of dense gas, where we find eight sources (sources IRS 2, IRS 3, and IRS 5, mm1, mm2, mm3, the Northern Hot Spot and the Southern Hot Spot), which seem to be (proto)stars coming from the same natal core. In addition, we found three clumps with characteristics similar to starless cores. The sources seem to be in different evolutionary stages,

with the infrared sources in the more advanced phases, the millimeter sources likely being in an earlier stage with no infrared emission associated yet, and the youngest sources having the properties of starless cores. We do not find different evolutionary stages only between the low-mass sources and the high-mass sources (which are expected because the high-mass sources evolve more rapidly to the main sequence than the low-mass sources), but among the low-mass sources as well, for which we expect similar rates of evolution to the main sequence. Thus, it seems stars are not forming simultaneously in this cluster environment. Rather, there may be different generations, as found toward L1551 by Moriarty-Schieven (2006).

6.5.4 Spatial distribution of the YSOs in the region

In this section we consider whether interaction between the different sources is important in the determination of the spatial distribution of the YSOs. We find that star formation is localized in the north of the main cloud, where there are around six YSOs, while in the south we find sources with properties of starless cores, and only one YSO.

We consider first whether the UCHII is responsible for such a spatial distribution. In section 6.5.2 we discussed some evidence of interaction of the UCHII region with the edges of the main cloud, mainly with BIMA 2. This suggests that mm2 and mm3 could have been triggered by the UCHII region. If this was the case, mm2 should be in an evolutionary stage older than mm3, which is farther away from the UCHII region. This is consistent with the dynamical timescales derived from the outflows associated, which are 12600 yr for mm2, and 2100 yr for mm3 (Beuther et al. 2004b). However, the formation of the other (not mm2 and mm3) YSOs in the north of the main cloud is not likely due to triggering by the UCHII region, since they are located farther away than mm2 and mm3 and do not seem to be in earlier evolutionary stages. Therefore, the UCHII region does not seem to be triggering star formation beyond mm2 and mm3.

Another possibility for the formation of the YSOs in the north of the main cloud could be the following. In Fig. 6.9, we found that the western cloud has an extension intersecting the main cloud, seen at velocities > 7 km s^{-1} in the channel maps (Fig. 6.7). In Fig. 6.8, we observed a slightly redshifted filament elongated in the northwest-southeast direction, with line broadening associated. This seems

to suggest that the extension of the western cloud could be merging with the main cloud, inducing the collapse in the northern side of the main cloud. Merging of two clouds has been proposed as a mechanism to trigger star formation in other regions, like L723 (Girart et al. 1997). Note however that this scenario is not very consistent with the gradient seen in the N_2H^+ p-v plot of Fig. 6.5b, since the merger of two clouds should yield two well differentiated components in velocity, and not the smooth and progressive gradient that we find. Furthermore, it would be a coincidence that the filament was elongated in the same direction as outflow B. Thus, although the data seems to suggest a merging of the main cloud with the western cloud, this scenario is not confirmed by a more detailed analysis of the data.

We thus conclude that while interaction between the different sources in this cluster environment is certainly important, and may have triggered star formation in particular cases, the overall spatial distribution of the YSOs does not seem to be the result of interaction between the different sources, rather it may be showing the different initial conditions in the main cloud. If the main cloud was much denser in the north than in the south, we would possibly observe a similar situation to what we have found.

6.6   Conclusions

We observed with the BIMA and VLA arrays the continuum emission at 3.15 mm, and the CH_3OH, N_2H^+ and NH_3 emission toward IRAS 20293+3952, a region in which star formation is taking place in a closely-packed environment. Our main conclusions can be summarized as follows:

1. The dense gas traced by N_2H^+ and NH_3 shows two different clouds, one to the east of the UCHII region (main cloud), of ~ 0.5 pc of size, and another cloud to the northwest (western cloud), of ~ 0.15 pc, and redshifted with respect the main cloud. The dust emission reveals two strong components in the northern side of the main cloud, BIMA 1 and BIMA 2, and two fainter components in the southern side, BIMA 3 and BIMA 4, together with extended dust emission forming a common envelope. Regarding the CH_3OH, we found strong emission in a fork-like structure associated with outflow B from Beuther et al. (2004b),

as well as two CH_3OH clumps forming a ridge associated with outflow A.

2. We found that the rotational temperature is higher in the northern side of the main cloud, around 22 K, than in the southern side, around 16 K. In contrast, the NH_3 column density distribution has the highest values in the south of the main cloud. The N_2H^+ column density distribution resembles the dust emission, strong in the northern side of the main cloud. We found three local temperature enhancements which seem to be associated with embedded YSOs, one of them associated with a 2MASS source, and the other two, the Northern Hot Spot and the Southern Hot Spot, associated with faint continuum infrared emission at 2.12 μm.

3. There is strong chemical differentiation in the region. In particular, we found low values of the NH_3/N_2H^+ ratio, ~ 50, associated with YSOs, and high values, up to 300, associated with starless cores. This is consistent with NH_3 being enchanced with respect N_2H^+ at moderate densities ($\lesssim 10^5$ cm^{-3}), while at densities around 10^6 cm^{-3} NH_3 may start to deplete and N_2H^+ likely remains undepleted up to higher densities.

4. We identified three cores in the NH_3 column density map, with low temperatures and with no infrared emission associated, similar to starless cores in low-mass star-forming regions, but with temperatures slightly higher, ~ 15 K, possibly due to external heating from the UCHII region and/or the nearby OB stars. These are associated with BIMA 3, the south of BIMA 4, and the western cloud.

5. Interaction between the different sources in the region is important. First, the UCHII region is interacting with the main cloud heating and enhancing the CN(1–0) emission in the edge of the main cloud which is facing the UCHII region. Second, one of the outflows in the region, outflow A, seems to be excavating a cavity and heating its walls. Third, another outflow in the region, outflow B, seems to be interacting with the starless core in the south of BIMA 4, likely producing the deflection of the outflow seen at this position. Such a shock could be illuminating a clump with narrow CH_3OH lines located ~ 0.2 pc to the northeast of the shock. We found that the Northern Hot Spot is likely the driving source of outflow B.

6. There are about eight YSOs in the dense gas nearby the UCHII region. For the YSOs for which we could estimate the circumstellar mass, we found values

ranging from < 0.4 to $\sim 4~M_\odot$. In addition, the YSOs seem to be in different evolutionary stages, even if we consider only the low-mass sources. Thus, stars do not seem to form simultaneously in this cluster environment.

7. While we cannot discard that interaction between the different sources may have triggered star formation in particular cases, triggering cannot explain the overall spatial distribution of the YSOs, suggesting that this may be essentially determined by the initial conditions in the cloud.

Chapter 7

General Discussion and Conclusions

7.1 Number of mm sources around the most massive star of the cluster

In the present work we have studied four cluster environments, three of them harboring at least one intermediate/high-mass YSO. Toward these three regions, we carried out observations with enough sensitivity to detect low-mass YSOs formed around the intermediate/high-mass star and to study the interaction betweeen them.

In Table 7.1 we list the three intermediate/high-mass regions studied (I00117, I20343, I20293) plus two additional regions from the literature (I20126, I19410) for which the sensitivity achieved with an interferometer allowed to detect condensations down to masses $\sim 0.5\ M_\odot$. From the table, we find that the median number of millimeter sources around the young high-mass star is of 5 sources.

Surveys conducted in the optical and near infrared toward Herbig Ae/Be stars reveal in general a larger number of sources around the massive star. For example, the survey by Hillenbrand (1995) has a median of 15 lower-mass stars in the vicinity of the intermediate/high-mass star, for stars with bolometric luminosities between 1000 and 10000 $L_\odot$, and for sensitivity limits of $\sim 0.2\ M_\odot$. The survey carried out by Testi et al. (1998) in the near infrared toward Herbig Ae/Be stars results in a median

135

Table 7.1: Summary of massive star-forming regions observed with interferometers with enough sensitivity to detect low-mass embedded sources

Region	L_{bol} ($L_\odot$)	Evolut. stage[a]	N[b]	$M_{\mathrm{sensitivity}}$[c] ($M_\odot$)	Spatial res. (AU)	FOV (pc)	Ref.
IRAS 00117+6412	1300	UCHII, B2	2	0.41	6800	0.47	1
IRAS 20343+4129	3200	UCHII, B2	7	0.21	4200	0.31	1
IRAS 20293+3952	6300	UCHII, B1	5[d]	0.87	2600	1.16	1,2
IRAS 20126+4104	7900	pre-UCHII, B0.5	2	0.34	2900	0.45	3
IRAS 19410+2336	10000	UCHII	11	0.63	2000	2×0.12	4

[a] Spectral type estimated from cm wavelength emission.

[b] Number of mm sources detected above the 5σ contour level, if this level is closed, without including the most massive source.

[c] Masses derived assuming $T_{\mathrm{d}} = 30$ K, a dust emissivity index of 1.5, and the opacity law of Beckwith et al. (1990), for a flux density of 5σ.

[d] The five mm sources are: three mm sources detected by Beuther et al. 2004c, plus two starless cores found in this work.

References: 1: this work; 2: Beuther et al. 2004c; 3: Cesaroni et al. 1999a; 4: Beuther & Schilke 2004.

of 10 infrared sources, for the same range of luminosities and for similar sensitivities, and the study by Massi et al. (2000; 2003) of luminous Class I sources gives a median of infrared sources in the K-band of 27, for the same range of luminosities and for mass sensitivities around 0.3 $M_\odot$. The numbers given by Testi et al. and Massi et al. are corrected for foreground/background contamination. Note that the mass sensitivities of the studies in the near-infrared refer to *stellar* masses, while the mass sensitivities in the mm/submm studies refer to *envelope/disk* masses (by 'envelope' we mean partially extended emission, including dust condensations with protostars or with no protostars yet). However, we assume as a first approximation that the mass of the dust condensations will be of the same order of the stellar mass, which is specially true for the youngest protostars (Class 0).

Thus, in general terms, it seems that the median value of 5 millimeter sources found around the intermediate/high-mass star is significantly smaller than the median value of infrared sources found toward (more evolved) intermediate/high-mass stars. Possible reasons for detecting less millimeter sources than infrared sources surrounding the massive star are enumerated below.

1. *Enough sensitivity of the mm observations?* The mass sensitivity limit calculated for each region (column 5 in Table 7.1) has been derived assuming a dust temperature, a dust emissivity index, and an opacity law. The dust temperature assumed was 30 K. If we take a dust temperature of 20 K, then the mass sensitivity estimated is 0.8 $M_\odot$, instead of 0.5 $M_\odot$. If we take a dust emissivity index β of 1 instead of 1.5, we are sensitive to lower masses, and if we take $\beta = 2$, the sensitivity limit goes to 1 $M_\odot$. However, the emissivity index is found to be 1 rather than 2 toward YSOs (e. g., Eislöffel et al. 2003; Beuther et al. 2004a; Beuther et al. 2004c; Felli et al. 2004; Chen et al. 2005), and thus assuming $\beta = 1.5$ seems to set an upper limit to the sensitivity. Finally, we assumed the opacity law of Beckwith et al. (1990). If we take an opacity law of 0.05 cm^2 g^{-1} at 300 μm (André et al. 1996; D'Alessio 1996; Motte et al. 2001), then the mass sensitivity is ~ 1 $M_\odot$. In conclusion, taking into account different temperatures, dust emissivity indices, and opacity laws for the cores, the worst case would increase twice the mass sensitivity stated in Table 7.1. The region most affected by this is I20293, which would have a mass sensitivity around 2 $M_\odot$, but the other regions would still have a reasonable mass sensitivity. However, the mass sensitivity of the works by Hillenbrand (1995) and Testi et al. (1998) was around ~ 0.1 $M_\odot$, which is

about one order of magnitude below our limit in the case of assuming the less favorable parameters. Thus, although we are in good position for considering the number of mm sources in each region, the possibility of not having reached enough sensitivity should be kept in mind, and we stress the importance of future observations reaching sensitivities down to 0.1–0.2 $M_\odot$.

2. *Enough spatial resolution and good uv-coverage?* The cluster of mm sources found by Beuther & Schilke (2004; region I19410 in the table) was studied with a spatial resolution around 2000 AU. For the regions in Table 7.1 the spatial resolutions are around 2000–4000 AU, with the exception of I00117. In fact, the low number of mm sources detected in this region could be partially due to this effect (note that the source mm1 in I00117 seems to have contributions from three different subcomponents). Another important aspect is the uv-coverage. Beuther & Schilke (2004) combined configurations B, C, and D of the PdBI, and configuration D was crucial to recover most of the flux (Beuther, priv. comm.). Therefore, future projects must assure high spatial resolution and good u-v-coverage, combining at least two different configurations.

3. *Is the dust emission tracing envelopes or compact disks?* If the lower-mass sources are in very early stages, the dust emission may be tracing the envelope, and a fraction of the envelope (harboring a protostar) will be finally accreted onto the star. Assuming a star formation efficiency of 20%, and in order to detect final stellar masses of $\sim 0.1\ M_\odot$, the mass of the envelope should be $\sim 0.5\ M_\odot$, which is around our sensitivity limit. However, the dusty envelopes may be partially resolved by the interferometer and this would decrease the detected flux. On the contrary, if the dust emission comes from a compact disk, then the measured mass will be a fraction of the stellar mass, about 0.3 times the stellar mass (Hollenbach et al. 1994; Shu et al. 1990). Assuming the lower-mass sources may have around 0.1 $M_\odot$, the disk masses would be $\sim 0.03\ M_\odot$. This is certainly below our sensitivity limit (and may be in fact the case of HH211 mm). In any case, we expect to find sources in intermediate stages between envelopes and compact disks, and thus it is still reasonable to look for millimeter sources. In addition, it should be considered whether the dust is a good tool to trace the embedded protostars with lowest masses. From this work, we have found at least two low-mass embedded sources through the study of dense gas tracers and calculating rotational temperature maps, finding this method to be a powerful tool for looking for embedded low-mass sources.

4. *Is the target massive enough to harbor a cluster?* A clear trend in the surveys of Hillenbrand, Testi et al., and Massi et al. is that the number of sources increase with the mass of the central massive star, the fields with less sources detected corresponding in general to central sources that are less luminous. In Table 7.1 we find in general the same trend: the less luminous source in the table, I00117, has only two mm sources surrounding the central 'massive' star, while I20343 and I20293, which are more luminous, show more mm sources, and I19410, the most luminous source in the table, has the highest number of mm sources. Thus, the low number of mm sources detected toward I00117 could be due to the fact that the 'massive' source is rather of intermediate mass. However, the luminosity of the central star cannot be the only factor determining the number of mm sources around it, because for I20126 we found the same number as for I00117, while I20126 is 6 times more luminous.

5. *Is the target in a 'young enough' evolutionary stage?* If the region is too evolved, most of the parental cloud has already been disrupted and there are no embedded sources, being most sources bright in the infrared. On the contrary, if the region is in a very early evolutionary stage, still deeply embedded in the cloud, the cluster could not be seen because members are still being born. McKee & Tan (2002) argue that the time for the formation of an individual star is around 10^5 yr, which is small compared to the estimated timescale of cluster formation, 10^6 yr. Therefore, if we have selected young enough regions, and if sources are not formed simultaneously, then it would be normal to find less mm sources around massive protostars than infrared sources around (more evolved) massive protostars. This is supported by the fact that I20126, the youngest source in Table 7.1, has almost no millimeter sources around it (I20126 has been proposed to be in a stage prior to developing an UCHII region, Cesaroni et al. 1999a), even with the good mass sensitivity and spatial resolution achieved in the obsrvations of Cesaroni et al. (1999a), as shown in the table. This issue will be adressed in § 7.3.

7.1.1 Considerations for further work

As a result of the present work, we suggest a few points to take into account in order to plan observations aiming at studying mm/submm clusters around intermediate/high-mass stars in very early evolutionary stages:

1. Reaching mass sensitivities down to 0.1 $M_\odot$. For this, the targets should be at distances smaller than ~ 3 kpc, depending on the interferometer used for the observations. Observations should be carried out combining at least two configurations and assuring spatial resolutions down to 2000 AU.

2. Using not only mm continuum emission, but also other tracers of YSOs, such as rotational temperature maps derived from NH_3. Both identification tools are required since mm emission finds the most embedded sources but not the less massive, while NH_3 seems to be a good tool to identify the less massive sources which are already heating the dense gas, but fails to indentify the coldest sources.

It is clear that the list in Table 7.1 must be improved with a larger number of regions and with higher mass sensitivity, in order to better determine the properties of the mm/submm 'clusters' around massive protostars. However, note that Table 7.1 constitutes the first list of intermediate/high-mass regions observed in the mm with sensitivities *similar* to those of the infrared. Thus, one can attempt to compare the results in the infrared with those in the mm, at least to have a first idea of the possible trends deserving further investigation.

7.2   Continuous star formation in the four cluster environments

A general result from the four cluster environments studied in this work is that we find sources in different evolutionary stages. In all four regions we find that the most massive source has weak mm continuum emission associated with it and/or weak emission from dense gas, suggesting that this source has already cleared up most of its surrounding material. Some of the other sources, which are low-mass sources, have strong mm continuum emission and/or emission from dense gas associated, suggestive of being still deeply embedded and thus in earlier evolutionary stages. However, this alone is not implying continuous (non-coeval) star formation, since high-mass stars evolve much faster to the main sequence than low-mass stars (e. g., Bernasconi & Maeder 1996), and the different evolutionary stages could be the result of evolution at different rates, depending on the mass of the YSO.

What is really suggesting that star formation has not been simultaneous in the four cluster environments is the different evolutionary stages found *among* the low-mass sources. In the case of HH 211, HH211 mm and IC348 MMS are classified as Class 0 sources, while most members in the IC 348 cluster are pre-main-sequence stars. As for the other three intermediate/high-mass star forming regions, we find in all cases low-mass sources with strong dust emission and very weak infrared emission along with other low-mass sources already bright in the infrared. Thus, we conclude that star formation in these cluster environments occurs in different episodes.

In addition, given that we observe different evolutionary stages for sources forming in the same molecular cloud, and given that, as seen in § 7.1, we find on average less mm sources around massive protostars than infrared sources around massive stars, this suggests that the timescale in which a YSO is bright in the mm/submm is smaller than the timescale in which a YSO is bright in the infrared. Again we are assuming here that the sensitivities reached in the mm studies and in the infrared studies are comparable, and this should be further investigated in a larger number of regions and assuring mass sensitivities $\sim 0.1\ M_\odot$, but this is however what the data available up to now suggest.

7.3 Spatial distribution of the sources in the four cluster environments

In this section we consider the spatial distribution of the different sources in the four regions studied taking into account the evolutionary stage estimated for each source. In Fig. 7.1 we show a sketch illustrating this for each region, drawn at the same physical scale.

In the IC 348 cluster, the region around HH 211 contains younger protostars than the other parts of the entire cluster (Eislöffel et al. 2003). In the figure we do not plot the pre-main-sequence stars belonging to IC 348, but they are to the north and to the east of the HH 211 region. Toward I20343, starless cores are found only to the east and to the west of the UCHII region, and the YSOs are located to the north. For I00117 the embedded sources lie only to the west of the UCHII region. This is also seen in Fig. 3.2, where we find the large-scale mm continuum emission shifted to the west of the UCHII region traced by the cm emission. Finally, the observations
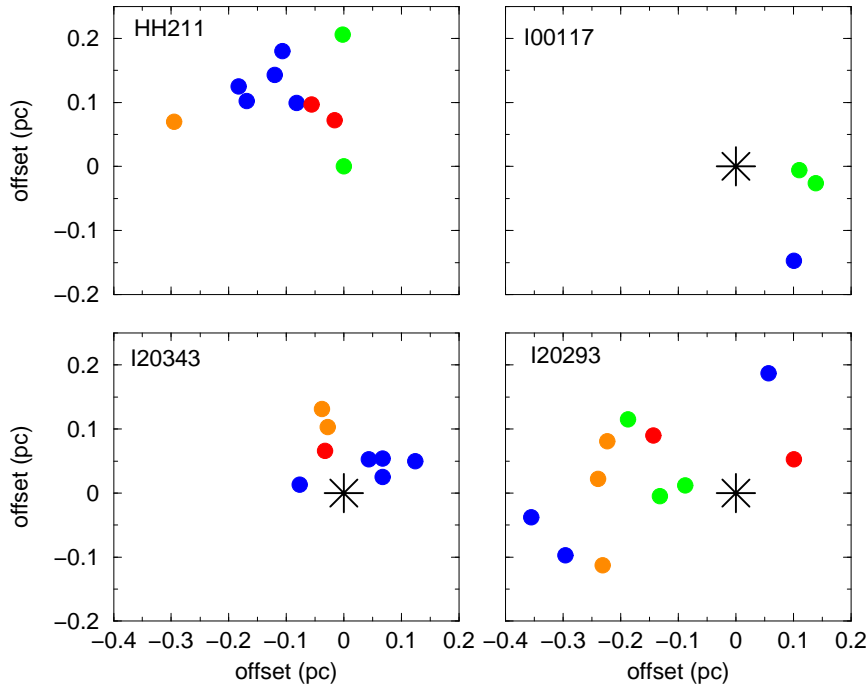
Figure 7.1: Sketch of the spatial distribution of the different sources in the fields of the studied regions. Colors refer to the evolutionary stage estimated for each source. The evolutionary sequence is: blue, starless cores; green, YSOs with mm emission but no infrared emission; orange, YSOs with mm and infrared emission; red, YSO with only infrared emission. The position of the UCHII region is marked with a black star.

toward I20293 have shown evidence of the YSOs having formed preferently in the north of the main cloud, while in the south we found two starless cores. For all four regions, the spatial scales associated with an "evolutionary stage" are ~ 0.1–0.3 pc. Note that the field of view of the observations is in general larger than this size scale, so that this scale is not due to a selection effect of spatial sampling of our observations (see Table 7.1). Thus, in these cluster environments there is star formation localized in regions of the parental cloud of ~ 0.2 pc in size. We note that this size scale is the same as the typical radii of the clusters found around intermediate/high-mass stars, as well as the size of the dense cores in molecular clouds which are likely the progenitors of stellar systems (Jijina et al. 1999; Testi et al. 2000). This suggests that star formation in these cluster environments occurs in dense cloud cores, and that each core started to form stars independently of the other cores.

Let us consider now why one core in a cloud may start to form stars sooner than another core. First, the dense gas may not be uniformly distributed in the cloud, and thus in those parts where the cloud is denser star formation may take place sooner than in lower-density parts. Therefore, the initial conditions of density in a cloud must be important to determine the final distribution of the YSOs. Second, the localized star formation suggests that interaction between the differnt YSOs may also play a role in the spatial distribution of the YSOs.

7.4 The role of interaction in cluster environments

We finally consider whether the spatial distribution of the different sources found in the cluster environments studied in this work is the result of interaction between the sources.

Regarding HH 211, we find that the outflow powered by HH 211 mm is interacting with the medium, entraining the surrounding material and putting it into motion up to high velocities. In addition to this, we do not find any other evidence of interaction of HH 211 mm with the surrounding medium, neither there are evidences of other nearby sources being interacting with HH 211 mm. Thus, for some cluster environments interaction between sources may not take place at all, being HH 211 a nice example.

However, this is not the case for the other regions where we have been able to study interaction. For the case of I20343, IRS 3 seems to be driving a cavity which would be compressing the surrounding material, with the starless cores found to the east and to the west of IRS 3 likely tracing the compression front. This could induce star formation in these cores. Toward I20293, we also find signs of the UCHII region interacting with the edge of the main cloud, where there are two YSOs, suggesting that the formation of these YSOs could have been triggered by the UCHII region. In addition, in I20293 we find evidences of interaction of one of the outflows with a dense NH_3 core in the south of the main cloud, and this could induce the collapse in this core.

From these results one could think that interaction may play an important role in the final distribution of the YSOs in a cloud. However, both in I20343 and I20293 we find that some YSOs cannot be explained through triggering from other sources. For

example, in I20343 the YSOs IRS 1 and IRS 1N are in more advanced evolutionary stages than the cores ahead of the cavity driven by IRS 3, but they are farther out, and this is not consistent with triggering from IRS 3. Similarly, the YSOs in the north of the main cloud in I20293 have evolutionary stages not consistent with triggering from the UCHII region. Thus, we conclude that while for particular cases star formation may have been triggered by other YSOs, triggering alone cannot explain the overall spatial distribution of YSOs in the cluster environments we have studied.

7.5   Conclusions

We have carried out a high-angular resolution and high sensitivity study toward four young cluster environments at mm/submm wavelengths, in order to characterize these clusters and study the interaction between the different members of the cluster. Our main conclusions are:

1. In all four cluster environments we find different evolutionary stages not only between the high-mass and the low-mass sources, but also *among* the low-mass sources, indicating that members in the cluster are not formed simultaneously.

2. We made the first list of massive star-forming regions that have been observed with enough sensitivity to detect the low-mass members around the most massive source at mm/submm wavelengths. From the list (including the regions studied in this work and two regions in the literature) we find that the median number of mm/submm sources around a massive YSO seems to be smaller than the median number of infrared sources around a massive star. Although this should be further confirmed through observations toward other massive star-forming regions, we suggest that the small number of mm sources is due to the fact that the members in a cluster are not formed simultaneously and that the timescale in which a YSO is bright at mm/submm wavelengths is shorter than the timescale in which a YSO is bright at infrared wavelengths.

3. For all four cluster environments we find groups of sources predominantly in a particular evolutionary stage associated with a spatial scale of 0.1–0.3 pc, similar to the size of clusters and dense cores. This suggests that star formation

in these cluster environments occurs in dense cloud cores, and that each core started to form stars independently of the other cores.

4. In the cluster environments forming intermediate/high-mass stars, interaction between the sources seems to be important, and may have triggered star formation in some cases. However, the overall spatial distribution of YSOs in the cluster environment cannot be explained only through triggering, and initial conditions in the cloud may be important as well.

5. From the experience acquired during this work, we find that future observations toward other very young massive star-forming regions must be carried out with sensitivities down to $\sim 0.1\ M_\odot$, and with very good u-v coverage. We additionally find that imaging the mm/submm continuum emission and building temperature maps of the region, for example through the study of NH_3, are complementary tools to indentify embedded low-mass sources. Finally, we find that chemical differentiation may be important in young cluster environments, and thus different dense gas tracers must be used to properly characterize these environments.

Bibliography

Aikawa, Y., Ohashi, N., & Herbst, E. 2003, ApJ, 593, 906

André, P., Ward-Thompson, D., & Barsony, M. 1993, ApJ, 406, 122

André, P., Ward-Thompson, D., Motte, F. 1996, A&A, 314, 625

Andrews, S.M., & Williams, J.P. 2005, ApJ, 619, L175

Anglada, G. 1995, RMxAA, 1, 67

Anglada, G., Estalella, R., Mauersberger, R., Torrelles, J. M., Rodríguez, L. F., Cantó, J., Ho, P. T. P., & D'Alessio, P. 1995, ApJ, 443, 682

Anglada, G., & Rodríguez, L. F. 2002, RMxAA, 38, 13

Arce, H. G., & Goodman, A. A. 2002, ApJ, 575, 911

Bachiller, R., Guilloteau, S., & Kahane, C. 1987, A&A, 173, 324

Bachiller, R., & Pérez Gutiérrez, M. 1997, in *Herbig-Haro Flows and the Birth of Low Mass Stars*, IAU Symp. 182, eds. B. Reipurth & C. Bertout, Kluwer: Dordrecht

Bally, J., & Zinnecker, H. 2005, AJ, 129, 2281

Beckwith, S. V., Sargent, A. I., Chini, R. S., & Güsten, R. 1990, AJ, 99, 924

Belikov, A. N., Kharchenko, N. V., Piskunov, A. E., & Schilbach, E. 1999, A&ASS, 134, 525

Beltrán, M. T., Brand, J., Cesaroni, R., Fontani, F., Pezzuto, S., Testi, L., & Molinari, S. 2006, A&A, astro-ph/0510422

Beltrán, M. T., Cesaroni, R., Neri, R., Codella, C., Furuya, R. S., Testi, L., & Olmi, L. 2004, ApJ, 601, L187

Beltrán, M. T., Estalella, R., Anglada, G., Rodríguez, L. F., Torrelles, J. M. 2001, AJ, 121, 1556

Beltrán, M. T., Girart, J. M., Estalella, R., Ho, P. T. P., & Palau, A. 2002, ApJ, 573, 246

Benson, P. J., Caselli, P., & Myers, P. C. 1998, ApJ, 506, 743

Benson, P. J., & Myers, P. C. 1989, ApJS, 71, 89

Bernasconi, P. A., & Maeder, A. 1996, A&A, 307, 829

Beuther, H., Hunter, T. R., Zhang, Q., Sridharan, T. K., Zhao, J.-H., Sollins, P., Ho, P. T. P., Ohashi, N., Su, Y. N., Lim, J., Liu, S.-Y. 2004a, ApJ, 616, L23

Beuther, H., & Schilke, P. 2004, Science, 303, 1167

Beuther, H., Schilke, P., & Gueth, F. 2004b, ApJ, 608, 330

Beuther, H., Schilke, P., Gueth, F., McCaughrean, M., Andersen, M., Sridharan, T. K., & Menten, K. M. 2002a, A&A, 387, 931

Beuther, H., Schilke, P., Menten, K. M., Motte, F., Sridharan, T. K., Wyrowski, F. 2002b, ApJ, 566, 945

Beuther, H., Schilke, P., Menten, K. M., Motte, F., Sridharan, T. K., Wyrowski, F. 2005a, ApJ, 633, 535

Beuther, H., Schilke, P., Sridharan, T. K., Menten, K. M., Walmsley, C. M., & Wyrowski, F. 2002c, A&A, 383, 892

Beuther, H., Schilke, P., & Stanke, T. 2003, A&A, 408, 601

Beuther, H., Schilke, P., & Wyrowsky, F. 2004c, ApJ, 615, 832

Beuther, H., Walsh, A., Schilke, P., Sridharan, T. K., Menten, K. M., & Wyrowski, F. 2002d, A&A, 390, 289

Beuther, H., Zhang, Q., Hunter, T. R., Sridharan, T. K., Zhao, J.-H., Sollins, P., Ho, P. T. P., Liu, S.-Y., Ohashi, N., Su, Y. N., Lim, J. 2004d, ApJ, 616, L19

Beuther, H., Zhang, Q., Sirdharan, T. K., & Chen, Y. 2005b, ApJ, 628, 800

Bica, E., Dutra, C. M., & Barbuy, B. 2003, A&A, 397, 177

Boger, G. I., & Sternberg, A. 2005, ApJ, 632, 302

Bonnell, I. A., Bate, M. R., Clarke, C. J., & Pringle, J. E. 2001, MNRAS, 323, 785

Bonnell, I. A., Bate, M. R., & Zinnecker, H. 1998, MNRAS, 298, 93

Bontemps, S., André, P., Terebey, S., Cabrit, S. 1996, A&A, 311, 858

Boogert, A. C. A., Blake, G. A., & Öberg, K. 2004, ApJ, 615, 344

Boulard, M.-H., Caux, E., Monin, J.-L., Nadeau, D., & Rowlands, N. 1995, A&A, 300, 276

Bronfman, L., Nyman, L. A., & May, J. 1996, A&ASS, 115, 81

Calvet, N., Patiño, A., Magris, G., & D'Alessio, P. 1991, ApJ, 380, 617

Caratti o Garatti, A., Giannini, T., Nisini, B. & Lorenzetti, D. 2006, A&A, astro-ph/0512098

Carpenter, J. M., Meyer, M. R., Dougados, C., Strom, S. E., & Hillenbrand, L. A. 1997, AJ, 114, 198

Carpenter, J. M., Snell, R. L., & Schloerb, F. P. 1990, ApJ, 362, 147

Carpenter, J. M., Snell, R. L., & Schloerb, F. P. 1995, ApJ, 450, 201

Carpenter, J. M., Snell, R. L., Schloerb, F. P., & Skrutskie, M. F. 1993, ApJ, 407, 657

Carpenter, J. M. 2000, AJ, 120, 3139

Carral, P., Kurtz, S., Rodríguez, L. F., Martí, J., Lizano, S., & Osorio, M. 1999, RMxA&A, 35, 97

Caselli, P., Benson, P., Myers, P. C., & Tafalla, M. 2002a, ApJ, 572, 238

Caselli, P., Walmsley, C. M., Zucconi, A., Tafalla, M., Dore, L., & Myers, P. C. 2002b, ApJ, 565, 344

Cesaroni, R., Felli, M., Jenness, T., Neri, R., Olmi, L., Robberto, M., Testi, L., & Walmsley, C. M. 1999a, A&A, 345, 949

Cesaroni, R., Felli, M., Testi, L., Walmsley, C. M., & Olmi, L. 1997, A&A, 325, 725

Cesaroni, R., Felli, M., & Walmsley, C. M. 1999b, A&AS, 136, 333

Chandler, C. J., & Richer, J. S. 2001, ApJ, 555, 139

Chen, H.-R., Welch, W. J., Wilner, D. J., Sutton, E. C. 2005, in *Protostars and Planets V*, Proceedings of the Conference held October 24-28, 2005, in Hilton Waikoloa Village, Hawaii, LPI Contribution No. 1286, p.8418

Churchwell, E. 1997, in *Herbig-Haro Flows and the Birth of Low Mass Stars*, eds. B. Reipurth, & C. Bertout, IAU Symposium 182, Kluwer Academic Publishers, p. 525

Clarke, C. J., Bonnell, I. A., & Hillenbrand, L. A. 2000, in *Protostars & Planets IV*, eds. V. Mannings, A. P. Boss, & S. S. Russell, (Tucson: University of Arizona Press) p. 151

Codella, C., & Felli, M. 1995, A&A, 302, 521

Codella, C., Lorenzani, A., Gallego, A. T., Cesaroni, R., & Moscadelli, L. 2004, A&A, 417, 615

Comerón, F., Pasquali, A., Rodighiero, G., Stanishev, V., De Filippis, E., López Martí, B., Gálvez Ortiz, M. C., Stankov, A., & Gredel, R. 2002, A&A, 389, 874

Comoretto, G., Palagi, F., Cesaroni, R., Felli, M., Bettarini, A., Catarzi, M., et al. 1990, A&AS, 84, 179

Crapsi, A., Caselli, P., Walmsley, C. M., Myers, P. C., Tafalla, M., Lee, C. W., & Bourke, T. L. 2005, ApJ, 619, 379

Cutri, R. M., Skrutskie, M. F., van Dyk, S., Beichman, C. A., Carpenter, J. M., Chester, T., Cambresy, L., Evans, T., Fowler, J., Gizis, J. et al. 2003, VizieR On-line Data Catalog: II/246, University of Massachusetts and Infrared Processing and Analysis Center, IPAC/California Institute of Technology

D'Alessio, P. 1996, PhD Thesis, Universidad Nacional Autónoma de México

Davis, C. J., Smith, M. D., Eislöffel, J., Davies, J. K. 1999, MNRAS, 308, 539

Davis, C. J., Varricatt, W. P., Todd, S. P., & Ramsay Howat, S. K. 2004, A&A, 425, 981

Deharveng, L., Zavagno, A., & Caplan, J. 2005, A&A, 433, 565

Dickman, R. L. 1978, ApJS, 37, 407

Dutra, C. M., & Bica, E. 2001, A&A, 376, 434

Dyson, J. E., & Williams, D. A. 1997, in *The Physics of the Interstellar Medium*, eds. R. J. Tayler, & M. Elvis, The Graduate Series in Astronomy

Edgar, R., & Clarke, C. 2004, MNRAS, 349, 678

Eislöfel, J., Froebrich, D., Stanke, T., & McCaughrean, M. J. 2003, ApJ, 595, 259

Elmegreen, B. G., Efremov, Y., Pudritz, R. E., & Zinnecker, H. 2000, in *Protostars & Planets IV*, eds. V. Mannings, A. P. Boss, & S. S. Russell, Tucson: University of Arizona Press, p. 179

Everett et al. 1995, AJ, 110, 1295

Felli, M., Massi, F., Navarrini, A., Neri, R., Cesaroni, R., & Jenness, T. 2004, A&A, 420, 553

Fich, M. 1993, ApJSS, 86, 475

Fontani, F., Cesaroni, R., Testi, L., Walmsley, C. M., Molinari, S., Neri, R., Shepherd, D., Brand, J., Palla, F., & Zhang, Q. 2004, A&A, 414, 299

Franco-Hernández, R., & Rodríguez, L. F. 2004, ApJ, 604, L105

Froebrich, D. 2005, ApJSS, 156, 169

Fuente, A., Martín-Pintado, J., Cernicharo, J., & Bachiller, R. 1993, A&A, 276, 473

Fuller, G. A., Williams, S. J., & Sridharan, T. K. 2005, A&A, 442, 949

Fürst, E., Reich, W., Reich, P., & Reif, K. 1990, A&ASS, 85, 805

Furuya, R. S., Cesaroni, R., Codella, C., Testi, L., Bachiller, R., & Tafall M. 2002, A&A. 390, L4

Garay, G., Ramírez, S., Rodríguez, L. F., Curiel, S., Torrelles, J. M. 1996, ApJ, 459, 193

Garay, G., & Lizano, S. 1999, PASP, 111, 1049

Garay, G., Rodríguez, L. F., & van Gorkom, J. H. 1986, ApJ, 309, 553

Garrod, R. T., Williams, D. A., Hartquist, T. W., Rawlings, J. M. C., & Viti, S. 2005, MNRAS, 356, 654

Gerhard, O., Arnaboldi, M., Freeman, K., & Okamura, S. 2002, ApJ, 580, L121

Gibb, A. G., Hoare, M. G.,Little, L. T., & Wright, M. C. H. 2003a, MNRAS, 339, 1011

Gibb, A. G., Hoare, M. G., Mundy, L. G., & Wyrowski, F. 2003b, in *Star formation at high angular resolution*, ASPCS, eds. R. Jayawardhana, M. G. Burton, & T. L. Bourke

Girart, J. M., Curiel, S., Rodríguez, L. F., & Cantó, J. 2002, RMxA&A, 38, 169

Girart, J. M., Estalella, R., Anglada, G., Torrelles, J. M., Ho, P. T. P., & Rodríguez, L. F. 1997, ApJ, 489, 734

Girart, J. M., Estalella, R., & Ho, P. T. P. 1998, ApJ, 495, L59

Girart, J. M., Rodríguez, L. F., Anglada, G., Estalella, R., Torrelles, J. M., Martí, J., Peña, M., Ayala, S., Curiel, S., & Noriega-Crespo, A. 1994, ApJ, 435, L145

Girart, J. M., Viti, S., Williams, D. A., Estalella, R., & Ho, P. T. P. 2002, A&A, 388, 1004

Gómez, M., Hartmann, L., Kenyon, S. J., & Hewett, R. 1993, AJ, 105, 1927

Gómez, Y., Rodríguez, L. F., Girart, J. M., Garay, G., & Martí, J. 2003, ApJ, 597, 414

Gordon, M. 1988, in *Galactic and Extragalactic Radio Astronomy*, eds. G. L. Verschuur, & K. I. Kellermann, New York: Springer-Verlag, p. 37

González-Avilés, M., Lizano, S., & Raga, A. 2005, ApJ, 2005, 621, 359

Graham, J. A., & Frogel, J. A. 1985, ApJ, 289, 331

Gueth, F., & S., Guilloteau 1999, A&A, 343, 571

Hartmann, L., Kenyon, S. J. 1985, ApJ, 299, 462

Hartmann, L., Kenyon, S. J. 1996, ARAA, 34, 207

Hartmann, L., Kenyon, S. J., Hewett, R., Edwards, S., Strom, K. M., Strom, S. E., & Stauffer, J. R. 1989, 338, 1001

Hatchell, J., Richer, J. S., Fuller, G. A., Qualtrough, C. J., Ladd, E. F., & Chandler, C. J. 2005, A&A, 440, 151

Healy, K. R., Hester, J. J., & Claussen, M. J. 2004, ApJ, 610, 835

Hennebelle, P., Whitworth, A. P., Gladwin, P. P., & André, Ph. 2003, MNRAS, 340, 870

Hester, J. J., & Desch, S. J. 2005, in *Chondrites and the Protoplanetary Disk*, eds. A. N. Krot, E. R. D. Scott, & B. Reipurth, San Francisco: Astronomical Society of the Pacific, 341, p. 107

Hillenbrand, L. A. 1995, PhD Thesis, University of Massachusetts

Hillenbrand, L. A., & Hartmann, L. W. 1998, ApJ, 492, 540

Hirano, N., Liu, S.-Y., Shang, H., Ho, P. T. P., Huang, H.-C., Kuan, Y.-J., McCaughrean, M. J., & Zhang, Q. 2006, ApJ, 636, L141

Ho, P. T. P., Moran, J.M., & Lo, K.Y. 2004, ApJ, 616, L1

Ho, P. T. P., & Townes, C. H. 1983, ARA&A, 21, 239

Hodapp 1994, ApJS, 94, 615

Hofner, P., Cesaroni, R., Rodríguez, L. F., Martí, J. 1999, A&A, 345, L43

Hollenbach, D., Johnstone, D., Lizano, S., & Shu, F. 1994, ApJ, 428, 654

Hotzel, S., Harju, J., & Walmsley, C. M. 2004, A&A, 415, 1065

Hughes, V. A., & MacLeod, G. C 1994, ApJ, 427, 857

Hunter, T. R., Phillips, T. G., & Menten, K. M. 1997, ApJ, 478, 283

Israel, F. P., & Felli, M. 1978, A&A, 63, 325

Jaffe, D. T., Hildebrand, R. H., Keene, J., Harper, D. A., Loewenstein, R. F., & Moran, J. M. 1984, ApJ, 281, 225

Jaffe, D. T., Zhu, Q., Lacy, J. H., Richter, M. J., & Greathouse, T. K. 2004, in *Proceedings of the ESO Workshop on High Resolution Infrared Spectroscopy in Astronomy*, Garching, Germany, astro-ph/0403454

Jenness, T., Scott, P. F., & Padman, R. 1995, MNRAS, 276, 1024

Jijina, J. & Adams, F. C. 1996, ApJ, 462, 874

Jijina, J., Myers, P. C., & Adams, F. C. 1999, ApJSS, 125, 161

Jones, T. J., Woodward, C. E., & Kelley, M. S. 2004, AJ, 128, 2448

Kahn, F. D. 1974, A&A, 37, 149

Kenyon, S. J., Hartmann, L., Gómez, M., Carr, J. S., & Tokunaga, A. 1993, AJ, 105, 1505

Keto, E. 2002, ApJ, 580, 980

Keto, E. 2003, ApJ, 599, 1196

Keto, E., & Wood, K. 2006, astro-ph/051006

Kim, K. T., & Koo, B. C. 2003, ApJ, 596, 362

Klein, R., Posselt, B., Schreyer, K., Forbrich, J., & Henning, T. 2005, ApJS, 161, 361

Krumholz, M. R., McKee, C. F., & Klein, R. I. 2005a, ApJ, 618, L33

Krumholz, M. R., McKee, C. F., & Klein, R. I. 2005b, Nature, 438, 332

Kumar, M.S.N., Bachiller, R., & Davis, C.J. 2002, ApJ, 576, 313

Kumar, M. S. N., Fernandes, A. J. L., Hunter, T. R., Davis, C. J., & Kurtz, S. 2003, A&A, 412, 175

Kumar, M. S. N., Keto, E., & Clerkin 2006, A&A, astro-ph/0512266

Kumar, M. S. N., Tafalla, M., & Bachiller, R. 2004, A&A, 426, 195

Kurtz, S., Churchwell, E., & Wood, D. O. S. 1994, ApJSS, 91, 659

Lada, C. J. 1999, in *The Origin of Stars and Planetary Systems*, eds. C. J. Lada, and N. D. Kylafis, Kluwer Acad. Publ., p. 143

Lada, C. J., & Lada, E. A. 2003, ARA&A, 41, 57

Lada, C. J., Young, E. T., & Greene, T. 1993a, ApJ, 408, 471

Lada,E. A., Bally, J., & Stark, A. A. 1991a, ApJ, 368, 432

Lada,E. A., DePoy, D. L., Evans, J. H., & Gatley, I. 1991b, ApJ, 371, 171

Lada, E. A., & Lada, C. J. 1995, AJ, 109, 1682

Lada, E. A., Strom, K. M., & Myers, P. C. 1993b, in *Protostars & Planets III*, eds. E. H. Levy and J. I. Lumine, Tucson: University of Arizona Press p. 245

Larson, R. B. 2003, Reports on Progress in Physics, 66, 1651, astro-ph/0306595

Le Duigou, J.-M. & Knödlseder, J. 2002, A&A, 392, 869

Lee, H.-T., Chen, W. P., Zhang, Z.-W., & Hu, J.-Y. 2005, ApJ, 624, 808

Lefloch, B., Castets, A., Cernicharo, J., Langer, W. D., & Zylka, R. 1998, A&A, 334, 269

Li, W., Evans, N. J., & Lada, E. A. 1997, ApJ, 488, 277

Li, D., Goldsmith, P. F., & Menten, K. 2003, ApJ, 587, 262

Luhman, K. L., Engelbracht, C. W., & Luhman, M. L. 1998, ApJ, 499, 799

Mac Low, M.-M., & Klessen, R. F. 2004, Reviews of Modern Physics, 76, 125

Maddalena, R., Morris, M., Moscowitz, J., & Thaddeus, P. 1986, ApJ, 303, 375

Massi, F., Lorenzetti, D., & Giannini, T. 2003, A&A, 399, 147

Massi, F., Lorenzetti, D., Giannini, T., Vitali, F. 2000, A&A, 353, 598

Masson, C. R., & Chernin, L. M. 1993, ApJ, 414, 230

McCaughrean, M. J., Rayner, J. T., & Zinnecker, H. 1994, ApJ, 436, L189

McCutcheon, W. H., Sato, T., Dewdney, P. E., & Purton, C. R. 1991, AJ, 101, 1435

McCutcheon, W. H., Sato, T., Purton, C. R., Matthews, H. E., & Dewdney, P. E. 1995, AJ, 110, 1762

McKee, C. F., & Tan, J. C. 2003, ApJ, 585, 850

McKee, C. F., & Tan, J. C. 2002, Nature, 416, 59

Megeath, S. T., Herter, T., Beichman, C., Gautier, N., Hester, J. J., Rayner, J., & Shupe, D. 1996, A&A, 307, 775

Miralles, M.P., Rodríguez, L.F., & Scalise, E. 1994, ApJSS, 92, 173

Molinari, S., Brand, J., Cesaroni, R., & Palla, F. 1996, A&A, 308, 573

Molinari, S., Brand, J., Cesaroni, R., Palla, F., & Palumbo, G.G.C. 1998a, A&A, 336, 339

Molinari, S., Testi, L., Brand, J., Cesaroni, R., & Palla, F. 1998b, ApJ, 505, L39

Molinari, S., Brand, J., Cesaroni, R., & Palla, F. 2000, A&A, 355, 617

Molinari, S., Testi, L., Rodríguez, L. F., & Zhang, Q. 2002, ApJ, 570, 758

Morata, O., Girart, J. M., & Estalella, R. 2003, A&A, 397, 181

Moriarty-Schieven, G. H., Johnstone, D., Bally, J., & Jenness, T. 2006, ApJ, 641, astro-ph/0512351

Moscadelli, L., Cesaroni, R., & Rioja, M.J. 2005, A&A, 438, 889

Motte, F., André, P., Ward-Thompson, D., Bontemps, S. 2001, A&A, 372, L41

Mueller, K. E., Shirley, Y. L., Evans II, N. J., & Jacobson, H. R. 2002, ApJS, 143, 469

Nakano, T. 1989, ApJ, 345, 464

Nikolić, S. 2004, in *Pre-Protostellar and Low-Mass Star Forming Clouds in Cepheus*, Pub. Astron. Obs. Belgrade, No. 78

Nisini, B., Codella, C., Giannini, T., & Richer, J. S. 2002, A&A, 395, 25

Ojha, D. K., Tamura, M., Nakajima, Y., Fukagawa, M., Sugitani, K., Nagashima, C., Nagayama, T., Nagata, T., Sato, S., Pickles, A. J., & Ogura, K. 2004, ApJ, 608, 797

Osorio, M., Lizano, S., & D'Alessio, P. 1999, ApJ, 525, 808

Padoan, P., & Nordlund, A., 2002, ApJ, 576, 870

Palla, F., & Stahler, S.W. 1994, ASPC, 62, 391

Panagia, N. 1973, AJ, 78, 929

Patel, N., Curiel, S., Sridharan, T. K., Zhang, Q., Hunter, T. R., Ho, P. T. P., Torrelles, J. M., Moran, J. M., Gómez, J. F., & Anglada, G. 2005, Nature, 437, 109

Peretto, N., André, P., & Belloche, A. 2006, A&A, 445, 979

Pestalozzi, M. R. 2004, PhD Thesis, Chalmers University of Technology

Phelps, R. L., & Lada, E. A. 1997, ApJ, 477, 176

Pirogov, L., Zinchenko, I., Caselli, P., Johansson, L. E. B., & Myers, P. C. 2003, A&A, 405, 639

Porras, A., Christopher, M., Allen, L., Di Francesco, J., Megeath, S. T., & Myers, P. C. 2003, AJ, 126, 1916

Quillen, A. C., Thorndike, S. L., Cunningham, A., Frank, A., Gutermuth, R. A., Blackman, E. G., Pipher, J. L., & Ridge, N. 2005, ApJ, 632, 941

Ramsay, S. K., Chrysostomou, A., Geballe, T. R., Brand, P. W. J. L., Mountain, M. 1993, MNRAS, 263, 695

Redman, R. O., Feldman, P. A., Wyrowski, F., Coté, S., Carey, S. J., & Egan, M. P. 2003, ApJ, 586, 1127

Reid, M. A., & Wilson, C. D. 2005, ApJ, 625, 891

Reipurth, B. & Bally, J. 2001, ARA&A, 39, 403

Reipurth, B., Bally, J., & Devine, D. 1997 AJ, 114, 2708

Reynolds, S. 1986, ApJ, 304, 713

Richards, P.J., Little, L.T., Toriseva, M., & Heaton, B.D. 1987, MNRAS, 228, 43

Rodríguez, M., Rodríguez, L. F., Gyulbudaghian, A.L., & May J. 2002, RMxA&A, 38, 161

Sandell, G., Goss, W. M., & Wright, M. 2005, ApJ, 621, 839

Sandell, G., Wright, M., & Forster, J. R. 2003, ApJ, 590, L45

Sault, R. J., Teuben, P. J., & Wright, M. C. H. 1995, in ASP Conf. Ser. 77, Astronomical Data Analysis Software and Systems IV, ed. R. A. Shaw, H. E. Payne, & J. J. E. Hayes, San Francisco: ASP, p. 433

Sepúlveda, I. 1993, Master Thesis, University of Barcelona

Sepúlveda, I. 2001, PhD Thesis, University of Barcelona

Setia Gunawan, D. Y. A., de Bruyn, A. G., van der Hucht, K. A., & Williams, P. M. 2003, ApJSS, 149, 123

Sewilo, M., Watson, C., Araya, E., Churchwell, E., Hofner, P., & Kurtz, S. 2004, ApJS, 154, 553

Shang, H., Shu, F. H., & Glassgold, A. E. 1998, ApJ, 493, L91

Shepherd, D. S., Borders, T., Claussen, M., Shirley, Y., & Kurtz, S. 2004a, ApJ, 614, 211

Shepherd, D. S., Nürnberger, D. E. A., & Bronfman, L. 2004b, ApJ, 602, 850

Shepherd, D. S., Testi, L., & Stark, D. P. 2003, ApJ, 584, 882

Shirley, Y. L., Evans, N. J., Young, K. E., Knez, C., Jaffe, D. T. 2003, ApJS, 149, 375

Shu, F. H., Adams, F. C., & Lizano, S. 1987, ARA&A, 25, 23

Shu, F. H., Ruden, S. P., Lada, C. J., & Lizano, S. 1991, ApJ, 370, 31

Shu, F. H., Najita, J. R., Shang, H., & Li, Z-Y 2000, in *Protostars & Planets IV*, eds. Mannings, V., Boss, A. P., Russell, S. S., Book-Tucson: University of Arizona Press, p. 789

Shu, F., Tremaine, S., Adams, F., & Ruden, S. 1990, ApJ, 358, 495

Shull, J. M. 1980, ApJ, 238, 860

Simon, R., Stutzki, J., Sternberg, A., & Winnewisser, G. 1997, A&A, 327, L9

Smith, M. D., Suttner, G., & Yorke, H. W. 1997, A&A, 323, 223

Sollins, P. K., & Ho, P. T. P. 2005, ApJ, 630, 987

Sollins, P. K., Hunter, T. R., Battat, J., Beuther, H., Ho, P. T. P., Lim, J., Liu, S. Y., Ohashi, N., Sridharan, T. K., Su, Y. N., Zhao, J.-H., & Zhang, Q. 2004, ApJ, 616, L35

Sollins, P. K., Zhang, Q., Keto, E., & Ho, P. T. P. 2005, ApJ, 624, L49

Sridharan, T. K., Beuther, H., Saito, M., Wyrowski, F., & Schilke, P. 2005, ApJ, 634, L57

Sridharan, T. K., Beuther, H., Schilke, P., Menten, K. M., & Wyrowski, F. 2002, ApJ, 566, 931

Stahler, S. W., Palla, E., & Ho. P. T. P. 2000, in *Protostars & Planets IV*, eds. V. Mannings, A. P. Boss, & S. S. Russell, Tucson: University of Arizona Press, p. 327

Strom, S. E., Strom, K. M., & Carrasco, L. 1974, PASP, 86, 798

Su, Y.-N., Liu, S.-Y., Lim, J., Ohashi, N., Beuther, H., Zhang, Q., Sollins, P., Hunter, T., Sridharan, T. K., Zhao, J.-H., & Ho, P. T. P. 2004, 616, L39

Sugitani, K., Fukui, Y., Mizuno, A., & Ohashi, N. 1989, ApJ, 342, L87

Sugitani, K., Fukui, Y., & Ogura, K. 1991, ApJS, 77, 59

Sugitani, K., Matsuo, H., Nakano, M., Tamura, M., & Ogura, K. 2000, AJ, 119, 323

Sugitani, K., Tamura, M., & Ogura, K. 1995, ApJ, 455, L39

Sung, H., Chun, M. Y., & Bessell, M. S. 2000, AJ, 120, 333

Tafalla, M., Myers, P. C., Caselli, P., & Walmsley, C. M. 2004, A&A, 416, 191

Tafalla, M., Myers, P. C., Caselli, P., Walmsley, C. M., & Comito, C. 2002, ApJ, 569, 815

Testi, L., Palla, F., Natta, A. 1997, A&A, 320, 159

Testi, L., Palla, F., Natta, A. 1998, A&AS, 133, 81

Testi, L., Palla, F., Natta, A. 1999, A&A, 342, 515

Testi, L., Palla, F., Natta, A. 2000, in *From Darkness to Light*, T. Montmerle & P. André eds., ASP Conference Series

Thompson, M. A., White, G. J., Morgan, L. K., Miao, J., Fridlund, C. V. M., & Huldtgren-White, M. 2004, A&A, 414, 1017

Tieftrunk, A. R., Gaume, R. A., Claussen, M. J., Wilson, T. L., & Johnston, K. J. 1997, A&A, 318, 931

Tofani, G., Felli, M., Taylor, G. B., & Hunter, T. R. 1995, A&ASS, 112, 299

Torrelles, J. M., Gómez, J. F., Anglada, G., Estalella, R., Mauersberger, R., & Eiroa, C. 1992a, ApJ, 392, 616

Torrelles, J. M., Rodríguez, L. F., Cantó, J., Anglada, G., Gómez, J. F., Curiel, S., & Ho, P. T. P. 1992b, ApJ, 396, L95

Turner, B. E., & Matthews, H. E. 1984, ApJ, 277, 164

Ungerechts, H., Walmsley, C. M., & Winnewisser, G. 1986, A&A, 157, 207

Usami, M., Hanawa, T., & Fujimoto, M. 1995, PASJ, 47, 271

Valleé, J. P. 1995, AJ, 110, 2256

van der Tak, F. F. S., Menten, K. M. 2005, A&A, 437, 947

van der Tak, F. F. S., van Dishoeck, E. F., Evans II, N. J., & Blake, G. A. 2000, ApJ, 537, 283

van der Walt, D. J., Churchwell, E., Gaylard, M. J., & Goedhart, S. 2003, MNRAS, 341, 270

Vázquez-Semadeni, E. 2004, in *Magnetic Fields and Star Formation: Theory versus Observations*, eds. A.I. Gomez de Castro et al., Kluwer Academic Publishers, Ap&SS, 292, 187, astro-ph/0311064

Walmsley, M. 1995, RMxAA Conference Series, 1, 137

Walsh, A. J., Burton, M. G., Hyland, A. R., & Robinson, G. 1998, MNRAS, 301, 640

Walsh, A. J., Macdonald, G. H., Alvey, N. D. S., Burton, M. G., & Lee, J. K. 2003, A&A, 410, 597

Ward-Thompson, D., Zylka, R., Mezguer, P. G., & Sievers, A. W. 2000, A&A, 355, 1122

Wilking, B. A., Blackwell, J. H., Mundy, L. G., Howe, J. E. 1989, ApJ, 345, 257

Wilking, B. A., Harvey, P. M., Lada, C. J., Joy, M., & Doering, C. R. 1984, ApJ, 279, 291

Williams, J. P., Blitz, L., & McKee, C. F. 2000, in *Protostars & Planets IV*, eds. V. Mannings, A. P. Boss, & S. S. Russell, Tucson: University of Arizona Press, p. 97

Williams, S. J., Fuller, G. A., & Sridharan, T. K. 2004, A&A, 417, 115

Wilner, D. J., Welch, W. J., & Forster, J. R. 1995, ApJ, 449, L73

Wilson, T. L, Boboltz, D. A., Gaume, R. A., & Megeath, S. T. 2003, ApJ, 597, 434

Wiseman, J. J. 2001, in ASP Conf. Ser. 235, Science with the Atacama Large Millimeter Array, ed. A. Wooten, San Francisco: ASP, 179

Wiseman, J. J., & Ho, P. T. P. 1996, Nature, 382, 139

Wolfire, M. G., & Casinelli, J. P. 1987, ApJ, 319, 850

Womack, M., Ziurys, L. M., Wyckoff, S. 1992, ApJ, 387, 417

Wood, D. O. S., & Churchwell, E. 1989, ApJ, 340, 265

Wu, Y., Wei, Y., Zhao, M., Shi, Y., Yu, W., Qin, S., & Huang, M. 2004, A&A, 426, 503

Wu, Y., Zhang, Q., Chen, H., Yang, C., Wei, Y., & Ho, P. T. P. 2005, ApJ, 129, 330

Wyrowski, F., Schilke, P., Walmsley, C. M., & Menten, K. 1999, ApJ, 514, L43

Yang, J., Fukui, Y., Umemoto, T., & Ogawa, H. 1990, ApJ, 362, 538

Yokogawa, S., Kitamura, Y., Momose, M., & Kawabe, R. 2003, ApJ, 595, 266

Yorke, H. W., & Sonnhalter, C. 2002, ApJ, 569, 846

Zapata, L. A., Rodríguez, L. F., Ho, P. T. P., Beuther, H., & Zhang, Q. 2005, astro-ph/0510761

Zavagno, A., Deharveng, L., Comerón, F., Brand, J., Massi, F., Caplan, J., & Russeil, D. 2006, A&A, astro-ph/0509289

Zhang Q., Hunter, T. R., Brand, J., Sridharan, T. K., Cesaroni, R., Molinari, S., Wang, J., & Kramer, M. 2005, ApJ, 625, 864

Zhang, Q., Hunter, T. R., Sridharan, T. K., & Ho, P. T. P. 2002, ApJ, 566, 982

Zhao, M., Wu, Y., Miller, M., & Mao, R. 2003, Acta Astronomica Sinica, 44, 103

Zheng, X. W., Zhang, Q., Ho, P. T. P., & Pratap, P. 2001, ApJ, 550, 301

Zinnecker, H., McCaughrean, M. J., & Wilking, B. 1993, in *Protostars & Planets III*, eds. E. H. Levy and J. I. Lumine, Tucson: University of Arizona Press, p. 429

Appendix

Total mass from thermal continuum emission from dust at mm/submm wavelengths

The total mass M of gas and dust from thermal continuum emission, assuming emission is optically thin is:

$$M = \frac{S_\nu D^2}{B_\nu(T_{\rm d})\kappa_\nu},$$ (1)

where S_ν is the flux density at the frequency ν, D is the distance to the Sun, $B_\nu(T_{\rm d})$ is the Planck function at the dust temperature $T_{\rm d}$, and κ_ν is the absorption coefficient per unit of total mass (gas and dust) density. Writing Eq. (1) in practical units:

$$\left[\frac{M}{M_\odot}\right] = 3.25 \left[\frac{\nu}{\rm GHz}\right]^{-3} \left[\frac{\kappa_\nu}{\rm cm^2~g^{-1}}\right]^{-1} \left[\exp\left(0.048\frac{[\nu/{\rm GHz}]}{[T_{\rm d}/{\rm K}]}\right) - 1\right] \left[\frac{S_\nu}{\rm Jy}\right] \left[\frac{D}{\rm pc}\right]^2$$ (2)

The absorption coefficient in the mm/submm range is adopted to be: $\kappa_\nu = \kappa_0(\nu/\nu_0)^\beta$, where β is the dust emissivity index. For the opacity law of Beckwith et al. (1990), $\left[\frac{\kappa_\nu}{\rm cm^2~g^{-1}}\right] = 0.1 \left[\frac{\nu}{1000~{\rm GHz}}\right]^\beta$, Eq.(2) reads:

$$\left[\frac{M}{M_\odot}\right] = 3.25 \times 10^{-8} \left[\frac{\nu}{1000~{\rm GHz}}\right]^{-(3+\beta)} \left[\exp\left(0.048\frac{[\nu/{\rm GHz}]}{[T_{\rm d}/{\rm K}]}\right) - 1\right] \left[\frac{S_\nu}{\rm Jy}\right] \left[\frac{D}{\rm pc}\right]^2$$ (3)

Physical parameters from cm continuum free-free emission

For free-free optically thin emission from ionized gas the flux density S_ν is:

$$S_\nu \simeq \frac{2k\nu^2}{c^2} T_e \tau \Omega_s, \tag{4}$$

where k is the Boltzman constant, c is the speed of light, T_e is the temperature of the electrons, τ is the opacity, and Ω_s is the solid angle of the source. The opacity is, in practical units (e.g., Gordon 1988):

$$\tau = 0.082 \left[\frac{EM}{\text{cm}^{-6}\text{pc}}\right] \left[\frac{T_e}{\text{K}}\right]^{-1.35} \left[\frac{\nu}{\text{GHz}}\right]^{-2.1}, \tag{5}$$

where EM is the emission measure.

For gas ionized by an OB star, the flux of ionizing photons is $\dot{N}_i = (4\pi/3)R^3 n_e^2 \alpha_2$, with α_2 being the recombination coefficient to the second or upper levels. Given that $EM \simeq n_e^2 2R$, with n_e the density of electrons and R the radius of the source, one cat write $\dot{N}_i$ in terms of the flux density as:

$$\left[\frac{\dot{N}_i}{\text{s}^{-1}}\right] = 7.24 \times 10^{40} \left[\frac{\nu}{8.4 \text{ GHz}}\right]^{0.1} \left[\frac{T_e}{10^4 \text{ K}}\right]^{0.35} \left[\frac{D}{\text{pc}}\right]^2 \left[\frac{S_\nu}{\text{Jy}}\right], \tag{6}$$

where we used $\pi R^2 = \Omega_s D^2$.

Column density of CO:

Let be:

- $J_\nu(T) \equiv \frac{h\nu/k}{e^{h\nu/kT}-1}$, intensity in units of temperature

- T_{ex}, excitation temperature

- $T_{\text{bg}} = 2.73$ K, background radiation temperature

Assuming:

- Local Termodinamic Equilibrium

- partially thick emission: $\int \tau(v)dv \simeq \frac{1}{J_\nu(T_{\text{ex}})-J_\nu(T_{\text{bg}})} \frac{\tau_0}{1-e^{-\tau_0}} \int T_{\text{L}}(v)dv$, being τ_0 the opacity at the line center

- $J_\nu(T_{\text{ex}}) \gg J_\nu(T_{\text{bg}})$

The column density of a linear molecule obtained from the transition $J \rightarrow J-1$ is:

$$N = \frac{3k^2}{4\pi^3 h} \frac{1}{\mu^2 \nu_{10}^2 J^2} T_{\text{ex}} \exp\left(\frac{J(J+1)}{2} \frac{h\nu_{10}}{kT_{\text{ex}}}\right) \frac{\tau_0}{1-e^{\tau_0}} \int T_{\text{L}}(v)dv, \qquad (7)$$

where μ is the electric dipolar momentum of the molecule, and ν_{10} is the frequency of the transition $J = 1 \rightarrow 0$.

For the case of CO, $\mu = 0.110 \times 10^{-18}$ (cgs), and $\nu_{10} = 115.271204$ GHz:

$$\left[\frac{N(\text{CO})}{\text{cm}^{-2}}\right] = 4.32 \times 10^{13} \frac{T_{\text{ex}}}{J^2} \exp\left(\frac{J(J+1)2.77}{T_{\text{ex}}}\right) \frac{\tau_0}{1-e^{\tau_0}} \left[\frac{\int T_{\text{L}}(v)dv}{\text{K km s}^{-1}}\right]. \qquad (8)$$

T_{ex} can be estimated from the intensity of the spectrum at the line center, T_{L0}, assuming the line of CO at the center is optically thick: $T_{\text{ex}} = \frac{h\nu/k}{\ln\left(1+\frac{h\nu/k}{T_{\text{L0}}+J_\nu(T_{\text{bg}})}\right)}$.

The total mass will be:
$$M = \frac{N}{X} A \, 2.8 \, m_{\text{H}}, \qquad (9)$$

where A is the area of the line emission, X is the relative abundance of the observed molecule, and m_{H} is the mass of the atom of hydrogen. We adopted 2.8 as the mean molecular weight per molecule of H_2, which corresponds to an helium abundance of 10%.

For CO, we adopted $X = \frac{N(\text{CO})}{N(H_2)} = 1.8 \times 10^{-4}$ (Dickman 1978):

$$\left[\frac{M}{M_\odot}\right] = 1.25 \times 10^{-16} \left[\frac{A}{\text{pc}^2}\right] \left[\frac{N_{12}}{\text{cm}^{-2}}\right] \qquad (10)$$

Column density of N_2H^+

We particularized for the case of $N_2H^+(1–0)$ the general expression of the column density of a molecule given in Caselli et al. (2002b, Eq. A1). By using the parameters listed in Table A1 from Caselli et al. (2002b) and approximating the partition function to kT_{ex}/hB, with B being the rotational constant of N_2H^+, we obtained:

$$\left[\frac{N(N_2H^+)}{cm^{-2}}\right] = 3.30 \times 10^{11} \frac{T_{ex}}{1 - e^{-4.47/T_{ex}}} \tau_{tot} \left[\frac{\Delta v}{km\ s^{-1}}\right], \tag{11}$$

where τ_{tot} is the total optical depth, and Δv is the intrinsic line width. This expression is given also in Benson et al. (1998).

We performed the simultaneous fit to the seven hyperfine lines of the $J = 1 \to 0$ transition of N_2H^+ by using the HFS method in CLASS. Contrary to the NH_3 hyperfine fits, whose parameters are already included in the CLASS package, for N_2H^+ one must input a file with the values of the relative velocity and strength of each hyperfine. We adopted as reference line for the fits (or main line) the line $F_1 = 2 - 1$, $F = 3 - 2$ and the values in the file were taken from Womack et al. (1992). The last two columns of Table 1 constitute the input file for CLASS.

The output parameters given by CLASS for any fit to hyperfine structure are: $A\tau_m$, the velocity of the reference line, the intrinsic line width and the optical depth of the main hyperfine, τ_m. In CLASS, $A = f(J_\nu(T_{ex}) - J_\nu(T_{bg}))$, with f being the filling factor (assumed to be $\simeq 1$). Note that in Eq. (11) T_{ex} is *not* directly obtained from the CLASS fits, but it must be isolated from the output parameter $A\tau_m$:

$$T_{ex} = \frac{h\nu/k}{\ln\left(1 + \frac{h\nu/k}{A\tau_m/\tau_m + J_\nu(T_{bg})}\right)} \tag{12}$$

Note that the optical depth that must be used in Eq. (11) is τ_{tot}. For $N_2H^+(1–0)$, $\tau_{tot} = \frac{27}{7}\ \tau_m$.

Rotational temperature and column density of NH_3

The rotational temperature derived from $NH_3(1,1)$ and $NH_3(2,2)$ is, following Ho & Townes (1983, Eq. 4):

Table 1: N_2H^+ $J = 1 - 0$ parameters

$F_1'F'$	F_1F	ν (GHz)	Relative veloc. (km s^{-1})	Relative intensity
01	12	93.176310	−8.0164	3
21	11	93.174016	−0.6209	3
23	12	93.173809	0.0000	7
22	11	93.173505	0.9460	5
11	10	93.172078	5.5352	3
12	12	93.171947	5.9742	5
10	11	93.171619	6.9260	1

$$T_{\mathrm{rot}}^{21} = \frac{-41.5}{\ln\left(-\frac{0.283}{\tau_{\mathrm{m}}^1} \ln\left[1 - \frac{T_{\mathrm{m}}^2}{T_{\mathrm{m}}^1}(1 - e^{-\tau_{\mathrm{m}}^1}) \right] \right)}, \tag{13}$$

where τ_{m}^1 is the opacity of the main line of $NH_3(1,1)$, and T_{m}^1 and T_{m}^2 are the antenna temperatures of the main line of $NH_3(1,1)$ and $NH_3(2,2)$ at the line center. To derive this expression, T_{ex} and Δv were asssumed to be the same for both $NH_3(1,1)$ and $NH_3(2,2)$.

By using the nh3(1,1) method of CLASS, one can fit simultaneously the magnetic hyperfine structure of $NH_3(1,1)$. The output parameters are the same as the HFS method described above for N_2H^+. Then:

$$T_{\mathrm{m}}^1 = A\tau_{\mathrm{m}}^1 \frac{1 - e^{-\tau_{\mathrm{m}}^1}}{\tau_{\mathrm{m}}^1} \tag{14}$$

For $NH_3(2,2)$ we fitted one single gaussian, and thus T_{m}^2 is directly an output parameter from the GAUSS method in CLASS.

We estimated the error of T_{rot}^{21} by assuming optically thin emission and that the main sources of error come from T_{m}^1 and T_{m}^2. Defining $R \equiv \frac{T_{\mathrm{m}}^2}{T_{\mathrm{m}}^1}$, the relative error is $\frac{\delta R}{R} = \sqrt{\left(\frac{\delta T_{\mathrm{m}}^1}{T_{\mathrm{m}}^1}\right)^2 + \left(\frac{\delta T_{\mathrm{m}}^2}{T_{\mathrm{m}}^2}\right)^2}$, with δT_{m}^1 and δT_{m}^2 given directly by the CLASS fit.

Then, the error in the rotational temperature has been estimated as:

$$\delta T_{\mathrm{rot}}^{21} = \frac{-41.5}{\ln^2(0.283R)} \frac{\delta R}{R} \tag{15}$$

We converted rotational temperatures to kinetic temperatures by following Tafalla et al. (2004):

$$T_{\mathrm{K}} = \frac{T_{\mathrm{rot}}^{21}}{1 - \frac{T_{\mathrm{rot}}^{21}}{42}\ln\left[1 + 1.1e^{-16/T_{\mathrm{rot}}^{21}}\right]}, \tag{16}$$

which is almost independent of the details of core density and size. This relation is recommended for the range $T_{\mathrm{K}} = 5\text{–}20$ K.

The NH$_3$ column density was derived by following the expression in Sepúlveda (1993; also Ungerechts et al. 1986) and summing up to the rotational level (3,3):

$$N(\mathrm{NH_3}) = N(1,1)\left[\frac{1}{3}e^{23.4/T_{\mathrm{rot}}^{21}} + 1 + \frac{5}{3}e^{-41.5/T_{\mathrm{rot}}^{21}} + \frac{14}{3}e^{-101.2/T_{\mathrm{rot}}^{21}}\right]. \tag{17}$$

Eq. (17) assumes that only metastable levels are populated and that T_{rot} is the same for each pair of rotational levels. $N(1,1)$ is the beam averaged column density in the (1,1) level (Anglada et al. 1995) (we assumed $f \simeq 1$):

$$\left[\frac{N(1,1)}{\mathrm{cm}^{-2}}\right] = 1.58 \times 10^{13} f \frac{e^{1.14/T_{\mathrm{ex}}} + 1}{e^{1.14/T_{\mathrm{ex}}} - 1}\tau_{\mathrm{m}}^1\left[\frac{\Delta v}{\mathrm{km\ s}^{-1}}\right]. \tag{18}$$

To derive Eq. (18), $N(1,1)$ is not approximated to $2N_{+}(1,1)$, but is taken as $N(1,1) = N_{+}(1,1)(1 + \exp(h\nu_{11}/kT_{\mathrm{ex}}))$ (see Sepúlveda (1993) for more details). T_{ex} is derived from the CLASS fits following Eq. (12).